PREPARATION AND OPERATIONS OF THE MISSION PERFORMANCE CENTRE (MPC) FOR THE COPERNICUS SENTINEL-3 MISSION

S3MPC OPT Annual Performance Report - Year 2019

Ref.: S3MPC.ACR.APR.005
Issue: 1.2
Date: 25/06/2020
Contract: 4000111836/14/I-LG

Customer:	ESA	**Document Ref.:**	S3MPC.ACR.APR.005
Contract No.:	4000111836/14/I-LG	**Date:**	25/06/2020
		Issue:	1.2

Project:	PREPARATION AND OPERATIONS OF THE MISSION PERFORMANCE CENTRE (MPC) FOR THE COPERNICUS SENTINEL-3 MISSION		
Title:	S3MPC OPT Annual Performance Report - Year 2019		
Author(s):	L. Bourg and D. Smith with inputs from all OPT ESLs, F. Rouffi, C. Hénocq, J. Bruniquel, C. Cox, M. Etxaluze, E. Polehampton		
Approved by:	O. Lesne, QA Manager	**Authorized by**	J. Bruniquel, Service Manager
Distribution:	Pierre Féménias and Steffen Dransfeld, ESA + S3MPC		
Accepted by ESA	S. Dransfeld, Deputy TO		P. Féménias, TO
Filename	S3MPC.ACR.APR.005 - i1r2 - OPT Annual Performance Report - Year 2019.docx		

ACRI-ST
260 route du Pin Montard
06904 Sophia-Antipolis, France
Tel: +33 (0)4 92 96 75 00 Fax: +33 (0)4 92 96 71 17
www.acri-st.fr

Disclaimer

The work performed in the frame of this contract is carried out with funding by the European Union. The views expressed herein can in no way be taken to reflect the official opinion of either the European Union or the European Space Agency.

Changes Log

Version	Date	Changes
1.0	28/02/2020	First version
1.1	03/03/2020	Updated version
1.2	25/06/2020	Minor updates to correct typos or incomplete statements

List of Changes

Version	Section	Answers to RID	Changes
1.1	6.2.4		Section on L2 cloud screening has been updated
1.2			

Table of content

List of Figures

List of Tables

1 Introduction

This document is the Year 3 (year 2019) Annual Performance Report version of the MPC Optical report prepared by the ACRI-ST consortium for the realisation of the "Preparation and Operations of the Mission Performance Centre (MPC) for the Copernicus Sentinel-3 Mission", ESA contract 4000111836/14/I-LG.

1.1 Scope of the document

This document provides a summary of the end-to-end mission performance from the 1st of January 2019 until the 31st of December 2019 carried out by the S3 Mission Performance Centre during the third year of the routine operations phase.

It addresses more specifically activities related to the Optical mission (an equivalent report – S3MPC.CLS.APR.006 – is issued to address STM activities).

1.2 Applicable documents

The full Applicable Documents (AD) ID correspondence is provided in the Configuration Item Data List (S3MPC.ACR.LST.002).

1.3 Reference documents

The full Reference Documents (RD) ID correspondence is provided in Configuration Item Data List (S3MPC.ACR.LST.002).

1.4 Acronyms and abbreviations

The definition of the acronyms and abbreviations used in this document is provided in the List of Acronyms and Definitions (S3MPC.ACR.LST.003).

2 Executive Summary

2.1 OLCI

Instrument performance

The OLCI-A and OLCI-B **instrument health is excellent**. The sensors temperatures are perfectly well controlled. The nominal radiometric diffusers ageing shows the expected magnitude and spectral behaviours: around 0.4% after 4 years for OLCI-A at 400 nm (Oa01), down to 0.1% at 510 nm (Oa05) and undetectable above; below 0.25% for OLCI-B. The **instrument sensitivity evolution so far is limited to less than 2.5% (OLCI-A)** and no evidence of degradation can be demonstrated: the variation of the instrument sensitivity seems more correlated with a potential spectral evolution of the correcting filters – inside the spectrometers – than to darkening of the optics or loss of sensitivity of the CCD sensors. Sensitivity **evolution of OLCI-B is similar to that of OLCI-A**, and maybe with a slightly higher magnitude for the 400 nm channel. The regularly monitored instrument **SNR performance is well within requirement**.

Spectral Calibration is monitored thanks to dedicated acquisition campaigns. The in-flight spectral campaigns reveal a **high agreement of the in-flight characterisation with the pre-flight** spectral calibration for both A and B sensors, with differences of the OLCI channels centre **smaller than 0.1 nm**, except for channels Oa01 (400 nm) and Oa21 (1020 nm), with up to 0.2 nm. A **small temporal evolution** is observed, different for each camera but approximately identical at all wavelengths; the **observed changes for OLCI-A after 4 years are smaller than 0.2 nm**, and even 0.1 nm for cameras 3 and 5; observed changes for OLCI-B are within 0.2 nm for all cameras but camera 3 have stabilised.

Level 1 products performance

The **geometric performance** is monitored using the ESA GeoCal tool CFI. It is currently **fully compliant for OLCI-A and OLCI-B** to the 0.5 pixel RMS requirement. However, a **significant along-track drift of OLCI-B cameras has been assessed, requiring frequent geometric re-calibration**.

The **OLCI-A** and **OLCI-B Radiometric Gain Models** (gain at reference date + time drift) are used to calibrate Earth Observation data at any date. Their current **performance is better than 0.1%** RMS.

Absolute and inter-band calibration performance is monitored by indirect methods over natural targets. Three methods are used within S3-MPC: the "Rayleigh" method (molecular atmospheric backscattering over clear sky off-glint open ocean) provides absolute calibration in the blue-to-red spectral domain; the "Glint" method (spectral dependency of the Sun specular reflection over ocean) provides inter-band calibration; and the PICS method (Pseudo-Invariant Calibration Sites, temporally stable desert areas) provides absolute calibration over the whole spectral domain as well as cross-mission comparisons for sensors with comparable channels. Two of these methods, Rayleigh and Glint, are undertaken by two different implementations providing very consistent results.

All methods point out an excess of brightness for OLCI-A radiances. Results are in pretty close agreement **around 2-3%** between 560 and 900 nm (Oa06 to Oa19). Rayleigh gives higher biases in the blue-green

(about 6 % while PICS remains around 2%) but this method is suspected to overestimate the simulated signal at those wavelengths so PICS are considered more reliable. Channel Oa21 (1020 nm) is only addressed by the Glint interband method and the results are much worse: 3 to 7%, depending on the reference band. **Radiometric validation for OLCI-B indicates performance within the 2% requirement** for all bands from 560 nm (Oa05) to 940 nm (Oa20). As for OLCI-A, the PICS method shows compliance also in the blue region (Oa1 to Oa4, 400 to 510 nm) while the Rayleigh method shows biases of about 3 to 5%, depending on implementation. The OLCI-B 1020 nm (Oa21) has a similar performance that its OLCI-A counterpart.

Level 2 products performance

Integrated Water Vapour

Integrated Water Vapour has been validated against available in-situ data, according to the surface type: GNSS and AERONET networks over Land, AERONET (coastal stations), AERONET-OC and AERONET Maritime networks over water.

Validation demonstrates that the product is of high quality (bias corrected RMS difference of ~ 0.8 to 1.5 kg/m^2) for retrievals above land surfaces, but there is a systematic overestimation of 9% to 13%. Validation for OLCI-B gives similar results.

The comparison with GNSS stations close to water shows a larger wet bias for the ocean retrievals (up to 25%), and in particular in transition zones between glint and off glint.

Land Products

OLCI Global Vegetation Index (O-GVI, a.k.a. FAPAR)

Quantitative validation against in-situ data is not possible so far, as no in-situ station provides directly comparable products. Several specific campaigns have been conducted however, and significant efforts are undertaken to generate adequate in-situ data. In the meantime, **OLCI FAPAR is regularly compared to MERIS 10-years climatology. There is a fairly good agreement**, accounting for the methodology limitations, with **high correlation, > 0.9** (when sufficient dynamics are present) **and good RMSD (<0.1)**.

OLCI Terrestrial Chlorophyll Index (O-TCI)

For the same reason as for O-GVI, no quantitative validation against in-situ data is available and **comparison with MERIS TCI (M-TCI) climatology** has been done over a number of sites, **showing high correlation, > 0.9** (when sufficient dynamics are present) **and good RMSD (<0.1).**

Marine Products

Water-Leaving reflectances

OLCI-A Level 2 product **validation against in situ measurements shows very good results up to 560 nm**. 665nm band shows poor statistics, longer wavelengths are not validated due to the lack of in situ data.

OLCI-B Level 2 product validation show much more performance, as expected since System Vicarious Calibration has not been applied yet.

Case 1 Chlorophyll product (CHL_OC4Me)

In situ chlorophyll concentration derived from HPLC analysis shows slight overestimation for higher values. Chlorophyll-a measurement shows some estimation errors, however this bias could be due to the low variability for in the HPLC in situ values (0.1-1 $mg.m^{-3}$). More measurement needs to be gathered in order to have a better insight of OLCI estimation on oligotrophic waters.

OLCI-B Level 2 product validation is not available due to lack of in-situ data.

Aerosol Optical Thickness and Angstrom Exponent (T865 and A865)

The validation of OLCI-A aerosol products shows a **high agreement for the aerosol optical thickness** (r^2 = 0.7, *rmsd* < 0.02), if the systematic overestimation of around 40% is corrected. The **Angstrom Exponent agrees with less accuracy** (r^2 = 0.2) but the order of magnitude (1.6) is almost met (bias = -0.2).

OLCI B shows the same pattern as for OLCI A. However, the number of matchups with maritime AERONET is still too low to reach valid quantitative results.

2.2 SLSTR

2.2.1 SLSTR-A

Instrument performance

The SLSTR-A instrument has performed exceptionally well for another year, with all parameters within safe limits. There have been no major anomalies, and only short gaps in data coverage due to ground station issues, manoeuvres or calibration observations.

The cooler has been performing well, with the IR detectors maintained at a stable temperature. Since the cooler cold tip temperature was increased by 1K in July 2018, the time between decontaminations has increased and further measures are planned to increase this further in future.

Radiometric noise levels for the TIR and VIS/SWIR channels have remained stable throughout at pre-launch values. NEDT for the S8 and S9 channels are below 20 mK with no indication of degradation.

Blackbody temperatures have shown a seasonal cycle on top of the daily/orbital temperature cycles, with the highest temperatures of 304.7 K reached during December. The maximum temperature has increased slightly from year to year and will be monitored carefully to prevent it reaching the limit of 305 K necessary to avoid the S7 saturation level.

The VISCAL system is illuminated by the Sun once per orbit and Vicarious calibration results suggest that the system is not degrading significantly over time. The stability is much better than that observed for AATSR on ENVISAT.

The scanners continue to perform well, with orbital mean deviation from the expected position for both nadir and oblique scanners less than 1.5", and a standard deviation less than 5". The flip mirror orbital mean deviation is also less than 1" with a standard deviation <7.4" in the nadir position and <13.6" in oblique position. The worst instantaneous jitter encountered is as good, or better, than previous years.

Level 1 products performance

Validation of the absolute radiometric calibration of the IR channels has been carried out at EUMETSAT using comparisons against IASI-A and B in 2018. The stability of the flight gains, radiometric noise and instrument temperatures suggest that the calibration has not drifted significantly since then.

The VIS and SWIR channels are calibrated via an on-board Solar diffuser-based calibration system. Evaluation of the radiometric calibration has used the techniques developed for AATSR and MERIS and show that the calibration system is stable. Assessment of the VIS channels S1-S3 show good agreement with OLCI and AATSR. At the SWIR wavelengths, there is a significant discrepancy between SLSTR and AATSR and MODIS that must be taken into account in any L2 processing. An adjustment to the L1 processing to correct the main calibration difference is foreseen. The root cause of the anomaly has not been found and is still under investigation.

Geometric calibration is monitored using the GEOCAL tool. Average absolute geometric offsets <0.1 km are achieved for the nadir view and oblique view across-track and <0.2 km for the oblique view along-track.

Several improvements were made in the SLSTR L1 processor from 15th January 2020, including revised ortho-regridding of all channels, revised geo-referencing of SLSTR F1 fire channel, improved geometric calibration for the oblique view, improved S7 brightness temperature upper limit, temporal interpolation of ECMWF meteorological fields, improved quality checks during instrument operations, removal of the SWIR channel 'C' stripe (time domain integrated map) from the L1 product, improved flags, and update of several NetCDF variable attributes.

Level 2 products performance

Marine Products

Validation results are showing that SLSTR-A is providing SSTs mostly within its target accuracy (0.3 K) aside from the N2 retrieval. From the dependence on TCWV, the N2 retrieval is not currently optimal for cases

where the TCWV is > 35 kg/m2, conditions which are especially challenging for the 2-channel nadir-only case. The dependence over time indicates SLSTR-A has been stable over the year.

Land Products

The SLSTR-A SL_2_LST product from SLSTR went operational in the Sentinel 3 PDGS on 5th July 2017 with PB 2.16. No additional updates to the retrieval algorithm have been implemented in the IPF since. However, Processing Baseline 2.29 released on 4th April 2018 included the new Probabilistic Cloud Mask implemented in the IPF at Level-1 and carried through to Level-2. Furthermore, from 26th February 2019 an updated ADF of retrieval coefficients has been implemented in PB 2.47, IPF 06.14. Matchups against ten "Gold Standard" in situ stations show that the overall absolute daytime accuracy is 0.81 K and the absolute night-time accuracy is 0.67 K, both of which are within the mission requirements for LST. Comparisons with respect to the operational LSA SAF LST product are within the uncertainty range when considering the uncertainties from the reference products, and thus the products can be interpreted as consistent with each other. Overall, the SL_2_LST product is performing in line with the 1 K mission requirement for LST.

2.2.2 SLSTR-B

Instrument performance

Instrument and blackbody temperatures for SLSTR-B have been stable on top of the daily/orbital and seasonal trends, and consistent with those for SLSTR-A. The cooler has been performing well, with the IR detectors maintained at a stable temperature.

The visible channel radiometric gain shows a variation from orbit to orbit especially in channels S1 and S2. The reason for this behaviour is thought to be due to partial motional chopping of the VIS detectors by an internal aperture in the VIS FPA. If this is correct, the effect will be present on the earth scene data for S1 and S2.

The NEDT levels are roughly consistent between SLSTR-A and SLSTR-B, except for F1, which shows more orbit-to-orbit variation and higher noise values. This may be caused by motional chopping of the SLSTR-B F1 detectors, which are known to be close to edge of the aperture for SLSTR-B.

The SLSTR-B scanner and flip mean and standard deviations from their expected positions are broadly consistent with SLSTR-A, although the oblique scanner has a slightly larger mean deviation of <3". However, the worst instantaneous jitter for SLSTR-B has increased since the previous year and is higher than SLSTR-A, particularly for the flip mirror.

Level 1 products performance

Initial validation of the absolute radiometric calibration of the IR channels has been carried out by EUMETSAT using comparisons against IASI-A and B. Analysis from the tandem phase comparisons show that the in-flight calibration of SLSTR-B is consistent with that of SLSTR-A.

The S3A and S3B satellites are configured to be 140 degrees out of phase in order to observe complimentary portions of the earth. Figure 1 shows an example combined Level-1 SLSTR-A/SLSTR-B image (daytime only) to show the combined daily SLSTR coverage.

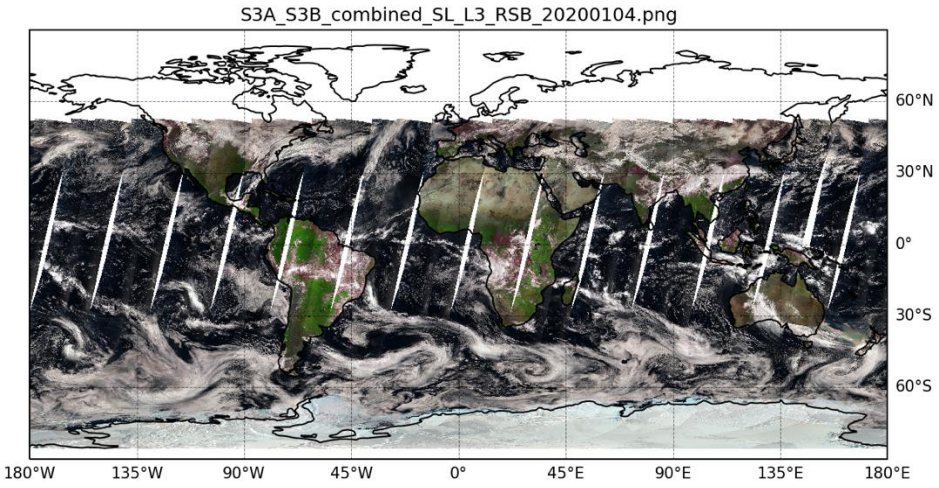

Figure 1: Daytime combined SLSTR-A and SLSTR-B Level-1 image for visible channels on 4th January 2020.

Level 2 products performance

Marine Products

Validation results are showing that SLSTR-B is providing SSTs mostly within its target accuracy (0.3 K) aside from the N2 retrieval. From the dependence on TCWV, the N2 retrieval is not currently optimal for cases where the TCWV is > 35 kg/m^2, conditions which are especially challenging for the 2-channel nadir-only case. The dependence over time indicates SLSTR-B has been stable over the year.

Land Products

The S3B SL_2_LST product from SLSTR went operational in the Sentinel 3 PDGS on 26th February 2019 with PB 1.19 IPF 06.14. Matchups against ten "Gold Standard" in situ stations show that the overall absolute daytime accuracy is 0.79 K and the absolute night-time accuracy is 0.64 K, both of which are within the mission requirements for LST. As for SLSTR-A, comparisons with respect to the operational LSA SAF LST product are within the uncertainty range when considering the uncertainties from the reference products, and thus the products can be interpreted as consistent with each other. Overall, the SL_2_LST product is performing in line with the 1 K mission requirement for LST.

2.3 SYN

Following the evolutions implemented in the SYNERGY L2 and VGS softwares, quality assessments have been re-conducted at the end of year 2018 and confirmed **the clear improvement of the SYN L2 and SYN VGT-P like products**. In particular, the correlation between the Aerosol Optical Thickness data provided by SYN L2 and provided by AERONET stations are close and, despite a bias of 0.2 due to remaining cloud contamination, a regression slope of 1.12 can be drawn comparing these two datasets. Similarly, we observe **a high correspondence between TOA reflectances provided by SYN VGT-like products and the ones provided by PROBA-V products**. A regression slope close to 1 is observed on the BLUE, Red and NIR radiometric measurements. For SWIR measurements however, systematic large differences are observed and could be linked to the SLSTR calibration of SWIR channels.

Several major improvements have been progressively brought to the SYN L2 products during the year 2018. Besides several bugs corrected on the cloud handling and on the handling of Sun Zenith Angles, the global quality of the SYN L2 and SYN VGT like products have been increased as a result of:

1. **A reduction of cloud contamination** with a more appropriate filtering of the cloudy pixels
2. **A discarding of the pixels flagged as affected by snow** from the aerosol retrieval section
3. An inclusion of the **CAMS reanalysis for climatologically filled pixels**
4. **The alignment between SYN VGT-like processing module and PROBA-V processing module** in terms of projection on the 1 km Plate-Carrée grid and in terms of VGT-S composite method

The composite method has been improved by the addition of relevant selection rules before the "maximum-NDVI" selection. Similarly, the projection on the 1 km Plate-Carrée is no longer performed through the duplication of the nearest neighbor but by a stretched bi-cubic interpolation. These two evolutions improve the handling of border pixels in the VGT-like products, decrease the level of noise and provide smoother visual aspect as well as better geographical details in composite products.

Previous SYN VGT-S like product	Current SYN VGT-S like product after the inclusion of improved composite method	
Improved visual aspect and more relevant radiometric content in case of geographical interfaces like river – Zoom over "La Seine"		
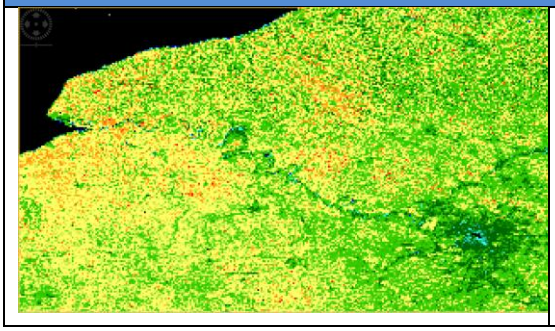	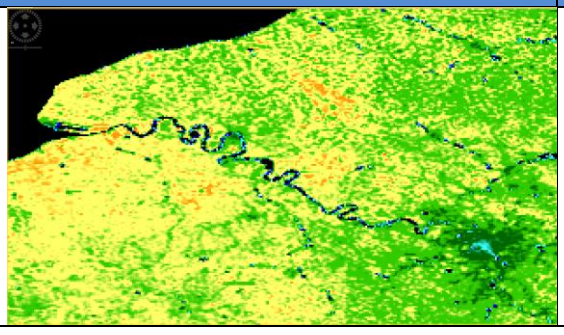	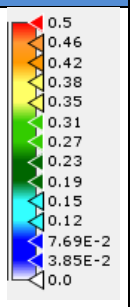

Figure 2: Evolution of VGT-S product after inclusion of improved composite method.

3 Processing baseline description

This section lists all processing baselines that have been delivered between the 1st of February 2017 and the 31st of December 2019, corresponding to year 1, year 2 and year 3 of the routine phase of the MPC contract.

3.1 OLCI

All OLCI processing baselines are listed in Table 1.

Table 1: OLCI Processing Baseline

Processing Baseline	Delivered to PDGS	Deployed in Land PDGS	Changes
2.11	13/02/2017	-	OLCI L2 ADF change (reverse latitudes) for marine ▪ S3A_OL_2_CLP_AX_[…]_MPC_O_AL_003.SEN3
2.13	31/03/2017	12/04/2017	OL_2 Land IPF v06.09 ▪ SIIIMPC-1549 - Degradation in execution time of OLCI L2 v6.8 ▪ OL_2 Marine IPF v06.09 ○ SIIIMPC-1549 “Degradation in execution time of OLCI L2 v6.8” ○ SIIIMPC-1617 “Wrong log-scaled interpolation of CHL_OC4ME LUTs”

Processing Baseline	Delivered to PDGS	Deployed in Land PDGS	Changes
2.16	09/06/2017	05/07/2017	Updated calibration files for reprocessing and OLCI degradation model implementation Updated for reprocessing ▪ OLCI L1 v06.07 ○ SIIIMPC-1618 “EUM/Sen3/NCR/3092: OLCI instrument degradation model is not implemented” ▪ OLCI L1 RAC v06.04 ○ SIIIMPC-1618 “EUM/Sen3/NCR/3092: OLCI instrument degradation model is not implemented” ▪ OLCI L1 SPC v06.03 ○ SIIIMPC-1618 “EUM/Sen3/NCR/3092: OLCI instrument degradation model is not implemented” ▪ OLCI L2 LAND v06.10 ○ SIIIMPC-1674 “no ERROR CODE returned at a failure of the SW” ▪ OLCI L2 MARINE v06.10 ○ SIIIMPC-1674 “no ERROR CODE returned at a failure of the SW” ○ SIIIMPC-1637 “OLCI L2 cloud flagging is contaminating data” ○ SIIIMPC-1639 ”L2 OLCI system vicarious calibration in the VIS is not available” ○ SIIIMPC-1640 “L2 OLCI system vicarious calibration in the NIR is not available” ○ SIIIMPC-1694 “OCNN_FAIL not raised by OutOfRangeOCNN_F OR OutOfScopeOCNN_F” ○ SIIIMPC-1695 ”OLCI L2: remove several useless NN for performances” ○ SIIIMPC-1757 ”OLCI L2 wrong TSM_NN equation”
2.21	04/09/2017	11/10/2017	▪ OL_1_CAL_AX update
2.23	15/09/2017	11/10/2017	OLCI L1, L2 ADF and OLCI L2 SW updated for reprocessing ▪ Calibration coefficient update ▪ Processing Control parameter update (dark coef) ▪ Ocean colour parameters update (Marine) ▪ OLCI L2 v06.11 ○ SIIIMPC-1925 “OLCI L2 GVI Nan on bright surfaces” ○ SIIIMPC-1924 “OLCI L2 inland waters gas correction”

Processing Baseline	Delivered to PDGS	Deployed in Land PDGS	Changes
2.29	16/02/2018	04/04/2018	▪ OL_1_CAL_AX update ○ SIIIMPC-2281 resolution of OLCI camera 3 drift + Dark offset coefficient update
2.38	19/07/2018	29/08/2018	▪ OLCI L1 v06.08 ○ SIIIMPC-1918 EUM/Sen3/AR/3404: Issue in L0 IPF in computing the ANX Cross Time ○ SIIIMPC-2784 EUM/Sen3/NCR/4530: S3B OL1 processing in segmentation fault ○ SIIIMPC-2589 EUM/Sen3/NCR/4324: PUG_SL_1_RBT, PUG_SL_2_WCT and PUG_SL_2_WST cannot find the start/stop orbitReference for the last manifest file ▪ OLCI L1 RAC v06.05 ○ SIIIMPC-1918 EUM/Sen3/AR/3404: Issue in L0 IPF in computing the ANX Cross Time ○ SIIIMPC-2589 EUM/Sen3/NCR/4324: PUG_SL_1_RBT, PUG_SL_2_WCT and PUG_SL_2_WST cannot find the start/stop orbitReference for the last manifest file ▪ OLCI L1 SPC v06.04 ○ SIIIMPC-1918 EUM/Sen3/AR/3404: Issue in L0 IPF in computing the ANX Cross Time ○ SIIIMPC-2589 EUM/Sen3/NCR/4324: PUG_SL_1_RBT, PUG_SL_2_WCT and PUG_SL_2_WST cannot find the start/stop orbitReference for the last manifest file ▪ OLCI L2 LAND v06.12 ○ SIIIMPC-1918 EUM/Sen3/AR/3404: Issue in L0 IPF in computing the ANX Cross Time ○ SIIIMPC-2589 EUM/Sen3/NCR/4324: PUG_SL_1_RBT, PUG_SL_2_WCT and PUG_SL_2_WST cannot find the start/stop orbitReference for the last manifest file ▪ OLCI L2 MARINE v06.12 ○ SIIIMPC-1918 EUM/Sen3/AR/3404: Issue in L0 IPF in computing the ANX Cross Time ○ SIIIMPC-2589 EUM/Sen3/NCR/4324: PUG_SL_1_RBT, PUG_SL_2_WCT and PUG_SL_2_WST cannot find the start/stop orbitReference for the last manifest file
2.42	23/11/2018	12/12/2018	▪ OL_1_CAL_AX update

Processing Baseline	Delivered to PDGS	Deployed in Land PDGS	Changes
2.43	07/12/2018	-	▪ OLCI L2 MARINE v06.13 ○ SIIIMPC-3217 Full orbit gap in S3B OL2 NTC production
S3A: 2.48 S3B: 1.20	22/03/2019	10/04/2019	▪ S3A OL_1 ○ Radiometric Gain Model (based on in-flight BRDF model) ○ Dark correction LUTs ○ Bug corrections ▪ S3B OL_1 ○ Geometric Calibration to correct the along-track drift
S3A: 2.55 S3B: 1.27	12/07/2019	29/07/2019	▪ S3A OL_1 ○ Geometric Calibration to correct the degraded performances at camera interfaces ○ Dark correction LUTs ▪ S3B OL_1 ○ Geometric Calibration to correct the degraded performances at camera interfaces ○ Dark correction LUTs
S3A: 2.58 S3B: 1.30	09/10/2019	29/10/2019	▪ S3A OL_1 ○ Gain model ○ Dark correction LUT ▪ S3B OL_1 ○ Gain model ○ Dark correction LUT ○ Geometric Calibration
S3A: 2.60 S3B: 1.32	25/10/2019	25/11/2019	▪ OLCI L2 product maps update
S3B: 1.34	06/12/2019	17/12/2019	▪ S3B OLCI Level 1 ADF update ○ Dark correction LUT ▪ Geometric calibration

3.2 SLSTR

All SLSTR processing baselines are listed in Table 2.

Table 2: SLSTR Processing Baseline

Processing Baseline	Delivered to PDGS	Deployed in Land PDGS	Changes
2.11	13/02/2017		▪ SLSTR L1 v06.10 ○ SIIIMPC-1476 "Systematic failure in IPF-SL-1 processor, version 06.09" ○ SIIIMPC-1444 "Added processing resources to VISCAL manifest" ○ SIIIMPC-1419 "To avoid the SL1 failure in DEM initialization, before the creation of the symbolic link dem.sen3, if another link already exists it is removed"

2.13	31/03/2017	27/04/2017 (NTC) 04/05/2017 (NRT)	▪ Update of SLSTR L1 TIR ADF (RAL) – SIIIMPC-1368 ○ S3A_SL_1_N_F1AX_[…]_MPC_O_AL_006.SEN3 ▪ S3A_SL_1_N_F2AX_[…]_MPC_O_AL_006.SEN3 ▪ S3A_SL_1_N_S7AX_[…]_MPC_O_AL_006.SEN3 ▪ S3A_SL_1_N_S8AX_[…]_MPC_O_AL_006.SEN3 ▪ S3A_SL_1_N_S9AX_[…]_MPC_O_AL_006.SEN3 ▪ S3A_SL_1_O_F1AX_[…]_MPC_O_AL_006.SEN3 ▪ S3A_SL_1_O_F2AX_[…]_MPC_O_AL_006.SEN3 ▪ S3A_SL_1_O_S7AX_[…]_MPC_O_AL_006.SEN3 ▪ S3A_SL_1_O_S8AX_[…]_MPC_O_AL_006.SEN3 ▪ S3A_SL_1_O_S9AX_[…]_MPC_O_AL_006.SEN3 ▪ VIS/SWIR Channel co-registration - SIIIMPC-980 ○ S3A_SL_1_ANC_AX_[…]_MPC_O_AL_009.SEN3 ▪ Updated geometric calibration of the oblique view (ESTEC) ○ S3A_SL_1_GEC_AX_[…]_MPC_O_AL_006.SEN3 ▪ Updated cloud LUT (RAL) ○ S3A_SL_1_CLO_AX_[…]_MPC_O_AL_004.SEN3 ▪ SST coefficient update (UoR) that refect the results of the inter-algorithm adjustment and uncertainty analysis work ○ S3A_SL_2_D2_CAX_[…]_MPC_O_AL_004.SEN3 ○ S3A_SL_2_D3_CAX_[…]_MPC_O_AL_004.SEN3 ○ S3A_SL_2_N2_CAX_[…]_MPC_O_AL_004.SEN3 ○ S3A_SL_2_N3_CAX_[…]_MPC_O_AL_004.SEN3 ○ S3A_SL_2_N3RCAX_[…]_MPC_O_AL_004.SEN3 ▪ SLSTR L1 v06.11 ○ SIIIMPC-1551 “EUM/Sen3/NCR/3021 - Degradation in execution time of SLSTR L1 v6.10” ○ SIIIMPC-1368 “Radiometric uncertainty field is not filled in SLSTR L1 quality annotation file” ○ SIIIMPC-1370 “Expected SL1 processor performance not met when using FRO or FPO” ○ SIIIMPC-980 “VIS/SWIR Channel co-registration (OIP -142)” ○ SIIIMPC-1622 “SLSTR L1 processor should end gracefully in case manoeuvers are found in the input NAVATT” ▪ SLSTR L2 LAND v06.11 ○ SIIIMPC-1545 “EUM/Sen3/NCR/2976: Failure of the SL_2_WST BRW production due to inconsistency in the input products size” ▪ SLSTR L2 MARINE v06.11

Processing Baseline	Delivered to PDGS	Deployed in Land PDGS	Changes
			○ SIIIMPC-1545 "EUM/Sen3/NCR/2976: Failure of the SL_2_WST BRW production due to inconsistency in the input products size" ○ SIIIMPC-1586 "SL_2_WST missing values in dt_analysis field" ○ SIIIMPC-1627 "Incorrect N3 uncertainties in WST product"
2.15	22/05/2017	05/07/2017	▪ SLSTR L1 v06.12 ○ SIIMPC-1682 "Anomaly in satellite azimuthal angle" ○ SIIIMPC-1774 "Some error log messages should be warnings"

2.16	09/06/2017	05/07/2017	▪ PCP: New switch ○ SW_CLOUD_FOG_LAND added to disable fog low stratus test over land (SIIIMPC-1573) ○ SW_CLOUD_16_SMALL_SCALE and SW_CLOUD_225_SMALL_SCALE switches enabled ○ S3A_SL_1_PCP_AX_[…]_MPC_O_AL_009.SEN3/ ▪ PCP: New switch ○ Value of threshold_3_1_6 has been changed from 0.3 to 0.07 ○ Value of threshold_3_2_25 has been changed from 0.3 to 0.07 ○ New variable min_refl_threshold_1_6 (=0.05) has been included ○ New variable min_refl_threshold_2_25 (=0.05) has been included ○ fog_low_stratus_threshold_na and fog_low_stratus_threshold_ob LUTs have been updated ○ S3A_SL_1_CLO_AX_[…]_MPC_O_AL_005.SEN3 ▪ Update ○ S3A_SL_2_PCP_AX_[…]_MPC_O_AL_003.SEN3 ○ S3A_SL_2_SSESAX_[…]_MPC_O_AL_003.SEN3 ○ S3__SL_2_SST_AX_[…]_MPC_O_AL_002.SEN3 ▪ SLSTR L1 v06.13 ○ SIIIMPC-1793 “SLSTR L1 fillvalues in geolocation” ○ SIIIMPC-1190 “Verification and improvement of the SLSTR 1.6/2.25 histogram cloud test” ○ SIIIMPC-1634 “Visible cloud tests run at night” ○ SIIIMPC-1573 “Fog test switch” ○ SIIIMPC-1777 “‘Boxy’ effect in 2.25 large scale histogram test” ○ SIIIMPC-1620 “EUM/Sen3/NCR/3097: Quality issue with SLSTR L1 cloud screening” ○ SIIIMPC-1723 “Interpolation issue in SLSTR L1 meteo data” ▪ SLSTR L2 LAND v06.12 ○ SIIIMPC-1850 “Implement customized cloud summary flag in SLSTR L2 IPF” ○ SIIIMPC-1565 “Basic clouds switches” ○ SIIIMPC-1859 “SLSTR L2 data over 2500 lines are not processed on some products” ▪ SLSTR L2 MARINE v06.12 ○ SIIIMPC-1026 “Different number of rows in WST compared to WCT” ○ SIIIMPC-1698 “Land flag incorrectly set for tidal regions in SLSTR L2”

Processing Baseline	Delivered to PDGS	Deployed in Land PDGS	Changes
			○ SIIIMPC-1488 “SLSTR Level 2 NEDT values decrease with lower BTs in some scans ○ SIIIMPC-1620 “EUM/Sen3/NCR/3097: Quality issue with SLSTR L1 cloud screening” ○ SIIIMPC-1656 “Incorrect "reference", "comment" and "long_name" attribute values of SL_2_WST___ dt_analysis variable” ○ SIIIMPC-1850 “Implement customized cloud summary flag in SLSTR L2 IPF” ○ SIIIMPC-1565 “Basic clouds switches” ○ SIIIMPC-1859 ”SLSTR L2 data over 2500 lines are not processed on some products”
2.17	26/06/2017	05/07/2017	▪ SLSTR L1 v06.14 ○ SIIIMPC-1885 “SLSTR L1 bug in meteo processing”
2.18	27/06/2017	-	▪ Marine branch ○ SLSTR L2 Change SLSTR L2 PCP thresholds for dt_analysis as a temporary fix to IPF code (by applying scaling factor) – SIIIMPC-1900 “Problem with implementation of dt_analysis quality check CR in SL_2_WST (L2P) - EUM/Sen3/NCR/3380”
2.29	16/02/2018	04/04/2018	▪ Evolution Cloud algorithm ▪ 7 new ADFs + 1 ADF from the SLSTR L2 processing (SL_2_LSTBAX - BIOME) are now included in the processor
2.30	23/02/2018	-	▪ SLSTR L2: IPF SL_2 in version 06.13 ○ New processing switches ○ Updated coefficients for MARINE processing ○ SIIIMPC-1918: AR/3404: Issue in L0 IPF in computing the ANX Cross Time ○ SIIIMPC-2234: Implementation the new bayesian cloud flag in SL2 ○ SIIIMPC-1881 Mistake in "long_name" attribute value of SL_2_WST___ sea_surface_temperature variable ○ SIIIMPC-2475: SL_2_WST___ dt_analysis overflow
2.33	14/03/2018	N/A	▪ IPF SL_2 marine branch in v06.14 ○ SIIIMPC-2510: Incorrect WST quality level assignment

Processing Baseline	Delivered to PDGS	Deployed in Land PDGS	Changes
2.37	17/07/2018	02/08/2018	▪ SL_1 in v06.16 ○ SIIIMPC-2570: The baseline collection for SLSTR chain will be changed from 002 to 003 ○ SIIIMPC-2582 Disable SLSTR c-stripe images ○ SIIIMPC-2589: PUG_SL_1_RBT, PUG_SL_2_WCT and PUG_SL_2_WST cannot find the start/stop orbitReference for the last manifest file ○ SIIIMPC-2600: Misalignment in the SLSTR met fields is impacting Bayesian cloudmask along the coastline ○ SIIIMPC-2606: Use of SST/skin temperature in Probabilistic and Bayesian Cloud detection ○ SIIIMPC-2733: Wrong naming of the meteo parameter SWVL1 ○ SIIIMPC-2839: SLSTR L1 Task tables: wrong ordering of the orbit files used for time initialization ▪ SL_2 Land in v06.14 ○ SIIIMPC-2844: SLSTR L2 issue on the bottom of the image detected during reprocessing ○ SIIIMPC-2589: PUG_SL_1_RBT, PUG_SL_2_WCT and PUG_SL_2_WST cannot find the start/stop orbitReference for the last manifest file ○ SIIIMPC-2875: IPF SL2 deactivate the TDI reading when not present in SL1 input ▪ SL_2 Marine in v06.15 ○ SIIIMPC-2844: SLSTR L2 issue on the bottom of the image detected during reprocessing ○ SIIIMPC-2589: : PUG_SL_1_RBT, PUG_SL_2_WCT and PUG_SL_2_WST cannot find the start/stop orbitReference for the last manifest file
2.43	7/12/2018	N/A	▪ SLSTR L2 Marine: SSES update : Modifications to bias and SD fields

Processing Baseline	Delivered to PDGS	Deployed in Land PDGS	Changes
S3A: 2.47 S3B: 1.19	18/02/2019	25/02/2019	▪ S3A SL_2 update ○ The LST retrieval algorithm has been generated with a new set of retrieval coefficients which utilises an enhanced approach to simulating the across track variation in LST performance when generating the coefficients. ○ Implementation of the new retrieval coefficients has improved the performance of the S3A LST product with respect to intercomparison against operational LSA SAF SEVIRI LST ▪ S3B SL_2 update ○ The LST retrieval algorithm has been generated with a set of retrieval coefficients which utilises an enhanced approach to simulating the across track variation in LST performance when generating the coefficients. ○ Implementation of the retrieval coefficients has improved the comparability between S3A and S3B LST during the Tandem Phase

3.3 SYN

All SYN processing baselines are listed in Table 3.

Table 3: SYN Processing Baseline

Processing Baseline	Delivered to PDGS	Deployed in Land PDGS	Changes
S3A: 2.40 S3B: 1.11	06/09/2018	13/09/2018	▪ First public version
S3A: 2.44 S3B: 1.16	13/12/2018	16/01/2019 (SY2) 21/01/2019 (SY2_VGS)	▪ New IDEPIX cloud flags now used in VGT-P/K products ▪ Correction of AG variable (T550) over ocean set to zero instead of fill value ▪ Correction of NDVI set to 0 instead of _FillValue over ocean in VG products ▪ Improving VGS composite method
S3A: 2.51 S3B: 1.23	24/05/2019	06/06/2019	▪ Corrections of o Synergy wrong generation of time.nc values o Typo in some SYN VGT-P /VGT-S attributes o SY_2_SYN products missing SLSTR oblique scans o SY_2_VGK products with wrong footprint

4 Calibration and characterisation changes

4.1 OLCI

4.1.1 Instrument settings

There has been no change to the OLCI-A or OLCI-B instrument setting during the reporting period.

4.1.2 Evolutions in Radiometric Calibration of EO data

4.1.2.1 OLCI-A

The following evolutions of the EO radiometric calibration auxiliary data have been implemented since beginning of 2018:

- 11/04/2019: PB S3A-2.48 updated the Radiometric Gain Models and Dark Correction tables
- 30/07/2019: PB S3A-2.55 updated the Dark Correction tables
- 29/10/2019: PB S3A-2.58 updated the Radiometric Gain Models and Dark Correction Tables.

4.1.2.2 OLCI-B

The following evolutions of the EO radiometric calibration auxiliary data have been implemented since beginning of 2018:

- 11/04/2019: PB S3B-1.20 updated the Radiometric Gain Models and Dark Correction tables
- 30/07/2019: PB S3B-1.27updated the Dark Correction tables
- 29/10/2019: PB S3B-1.30 updated the Radiometric Gain Models and Dark Correction Tables.

4.2 SLSTR

4.2.1 Instrument settings

4.2.1.1 SLSTR-A

No changes to the SLSTR-A instrument settings were made during the reporting period.

4.2.1.2 SLSTR-B

No changes to the SLSTR-B instrument settings were made during the reporting period.

4.2.2 Evolutions in Radiometric Calibration of EO data

No updates to the SLSTR-A or SLSTR-B radiometric calibration parameters have been applied in the reporting period. Note that the cold tip temperature update in July 2018 had a small effect on the bias in all Level-2 SST retrievals and this will be corrected by an update to the Level-2 ADFs in the future.

From 26th February 2019 an updated ADF of LST retrieval coefficients has been implemented in PB 2.47, IPF 06.14.

5 Summary of performances – OLCI

5.1 Instrument performances

5.1.1 Temperature stability

5.1.1.1 OLCI-A

CCD temperatures are monitored on the long-term using data from Radiometric Calibration acquisitions (see Figure 3). Variations are very small (0.09 C peak-to-peak) and no trend can be identified.

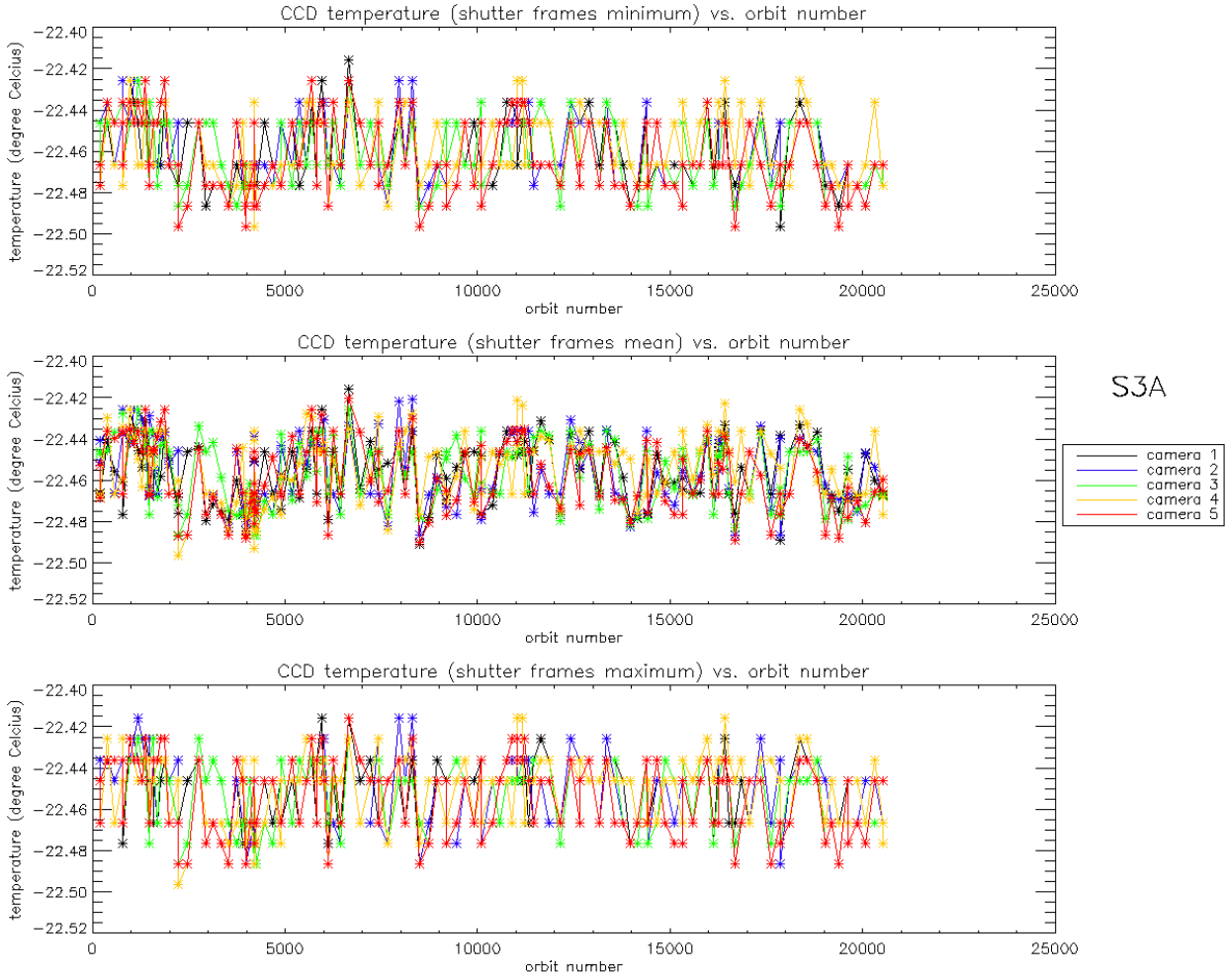

Figure 3: long term monitoring of CCD temperatures using minimum value (top), time averaged values (middle), and maximum value (bottom) provided in the annotations of the Radiometric Calibration Level 1 products, for the Shutter frames, all radiometric calibrations so far.

5.1.1.2 OLCI-B

As for OLCI-A, the variations of CCD temperature are very small (0.08 C peak-to-peak) and no trend can be identified.

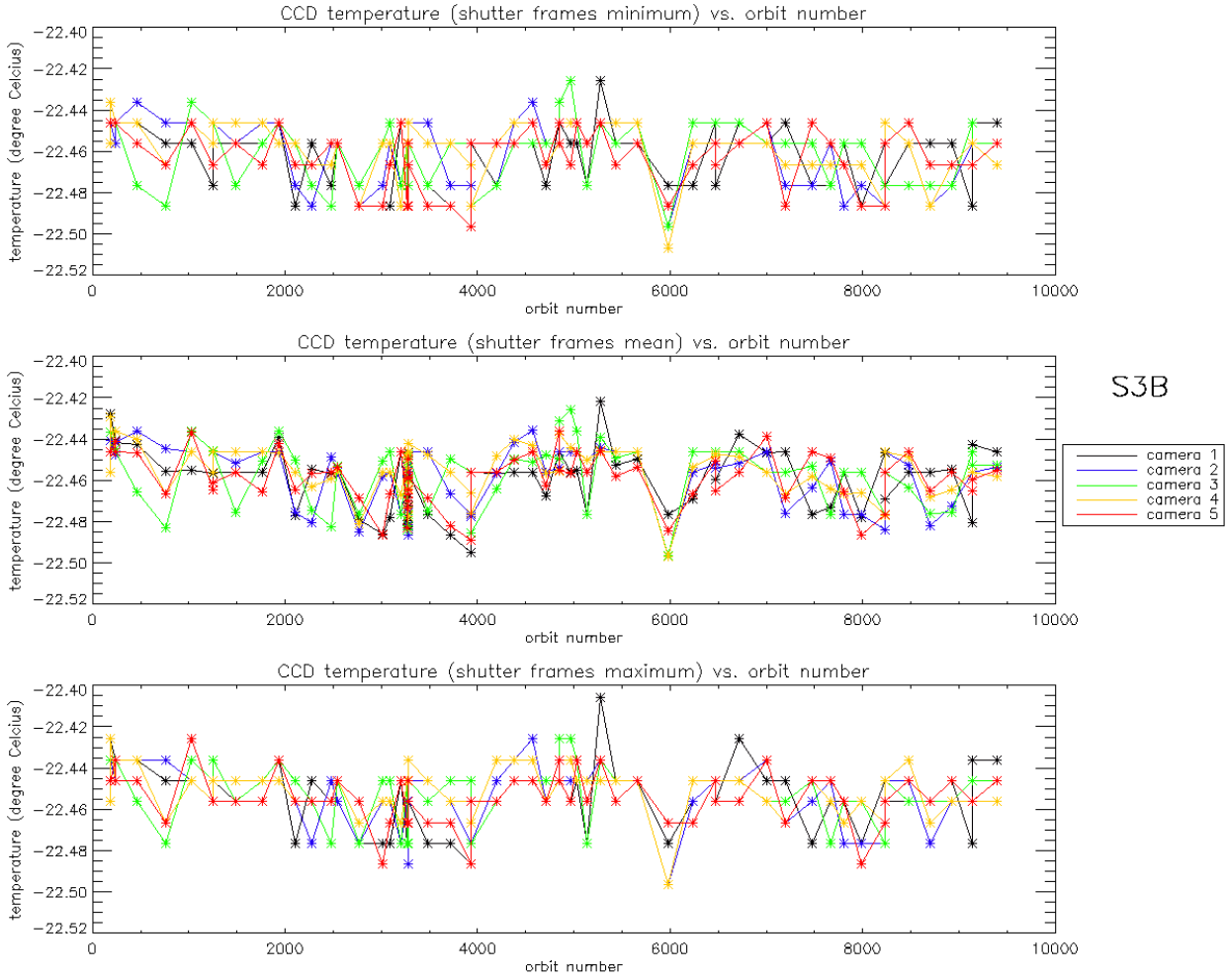

Figure 4: long term monitoring of OLCI-B CCD temperatures using minimum value (top), time averaged values (middle), and maximum value (bottom) provided in the annotations of the Radiometric Calibration Level 1 products, for the Shutter frames, all radiometric calibrations so far except the first one (absolute orbit 167) for which the instrument was not yet thermally stable.

5.1.2 Signal to noise ratio

5.1.2.1 OLCI-A

OLCI signal to noise ratio (SNR) is monitored using Radiometric Calibration data acquired on the radiometric diffuser that provides a signal smoothly varying with time. After correction for the variation due to the variation of the illumination with illumination geometry during the 24 seconds of acquisitions, variability is assessed and SNR is derived, as the incoming radiance is known. SNR values obtained at the

Calibration signal level are then downscaled to a typical clear sky ocean signal level, as defined in the mission requirements.

SNR computed for all radiometric calibration data is presented on Figure 5 as a function of band number. Stability with time is shown on Figure 6: SNR of band Oa01 (400nm, the most varying) is plotted against orbit number.

There is no significant evolution of this parameter over the mission and the ESA requirement is fulfilled for all bands.

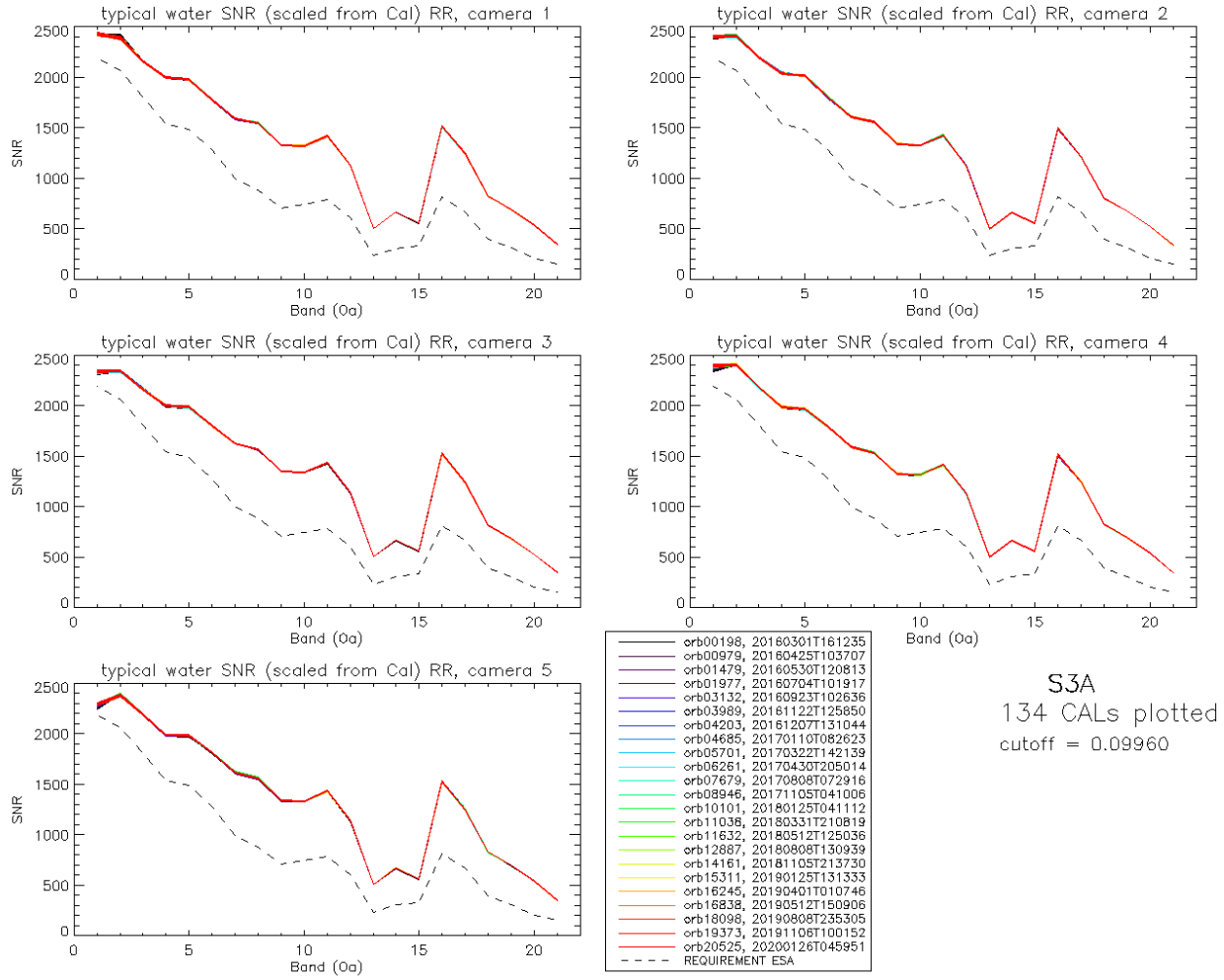

Figure 5: OLCI-A Signal to Noise ratio as a function of the spectral band for the 5 cameras. These results have been computed from radiometric calibration data. All calibrations except first one (orbit 183) are present with the colours corresponding to the orbit number (see legend). The SNR is very stable with time: the curves for all orbits are almost superimposed. The dashed curve is the ESA requirement.

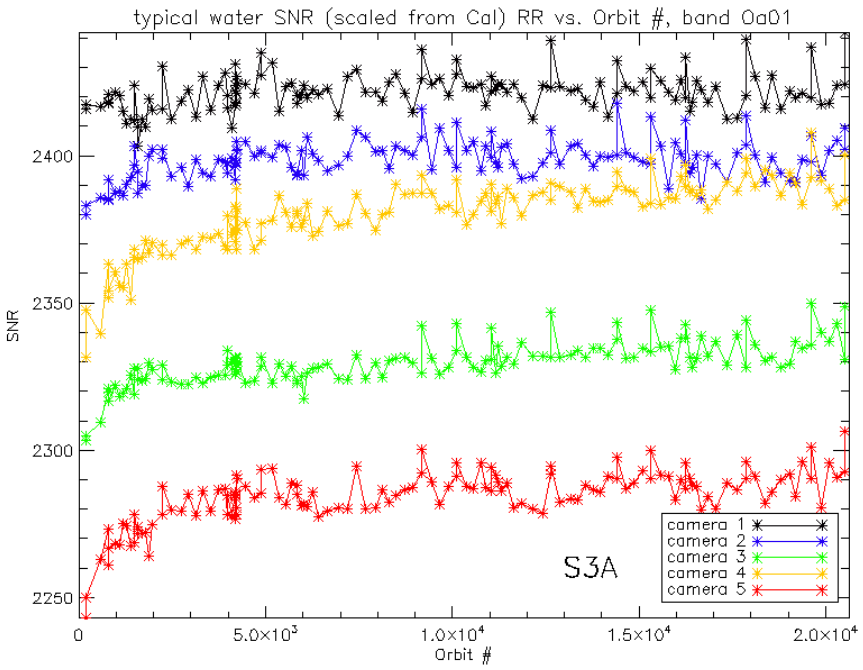

Figure 6: OLCI-A long-term stability of the SNR estimates from Calibration data, example of channel Oa01.

The mission averaged SNR figures are provided in Table 4, together with their radiance reference level. According to the OLCI SNR requirements, these figures are valid at these radiance levels and at Reduced Resolution (RR, 1.2 km). They can be scaled to other radiance levels assuming shot noise (CCD sensor noise) is the dominating term, i.e. radiometric noise can be considered Gaussian with its standard deviation varying as the square root of the signal: $SNR(L) = SNR(L_{ref}) \cdot \sqrt{\frac{L}{L_{ref}}}$. Following the same assumption, values at Full Resolution (300 m) can be derived from RR ones as 4 times smaller.

Table 4: OLCI-A SNR figures as derived from Radiometric Calibration data. Figures are given for each camera (time average and standard deviation), and for the whole instrument. The requirement and its reference radiance level are recalled (in $mW.sr^{-1}.m^{-2}.nm^{-1}$).

	L_{ref}	SNR	C1		C2		C3		C4		C5		All	
nm	LU	RQT	avg	*std*	avg	*std*	avg	*std*	avg	*std*	avg	*std*	avg	*std*
400	63.0	2188	2421	6.3	2398	6.6	2329	7.5	2379	12.1	2284	9.3	2362	7.1
412.5	74.1	2061	2391	8.6	2406	5.9	2339	4.8	2401	4.9	2383	8.1	2384	4.9
442.5	65.6	1811	2160	5.2	2198	5.8	2164	4.9	2186	4.2	2195	5.3	2180	3.6
490	51.2	1541	2000	4.7	2037	5.2	1997	4.1	1983	4.4	1988	4.8	2001	3.4
510	44.4	1488	1979	5.3	2014	4.7	1985	4.6	1967	4.6	1985	4.5	1986	3.7
560	31.5	1280	1776	4.5	1802	4.2	1803	4.9	1794	4.0	1818	3.4	1799	3.1
620	21.1	997	1591	4.0	1609	4.1	1624	3.2	1593	3.3	1615	3.6	1607	2.6
665	16.4	883	1546	4.1	1558	4.3	1567	3.8	1533	3.6	1561	3.9	1553	3.1
673.75	15.7	707	1329	3.4	1337	3.6	1350	2.8	1323	3.2	1342	3.6	1336	2.5
681.25	15.1	745	1319	3.7	1326	3.1	1338	2.7	1314	2.4	1333	3.6	1326	2.2
708.75	12.7	785	1421	4.4	1420	4.1	1435	3.4	1414	3.5	1430	3.2	1424	2.8
753.75	10.3	605	1127	3.2	1120	3.0	1135	3.5	1124	2.5	1139	3.0	1129	2.4
761.25	6.1	232	502	1.1	498	1.2	505	1.2	500	1.1	508	1.4	503	0.9
764.375	7.1	305	663	1.6	658	1.6	668	2.1	661	1.6	670	2.2	664	1.4
767.5	7.6	330	558	1.5	554	1.3	562	1.3	557	1.5	564	1.3	559	1.1
778.75	9.2	812	1516	4.8	1498	4.9	1525	5.4	1511	5.1	1526	5.0	1515	4.3
865	6.2	666	1244	3.6	1213	3.6	1239	4.0	1246	3.6	1250	2.8	1238	3.0
885	6.0	395	823	1.7	801	1.7	814	2.0	824	1.5	831	1.7	819	1.2
900	4.7	308	691	1.6	673	1.3	683	1.7	693	1.4	698	1.5	688	1.0
940	2.4	203	534	1.1	522	1.1	525	0.9	539	1.1	542	1.4	532	0.7
1020	3.9	152	345	0.9	337	0.9	348	0.7	345	0.9	351	0.8	345	0.5

5.1.2.2 OLCI-B

As for OLCI-A there is no significant evolution of the SNR over the mission and the ESA requirement is fulfilled for all bands.

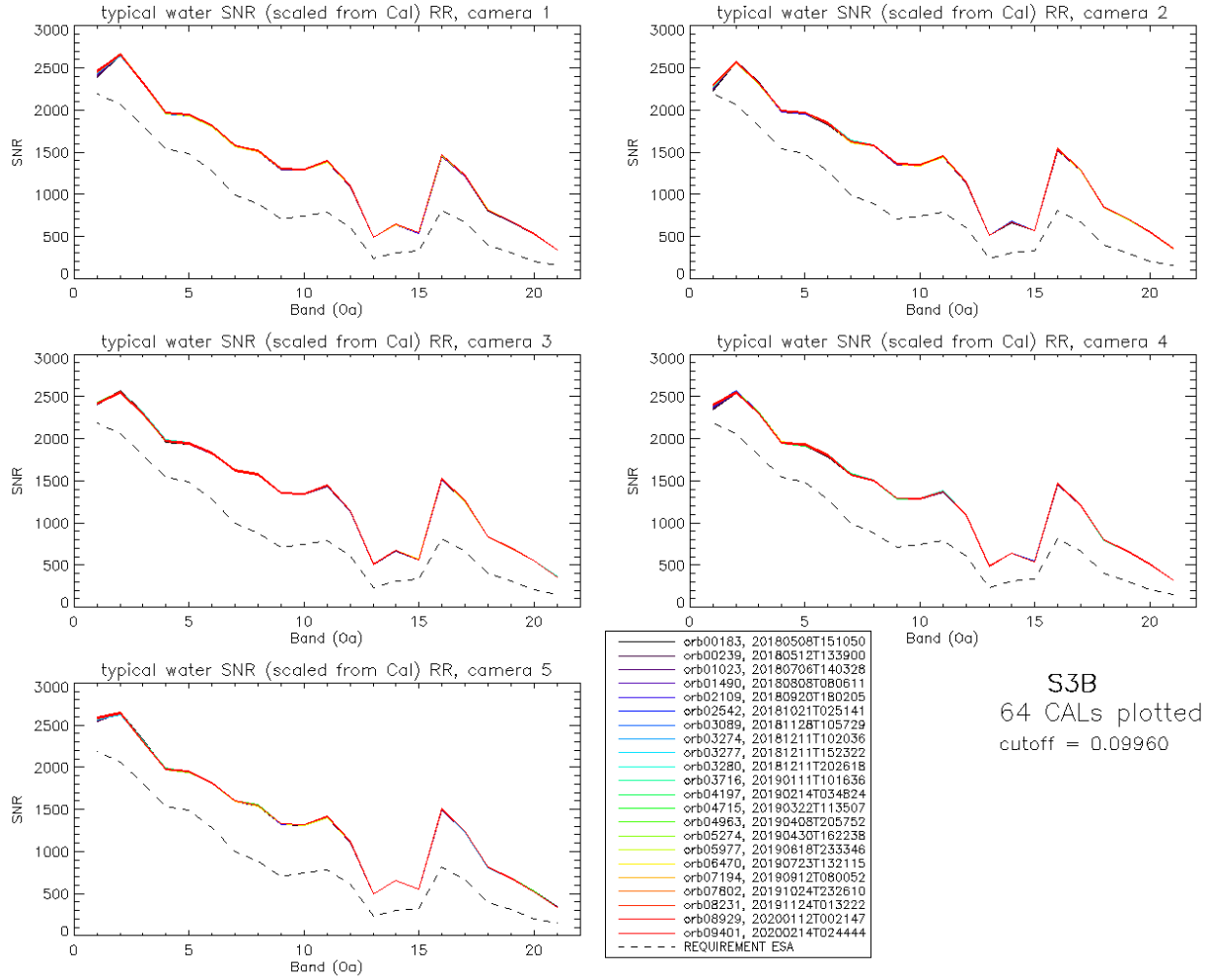

Figure 7: OLCI-B Signal to Noise ratio as a function of the spectral band for the 5 cameras. These results have been computed from radiometric calibration data. All calibrations except first one (orbit 167) are presents with the colours corresponding to the orbit number (see legend). The SNR is very stable with time: the curves for all orbits are almost superimposed. The dashed curve is the ESA requirement.

As for OLCI-A, the mission averaged SNR figures are provided in Table 5 below, together with their radiance reference level.

Table 5: OLCI-B SNR figures as derived from Radiometric Calibration data. Figures are given for each camera (time average and standard deviation), and for the whole instrument. The requirement and its reference radiance level are recalled (in mW.sr^{-1}.m^{-2}.nm^{-1}).

	L_{ref}	SNR	C1		C2		C3		C4		C5		All	
nm	LU	RQT	avg	*std*	avg	*std*	avg	*std*	avg	*std*	avg	*std*	avg	*std*
400	63.0	2188	2442	20.1	2282	16.5	2417	5.9	2388	14.2	2576	12.4	2421	12.8
412.5	74.1	2061	2656	6.7	2570	6.1	2548	8.4	2549	6.1	2640	6.7	2593	5.0
442.5	65.6	1811	2326	6.2	2318	6.1	2303	6.1	2306	6.2	2311	6.0	2313	5.0
490	51.2	1541	1966	4.9	1987	5.8	1971	5.1	1951	4.9	1978	5.0	1971	4.0
510	44.4	1488	1937	5.3	1966	5.5	1942	5.2	1922	5.3	1951	4.8	1944	4.2
560	31.5	1280	1813	5.1	1847	5.6	1829	4.8	1803	5.3	1816	4.6	1821	4.1
620	21.1	997	1573	4.4	1626	4.9	1625	3.9	1576	4.2	1602	3.3	1600	3.1
665	16.4	883	1513	4.3	1579	4.0	1574	4.2	1501	3.1	1546	3.9	1543	2.9
673.75	15.7	707	1301	3.7	1358	4.0	1353	3.5	1292	2.9	1329	3.1	1327	2.6
681.25	15.1	745	1293	3.6	1347	3.2	1343	3.0	1285	2.8	1316	2.9	1317	2.2
708.75	12.7	785	1390	4.5	1447	4.2	1443	4.7	1373	3.2	1412	4.2	1413	3.5
753.75	10.3	605	1095	4.3	1142	4.1	1141	3.9	1088	3.0	1115	3.8	1116	3.4
761.25	6.1	232	487	1.3	509	1.3	508	1.4	485	1.2	497	1.5	497	1.1
764.375	7.1	305	643	1.7	672	2.1	672	2.0	640	1.7	657	2.0	657	1.6
767.5	7.6	330	541	1.6	567	1.5	564	1.4	540	1.4	554	1.7	553	1.2
778.75	9.2	812	1466	4.7	1534	5.1	1525	6.1	1465	3.9	1505	5.0	1499	4.3
865	6.2	666	1220	4.1	1286	4.0	1258	4.0	1204	3.7	1237	3.2	1241	3.2
885	6.0	395	808	2.6	847	1.9	834	2.1	798	1.8	814	2.0	820	1.6
900	4.7	308	679	1.5	714	2.0	704	1.6	669	1.5	682	1.6	690	1.2
940	2.4	203	527	1.3	550	1.6	550	1.3	509	1.2	522	1.4	532	1.0
1020	3.9	152	336	0.8	359	1.2	358	0.9	318	0.8	339	1.2	342	0.7

5.1.3 Spectral Calibration

5.1.3.1 OLCI-A

OLCI's spectral characteristics are regularly monitored in-flight by different spectral campaigns, which are shortly outlined in the following. A detailed description is given in *S3-TN-ESA-OL-660*. The procedures use the programming capability of OLCI to define 45 bands around stable spectral features, to characterize the spectral dispersion of each camera system with respect to the spectral dimension and the spatial (across track) dimension. Simulations of OLCI measurements in the 45 bands are optimized for best agreement with the spectral features, as a function of individual bandwidth and band centre wavelength. Depending on the used spectral feature the achieved accuracy for the centre wavelength is in the order of 0.1-0.2 nm, the precision (repeatability) is better than 0.05 nm.

Three different calibration sequences **S0*** are used regularly:

- **S09**: The 45 bands are grouped around the atmospheric oxygen absorption band at 770 nm and around distinct solar Fraunhofer lines at 485 nm, 656 nm and 854 nm. To increase the feature stability, the same few hundred frames are acquired at the same orbit cycle (number 24), belonging to Libyan Desert. Since the end of the commissioning phase in June 2016, four S09 campaigns have been performed.
- **S02/S03**: The 45 bands are grouped around three spectral features of the on-board spectral diffusor at 405 nm, 520 nm and 800 nm. 500 frames are acquired on the white diffusor (**S02**) as reference and on the spectral (so called pink) diffusor (**S03**). Since the end of the commissioning phase in June 2016 three **S02/S03** campaigns have been performed.
- **S02 solar:** Solely the white diffusor data is used to identify and utilize solar Fraunhofer lines and to provide therewith a spectral characterization independent from the on-board spectral diffusor.

The spectral campaigns performed during and after the commissioning phase reveal a high agreement of the in-flight characterisation with the pre-flight spectral calibration. The resulting differences of the centre wavelengths of the nominal OLCI bands between pre- and in-flight calibration are smaller than 0.1 nm, despite of band 1 and 21, where differences <= 0.2 nm have been detected.

A small temporal evolution can be observed since the first in-flight characterisation. This is shown in Figure 8 (S02/S03) and Figure 9 (S09), where the camera mean spectral distance to its value since orbit 380 (March 2016) is plotted.

The evolution of the centre wavelength is different for each camera but approximately the same for all wavelengths. Since the end of the commissioning phase (June 2016, ~ orbit 1800) the observed changes are smaller than 0.15 nm (0.2 nm for camera 5).

We see that the long-term evolution of the spectral calibration obtained with sequence S09 is in rather good agreement with the one obtained with sequence S02/S03.

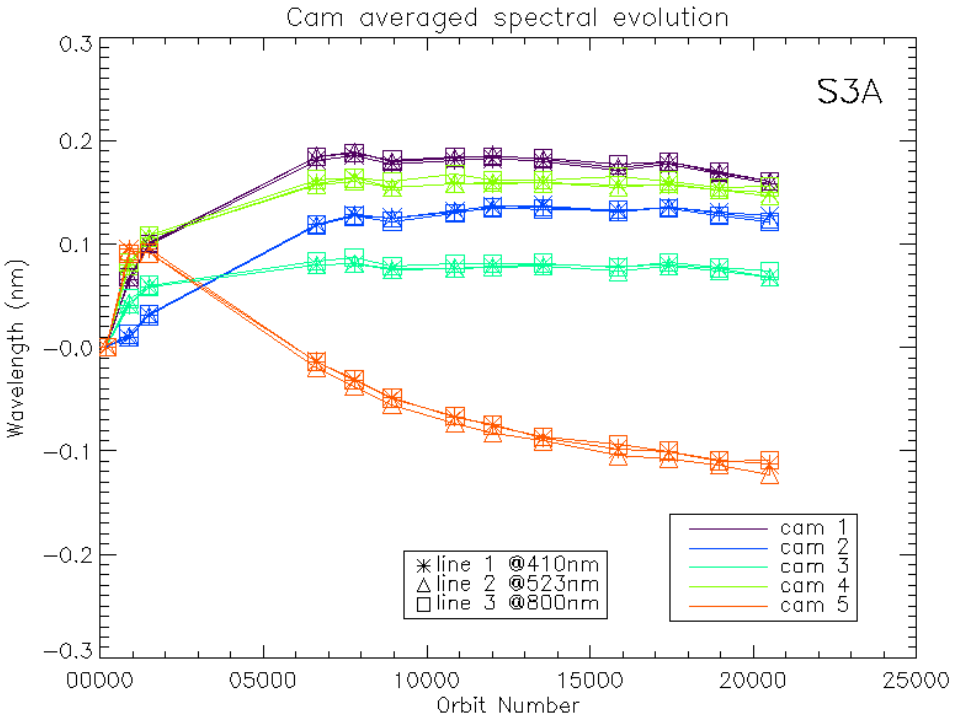

Figure 8: OLCI-A camera averaged spectral calibration evolution as a function of absolute orbit number (all spectral S02/S03 calibrations since the beginning of the mission are included).The data are normalized with the first Spectral Calibration. The first (reference) calibration is from March 2016, the last from Jan. 2020.

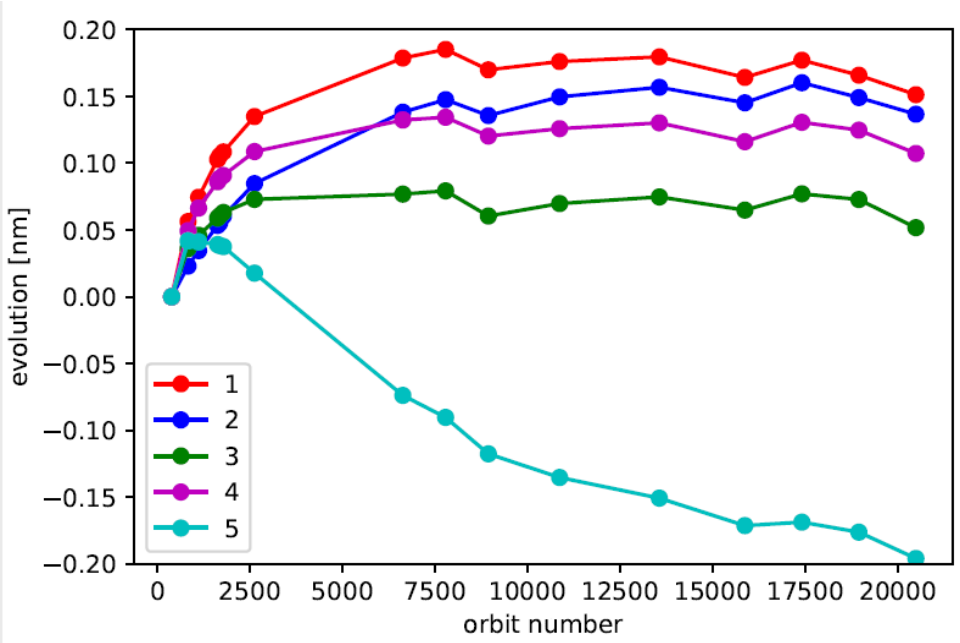

Figure 9: OLCI-A line-averaged spectral calibration relative to the one at orbit 380 (March 2016), as a function of time derived from all S09 sequences. The last calibration is from 23 January 2020. For each camera, the spectral evolution derived from spectral lines at 485 nm, 656 nm, 770 nm and 854 nm have been averaged.

5.1.3.2 OLCI-B

ACT profiles of absolute spectral calibration obtained with all S02/S03 sequences, including comparison with on-ground characterisation, are plotted in Figure 10 showing the very good agreement between pre-flight and in-flight spectral calibrations. Differences are roughly < 0.2 nm except for line 3 camera 2, which is < 0.3 nm.

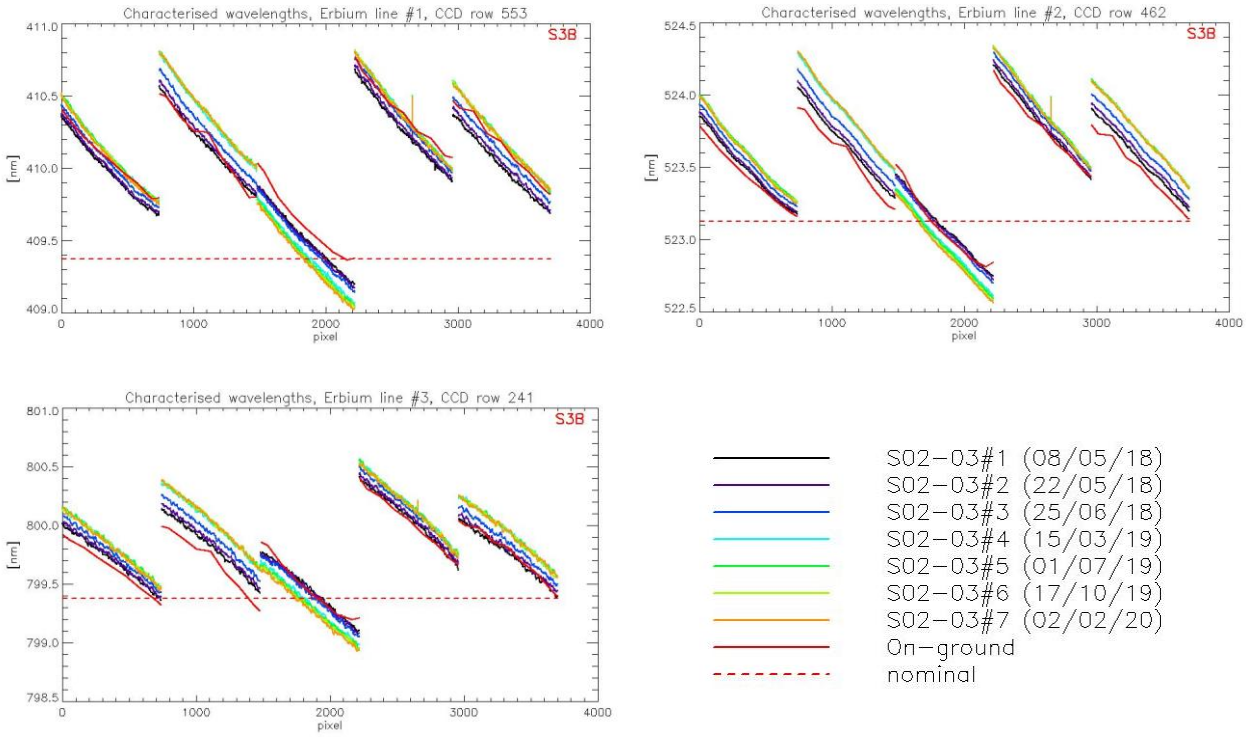

Figure 10: OLCI-B across track spectral calibration from all S02/S03 sequences since the beginning of the mission. Left top plot is spectral line 1; Right top plot is spectral line 2 and bottom plot spectral line 3. On-ground spectral characterisation is in red.

Figure 11 shows the temporal evolution of the spectral calibration obtained with all S02/S03 sequences since the beginning of the mission. As for OLCI-A a small drift is observed. For OLCI-B, this drift is positive for camera 1, 2, 4 and 5 and negative for camera 3.

Evolution derived from the S09 calibration sequence (spectral calibration using O2 absorption and Fraunhofer lines) is presented in Figure 12. As for OLCI-A, we see that the long-term evolution of the spectral calibration obtained with sequence S09 is in rather good agreement with the one obtained with sequence S02/S03.

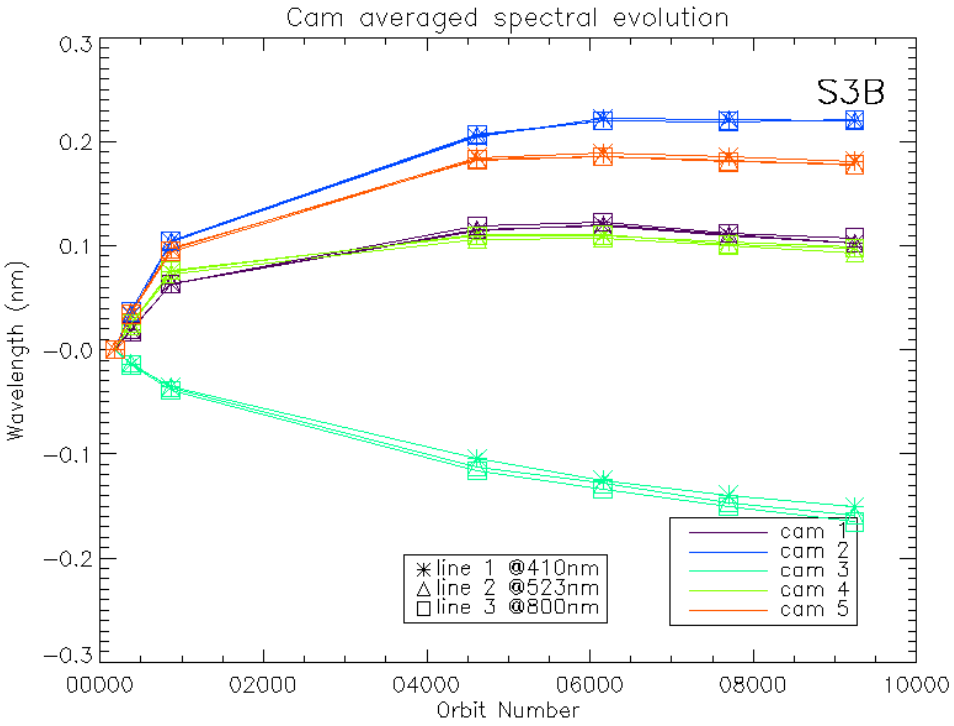

Figure 11: OLCI-B camera averaged spectral calibration evolution as a function of absolute orbit number (all spectral S02/S03 calibrations since the beginning of the mission are included). The data are normalized with the first Spectral Calibration. The first (reference) calibration is from May 2018, the last from Feb 2020.

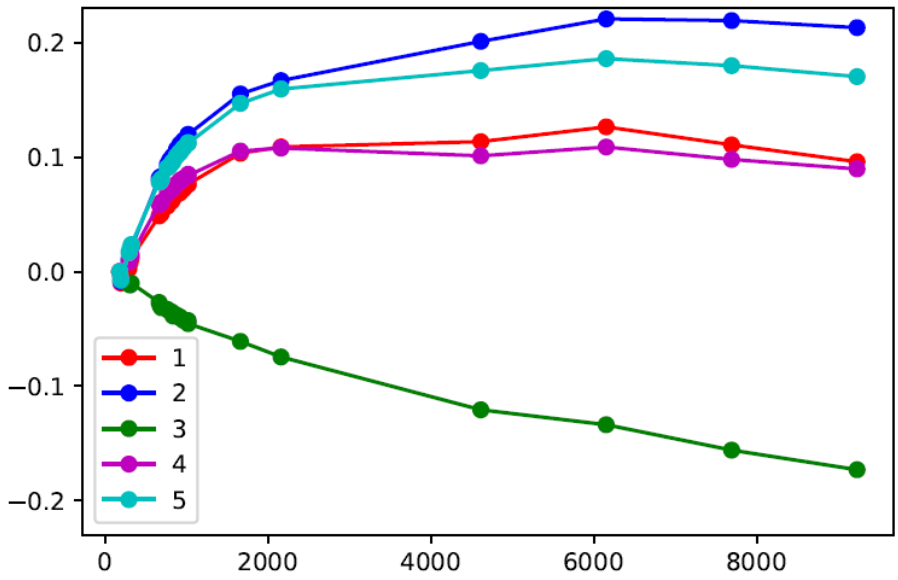

Figure 12: OLCI-B camera averaged spectral calibration evolution as a function of absolute orbit number from S09 calibrations since the beginning of the mission. The last calibration for S09 is from 02 February 2020. For each camera, the spectral evolution corresponding derived from spectral lines at 485 nm, 656 nm, 770 nm and 854 nm have been averaged. The data are normalized with the first Spectral Calibration.

5.1.4 Radiometric stability

5.1.4.1 OLCI-A

The stability with time of the instrument sensitivity is monitored through the radiometric calibration processing results: time series of radiometric gains normalised to a given date are analysed. This is done at the full spatial resolution before being summarised by spatial averaging over each camera: if there is some variability of the sensitivity evolution for a given channel inside a given camera, it remains limited with respect to camera-to-camera variability.

The overall instrument evolution (since channel programming change, 25/04/2016 to 26/01/2020) is shown on Figure 13: a maximum of about 2% is reached at 400 nm, with a high inter-camera variability, while other bands show much lower values, within ± 0.8%. The spectral behaviour of the 5 cameras is very similar, to the exception of camera 1 at the blue edge (bands Oa1 and Oa2, 400 & 412 nm), and camera 5 in the red to NIR spectral range.

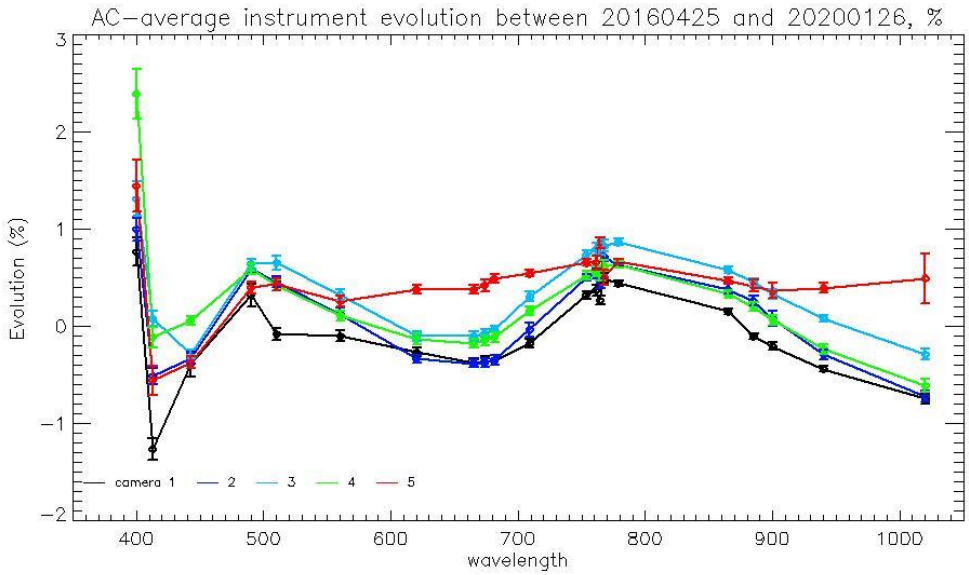

Figure 13: OLCI-A camera-averaged instrument evolution since channel programming change (25/04/2016) and up to most recent calibration (26/01/2020) versus wavelength.

Time series of sensitivity evolution are shown on Figure 14 one plot per camera, as a function of elapsed time since launch. It shows that, if a significant evolution occurred during the early mission, the trends tend to stabilize, with the notable exception of band 1 in particular for camera 4. An example of an evolution surface for channel Oa2 (412 nm) is given below for Camera 1 (Figure 15), justifying the use of spatial averages for long-term monitoring.

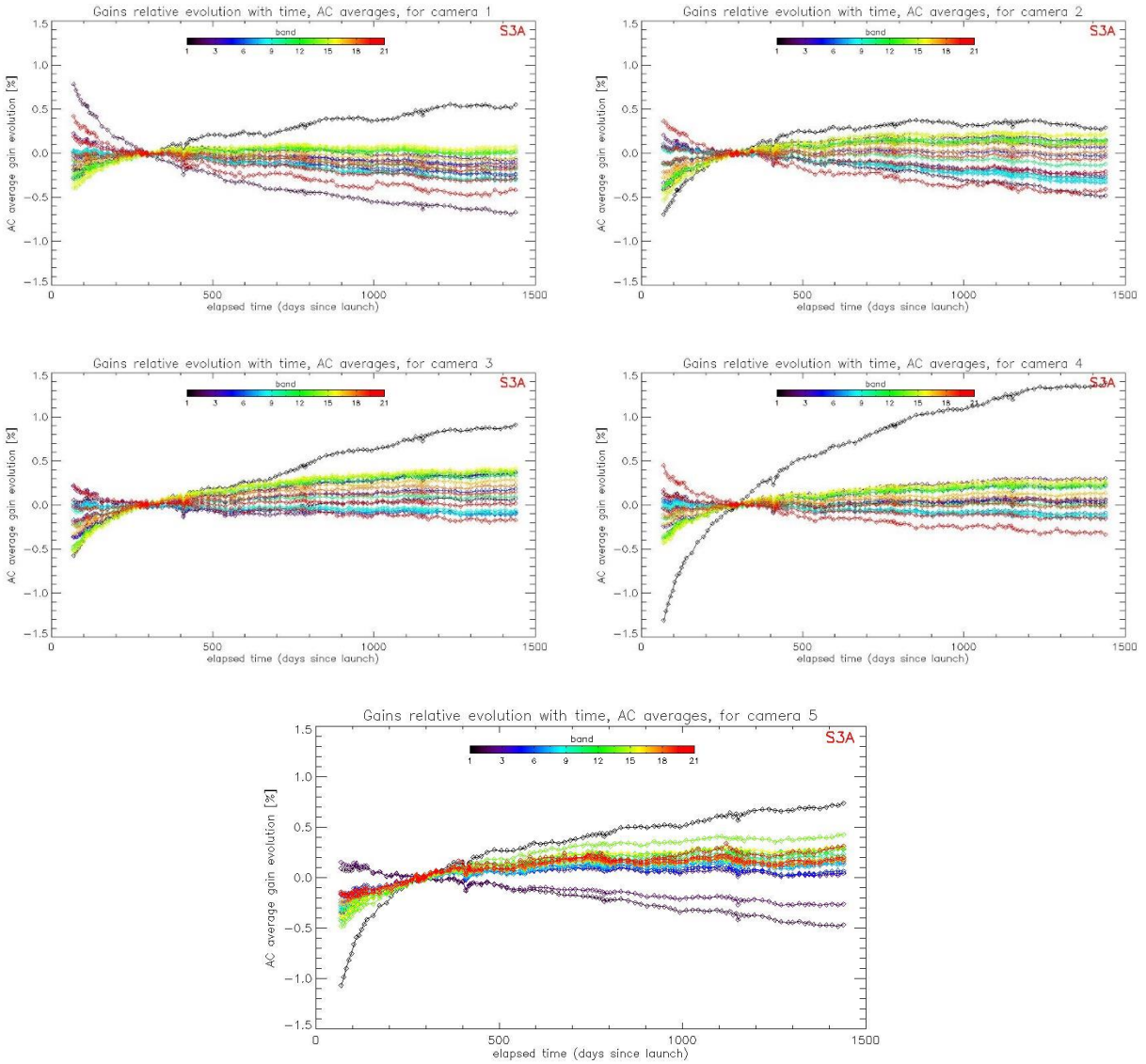

Figure 14: OLCI-A camera averaged gain relative evolution with respect to "best geometry" calibration (22/11/2016), as a function of elapsed time since launch; one curve for each band (see colour code on plots), one plot for each module. Early mission data (16 Feb. to 26 April) is not available due to missing information required for accurate gain computation.

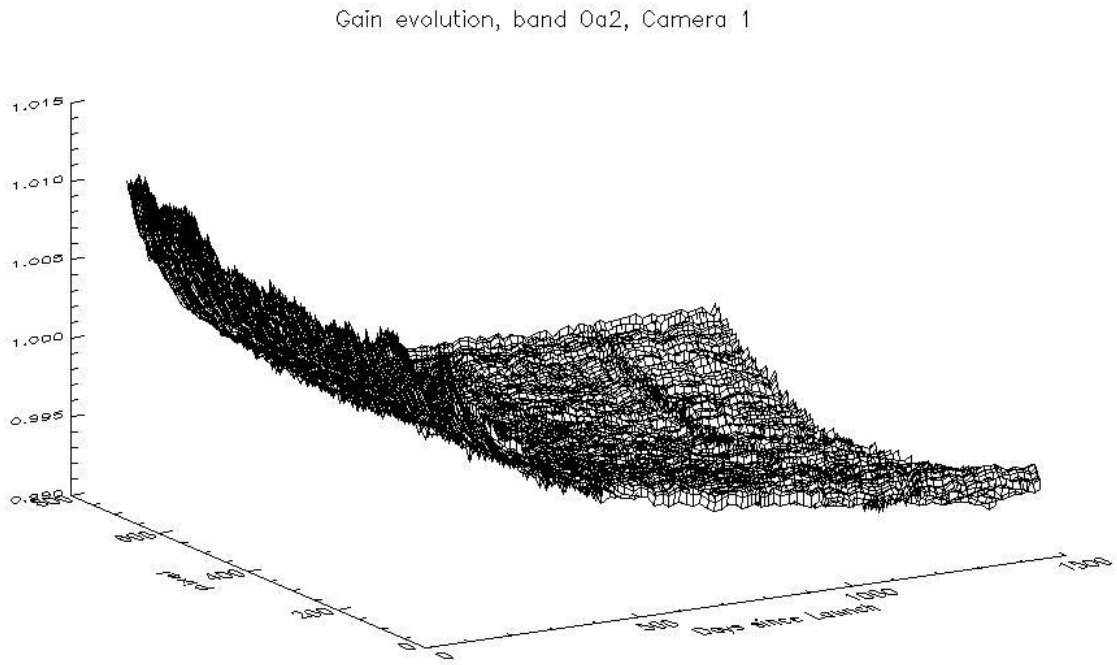

Figure 15: OLCI-A gain relative evolution with respect to "best geometry" calibration (22/11/2016), as a function of elapsed time since launch (x axis) and spatial pixel (y axis) for Channel Oa2 (412.5 nm), Camera 1.

5.1.4.2 OLCI-B

The overall instrument evolution (18/06/2018 to 14/02/2020) is shown on Figure 16: a maximum of about 4% is reached at 400 nm, while other bands show lower values, within ± 1.5%. The spectral behaviour of the 5 cameras is very similar, to the exception of camera 3 at both edges (bands Oa1 and Oa21, 400 & 1020 nm).

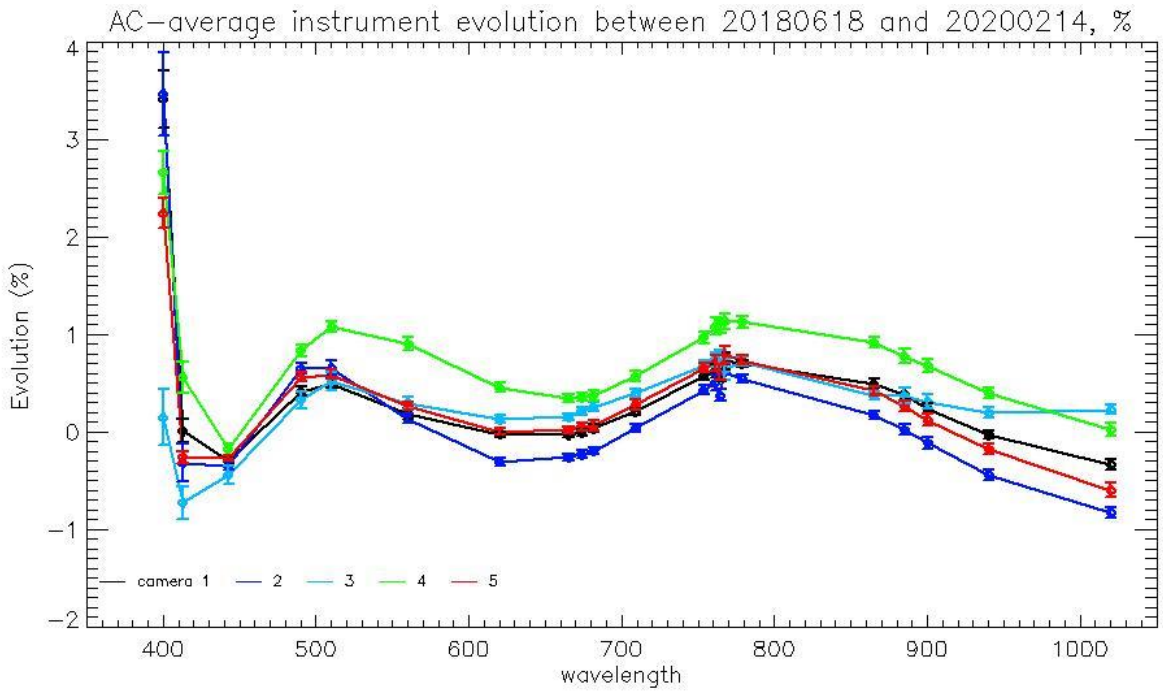

Figure 16: OLCI-B camera-averaged instrument evolution since channel programming change (18/06/2018) and up to most recent calibration (14/02/2020) versus wavelength.

Time series of sensitivity evolution are shown on Figure 17, one plot per camera, as a function of elapsed time since launch. It shows that, if a significant evolution occurred during the early mission, the trends tend to stabilize.

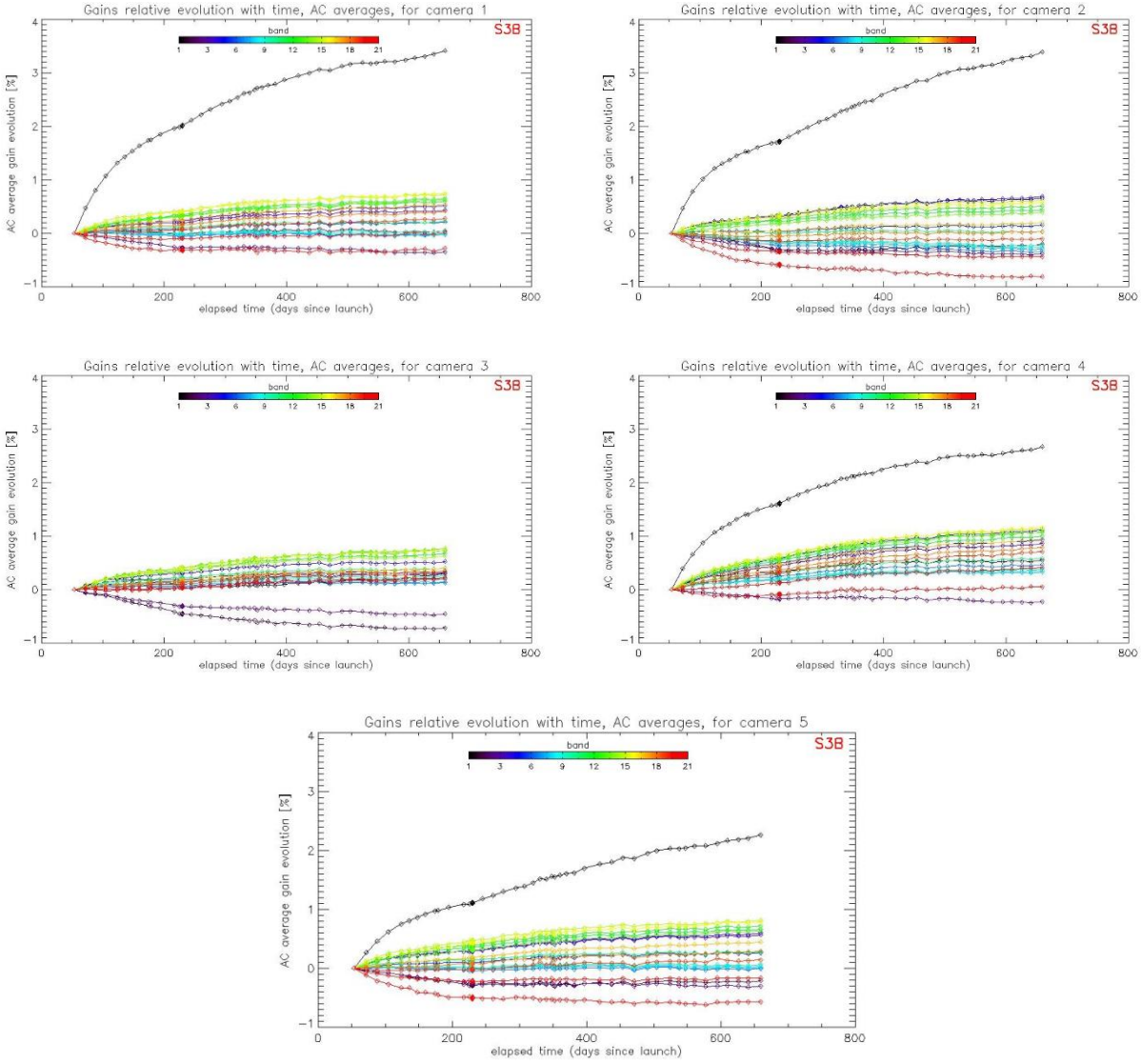

Figure 17: OLCI-B camera averaged gain relative evolution with respect to first calibration after channel programming change (18/06/2018), as a function of elapsed time since the beginning of the mission; one curve for each band (see colour code on plots), one plot for each module. The diffuser ageing has been taken into account.

5.1.5 Ageing of radiometric diffuser

5.1.5.1 OLCI-A

The ageing of the nominal radiometric solar diffuser is monitored using a second, or reference, radiometric diffuser. The relative darkening of the solar diffuser, expected to be measurable after significant cumulated exposure to UV light, is assessed at every channel through the evolution with time of the relative response of the nominal diffuser with respect to that of the reference one acquired under

almost identical illumination conditions one orbit after the nominal one; the first pair of measurements is used as the reference point. Ageing is first assessed at every spatial pixel and then averaged over the field-of-view (FOV) as independent of the instrument itself.

FOV-averaged ageing as a function of wavelength is represented in Figure 18 for all available ageing acquisition (17 so far, excluding the first sequence used as the reference). As expected, ageing is rather low (<0.45% after about 4 years) and stronger for the 'bluest' spectral bands (short wavelengths). Ageing is clearly visible only for the 6 first spectral bands so far in the OLCI mission life.

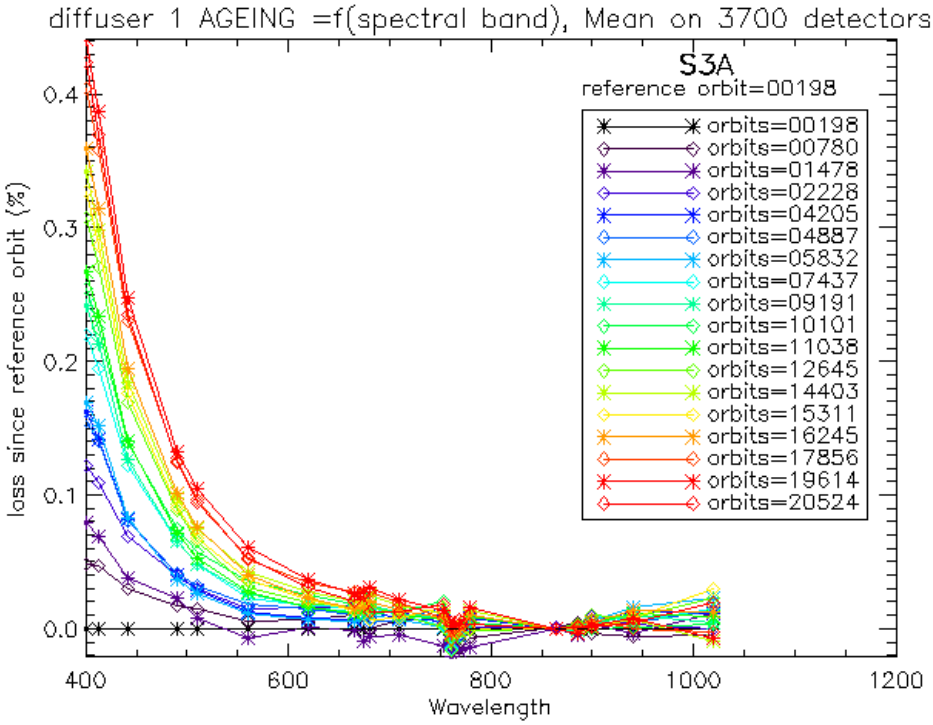

Figure 18: OLCI-A Diffuser 1 ageing as a function of wavelength (or spectral band). Ageing is clearly visible in spectral band #1 to #6.

A model of the nominal diffuser ageing is derived by fitting the measured ageing against cumulated exposure to light, so that it can be used to accurately predict (or model) the nominal diffuser reflectance at any time. This model is used to derive the OLCI Radiometric Gain Model (see section 5.2.1.2). The slope of this ageing model (% of reflectance loss per exposure) as a function of wavelength is presented in Figure 19 for eleven consecutive estimations (during orbit cycles 20, 24,27, 29, 33, 38, 40, 43, 47, 52 & 54 i.e. between July 2017 and January 2020), the first one being that used to build the current Radiometric Gain Model. It shows that the stability is excellent.

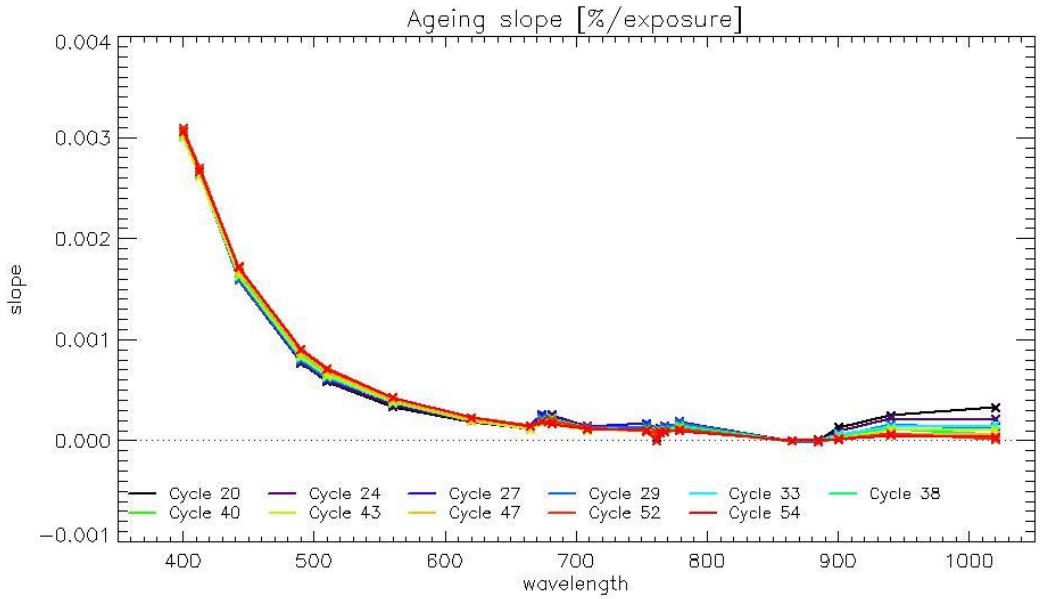

Figure 19: Slope of ageing fit (% of loss per exposure) vs wavelengths, using all the available ageing sequence at the time of the current cycle (#54 = red curve), and at the time of the ten previous cycles with an aging sequence (see legend below the curves).

5.1.5.2 OLCI-B

OLCI-B FOV-averaged ageing as a function of wavelength is represented in Figure 20 for all available ageing acquisition (9 so far, excluding the first sequence used as the reference). The ageing is clearly visible in spectral band Oa01 to Oa05, with the expected spectral shape and order of magnitude. However, we also observe some ageing in bands Oa06 to Oa11; such an unexpected behaviour is under investigation and prevents further use of the nominal ageing assessment method until fully understood. An alternative assessment method, based on direct comparison of nominal diffuser observations during the same day (as part of a specific campaign referred to as the Yaw Manoeuvres) has provided reliable results very close to those of the nominal method for channels Oa01 to Oa05 and negligible ageing at higher wavelengths, as expected.

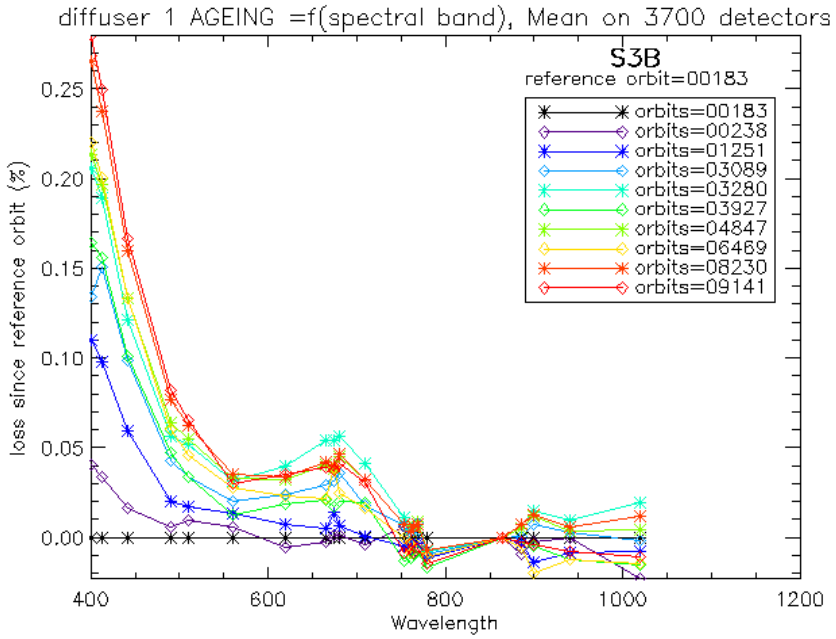

Figure 20: OLCI-B Diffuser 1 ageing as a function of wavelength (spectral bands).

As for OLCI-A, the OLCI-B Diffuser Ageing has been modelled as a function of cumulated exposure time (i.e. number of acquisition sequence on nominal diffuser, regardless of the band setting). The OLCI-A modelling methodology has been applied to OLCI-B. The results of this modelling, iterated at each new Ageing Sequence acquisition, expressed as the rate of ageing (% of loss per exposure) as a function of wavelength is presented in Figure 21. The unexpected bump near 650-700 nm mentioned in the previous annual report seems to decrease with time (i.e with the quantity of data used for modelling the ageing) which is a good point since there is no expected significant ageing at these wavelengths.

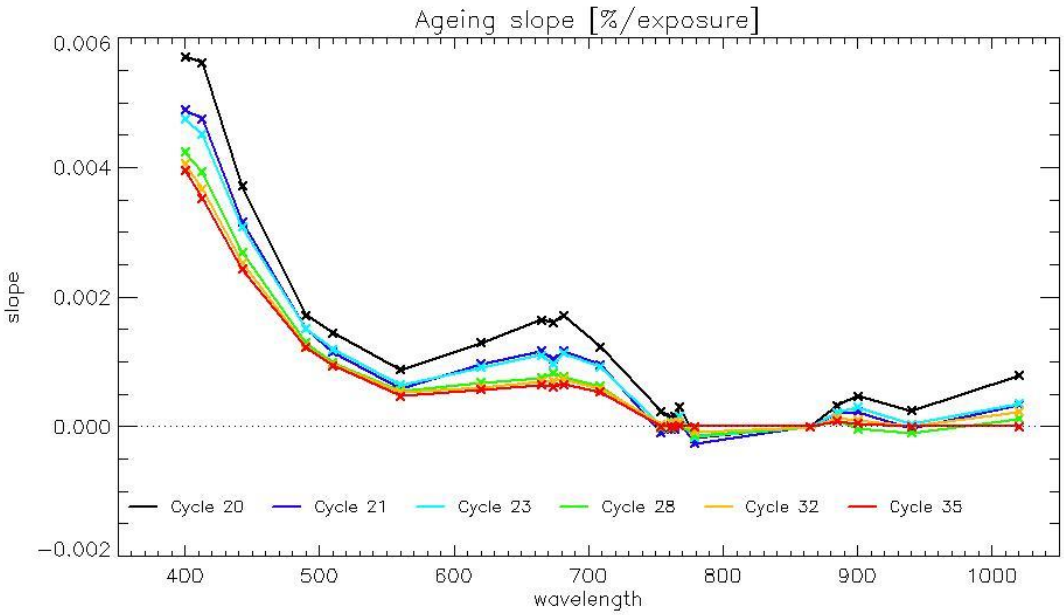

Figure 21: OLCI-B: Slope of ageing fit (% of loss per exposure) vs wavelengths, using all the available ageing sequence at the time of the current cycle (red curve) and at the time of previous cycle for which an ageing sequence was measured (see legend within the figure).

5.2 L1 products performances

5.2.1 Geometric Performance

Regular monitoring of the geolocation performance by correlation with GCP (Ground Control Points) imagettes using the so-called GeoCal Tool is done continuously.

5.2.1.1 OLCI-A

The good performance of OLCI-A georeferencing since the introduction of the upgraded Geometric Calibration on 14/03/2018 is confirmed. It has however significantly improved after its last full revision of GCMs (Geometric Calibration Models, or platform to instrument alignment quaternions) and IPPVMs (Instrument Pixels Pointing Vectors) both derived using the GeoCal Tool and put in production on 30/07/2019. The following figures show time series of the overall RMS performance (Figure 22, requirement criterion) and of the across-track and along-track biases for each camera (Figure 23 to Figure 27). Two additional set of figures have been introduced in this year report addressing monitoring of the performance homogeneity within the field of view: georeferencing errors in each direction at camera transitions (difference between last pixel of camera N and first pixel of camera N+1) and within a given camera (maximum bias minus minimum inside each camera).

The performance improvement since the 30/07/2019 is significant on most figures: the global RMS value decreases form around 0.35 to about 0.2 (Figure 22), the across-track biases decrease significantly for all cameras (Figure 23 to Figure 27) , the along-track bias reduces for at least camera 3 (Figure 25) and the field of view homogeneity improves drastically (Figure 28 and Figure 29, but also reduction of the dispersion – distance between the ± 1 sigma lines – in Figure 23 to Figure 27). Along-track biases of cameras 3 to 5 are however still slightly drifting, resulting in slowly degrading RMS performance (Figure 22), but this is closely monitored so that appropriate actions can be taken.

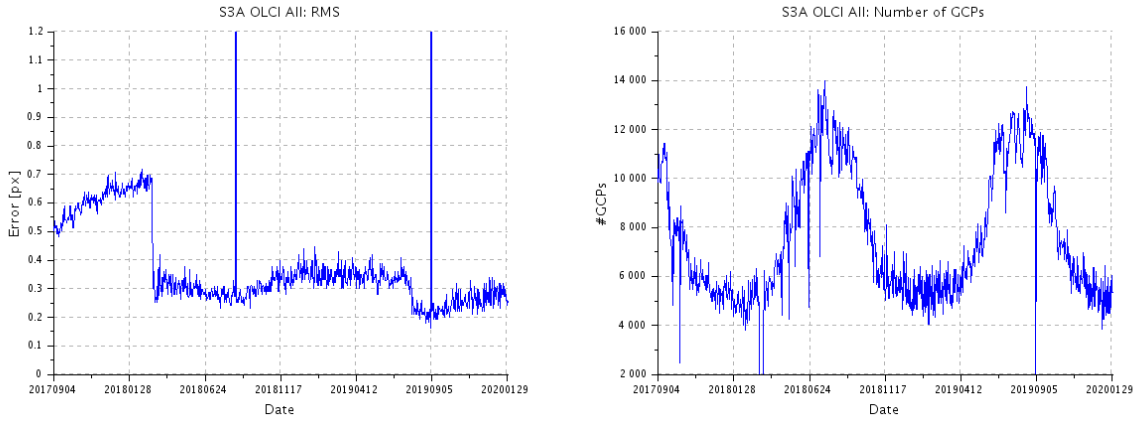

Figure 22: overall OLCI-A georeferencing RMS performance time series over the whole monitoring period (left) and number of validated control points corresponding to the performance time series (right)

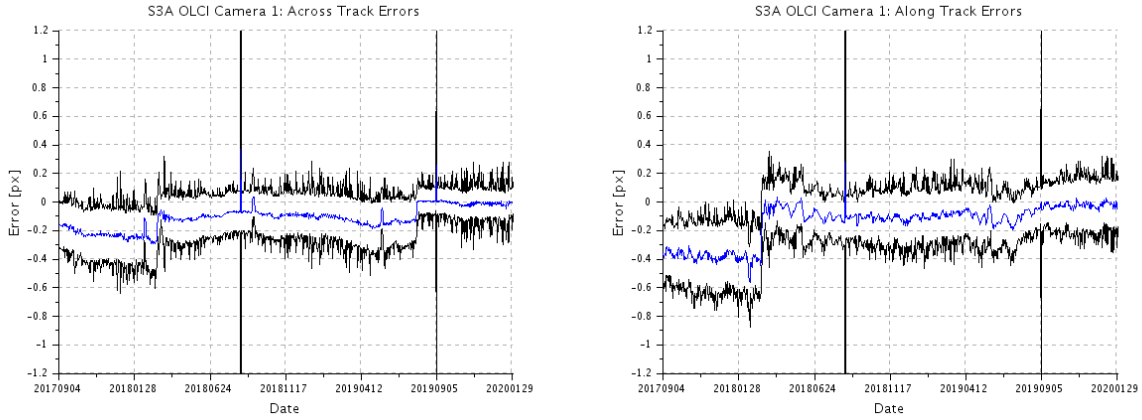

Figure 23: across-track (left) and along-track (right) georeferencing biases time series for Camera 1 (starting 01/03/2018).

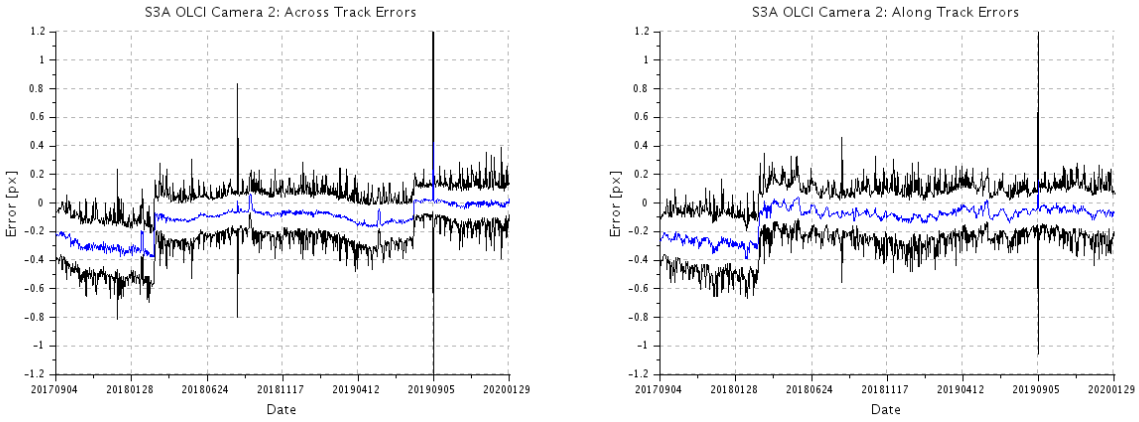

Figure 24: same as Figure 23 for Camera 2.

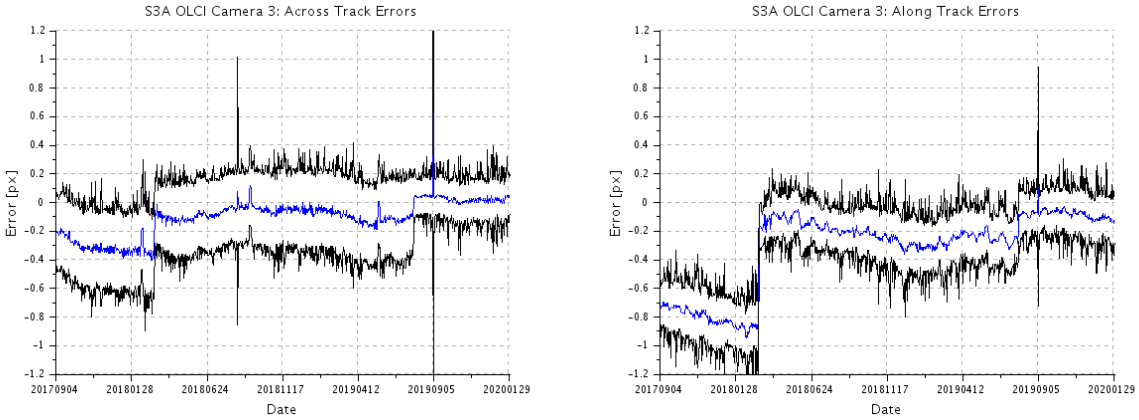

Figure 25: same as Figure 23 for Camera 3.

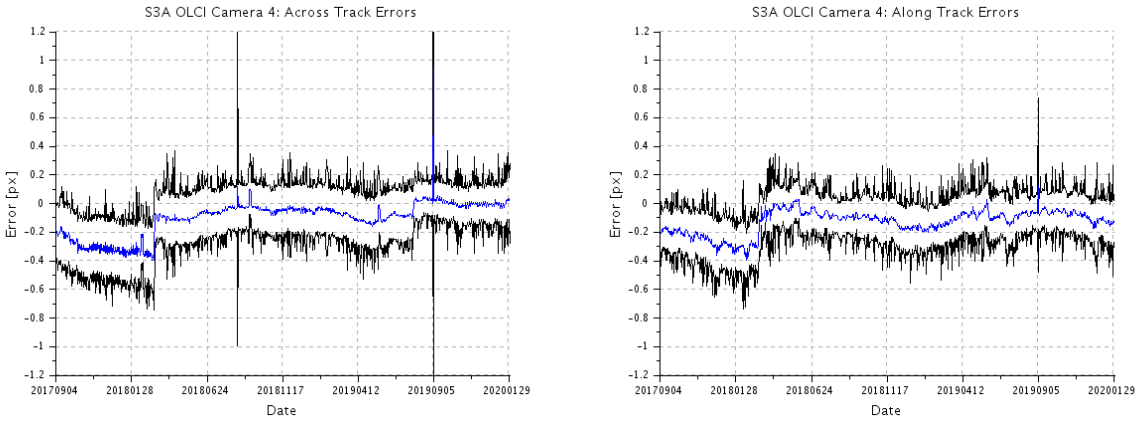

Figure 26: same as Figure 23 for Camera 4.

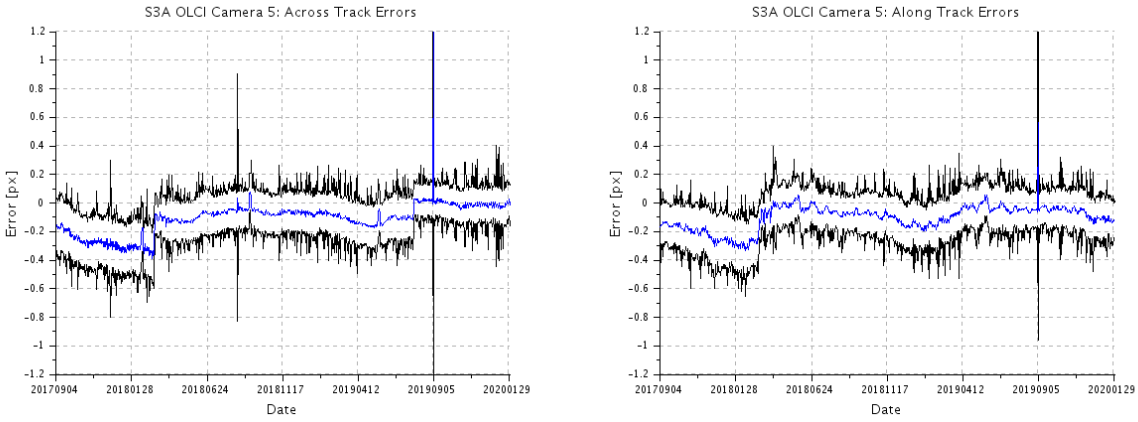

Figure 27: same as Figure 23 for Camera 5.

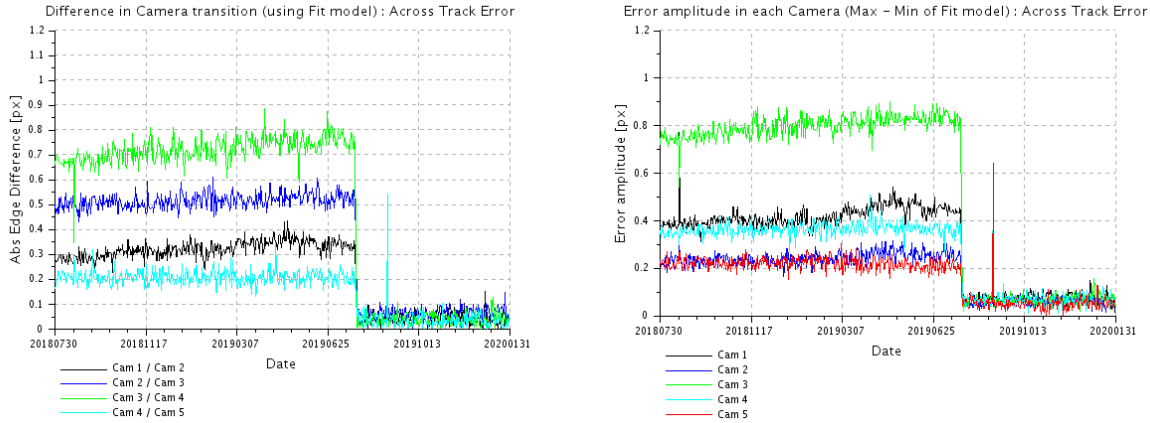

Figure 28: OLCI-A spatial across-track misregistration at each camera transition (left) and maximum amplitude of the across-track error within each camera (left).

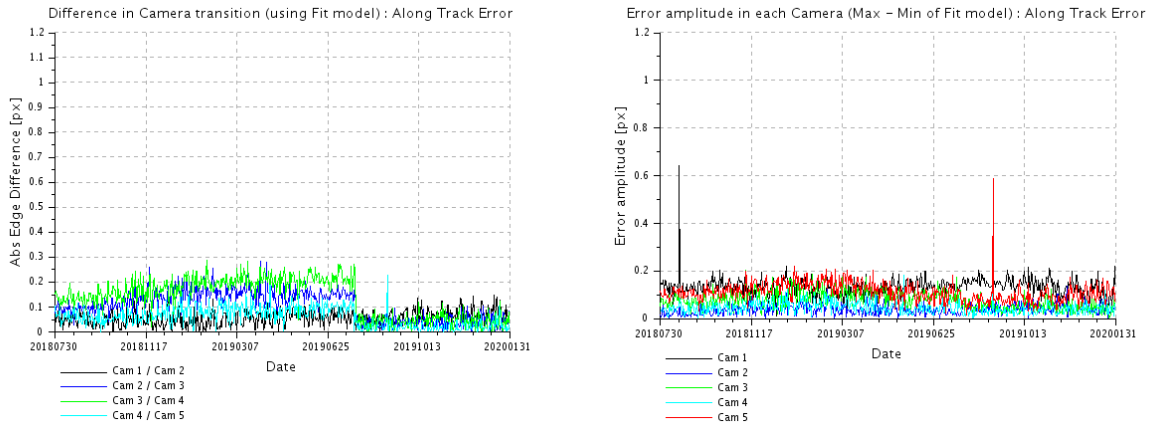

Figure 29: OLCI-A spatial along-track misregistration at each camera transition (left) and maximum amplitude of the along-track error within each camera (left).

5.2.1.2 OLCI-B

The performance of OLCI-B georeferencing is within requirements since the introduction of the 3rd Geometric Calibration on 12/12/2018. The following figures show time series of the overall RMS performance (Figure 30, requirement criterion) and of the across-track and along-track biases for each camera (Figure 31 to Figure 35). The Geometric Calibration currently in production is the fourth one, introduced the 30/07/2019. As for OLCI-A, despite compliance to the RMS requirement of 0.5 pixel, OLCI-B showed significant heterogeneity of the performance within the field of view, with discrepancies at camera transitions of up to 1 pixel. Introduction of upgraded IPPVMs greatly improves many performance indicators: the global RMS value decreases form around 0.4 to about 0.3 (Figure 30), the across-track biases decrease significantly for all cameras (Figure 31 to Figure 35) and the field of view homogeneity improves drastically (Figure 36 and Figure 37, but also reduction of the dispersion – distance between the ± 1 sigma lines – in Figure 31 to Figure 35).

The global RMS performance as well as the along and across-track average biases are quite stable since last calibration, however in-FOV across-track pointing homogeneity slowly degrades (Figure 36) and a re-calibration of the IPPVMs will likely be necessary in the coming months.

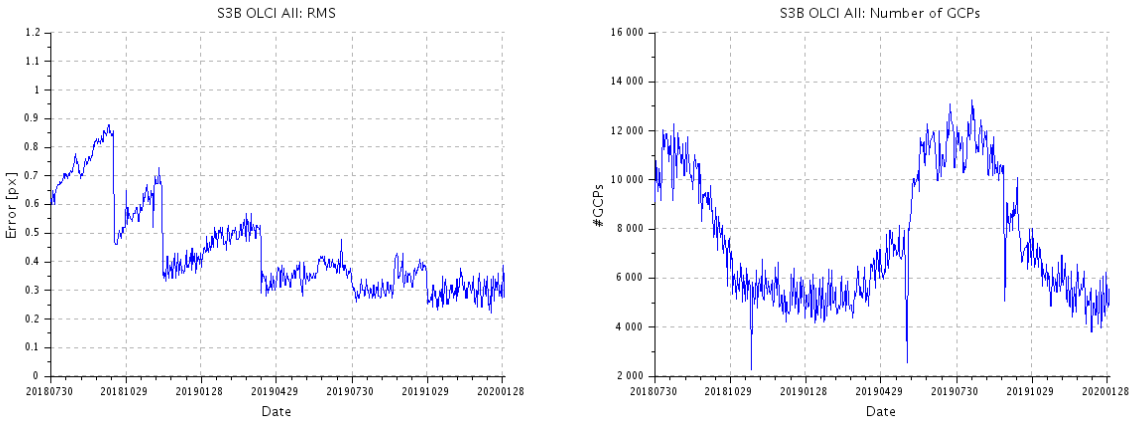

Figure 30: overall OLCI-B georeferencing RMS performance time series (left) and number of validated control points corresponding to the performance time series (right) over the whole monitoring period.

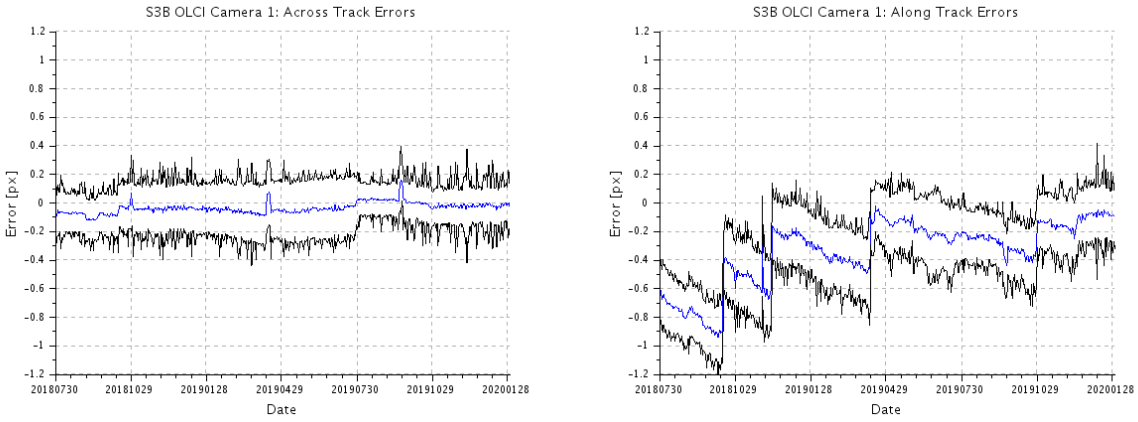

Figure 31: across-track (left) and along-track (right) georeferencing biases time series for Camera 1.

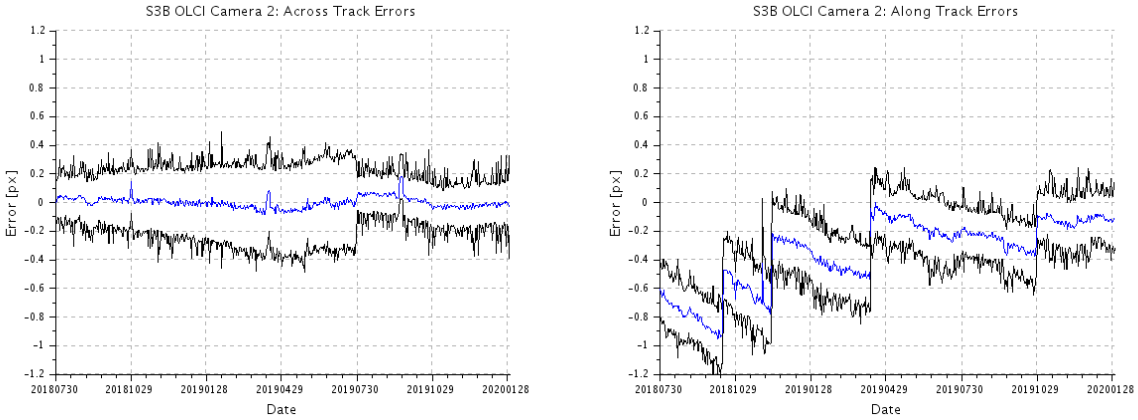

Figure 32: same as Figure 31 for Camera 2.

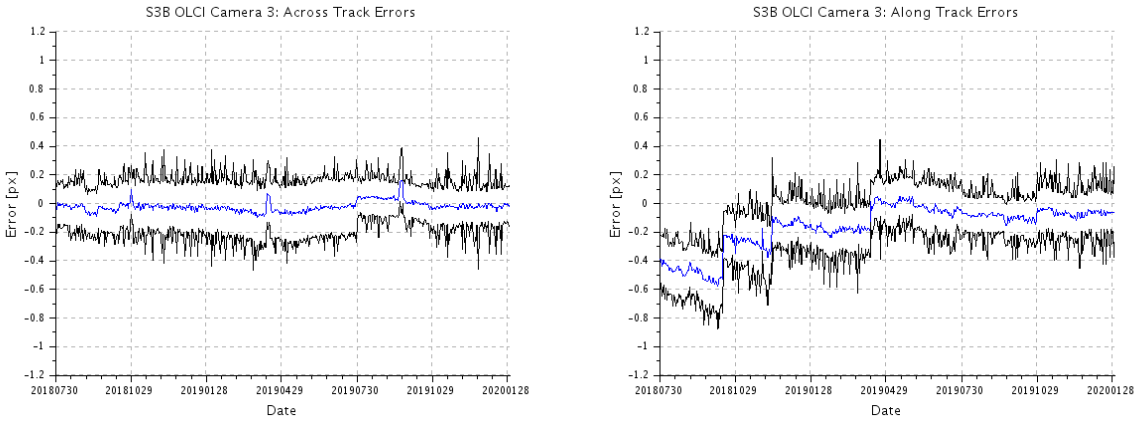

Figure 33: same as Figure 31 for Camera 3.

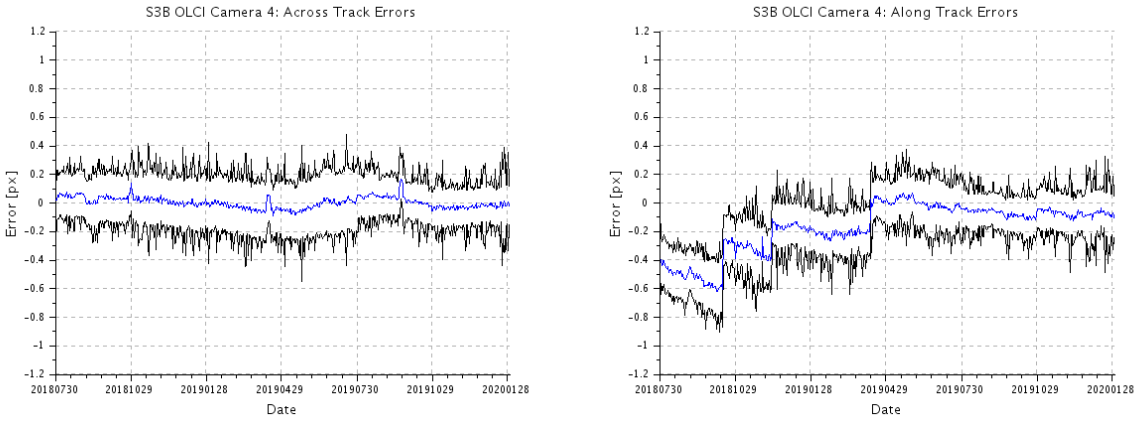

Figure 34: same as Figure 31 for Camera 4.

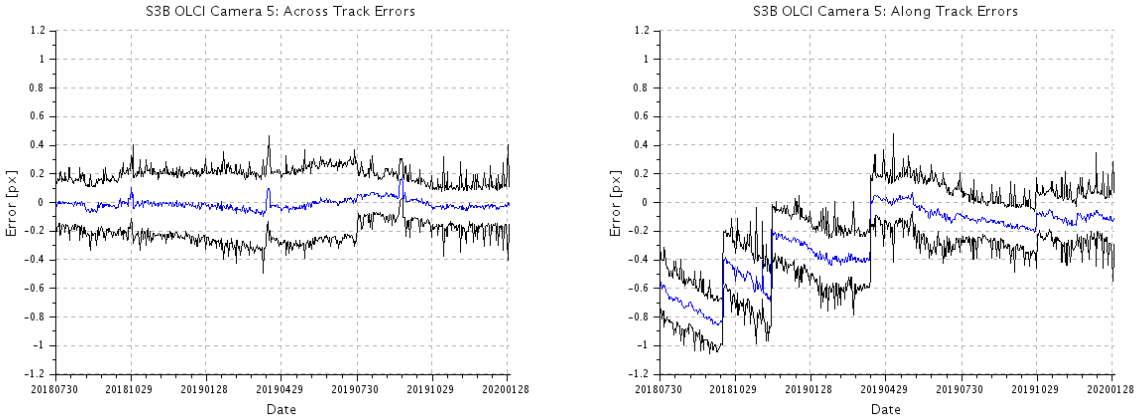

Figure 35: same as Figure 31 for Camera 5.

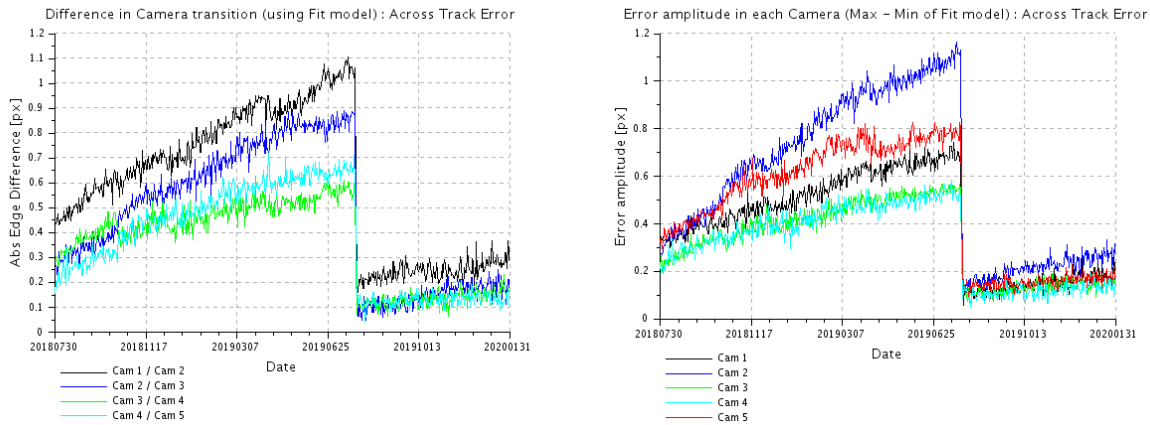

Figure 36: OLCI-B spatial across-track misregistration at each camera transition (left) and maximum amplitude of the across-track error within each camera (left).

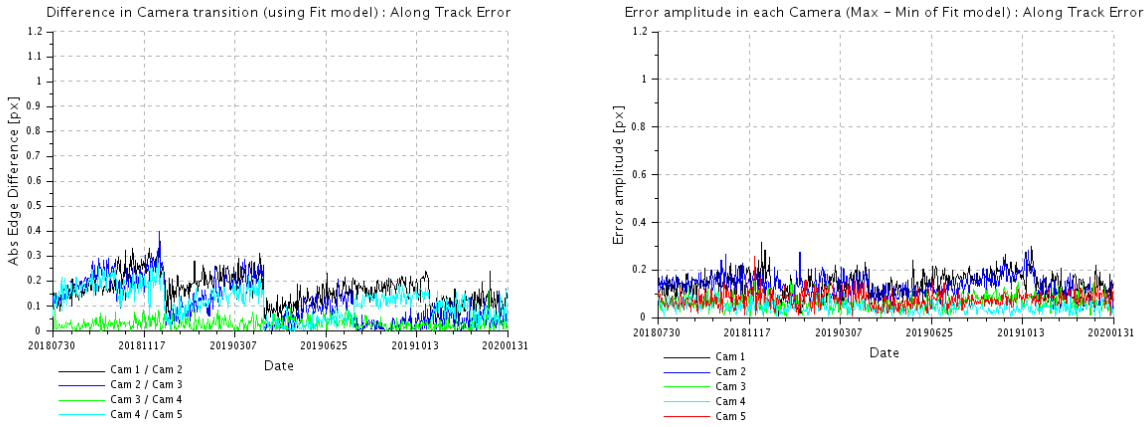

Figure 37: OLCI-B spatial along-track misregistration at each camera transition (left) and maximum amplitude of the along-track error within each camera (left).

5.2.2 Radiometric Gain Model Performance

5.2.2.1 OLCI-A

OLCI radiometric Calibration is based on its on-board calibration system: a carefully characterised solar diffuser is used as a secondary radiometric standard to derive instantaneous radiometric gains from diffuser measurements and computation of the incoming radiance, by use of diffuser characterisation, illumination and viewing geometry as well as spectral response functions.

OLCI Level 1 data processing to calibrate measured radiances using a Radiometric Gain Model (RGM) includes a long term drift correction, in order to avoid radiometric discontinuities between successive gain estimates as well as simplifying maintenance of operational processing configuration. The model is expressed as a bounded exponential time evolution applied onto the gain at a reference date. The time evolution model is fitted, on a per band and per pixel basis, on the evolution data presented above (section 5.1.4.1); the Gain at the reference date is obtained by time averaging after correction of the evolution. Diffuser ageing (see section 5.1.5) is of course accounted for during this process.

Consequently, the model is always used in extrapolation for routine production, as derived from already acquired data; it can only be used in interpolation for data reprocessing. Its performance is thus continuously monitored against new radiometric calibration, regularly acquired. The current operational RGM has been derived from data spanning 25/04/2016 to 28/08/2019 and put in operations the 29/10/2019. It includes the correction of the diffuser ageing for the five bluest bands (Oa1 to Oa5) for which it is clearly measurable.

The model RMS performance over the complete dataset (including the 10 calibrations in extrapolation over about 6 months) remains largely below than 0.1% – except for channels Oa1 (400 nm) that reaches 0.1% for the most recent calibration and 0.2% for the earliest – when averaged over the whole field of

view (Figure 38) even if a small drift of the model with respect to most recent data is now visible some channels.

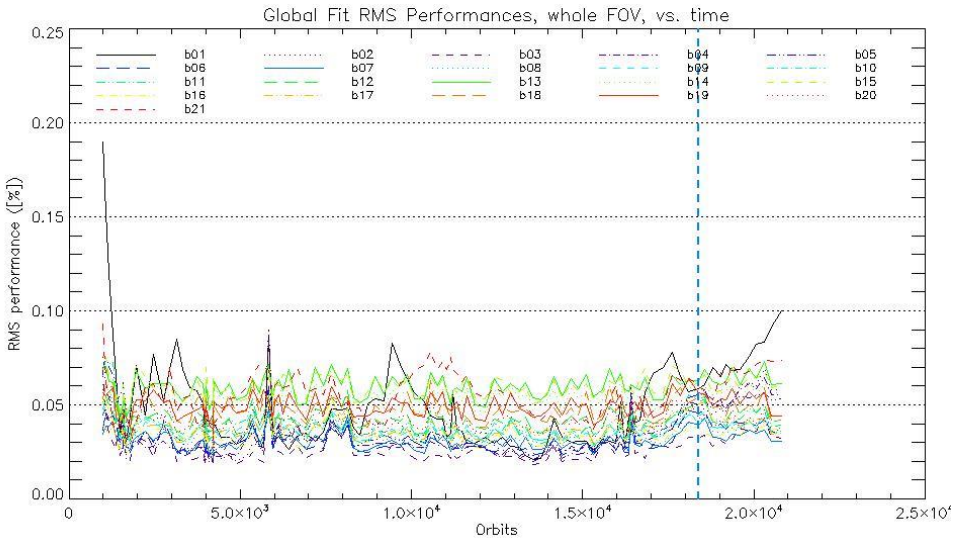

Figure 38: RMS performance of the Gain Model of current Processing Baseline as a function of orbit. The dashed vertical line shows the last calibration used in the model derivation.

More details are provided on Figure 39 on which per camera mean and standard deviation of Model over Data ratios are plotted against wavelength for each orbit. Conclusions are however the same with performances within 0.1% (1-σ) but for Oa1 and Oa21, the former reaching 0.3% in cameras 4, while the latter has a large dispersion (up to 0.5%) in camera 5, due to a group of pixels with an anomalous behaviour that cannot be fully captured by the model mathematical expression.

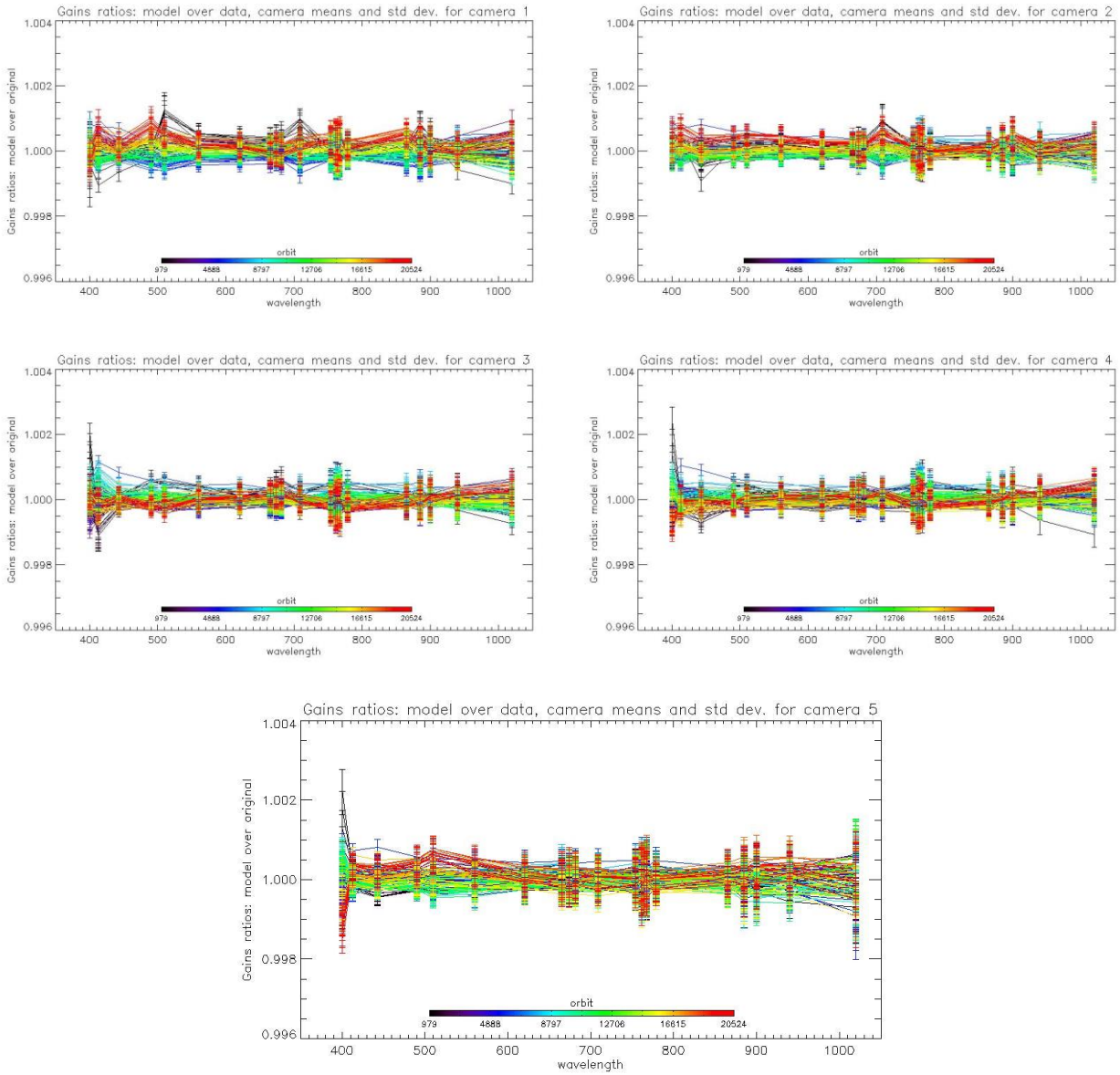

Figure 39: For the 5 cameras: Evolution model performance, as camera-average and standard deviation of ratio of Model over Data vs. wavelength, for each orbit of the test dataset, including 10 calibrations in extrapolation, with a colour code for each calibration from blue (oldest) to red (most recent).

5.2.2.2 OLCI-B

Instrument response and degradation modelling for OLCI-B, including the use of the in-flight BRDF model (based on 11th December 2018 Yaw Manoeuvres), has been refreshed and deployed at PDGS on 29th October 2019 (Processing Baseline 1.30). The model has been derived on the basis of an extended Radiometric Calibration dataset (from 11/05/2018 to 02/10/2019). It includes the correction of the diffuser ageing for the five bluest bands (Oa1 to Oa5) for which it is clearly measurable. The model performance over the complete dataset (including the 9 calibrations in extrapolation over about 5 months) is illustrated in Figure 40. It remains better than 0.1% when averaged over the whole field of view despite a small drift with respect to the most recent data.

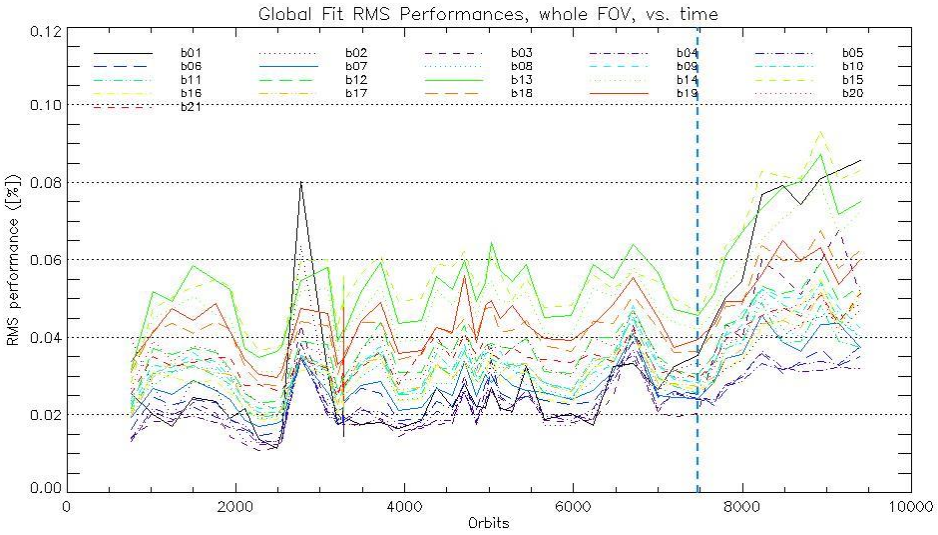

Figure 40: RMS performance of the OLCI-B Gain Model of the current processing baseline as a function of orbit. The dashed vertical line shows the last calibration used in the model derivation.

More details are provided on Figure 43 on which per camera mean and standard deviation of Model over Data ratios are plotted against wavelength for each orbit.

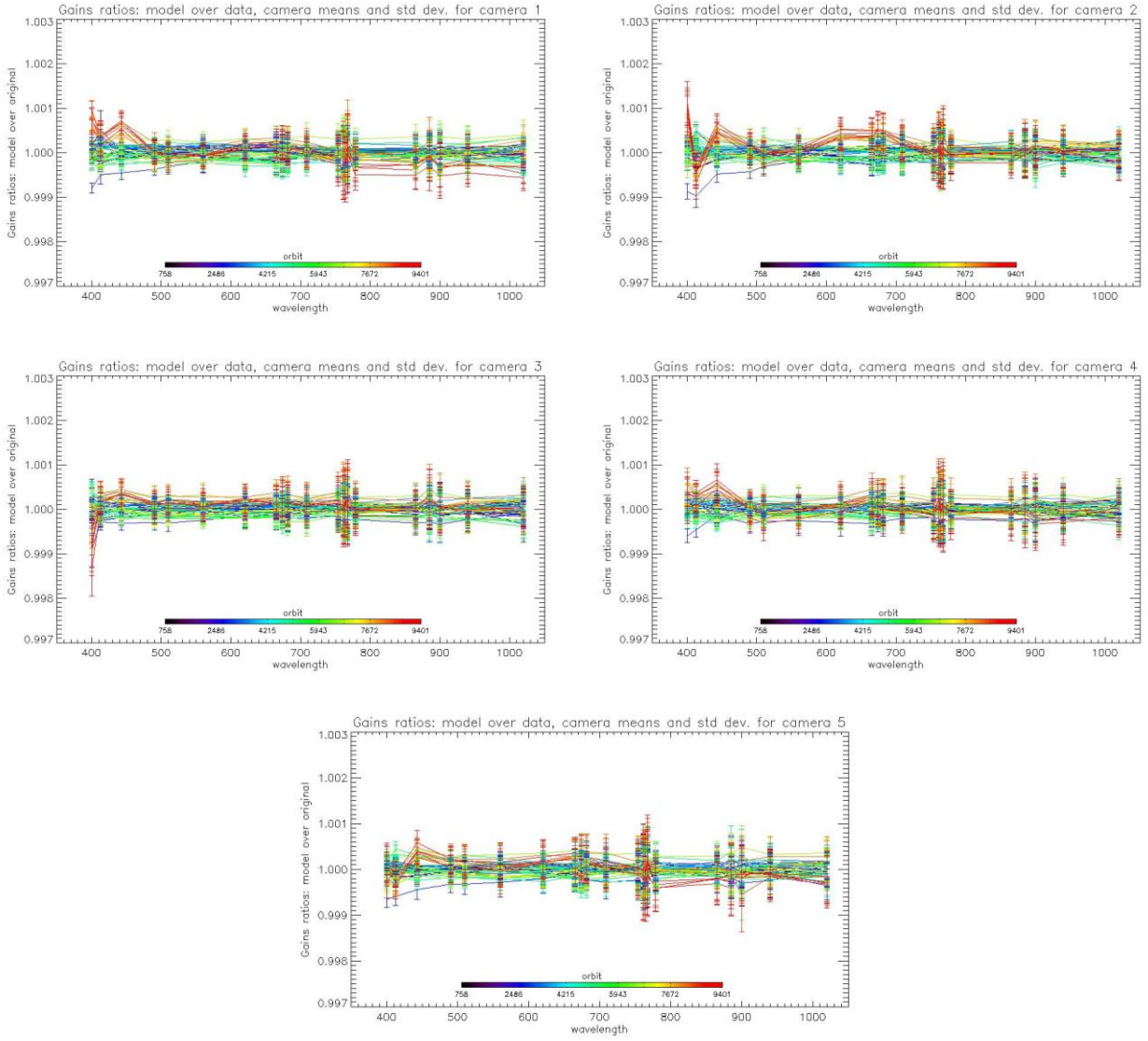

Figure 41: For the 5 cameras: Evolution model performance, as camera-average and standard deviation of ratio of Model over Data vs. wavelength, for each orbit of the test dataset, including 9 calibrations in extrapolation, with a colour code for each calibration from blue (oldest) to red (most recent).

5.2.3 Radiometric Validation

Radiometric Validation is performed at S3-MPC using three indirect methods, comparing simulated TOA radiances to that measured by the OLCI instrument.

- The “Rayleigh” method: measurement of the Rayleigh atmospheric backscattering over open ocean sites in clear sky off-glint conditions with low aerosol load to provide absolute calibration in the blue-to-red spectral domain.
- The “Glint” method: using the specular reflection of the sun (i.e. sun glint) on the open ocean surface and its known spectral dependency to assess inter-band calibration in the red-to-NIR spectral range.

- The PICS method: measurement over well characterized, temporally stable desert areas (Pseudo-Invariant Calibration Sites or PICS) to provide absolute calibration over the whole spectral domain. This method also allows cross-mission intercomparison with other sensors providing comparable spectral channels (e.g. Aqua/MODIS, S2A/MSI and MERIS/3REP).

The first two methods are undertaken by two different implementations: DIMITRI operated by ARGANS, and OSCAR operated by VITO.

Despite their discrepancies, more or less within their claimed accuracies, all methods do point out an excess of brightness for OLCI-A radiances (Figure 42, Figure 45, Figure 47 and Figure 50, Table 6 and Table 9). Results are in pretty close agreement around 2-3% between 560 and 900 nm, except at 709 nm, likely because of the H2O absorption correction accuracy. Biases are a bit worse in the blue, but the different methods (Rayleigh and PICS) do not agree in that spectral range: Rayleigh gives about 5-6 % while PICS remains around 2%. The Rayleigh method is however suspected to underestimate the simulated signal in the blue region whatever the sensor and the implementation, so that the 2-3% estimate of the PICS method is more reliable. Results for 1020 nm are much worse (5 to 6%, depending on the reference band).

The same figures for OLCI-B show current performance within the 2% requirement for all bands from 510 nm (Oa04) to 940 nm (Oa20) with remarkable agreement for all methods but DIMITRI Rayleigh. As for OLCI-A, the two Rayleigh methods indicate excess of brightness for the 4 bluest channels, between 2 and 4 %, while the PICS results provide very good performance estimates.

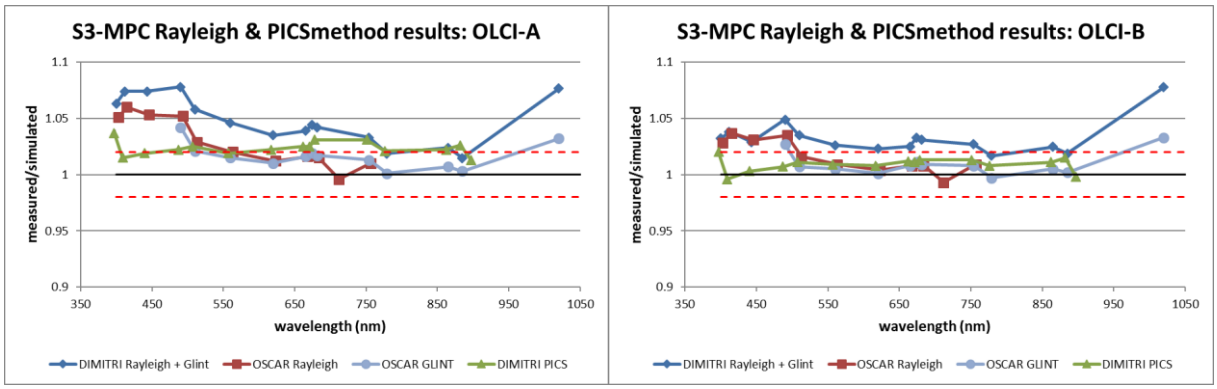

Figure 42: comparison of OSCAR and DIMITRI results for the various methods.

5.2.3.1 DIMITRI results

The time-series from Rayleigh and PICS methods over both the operational and reprocessed products display a good consistency, overall the used CalVal sites (Figure 43) and highlights a good stability of both sensors (OLCI-A and OLCI-B) over the analysed period.

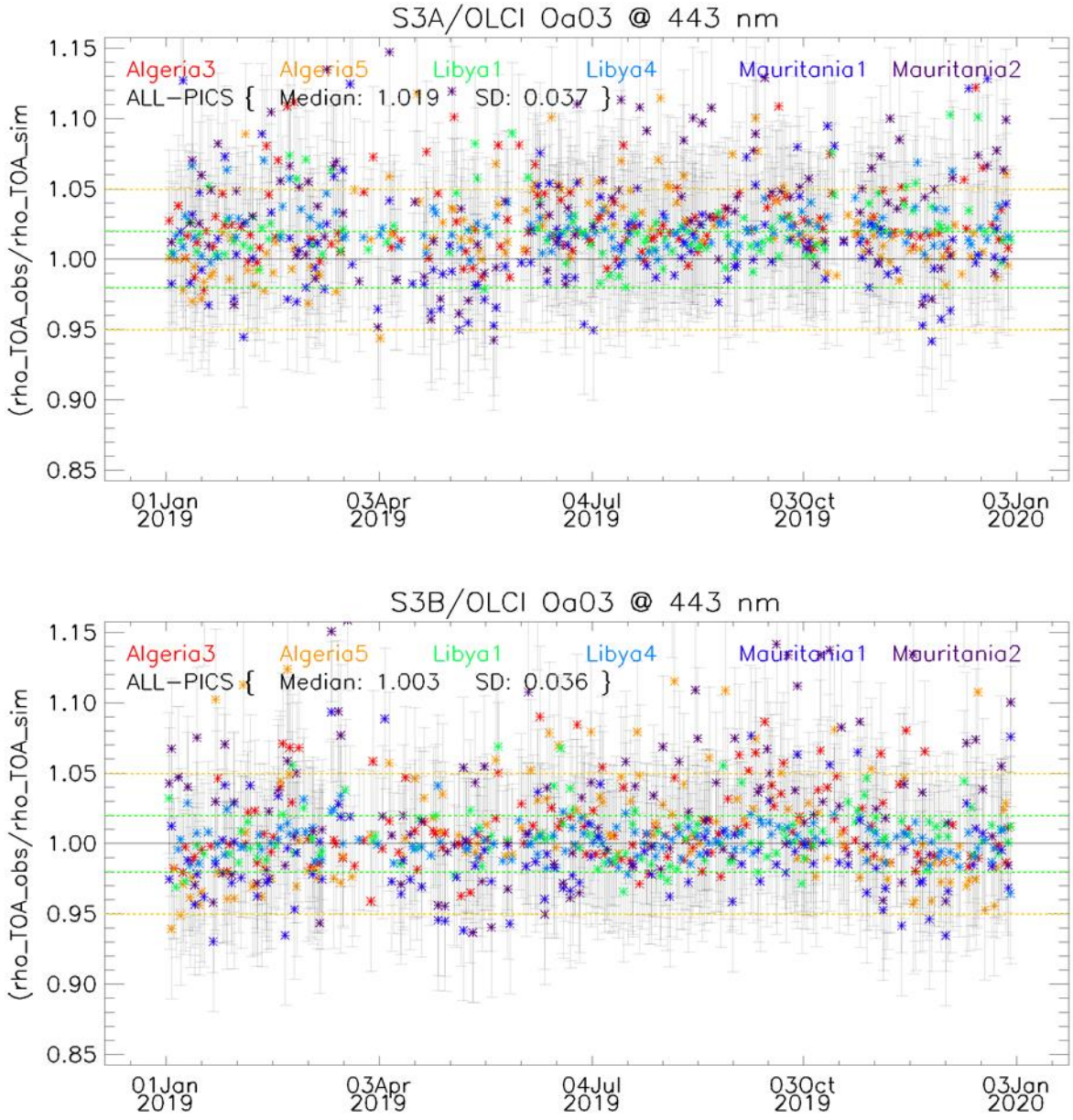

Figure 43: Time-series of the elementary ratios (observed/simulated) signal from S3A/OLCI (top) and S3B/OLCI (bottom) for band Oa03 over Six PICS Cal/Val sites. Dashed-green and orange lines indicate the 2% and 5% respectively. Error bars indicate the desert methodology uncertainty.

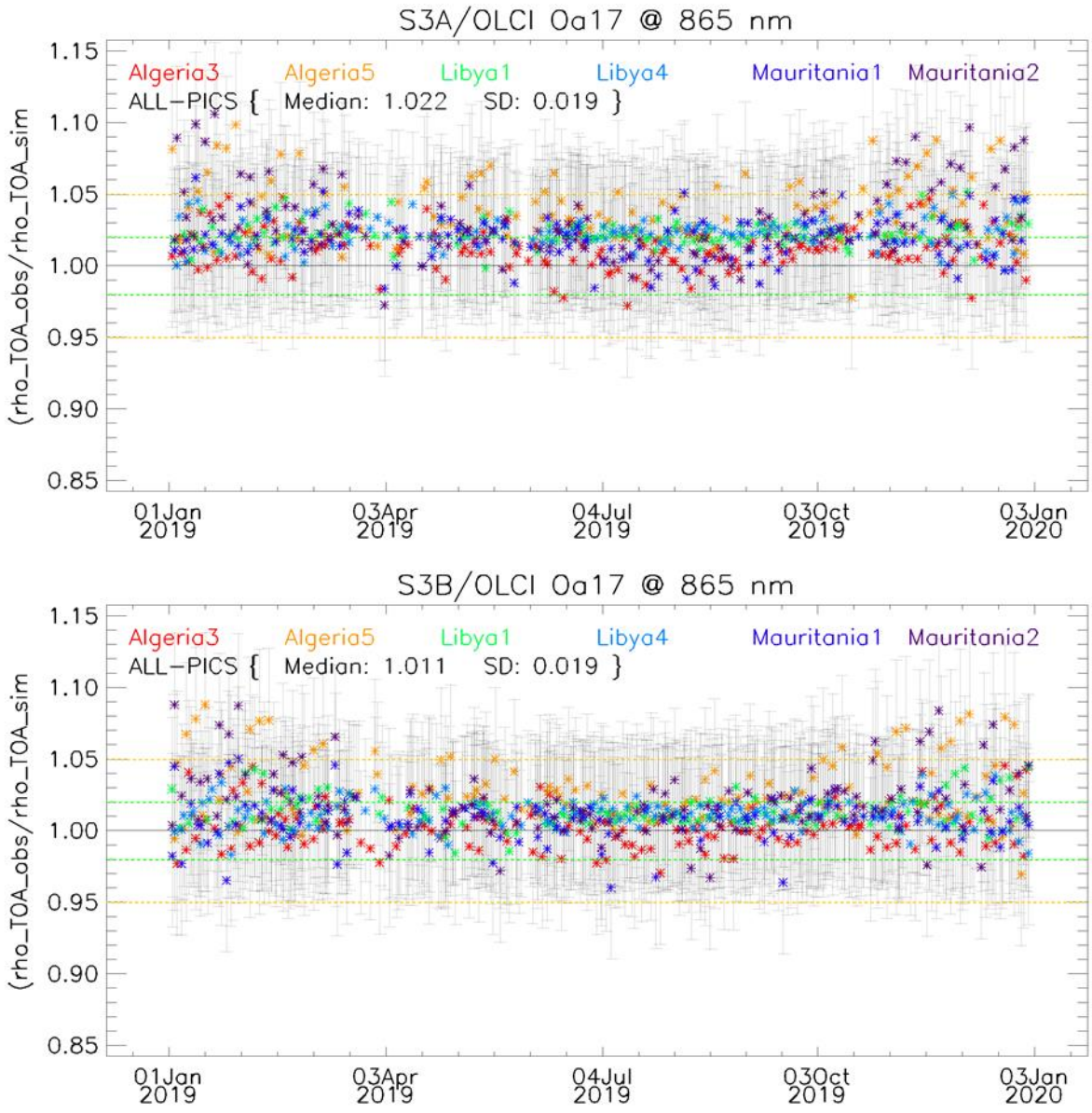

Figure 44: same as Figure 43 for band Oa17.

The synthesis of the results shows a good consistency over Rayleigh, Glint and PICS methods (Table 6 & Figure 45, Table 7 & Figure 45). While OLCI-A is within 2-3% (thus outside the 2% requirement limit) for almost all channels (but 412 nm, 779, 865 & 885 nm), OLCI-B display compliant biases values below 2% for almost all channels and methods. However, bands Oa10 (681 nm), Oa12 (754 nm) & and Oa18 (885 nm) are slightly above 2% according to the PICS method and channels Oa01 to Oa05 (400 to 510 nm) are above 3% according to the Rayleigh method.

Table 6: Synthesis of the DIMITRI results: estimated gain values for S3A/OLCI from Glint, Rayleigh and PICS over the period January 2018 – January 2019

S3A-OLCI		Rayleigh Over Jan'18-Jan'19		Glint Over Jan'18-Jan'19		PICS Over Jan'18-Jan'19	
Band	Wavelength (nm)	Average	Standard deviation	Average	Standard deviation	Average	Standard deviation
Oa01	400	1.063	0.036	NA	NA	1.037*	0.049
Oa02	412	1.074	0.038	NA	NA	1.015	0.027
Oa03	443	1.074	0.037	NA	NA	1.019	0.037
Oa04	490	1.078	0.036	NA	NA	1.022	0.041
Oa05	510	1.058	0.033	NA	NA	1.025	0.041
Oa06	560	1.046	0.029	1.026	0.018	1.019	0.040
Oa07	620	1.035	0.024	1.023	0.004	1.022	0.020
Oa08	665	1.039	0.022	1.025	0.000	1.025	0.023
Oa09	674	1.039	0.023	1.030	0.002	1.025	0.020
Oa10	681	NA	NA	1.028	0.003	1.031	0.022
Oa11	709	NA	NA	NA	NA	NA	NA
Oa12	754	NA	NA	1.019	0.011	1.031	0.019
Oa13	761	NA	NA	NA	NA	NA	NA
Oa14	764	NA	NA	NA	NA	NA	NA
Oa15	768	NA	NA	NA	NA	NA	NA
Oa16	779	NA	NA	1.005	0.013	1.021	0.020
Oa17	865	NA	NA	1.010	0.021	1.022	0.019
Oa18	885	NA	NA	1.001	0.025	1.026	0.018
Oa19	900	NA	NA	NA	NA	1.013*	0.033
Oa20	940	NA	NA	NA	NA	NA	NA
Oa21	1020	NA	NA	1.062	0.030	NA	NA

DIMITRI PICS results for band Oa01 and Oa19 have to be considered with care due to larger uncertainty in the signal simulation.

Table 7: Synthesis of the DIMITRI results: estimated gain values for S3B/OLCI from Glint, Rayleigh and PICS over the period October 2018 – February 2019

S3B-OLCI		Rayleigh Over Jan'18-Jan'19		Glint Over Jan'18-Jan'19		PICS Over Jan'18-Jan'19	
Band	Wavelength (nm)	Average	Standard deviation	Average	Standard deviation	Average	Standard deviation
Oa01	400	1.032	0.036	NA	NA	1.020*	0.050
Oa02	412	1.038	0.037	NA	NA	0.996	0.031
Oa03	443	1.029	0.035	NA	NA	1.003	0.036
Oa04	490	1.049	0.036	NA	NA	1.007	0.043
Oa05	510	1.035	0.032	NA	NA	1.011	0.040
Oa06	560	1.026	0.028	1.016	0.008	1.009	0.035
Oa07	620	1.023	0.025	1.011	0.002	1.008	0.019
Oa08	665	1.025	0.022	1.013	0.000	1.012	0.024
Oa09	674	1.031	0.022	1.019	0.002	1.011	0.020
Oa10	681	NA	NA	1.017	0.001	1.013	0.022
Oa11	709	NA	NA	NA	NA	NA	NA
Oa12	754	NA	NA	1.013	0.004	1.013	0.018
Oa13	761	NA	NA	NA	NA	NA	NA
Oa14	764	NA	NA	NA	NA	NA	NA
Oa15	768	NA	NA	NA	NA	NA	NA
Oa16	779	NA	NA	1.003	0.006	1.008	0.018
Oa17	865	NA	NA	1.011	0.009	1.011	0.019
Oa18	885	NA	NA	1.005	0.011	1.015	0.017
Oa19	900	NA	NA	NA	NA	0.998*	0.030
Oa20	940	NA	NA	NA	NA	NA	NA
Oa21	1020	NA	NA	1.063	0.019	NA	NA

DIMITRI PICS results for band Oa01 and Oa19 have to be considered with care due to larger uncertainty in the signal simulation.

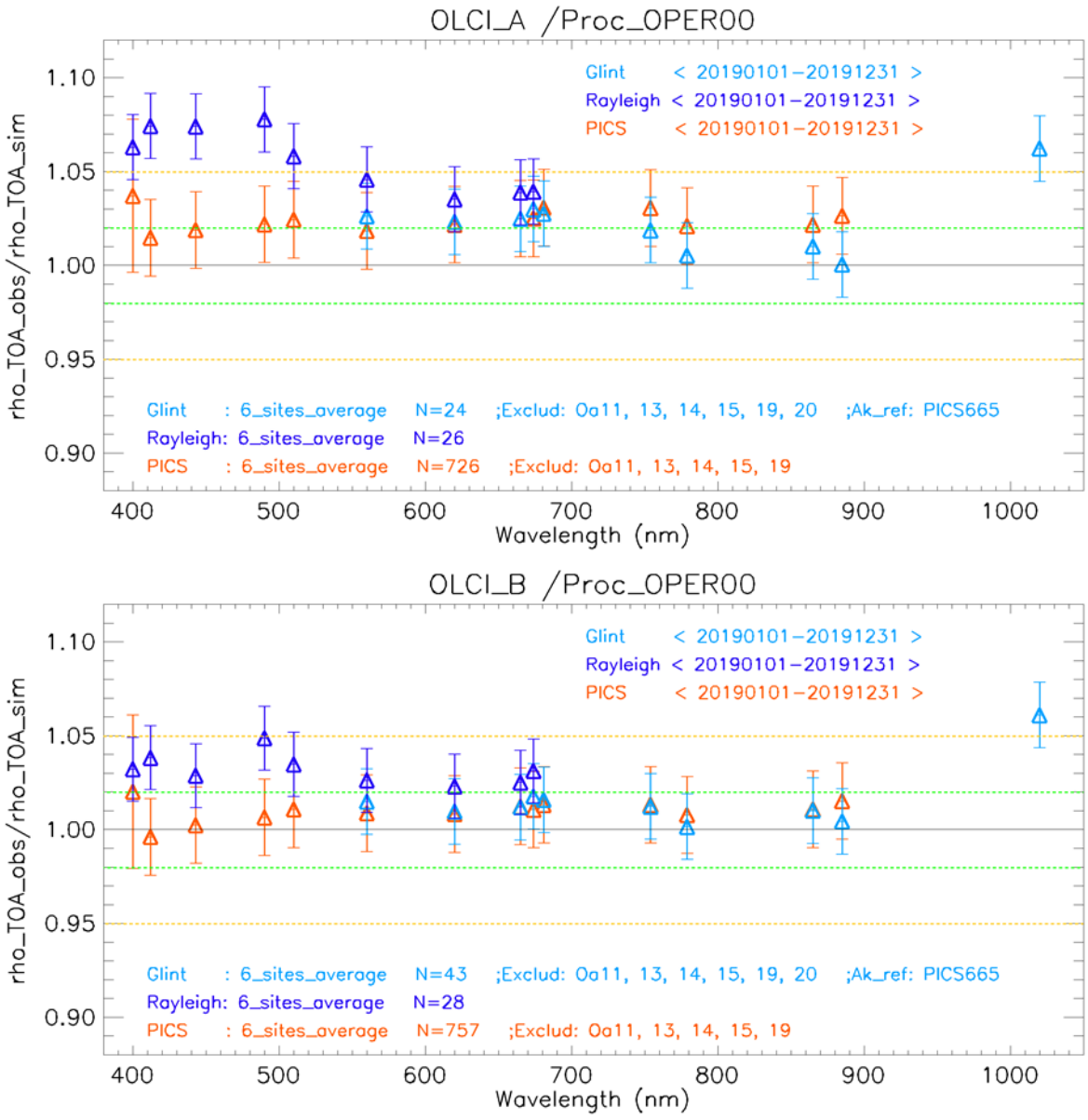

Figure 45: Estimated gain values for (top) S3A/OLCI and (bottom) S3B/OLCI from Glint, Rayleigh and PICS methods as a function of wavelength. We use the gain value of Oa8 from PICS method as reference gain for Sunglint method. Dashed-green and orange lines indicate the 2% and 5% respectively. Error bars indicate the methods uncertainties.

Cross-mission Intercomparison with MERIS (3REP archive), MSI-A and MODIS-A has been performed until January 2020. Figure 46 shows the estimated gain over different time-series for different sensors over PICS. The spectral bands with significant absorption from water vapour and O2 are excluded. OLCI-A seems to have higher gains with respect to the other sensors, and about 1-2% higher gain with respect to OLCI-B over the VNIR spectral range.

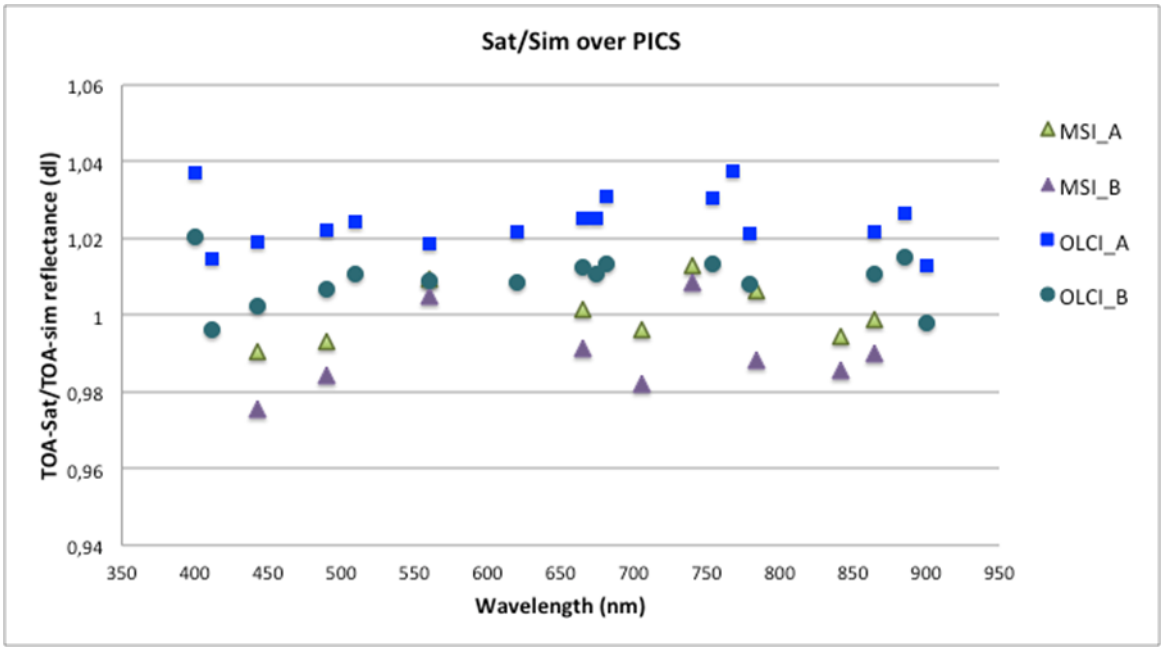

Figure 46: Ratio of observed TOA reflectance to simulated one for (black) MERIS/3REP, (green) S2A/MSI, (cyan) Aqua/MODIS and (blue) S3A/OLCI averaged over the six PICS test sites as a function of wavelength.

5.2.3.2 OSCAR results

The OSCAR Rayleigh and Glint methods have been applied to the S3A and S3B S3ETRAC data from the 6 oceanic calibration sites listed in Table 8.

Table 8: S3ETRAC Rayleigh Calibration sites

Site Name	Ocean	North Latitute	South Latitude	East Longitude	West Longitude
PacSE	South-East of Pacific	-20.7	-44.9	-89	-130.2
PacNW	North-West of Pacific	22.7	10	165.6	139.5
PacN	North of Pacific	23.5	15	200.6	179.4
AtlN	North of Atlantic	27	17	-44.2	-62.5
AtlS	South of Atlantic	-9.9	-19.9	-11	-32.3
IndS	South of Indian	-21.2	-29.9	100.1	89.5

OSCAR Rayleigh results

In Figure 47, the average OSCAR OLCI-A and OLCI-B Rayleigh results are given for year 2019. A bias is observed between OLCI-A and OLCI-B with OLCI-A about 2 % brighter than OLCIB in blue bands (i.e. Oa1 to Oa4) and about 0.7-1% brighter in green and red bands (i.e. Oa5 to Oa10).

In Figure 48 the average OSCAR OLCI-A results for 2016 to 2019 are plotted per year. ***Figure 49*** gives the OSCAR OLCI-B results for 2018 and 2019. Overall results seem to be consistent between the years, both for OLCI -A and OLCI-B.

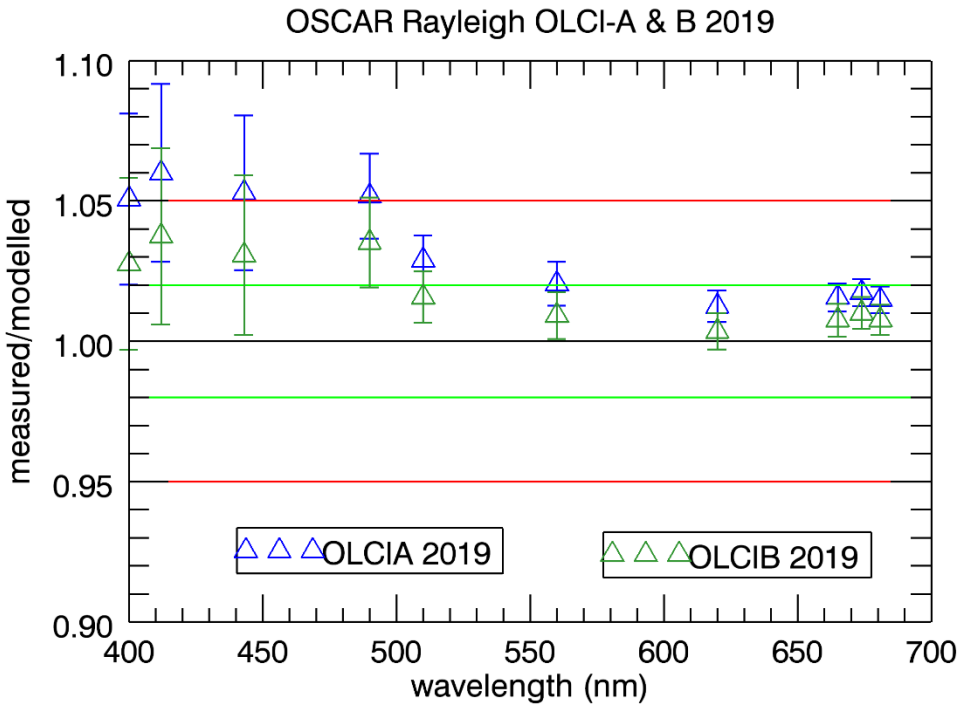

Figure 47: OSCAR Rayleigh S3A and S3B Calibration results for 2019 as a function of wavelength.

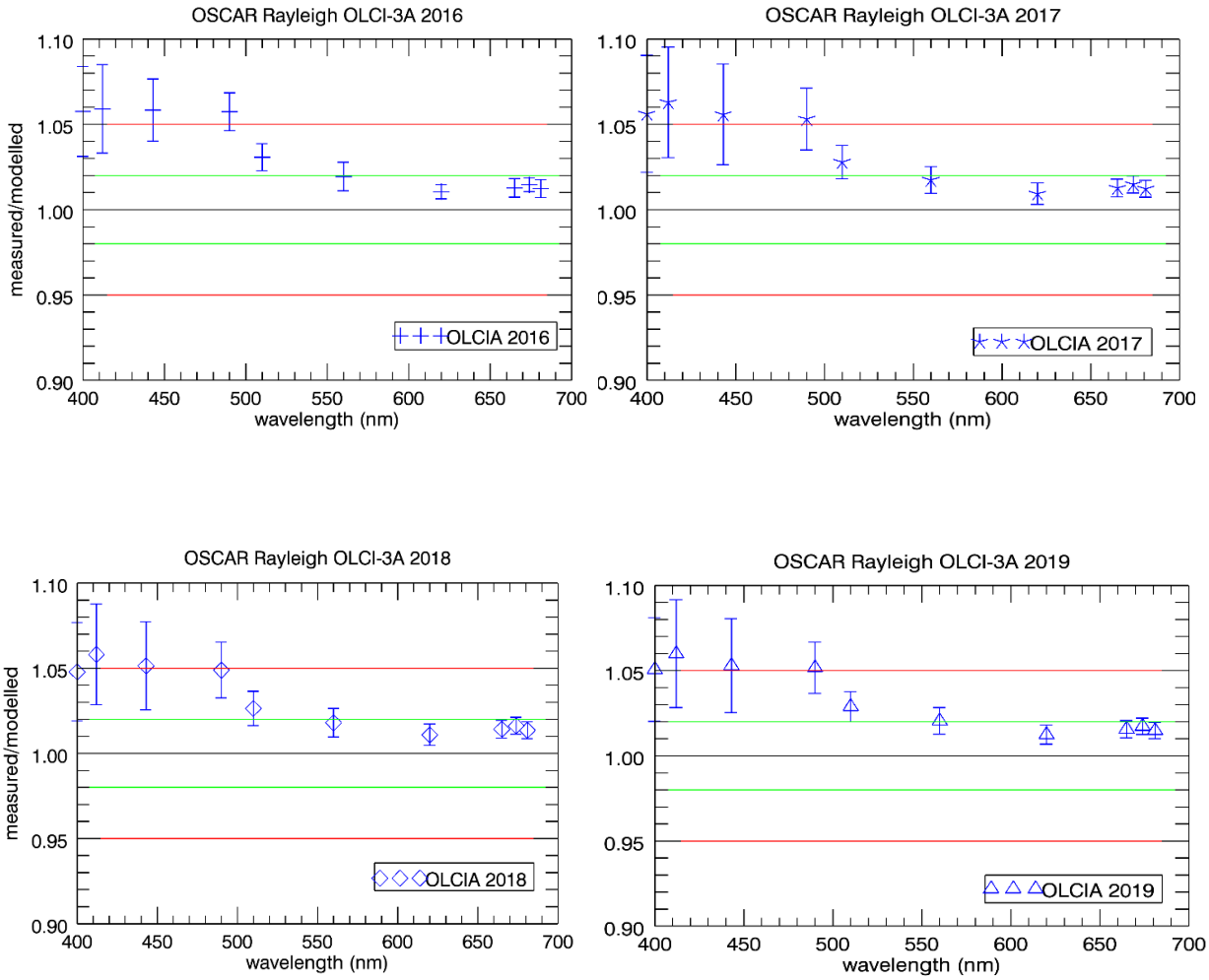

Figure 48: OSCAR Rayleigh S3A Calibration results for 2016, 2017, 2018 and 2019 as a function of wavelength.

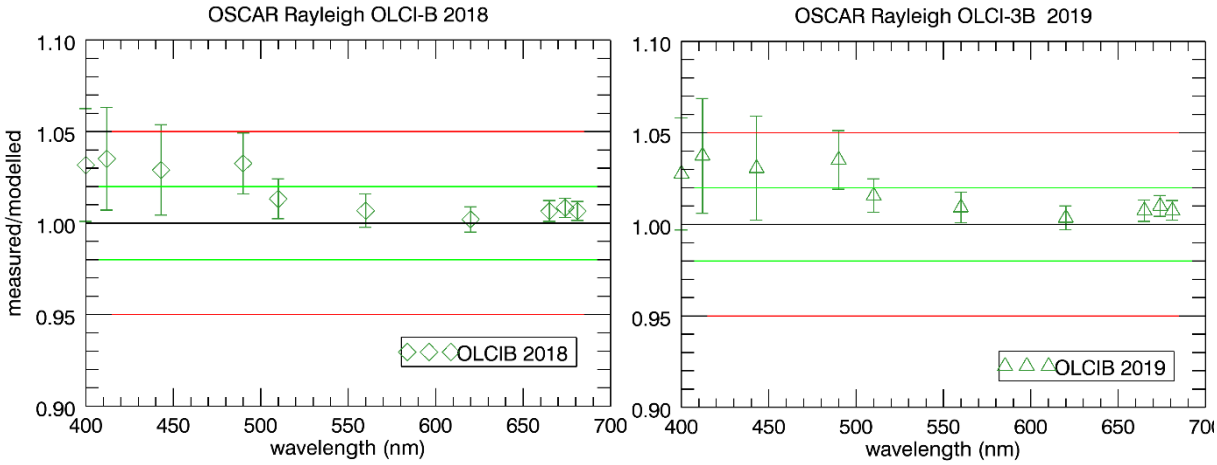

Figure 49: OSCAR Rayleigh S3B Calibration results for 2018 and 2019 as a function of wavelength.

OSCAR Glitter results

In Figure 50, the average OSCAR OLCI-A and OLCI-B Glitter results are given for year 2019. Similarly, as for the Rayleigh results a bias is observed between OLCI-A and OLCI-B with OLCI-A being slightly brighter than OLCI-B. The bias seems to decrease with the wavelength.

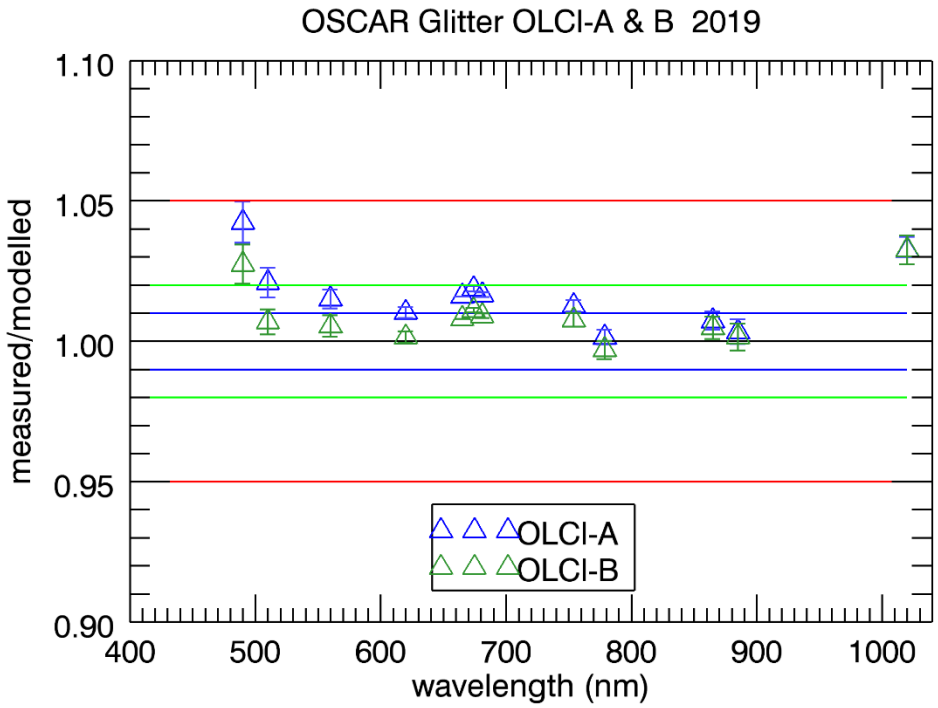

Figure 50: OSCAR Glitter S3A and S3B Calibration results (adapted to Rayleigh result at 665 nm) for 2019 as a function of wavelength.

Synthesis OSCAR Results

The synthesis of the OSCAR results given in Table 9 shows a good consistency between the Rayleigh and Glitter results.

Table 9. Overview of the OSCAR Rayleigh and Glitter calibration results for S3A and S3B for 2019

OLCI band	Wavelength	Oscar Rayleigh S3A 2919		Oscar Glint S3A 2919		Oscar Rayleigh S3B 2919		Oscar Glint S3B 2919	
	(nm)	avg	stdev	avg	stdev	avg	stdev	avg	stdev
Oa01	400	1.051*	0.031	NA	NA	1.028*	0.031	NA	NA
Oa02	412	1.060	0.032	NA	NA	1.037	0.031	NA	NA
Oa03	443	1.053	0.027	NA	NA	1.031	0.029	NA	NA
Oa04	490	1.052	0.015	1.042	0.007	1.035	0.016	1.027	0.007
Oa05	510	1.029	0.009	1.021	0.005	1.016	0.009	1.007	0.004
Oa06	560	1.020	0.008	1.015	0.003	1.009	0.008	1.005	0.004
Oa07	620	1.012	0.006	1.010	0.002	1.004	0.007	1.001	0.002
Oa08	665	1.016	0.005	1.016	NA	1.008	0.006	1.008	NA
Oa09	674	1.017	0.005	1.019	0.001	1.010	0.006	1.011	0.001
Oa10	681	1.015	0.005	1.017	0.001	1.008	0.005	1.009	0.001
Oa11	709	0.996	0.008	NA	NA	0.993	0.008	NA	NA
Oa12	754	1.010	0.002	1.013	0.002	1.009	0.002	1.008	0.002
Oa13	761.25	NA	NA	NA	NA	NA	NA	NA	NA
Oa14	764.375	NA	NA	NA	NA	NA	NA	NA	NA
Oa15	767.5	NA	NA	NA	NA	NA	NA	NA	NA
Oa16	778.75	NA	NA	1.001	0.003	NA	NA	0.997	0.003
Oa17	865	NA	NA	1.007	0.003	NA	NA	1.005	0.004
Oa18	885	NA	NA	1.003	0.004	NA	NA	1.002	0.005
Oa19	900	NA	NA	NA	NA	NA	NA	NA	NA
Oa20	940	NA	NA	NA	NA	NA	NA	NA	NA
Oa21	1020	NA	NA	1.032	0.005	NA	NA	1.033	0.005

*OSCAR Rayleigh results for band Oa01 have to be considered with care due to larger uncertainty in the radiative transfer calculation

5.3 L2 product performances

5.3.1 Level 2 cloud screening

5.3.1.1 Introduction

Providing clear sky conditions for production of Sentinel-3 OLCI Level 2 products is essential to ensure a good and reliable Level 2 product quality for the users. After issues with the cloud screening in the initial processing baseline, a big effort was made by the Sentinel-3 MPC to improve the level 2 cloud flagging algorithms. Since 2017 a new cloud flagging is implemented in the current operational and reprocessed products. This had been extensively validated during 2019 and is documented in the Annual Report 2018. In brief summary, the overall accuracy is 86%, and the user accuracy for clear sky conditions which is the most relevant criteria for users, is 92.1%.

The work in the year 2019 focussed on improving the limitations which are still in the cloud screening. The achievement is summarized below. Since these improvements do not depend on the platform (S-3A or B) we do not differentiate.

5.3.1.2 Improvements over glint

The differentiation between clouds and sun glint over the ocean is problematic because sun glint has very similar spectral behaviour as clouds. The current masking is thus sometime identifying sun glint areas as clouds. This issue occurs in high glint conditions when the ocean atmospheric correction cannot be applied. Thus, it is not a problem for the ocean Level 2 products, but this behaviour is confusing to users. Further, any user processing which may use the flag may be mislead.

An adaptation of the neural net threshold based on the theoretical glint reflectance (rho_gli) had already been used in MERIS processing. This approach was tested. An improvement was observed, but the difference was not large. In parallel with the dedicated glint investigations, the new neural net (see below) was developed which benefits from improvements in the usage of the O2 bands. The distinction between glint and clouds also benefits from this and thus we stopped a dedicated treatment of glint, because this would always include the risk of artificial boundaries in the image when we switch cloud flagging from “outside glint” to “inside glint”.

5.3.1.3 Improvements due to usage of O2 bands

The oxygen absorption bands of OLCI (Oa13, Oa14 and Oa15) are sensitive to the absorption of oxygen in the atmosphere which scales with the airmass between the sensor and scattering target (= height of cloud) and thus is an indicator for clouds, in general. The usage is limited by the spectral differences per detector, and if this is not taken into account properly, the usability is rather limited.
Thanks to R. Preusker (Spectral Earth) a method to harmonise the wavelength per detector for the O2 bands was developed, called O2 harmonisation. It has been implemented as a SNAP processor and made available publicly. Once the bands are harmonised, they can be used much better for cloud

screening purpose, e.g. for the separation between snow and ice, and likewise for distinction between glint and clouds.

R. Preusker also calculated a large number of TOA spectra for the O2 bands for the nominal wavelengths, and covering a large number of cloud and surface conditions. With these simulations we calculated a neural net which provides an estimate of the cloud top height (CTH, example see figure below). The method has been optimised to be fast and robust, but it is not very precise. The purpose is to use this as one information for cloud screening, and also use it for the calculation of cloud shadow (see next paragraph).

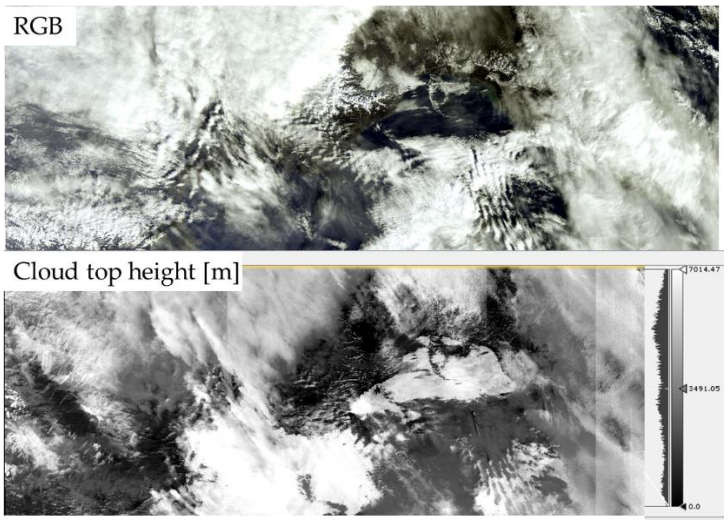

Figure 51: Cloud top height rough estimate for cloud screening and cloud shadow calculation.

5.3.1.4 New PixBox dataset

A new PixBox data set of manually selected and labelled pixels has been collected. This data includes samples from OLCI-A (10400 pixels) and OLCI-B (9800 pixels). It has a better temporal coverage and newer acquisition dates than the dataset used so far. This dataset was completed in December 2019. It will be used for validation of the reprocessed data in 2020.

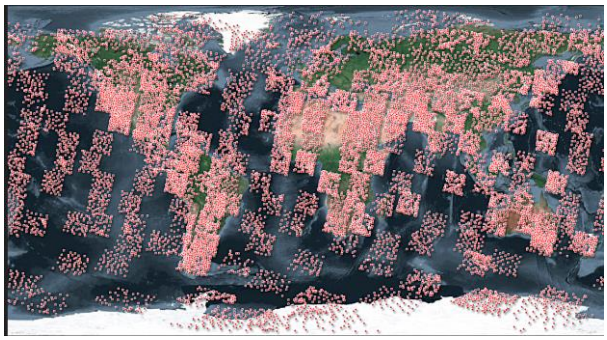

Figure 52: Spatial distribution of the 20200 samples of the new validation dataset.

5.3.1.5 Neural Network upgrade

The current neural network is a multilayer perceptron, trained feedforward backpropagation. I take the top-of-atmosphere radiances as input and has one output neuron. The values of this single output neuron represent the different classes (snow, opaque cloud, transparent cloud, clear land, clear water, etc.).

During 2019 we started to question all aspects of the neural net and renovate if from scratch where necessary. The underlying neural net training software we used so far is the SNNS tool from the early 1990's. Neural nets are stored as ADF in a proprietary format, developed within the MERIS ground segment contract, and the library to read and execute the net was also a dedicated development. We changed this now to the contemporary and widely used Tensorflow / KERAS (TF) software and associated format. This is open source software. With the change to TF we tested different neural net types and training processes, but concluded that a classical MLP is most appropriate for our problem.

A significant change, however, is a development which has been started in 2019 and will be continued in 2020. The target of the training process will be the identification of clear sky conditions. The rationale is that this is the real interest of the cloud screening and not the cloud itself. In a first step the neural net is trained distinguish between clear sky and non-clear sky conditions. The training is specifically done for land, water and snow surfaces. In terms of architecture this means that the neural net has 3 output neurons, one for each of the surface classes, and each neuron has two states: clear / non-clear. This is the critical step for subsequent L2 processing. In a second step the non-clear pixels are further investigated (second neural net) to delineate the cases (opaque cloud, dust, high aerosol, semi-transparent cloud etc). Step 1 has been implemented in 2019 and shows good first results. Figure 51 shows the training validation for the 3 surface types. The smaller the histogram, the better the performance. Surprisingly, the identification of clear sky land conditions works better than the one of water surfaces. Optimisation is possible by defining the cut value between clear and non-clear conditions per surface.

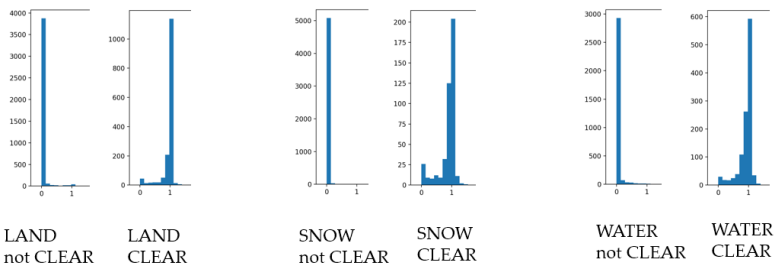

Figure 53: Training result of the new NN architecture, implemented with Tensorflow.

5.3.1.6 Cloud Shadow

Once the cloud top height was available (see above) the calculation of a cloud shadow is possible. The algorithm is basically the same as it was already in place for MERIS. It uses the geometry of sun and projects the cloud on the surface. We assume that the cloud base is located in the same pixel as the cloud top, i.e. we do not apply a dedicated cloud bottom treatment. A novelty developed here is the adjustment

of the sun azimuth, as the apparent position of clouds in the scene depends on the viewing geometry. Only in nadir view the position of an elevated object is located at the correct position.

An implementation challenge of such a geometrical approach occurs always at tile borders. In particular, highly parallel processing can become an issue if small tiles are distributed in the processing system and if tiles cannot use information from other tiles.

The cloud shadow has been implemented as a SNAP processor. A technical note has been drafted and given to the implementation team of the IPF for assessment. Figure 54 shows an example of the cloud shadow for OLCI.

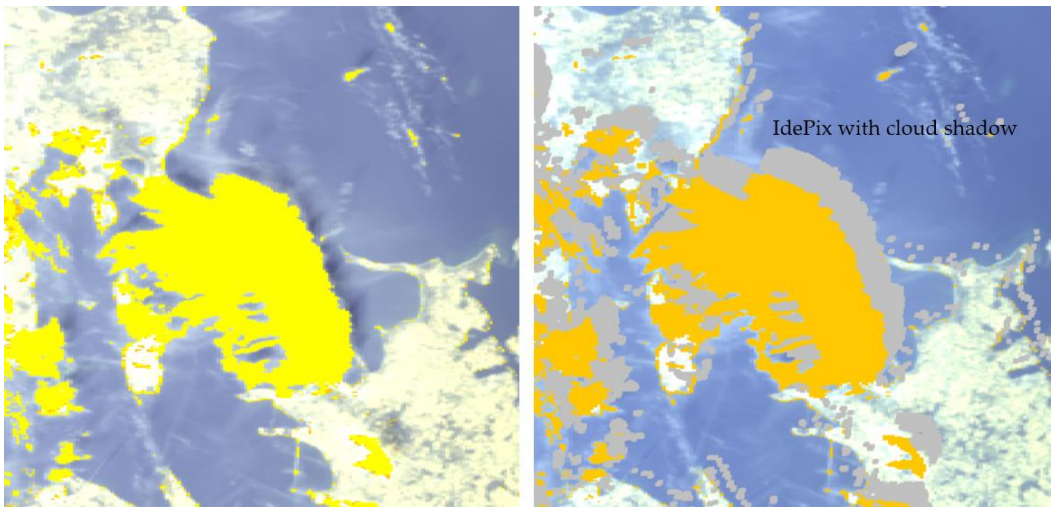

Figure 54: Cloud and cloud shadow in an OLCI image. SNAP IdePix implementation.

5.3.1.7 Land Water Mask

The ADFs in OLCI processing used for land-water mask, as well as for intertidal areas and inland waters, uses as one underlying base information the Water Bodies Mask from the ESA Land Cover CCI project. In the current IPF the LC CCI WB mask v3 is used. During 2018, version 4 of the LC CCI Water Bodies was produced. The main difference is that this dataset is available with a spatial resolution of 150 m (instead of 300 m for v3), and the input data used for the classification was extended.

Early 2019, we compared the v3 and v4 of the mask using google earth as reference. In some areas the classification of v4 was improved compared to v3 but in other areas it was degraded. The spatial improvement would not impact the usage in the ground segment as the target resolution is 300 m. It was therefore concluded to not change the ADF.

5.3.2 Integrated Water Vapour (IWV)

The OLCI L2 IWV processor distinguishes between ocean and land surfaces and works very differently above the respective surfaces. The algorithm above water shows some serious flaws and therefor is under development. OLCI's IWV above land surface is validated using the following ground truth data:

1. Global GNSS data, with a focus to north America (SUOMI NET, Ware et al. 2000)
2. Microwave radiometer measurements at the *Atmospheric Radiation Measurement* (ARM) *Climate Research Facility* of the US Department of Energy (Turner et al. 2003, Turner et al. 2007)
3. GRUAN radiosonde observations IWV (Immler et al 2010, Bodeker 2015)
4. AERONET (Holben et al 1998), using atmospheric transmission measurements at 0.9µm

All L2 product types have been validated: full resolution and reduced resolution, near real time and non time critical, Ocean Colour (*wrr, wfr*) and Land Colour (*lrr, lfr*). The found results for all product types are identical, as expected, since the used processor is the same. The following quantitative comparisons are hence restricted to *wrr NT* (Ocean Colour Product, reduced resolution, non time critical). Since the ocean colour product and the land colour product provide water vapour above land **and** water surfaces, the comparison is comprehensive. OLCI A data partly belong to reprocessed data if processed before Nov/2017. The ocean colour products from OLCI A have been taken from Eumetsats CODA (Copernicus Online Data Access, https://coda.eumetsat.int/#/home) or reprocessed OLCI A CODAREP (https://codarep.eumetsat.int/#/home) websites. All OLCI B data is from Eumetsats CODA (Copernicus Online Data Access, https://coda.eumetsat.int/#/home).

5.3.2.1 Integrated water vapour above land

5.3.2.1.1 Validation of OLCI A IWV using GNSS

380,000 potential matchups within the period of June 2016 to January 2020 have been analysed yet. The scenes cover high and low elevations; however, the majority of the used SUOMI-NET ground stations are in North and Central America. Only OLCI measurements are taken for the validation which are above land and are cloud-free in an area of about 10x10 km^2 around the GNSS stations. For the cloud detection, the standard L2 cloud-mask has been applied (including the cloud ambiguous and cloud margin flags). The comparison of OLCI and GNSS shows a very high agreement (Figure 55). The correlation between both quantities is 0.98. The root-mean-squared-difference is 2.2 kg/m^2. The systematic overestimation by OLCI is 12%. The bias corrected *rmsd* is 1.3 kg/m^2. Interesting is the strong seasonal pattern of the bias. This clearly belongs to the seasonality of water vapor in North Amerika. It is also partly visible in the systematic overestimation swinging between 7 and 12 %. This however could be a sampling effect too.

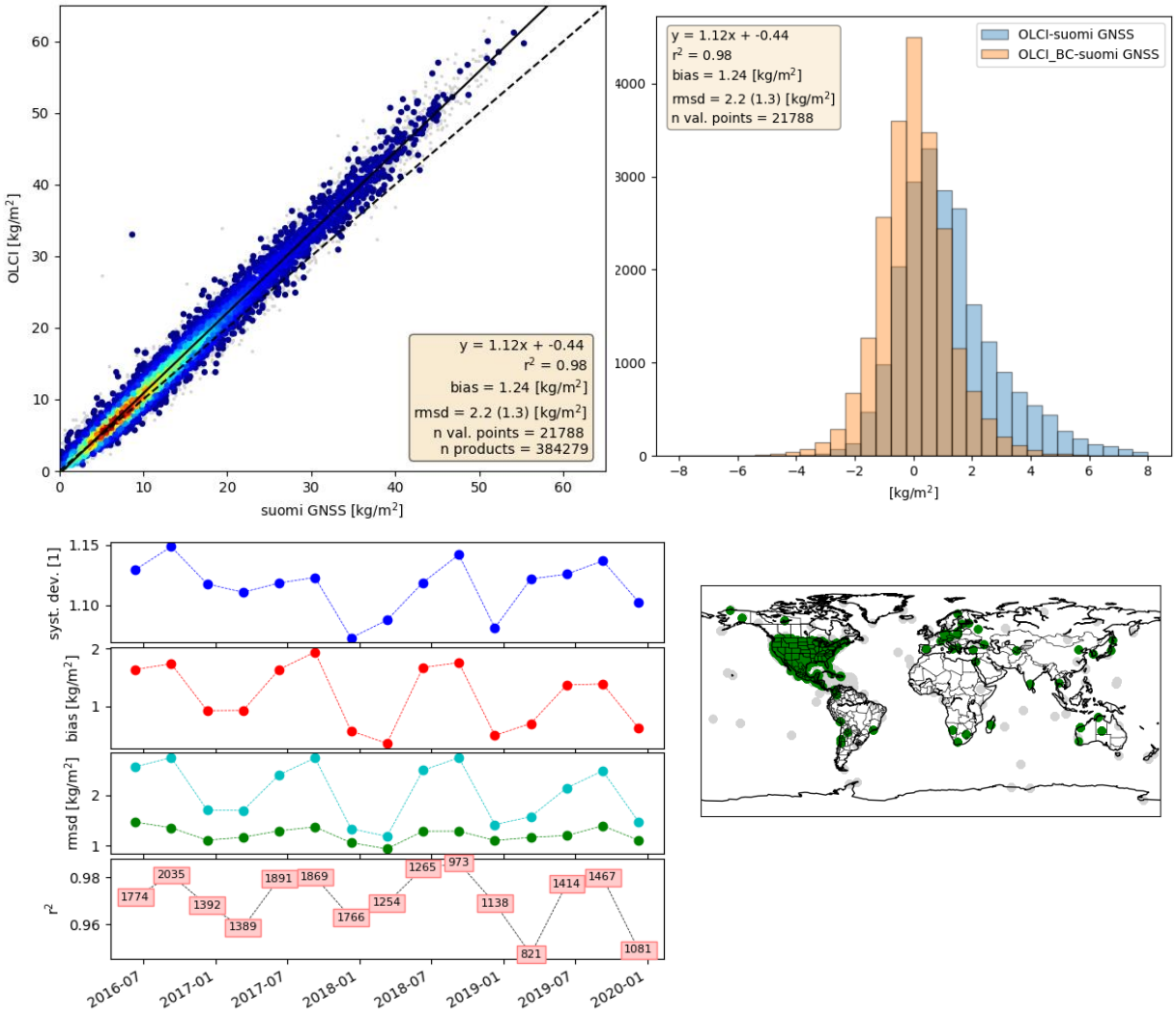

Figure 55: Upper left: Scatter plot of the IWV products, derived from OLCI A above land and from SUOMI NET GNSS measurements. Upper right: Histogram of the difference between OLCI and GNSS (blue: original OLCI, orange: bias corrected OLCI). Lower left: Temporal evolution of different quality measures (from top to bottom: systematic deviation factor, bias, root mean squared difference (with and without bias correction), explained variance (number in boxes are the numbers of matchups)). Lower right: Positions of the GNSS stations (grey: no valid matchup).

5.3.2.1.2 Validation of OLCI A IWV using passive microwave radiometer at ARM sites

Microwave radiometer measurements at the *Atmospheric Radiation Measurement* (ARM) *Climate Research Facility* of the US Department of Energy provides the ground truth with the highest accuracy (0.6 kg/m^2). Currently 3 ARM sites are operated continuously, only the SGP (southern great planes) site provided cloud free measurements. 2600 potential matchups within the period of June 2016 to November 2019 have been analysed yet. Only OLCI measurements are taken for the validation which are above land and are cloud-free in an area of about 10x10 km^2 around SGP. For the cloud detection, the standard L2 cloud-mask has been applied (including the cloud ambiguous and cloud margin flags), resulting in 110

valid matchups. The comparison shows a very high agreement (Figure 56 and Figure 55). The correlation between both quantities is 0.99. The root-mean-squared-difference is 1.4 kg/m^2. The systematic overestimation by OLCI is 8%. The bias corrected *rmsd* is 0.8 kg/m^2, close to the uncertainty of ARM. The investigation of the temporal evolution shows the same seasonal pattern as the GNSS comparisons, again belonging to the same seasonality of water vapor in North Amerika.

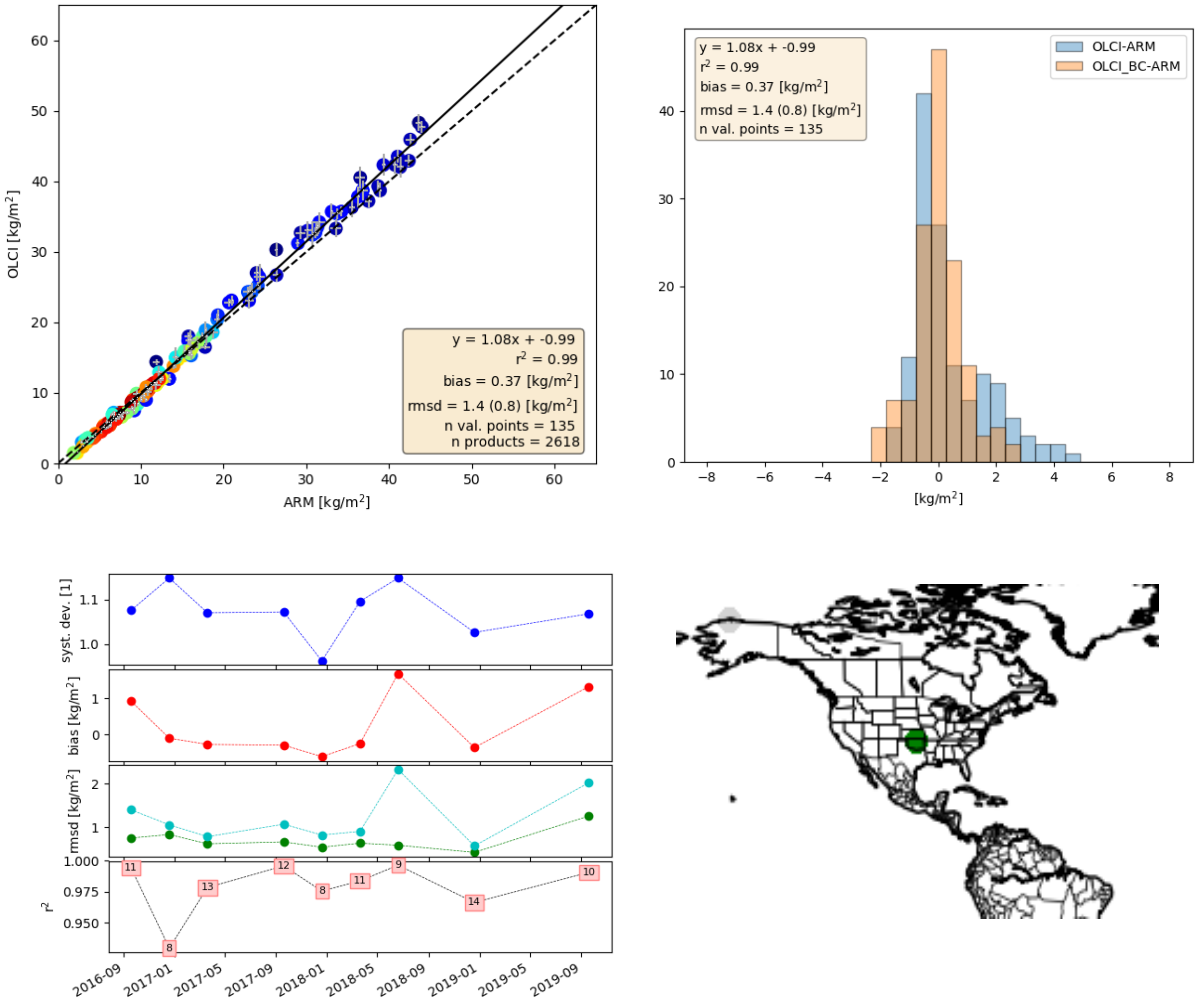

Figure 56: Upper left: Scatter plot of the IWV products, derived from OLCI A above land and from AMR MWR. Upper right: Histogram of the difference between OLCI and ARM (blue: original OLCI, orange: bias corrected OLCI). Lower left: Temporal evolution of different quality measures (from top to bottom: systematic deviation factor, bias, root mean squared difference (with and without bias correction), explained variance (number in boxes are the numbers of matchups)). Lower right: Position of ARM SGP.

5.3.2.1.3 Validation of OLCI A IWV using GRUAN radiosonde observations

Radiosonde observations of temperature, humidity and pressure allow a direct integration of water vapour. The emphasis of GRUAN is to provide long-term, highly accurate measurements of the

atmospheric profile. This is achieved by a very rigid quality control and uncertainty quantification. From the 3200 potential matchups within the period of June 2016 to November 2019, only OLCI measurements are taken for the validation which are above land and are cloud-free in an area of about 10x10 km^2 around the radiosonde launch place. For the cloud detection, the standard L2 cloud-mask has been applied (including the cloud ambiguous and cloud margin flags). Eventually only 38 valid matchups could be used. This number is less than the number of valid matchups for the ARM site, since radiosondes launches are rare. That is why the time constraints have been relaxed to 6h. Still, the comparison shows a very high agreement (Figure 57). The correlation between both quantities is 0.99. The root-mean-squared-difference is 2.4 kg/m^2. The systematic overestimation by OLCI is 12%. The bias corrected *rmsd* is 1.3 kg/m^2. The number of valid matchups is currently too low to investigate a temporal evolution.

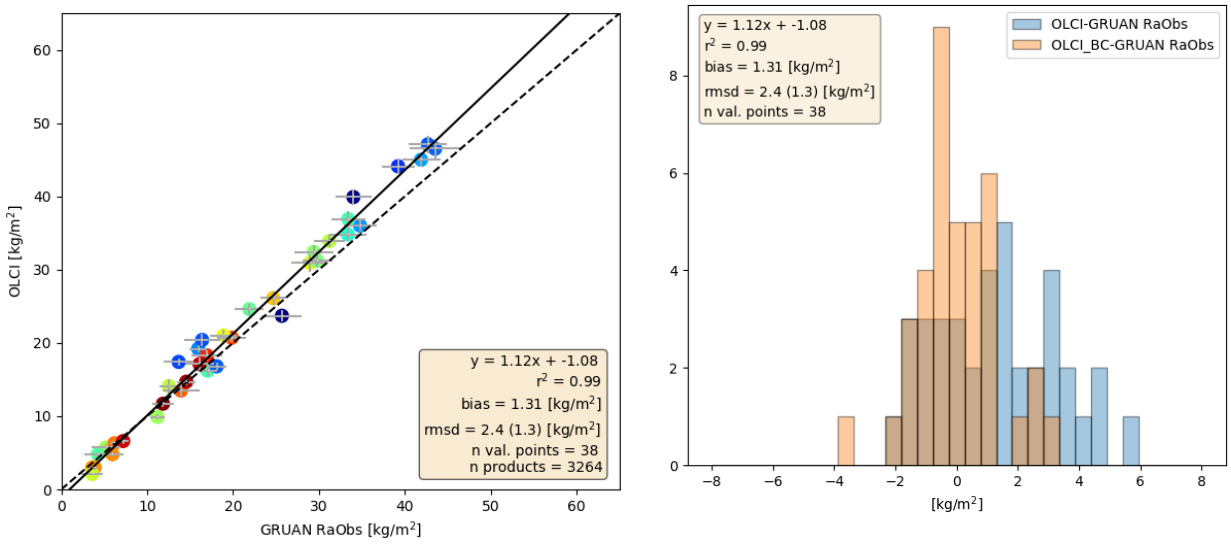

Figure 57: Left: Scatter plot of the IWV products, derived from OLCI A above land and from GRUAN radiosonde measurements. Right: Histogram of the difference between OLCI and GRUAN (blue: original OLCI, orange: bias corrected OLCI).

5.3.2.1.4 Validation of OLCI A IWV using AERONET observations

AERONET observations, regardless not primary made for water vapour, allow the direct estimation of the total column of water vapour by measuring the extinction of the direct solar irradiance at 900 nm. The used operational algorithm is quite simple and eventually relies on a logarithmic fit (incl. quadratic corrections). We are using AERONET for the IWV comparison, since AERONET data are better globally distributed, than ARM and SUOMINET, and are more frequent than GRUAN. Since, the AERONET L2 is stringently quality controlled, it is published with a delay of up to 1 year, thus the latest AERONET data used here is from early Summer 2019. Only OLCI measurements are used for the validation which are cloud-free (according to the standard cloud flags: *cloud, cloud margin and cloud ambiguous*) in an area of about 10x10 km^2 around the AERONET acquisition. From the 87000 potential matchups within the period

of June 2016 to September 2019, 17000 valid matchups could be used (Figure 58). The correlation between both quantities is 0.96. The root-mean-squared-difference is 3.7 kg/m^2. The systematic overestimation by OLCI is 19%. The bias corrected *rmsd* is 1.8 kg/m^2. The systematic deviation between OLCI and AERONET of 19% is significantly larger than the one found for GNSS, ARM and GRUAN (~10%). We think that this stems from a dry bias of AERONET and accordingly deficits in the operational algorithm, but we have not investigated it deeper.

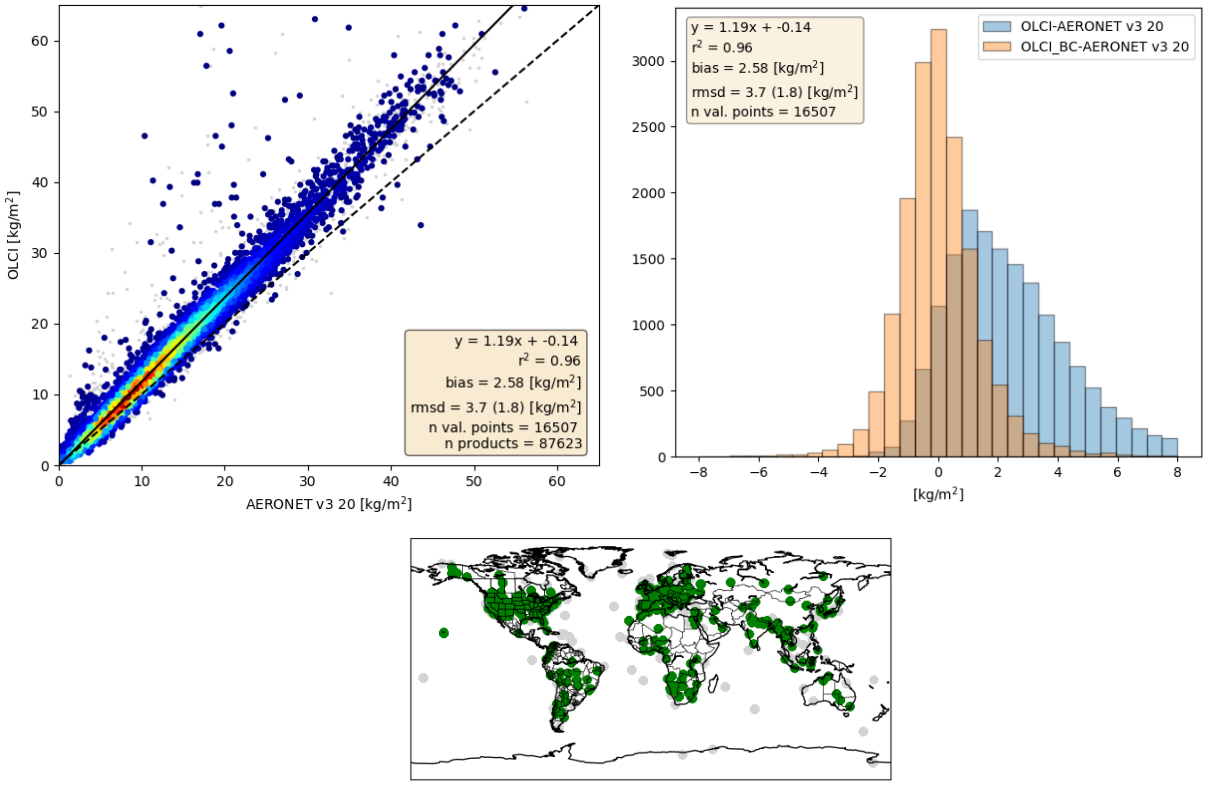

Figure 58: Upper left: Scatter plot of the IWV products, derived from OLCI A above land and from AERONET. Upper right: Histogram of the difference between OLCI and AERONET (blue: original OLCI, orange: bias corrected OLCI). Lower: Positions of the used AERONET stations (grey: no valid matchup).

5.3.2.1.5 Validation of OLCI B IWV

74000 potential matchups within the period of June 2018 to November 2019 have been analysed yet. 5000 of them are valid for SUOMI-NET CONUS ground stations in North and Central America, 34 for ARM MWR and 6500 for AERONET. As for OLCI A, only measurements are taken for the validation which are above land and are cloud-free in an area of about 10x10 km^2 around the corresponding stations. For the cloud detection, the standard L2 cloud-mask has been applied (including the cloud ambiguous and cloud margin flags). The comparison of OLCI B shows almost identical results as for OLCI A (Figure 59).

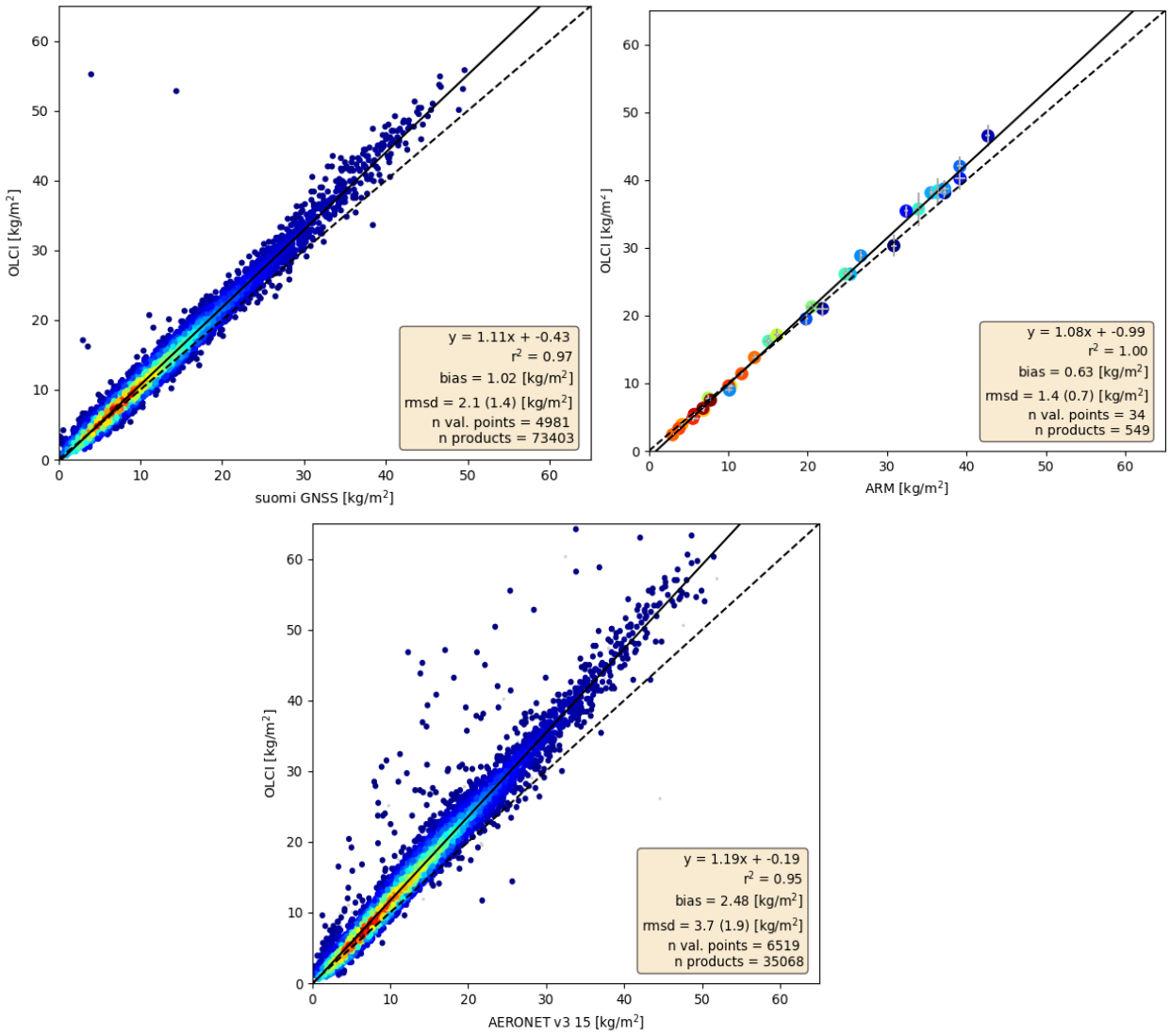

Figure 59: Scatter plot of the IWV products, derived from OLCI B above land and from SUOMI NET GNSS measurements (upper left), from ARM MWR (upper right) and AERONET (lower)

5.3.2.2 Summary

The validation exercise of the OLCI A IWV over land product using 4 different sources of ground truth showed consistency, that the product is of high quality (bias corrected root mean squared distance of down to 1.5 -0.8 kg/m^2). However, there is a systematic overestimation of 9% to 13%. Validation of OLCI B shows the same results.

5.3.2.3 References

- Bodeker, G. E., Bojinski, S., Cimini, D., Dirksen, R. J., Haeffelin, M., Hannigan, J. W., Hurst, D. F., Leblanc, T., Madonna, F., Maturilli, M., Mikalsen, A. C., Philipona, R., Reale, T., Seidel, D. J., Tan,

D. G. H., Thorne, P. W., Vömel, H., and Wang, J.: Reference upper-air observations for climate: From concept to reality, B. Am. Meteorol. Soc., doi:10.1175/BAMS-D-14-00072.1, 2015.

- Holben, B. N., et al., AERONET—A federated instrument network and data archive for aerosol characterization, Remote Sens. Environ.,66, 1–16, 1998.)
- Immler, F. J., Dykema, J., Gardiner, T., Whiteman, D. N., Thorne, P.W., and Vömel, H.: Reference Quality Upper-Air Measurements: guidance for developing GRUAN data products, Atmos. Meas.Tech., 2, 1217–1231, doi:10.5194/amt-3-1217-2010, 2010.
- Pérez-Ramírez, D., D. N. Whiteman, A. Smirnov, H. Lyamani, B. N. Holben, R. Pinker, M. Andrade, and L. Alados- Arboledas (2014), Evaluation of AERONET precipitable water vapor versus microwave radiometry, GPS, and radiosondes at ARM sites, J. Geophys. Res. Atmos., 119, 9596–9613, doi:10.1002/2014JD021730
- Smirnov, A., Holben, B.N., Slutsker, I., Giles, D.M., McClain, C.R.,Eck, T.F., Sakerin, S.M., Macke, A., Croot, P., Zibordi, G., Quinn, P.K., Sciare, J., Kinne, S., Harvey, M., Smyth, T.J., Piketh, S.,Zielinski, T., Proshutinsky, A., Goes, J.I., Nelson, N.B., Larouche,P., Radionov, V.F., Goloub, P., Krishna Moorthy, K., Matarrese, R.,Robertson, E.J., Jourdin, F., 2009. Maritime aerosol network as acomponent of aerosol robotic network. J. Geophys. Res. 114, 1—10, http://dx.doi.org/10.1029/2008JD011257.
- Ware, R. H., D. W. Fulker, S. A. Stein, D. N. Anderson, S. K. Avery, R. D. Clark, K. K. Droegemeier, J. P. Kuettner, J. B. Minster, and S. Sorooshian (2000), SuomiNet: A real-time national GPS network for atmospheric research and education, Bull. Am. Meteorol. Soc., 81(4), 677–694.
- Zibordi G., B.Holben, I.Slutsker, D.Giles, D.D'Alimonte, F.Mélin, J.-F. Berthon, D. Vandemark, H.Feng,G.Schuster, B.Fabbri, S.Kaitala, J.Seppälä. AERONET-OC: a network for the validation of Ocean Color primary radiometric products. Journal of Atmospheric and Oceanic Technology , 26, 1634-1651, 2009.

5.3.3 OLCI Global Vegetation Index (OGVI), a.k.a. FAPAR, and OLCI Terrestrial Chlorophyll Index (OTCI)

This section presents the performance of two Level 2 products routinely generated from OLCI: the OLCI Terrestrial Chlorophyll Index (OTCI) and OLCI Green Vegetation Index (OGVI). The former is a proxy of canopy chlorophyll content (CCC), whereas the latter is an estimation of the Fraction of Absorbed Photosynthetically Active Radiation (FAPAR). The performance evaluation activities over the past year include comparison of OTCI and OGVI to the Medium Resolution Imaging Spectrometer (MERIS) climatology at validation sites, spatial comparison of Sentinel-3 A and B units and global composites

consistency assessment. Other activities include the development and maintenance of a web interface for interactive verification after each orbital cycle.

5.3.3.1 Indirect verification

The indirect verification involves evaluating the spatial and temporal consistency of OLCI products to the MERIS archive. This is conducted by examining the seasonal trajectory of the products over >50 validation sites. The sites include a variety of representative land cover types and are distributed across the globe (Table 10). Pixels extractions are quality filtered and aggregated to monthly time steps. Comparison statistics such as coefficient of determination (R^2), normalised squared difference (NRMSD) and mean difference or Bias are computed. Overall, OTCI and OGVI have shown to be in line with the seasonal and local trend. Both products follow the seasonal pattern without depicting major abrupt changes from one cycle to the other. For most sites, R^2 remains >=0.8, NRMSD <0.1 and Bias <0.1. Figure 60 shows the products acquisitions as a function of time and the correspondence to the archive over a Broadleaved deciduous forest in France. In this example, R^2 is generally >0.9 and NRMSD < 0.1; OTCI shows a slight negative bias whereas OGVI presents a slight positive bias. Table 11 provides the summary statistics for the rest of the validation routinely monitored at each orbital cycle.

Table 10. Validation sites analysed in report S3A 51/S3B 32. Land cover data from GLC2000.

Acronym	Contry	Network	Lat	Lon	Land cover
US-Smithsonian	United States	NEON, AERONET	38.89	-78.14	Broadleaved, deciduous, closed
BE-Brasschaat	Belgium	ICOS	51.31	4.52	Needle-leaved, evergreen
DE-Hones-Holz	Deutschland	ICOS	52.09	11.22	Broadleaved, deciduous, closed
FR-Montiers	France	ICOS	48.54	5.31	Broadleaved, deciduous, closed
US-Harvard	United States	NEON, AERONET	42.54	-72.17	Broadleaved, deciduous, closed
DE-Haininch	Deutschland	ICOS Associated	51.08	10.45	Broadleaved, deciduous, closed
IT-Collelongo	Italy	EFDC	41.85	13.59	Broadleaved, deciduous, closed
IT-Isp	Italy	CORE	45.81	8.64	Mixed forest
UK-NFo	United Kingdom	CORE	50.85	-1.54	Deciduous forest
US-Mountain-Lake	United States	NEON, AERONET	37.38	-80.53	Broadleaved, deciduous, closed
US-Oak-Rige	United States	NEON, AERONET	35.96	-84.28	Broadleaved, deciduous, closed
BR-Mata-Seca	Brazil	ENVIRONET	-14.88	-43.97	Herbaceous, closed-open
CR-Santa-Rosa	Costa Rica	ENVIRONET	10.84	-85.62	Broadleaved, evergreen
IT-Lison	Italy	ICOS	45.74	12.75	Cropland
US-Talladega	United States	NEON, AERONET	32.95	-87.39	Needle-leaved, evergreen
US-Steigerwarldt	United States	NEON	45.51	-89.59	Broadleaved, deciduous, closed
AU-Great-Western	Australia	TERN-SuperSites, AusCover/OzFlux	-30.19	120.65	Broadleaved, deciduous, open
AU-Robson-Creek	Australia	TERN-SuperSites, AusCover/OzFlux	-17.12	145.63	Broadleaved, evergreen
IT-Casterporziano2	Italy	ICOS	41.70	12.36	Tree Cover, mixed leaf type
US-Bartlett	United States	NEON, AERONET	44.06	-71.29	Broadleaved, deciduous, closed
FR-Estrees-Mons	France	ICOS Associated	49.87	3.02	Cultivated and managed areas
AU-Tumbarumba	Australia	TERN-SuperSites, AusCover/OzFlux	-35.66	148.15	Broadleaved, evergreen
AU-Litchfield	Australia	TERN-SuperSites, AusCover/OzFlux	-13.18	130.79	Broadleaved, evergreen
CA-Mer-Bleue	Canada	National Capitol Comission	45.40	-75.49	Peatland
UK-Wytham-Woods	United Kingdom	ForestGeo - NPL	51.77	-1.34	Broadleaved, deciduous, closed
AU-Cape-Tribulation	Australia	TERN-SuperSites, OzFlux	-16.11	145.38	Broadleaved, evergreen
DE-Tharandt	Deutschland	ICOS	50.96	13.57	Needle-leaved, evergreen
IT-Sro	Italy	CORE	43.73	10.28	Mixed forest
DE-Geb	Deutschland	CORE	51.10	10.91	Cropland
US-Jornada	United States	LTER	32.59	-106.84	Shrub, closed-open, deciduous
AU-Cumberland	Australia	TERN-SuperSites, AusCover/OzFlux	-33.62	150.72	Broadleaved, evergreen
BE-Vielsalm	Belgium	ICOS	50.31	6.00	Needle-leaved, evergreen
DE-Selhausen	Deutschland	ICOS	50.87	6.45	Cropland
FR-Puechabon	France	ICOS	43.74	3.60	Needle-leaved, evergreen
NE-Loobos	Netherlands	ICOS Associated	52.17	5.74	Needle-leaved, evergreen

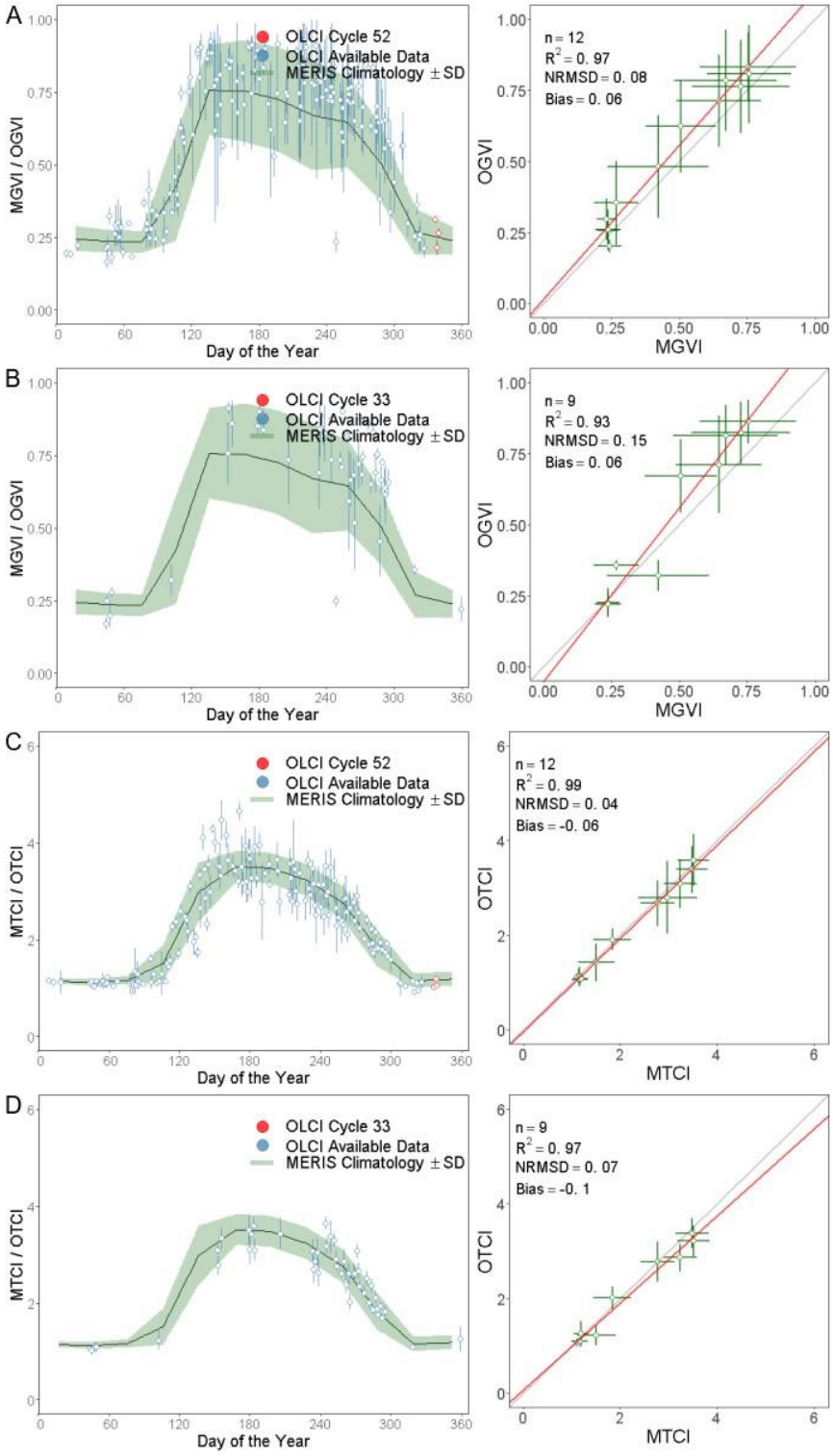

Figure 60. Time-series OGVI and OTCI and corresponding scatterplot of monthly mean for site FR-Montiers, France, land cover Broadleaved, deciduous, closed. A and C represent S3A; B and D represent S3B.

Table 11. Summary of indirect verification OLCI-MERIS climatology for ESA core and CEOS validation sites.

Site Acronym	S3A								S3B							
	OTCI vs MTCI				OGVI vs MGVI				OTCI vs MTCI				OGVI vs MGVI			
	n	R2	NRMSD	Bias	n	R2	NRMSD	Bias	n	R2	NRMSD	Bias	n	R2	NRMSD	Bias
US-Smithsonian	10	1	0.03	-0.21	10	0.98	0.07	0.02	10	0.98	0.07	-0.18	10	0.99	0.07	0
BE-Brasschaat	10	0.99	0.03	-0.1	10	0.98	0.05	0.04	9	0.9	0.08	-0.18	9	0.88	0.11	0.01
DE-Hones-Holz	11	0.99	0.04	0.05	11	1	0.02	0.04	9	0.89	0.15	-0.22	9	0.9	0.15	-0.01
FR-Montiers	12	0.99	0.04	-0.06	12	0.97	0.08	0.06	9	0.97	0.07	-0.1	9	0.93	0.15	0.06
US-Harvard	12	0.99	0.03	-0.13	12	0.97	0.09	0.05	10	0.97	0.05	-0.2	10	0.9	0.18	0.01
DE-Hainich	10	0.98	0.08	-0.08	10	0.99	0.08	0.07	10	0.92	0.16	-0.12	10	0.96	0.13	0.06
IT-Collelongo	12	0.98	0.06	-0.02	12	0.98	0.08	0.01	11	0.81	0.24	0.03	11	0.86	0.22	0.01
IT-Isp	12	0.98	0.04	0.04	12	0.99	0.06	0.07	10	0.91	0.09	-0.07	10	0.78	0.22	0.03
UK-NFo	11	0.98	0.04	-0.23	11	0.96	0.08	0.07	10	0.97	0.05	-0.24	10	0.96	0.11	0.05
US-Mountain-Lake	12	0.98	0.05	-0.35	12	0.98	0.08	0.01	11	0.96	0.06	-0.52	11	0.97	0.08	0
US-Oak-Rige	12	0.98	0.05	-0.05	12	0.99	0.05	0.04	11	0.99	0.05	-0.12	11	0.94	0.12	0.03
BR-Mata-Seca	12	0.97	0.06	-0.02	12	0.99	0.07	0.01	12	0.95	0.06	-0.12	12	0.98	0.07	0.01
CR-Santa-Rosa	12	0.97	0.05	0.08	12	0.65	0.2	0.12	12	0.84	0.12	-0.04	12	0.38	0.29	0.07
IT-Lison	12	0.97	0.04	-0.05	12	0.97	0.07	0.07	11	0.88	0.07	-0.07	11	0.92	0.13	0.08
US-Talladega	12	0.97	0.02	-0.12	12	0.97	0.05	0.07	10	0.91	0.05	-0.2	10	0.93	0.1	0.09
US-Steigerwarldt	11	0.96	0.06	0.09	11	0.97	0.1	0	7	0.81	0.11	-0.1	7	0.94	0.13	0.02
AU-Great-Western	12	0.95	0.02	0.12	12	0.92	0.1	0.04	12	0.89	0.03	0.13	12	0.75	0.1	0.03
AU-Robson-Creek	12	0.95	0.02	-0.08	12	0.69	0.09	0.1	12	0.81	0.05	-0.17	12	0.68	0.13	0.1
IT-Casterporziano2	12	0.95	0.03	-0.06	12	0.76	0.05	0.08	12	0.75	0.08	0.02	12	0.38	0.1	0.08
US-Bartlett	12	0.95	0.05	-0.04	12	0.97	0.1	0.06	11	0.81	0.1	0.02	11	0.87	0.22	0.02
FR-Estrees-Mons	12	0.93	0.08	0.07	12	0.86	0.14	0.06	10	0.89	0.11	0.11	10	0.91	0.11	0.05
AU-Tumbarumba	12	0.92	0.03	0.33	12	0.79	0.06	0.12	12	0.91	0.03	0.26	12	0.06	0.16	0.07
AU-Litchfield	12	0.91	0.03	-0.03	12	0.92	0.09	0.03	12	0.61	0.07	0	12	0.76	0.09	0
CA-Mer-Bleue	9	0.91	0.07	0.01	9	0.99	0.03	0.05	7	0.91	0.06	-0.06	7	0.96	0.08	0.02
UK-Wytham-Woods	12	0.89	0.09	0.05	12	0.87	0.12	0.08	10	0.89	0.08	-0.15	10	0.82	0.21	0.05
AU-Cape-Tribulation	12	0.87	0.04	-0.08	12	0.24	0.08	0.15	10	0.89	0.02	-0.21	10	0.53	0.12	0.14
DE-Tharandt	10	0.87	0.09	0	10	0.91	0.16	0.12	10	0.94	0.07	-0.24	10	0.98	0.09	0.09
IT-Sro	12	0.87	0.02	-0.24	12	0.92	0.06	0.08	12	0.68	0.05	-0.26	12	0.55	0.13	0.08
DE-Geb	12	0.86	0.12	-0.12	12	0.87	0.18	0.03	10	0.81	0.1	-0.07	10	0.61	0.23	-0.02
US-Jornada	9	0.83	0.04	0.03	9	0.81	0.2	0.01	8	0.69	0.04	0.11	8	0.28	0.2	-0.01
AU-Cumberland	12	0.8	0.03	0.01	12	0.55	0.07	0.08	12	0.5	0.06	0.02	12	0.33	0.17	0.06
BE-Vielsalm	11	0.8	0.07	0.06	11	0.94	0.08	0.11	7	0.72	0.08	-0.01	7	0.83	0.2	0.1
DE-Selhausen	12	0.8	0.12	-0.04	12	0.26	0.27	0.05	10	0.74	0.09	-0.2	10	0.17	0.27	-0.01
FR-Puechabon	12	0.8	0.04	-0.06	12	0.82	0.06	0.09	12	0.82	0.05	0.04	12	0.87	0.09	0.04
NE-Loobos	12	0.8	0.06	-0.01	12	0.91	0.1	0.04	10	0.54	0.07	0.07	10	0.88	0.1	0.04

Southampton has been working on the development and maintenance of a web interface used for indirect verification of OTCI and OGVI data collected over an orbital cycle. The tool is developed using the shiny package in R programming language. The interface shows comparison statistics over 53 validation sites. The information is updated at the end of each orbital cycle. The application is still at an early stage but some progress has been made over the past year. There have been improvements on the visualisations and statistics display as well as in the reactivity. It is now possible to interactively click on the map and update the plots and sites details. In addition, the interface shows scatterplots and statistics of all sites pooled together coloured by land cover. This enables to detect systematic biases. The interface is found in the following link: https://s3mpc-soton.shinyapps.io/s3mpc_gui/.

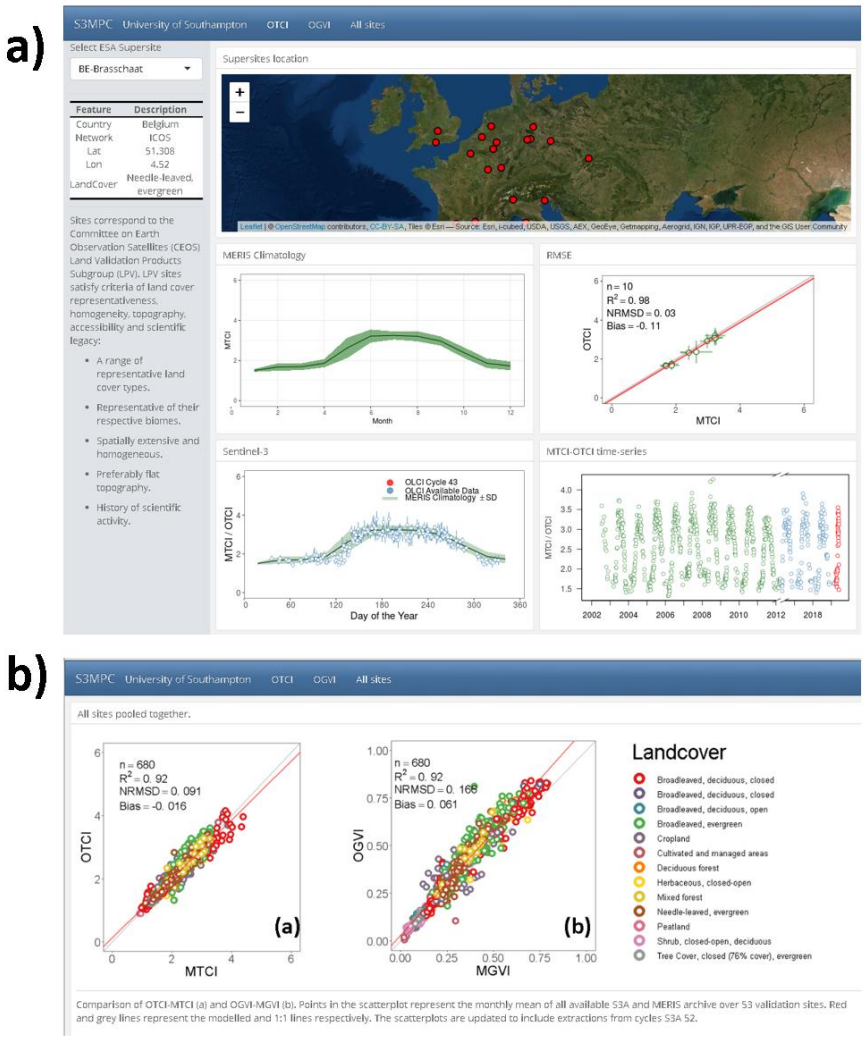

Figure 61: Web app under development for interactive product inter-comparison.

5.3.3.2 Sentinel-3 A &B product comparison

Since the incorporation of the 3rd Geometric Calibration on 12 December 2018, OLCI-B georeferencing is within requirements. Further improvement was introduced on 30 July 2019 on the instrument pixels pointing vectors (IPPVM) which increased coregistration at camera boundaries. To assess the impact of these improvements on the OLCI land products, regions of interest of 100 km around six sites were selected to conduct S3A and S3B scene intercomparisons. Scenes with acquisition time before and after the introduction of georeferencing improvements (30 July 2019) were selected for this task.

Figure 62 and Figure 63 show a comparison of scenes over the validation site FR-Montiers. In Figure 62, the S3A and S3B scenes are six days apart and in Figure 63 the scenes are only one day apart. In general, A and B scenes consistently capture the spatial structure of OTCI values. Higher R^2, lower Bias and lower NRMSD were observed for the post 30 July 2019 scene comparison. The image difference (Figure 62c on the right and Figure 63c on the left) depicts a feature on camera interfaces. Looking at the rest of the

scenes comparisons (Table 12), lower absolute Bias is observed post 30 July 2019. OGVI presented improvements in all indicators post 30 July 2019, this is, generally higher R^2 lower NRMSD and lower Bias.

The scenes were obtained during the growing season in the northern hemisphere. Rapid changes in vegetation activity, remaining geometric inaccuracies and camera boundaries misregistration effects could be contributing to OTCI and OGVI slight inconsistencies between units. Further inspection of the sources of discrepancies and comparison of Level 3 products will continue.

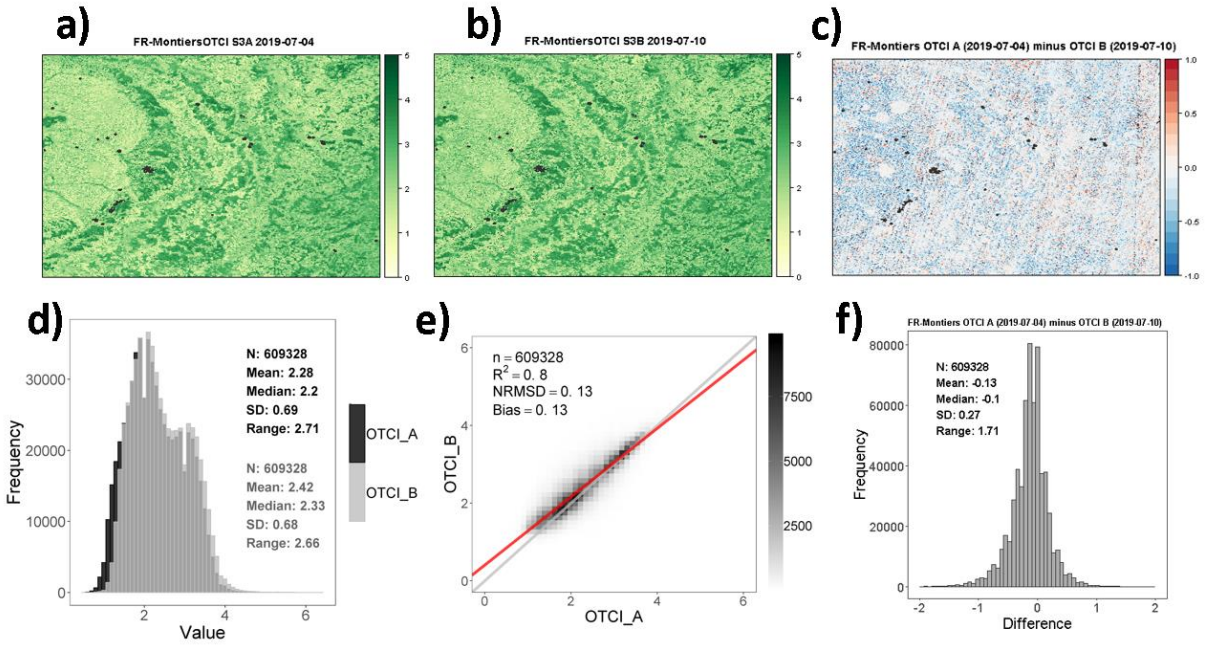

Figure 62: Sentinel-3 A (04 July 2019) and B (10 July 2019) acquired over FR-Montiers. Panels a) and b) OTCI A and B, respectively; c) shows the scenes difference; d) distribution of OTCI values, e) agreement between the two scenes and f) distribution of difference.

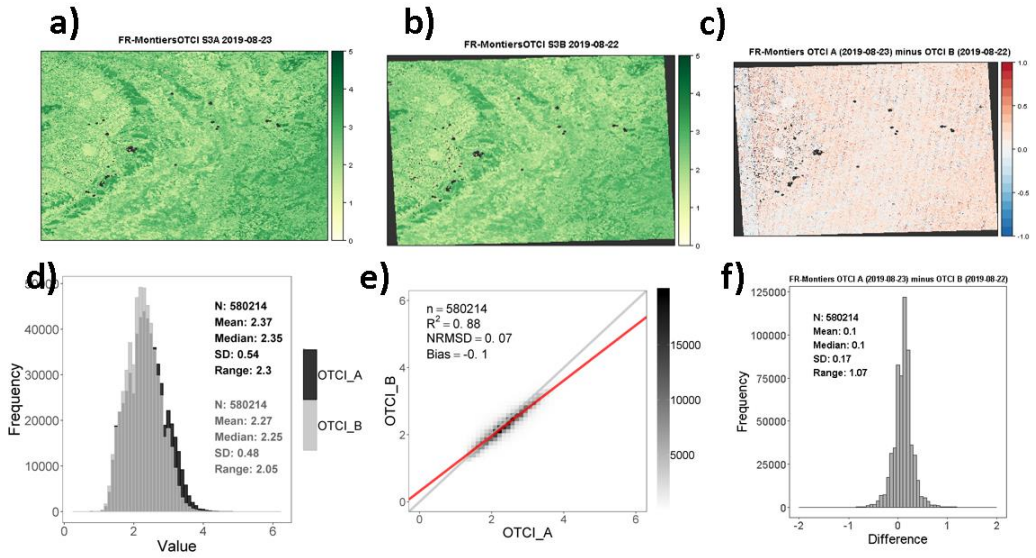

Figure 63: Sentinel-3 A (23 August 2019) and B (22 August 2019) acquired over FR-Montiers. Panels a) and b) OTCI A and B, respectively; c) shows the scenes difference; d) distribution of OTCI values, e) agreement between the two scenes and f) distribution of difference.

Table 12. Summary statistics of Sentinel-3 A and B products comparison.

Timing	S3A Product Date	S3B Product Date	Site	OTCI R^2	OTCI NRMSE	OTCI Bias	OGVI R^2	OGVI NRMSE	OGVI Bias
Prior 30-Jul-2019	04/07/2019	10/07/2019	FR-Montiers	0.80	0.13	0.13	0.86	0.17	-0.07
	27/06/2019	26/06/2019	IT-Lison	0.85	0.08	-0.22	0.88	0.14	0.05
	14/05/2019	13/05/2019	US-Jornada	0.81	0.08	-0.01	0.87	0.25	0.02
	09/05/2019	12/05/2019	BR-Mata-Seca	0.89	0.06	-0.15	0.75	0.14	0.03
	22/02/2019	05/02/2019	Gulf-Cadiz	0.54	0.12	-0.14	0.70	0.17	-0.03
	04/05/2019	06/05/2019	AU-Tumbarumba	0.94	0.07	0.03	0.71	0.24	-0.04
Post 30-Jul-2019	23/08/2019	22/08/2019	FR-Montiers	0.88	0.07	-0.10	0.92	0.16	0.03
	20/08/2019	27/08/2019	IT-Lison	0.79	0.09	-0.30	0.66	0.16	0.05
	11/09/2019	13/09/2019	US-Jornada	0.76	0.12	0.17	0.87	0.19	-0.02
	18/09/2019	20/09/2019	BR-Mata-Seca	0.82	0.07	0.09	0.95	0.13	-0.02
	30/09/2019	28/09/2019	Gulf-Cadiz	0.89	0.08	0.01	0.90	0.15	-0.03
	24/08/2019	26/08/2019	AU-Tumbarumba	0.91	0.07	0.04	0.84	0.17	-0.05

5.3.3.3 OTCI Level-3 product

Level 3 products or composites are spatial and temporal aggregations of the best quality pixels of the biophysical OLCI products within a period (i.e. four days, week, month). These composites have commercial and scientific applications and are experiencing growing demand. In this section, monthly global composites of OTCI were generated for 2018 and were compare to the MERIS archive. OTCI composites were produced at 4.6 km spatial resolution with the ESA SNAP Binning tool using reduced resolution products.

Figure 64 and Figure 65 show the comparison of global OTCI and MTCI for January and July, respectively. These two months were selected because in the northern hemisphere they correspond to contrasting times of vegetation photosynthetic activity. In the case of MTCI, the composite is the mean of all January (2002-2012) composites, whereas in the case of OTCI it only corresponds to January and July 2018. Visual inspection of the composites reveal that they maintain the global pattern of greenness; higher values in the Amazon, Congo Basin and South-east Asia. July shows higher values in agricultural areas in the United States and China. A higher number of pixel counts are reported for July as compared to January, this could be explained by the removal of cloud and snow cover pixels. Notably, the agreement between composites is higher in July (R^2= 0.86; NRMSD=0.12; Bias=0.02) than in January (R^2= 0.77; NRMSD=0.16; Bias=0.05).

Discrepancies between composites can be attributed to the timeframe between products (i.e. MTCI composite includes data from 2002 to 2012, whereas OTCI composite was computed with 2018 only) and inter-annual variability. Given the improvements in OTCI compared to MTCI (pixel flagging, OLCI tilt angle, signal-to-noise ratio) there is a need to evaluate products' consistency and compatibility to guarantee continuity of MERIS. Further assessment of global composites including all available years (2016-2020) of OLCI data is undergoing.

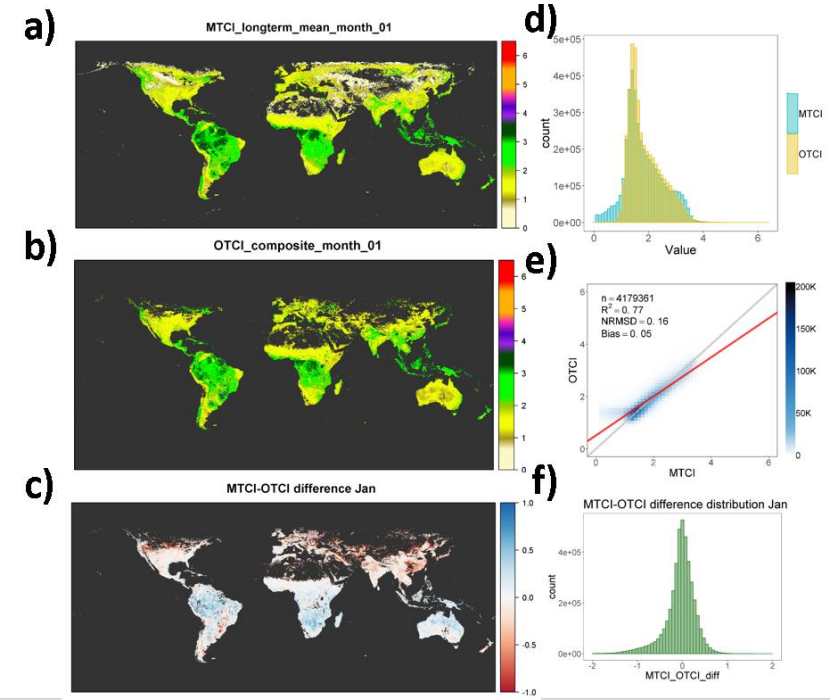

Figure 64: Comparison of global composites of OTCI and MTCI for January; a) and b) spatial arrangement of index values; c) image differencing; d) distribution of index values; e) one to one comparison and f) difference distribution.

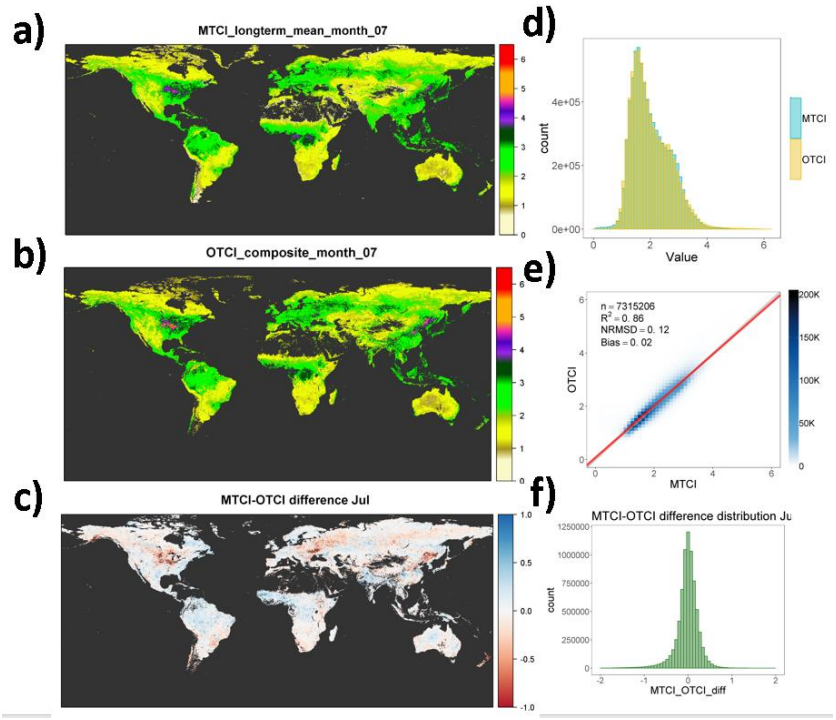

Figure 65: Comparison of global composites of OTCI and MTCI for July; a) and b) spatial arrangement of index values; c) image differencing; d) distribution of index values; e) one to one comparison and f) difference distribution.

5.3.3.4 OLCI FAPAR cross-mission comparisons

The monitoring of S3VT sites ['DE-Geb', 'IT-Cat', 'IT-Isp', 'IT-Sro', 'IT-Tra', 'UK-NFo', 'UK-NF2', 'SP-Ala', 'SP-Val', 'US-Ne1', 'US-Ne2', 'US-Ne3', "DE-THF", "DE-Rod", "RU-Bol", "RU-Kul"] has continued during 2019.

Extracted values for the specific points under observation (3x3 pixels) are used to produce time series (not shown) and scatter plots for comparison between OLCI (reprojected on 250 m) and MODIS JRC FAPAR (see Figure 66).

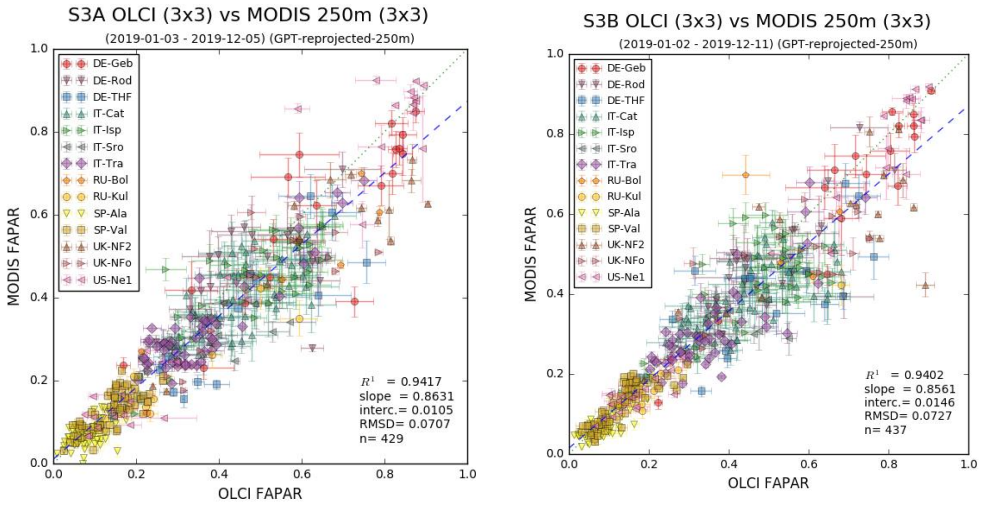

Figure 66: Benchmark between OLCI FAPAR and MODIS JRC FAPAR in 2019 over S3VT sites. Left and right hand panels are for Sentinel 3A and B, respectively.

Figure 67 shows comparisons between S3A and S3B FAPAR values, for overpasses on the same day (in which time differences are usually of the order of 40 minutes). Agreement varies considerably across the various S3VT sites, with excellent correlations for the US-Ne sites and poorer ones elsewhere. This may be a result of a problem of the accurate geo-referencing of the pixel, which could explain the difference in local correlation values, the US-Ne sites being homogenous over large distances around the monitored points, while the converse being true for the European points.

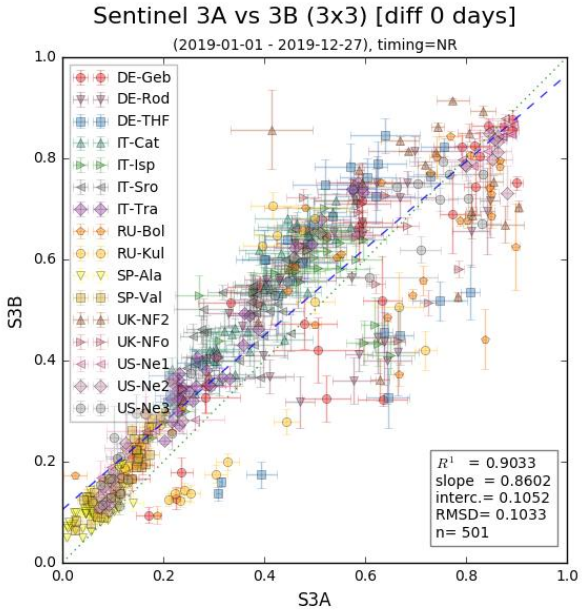

Figure 67: Benchmark between Sentinel3A and Sentinel3B FAPAR in 2019 over S3VT sites.

The various summary statistics for the different sites are presented in Table 13.

Table 13: Statistics of comparison between S3A and S3B over S3VT sites in 2019.

Site	R	Slope	Intercept	RMSD	N
DE-Geb	**0.928959**	0.87919	0.059972	0.097237	33
DE-Rod	*0.419947*	0.39014	0.362254	*0.111535*	39
DE-THF	0.599627	0.709848	0.195941	0.160145	31
IT-Cat	**0.905799**	1.16624	0.062568	0.050218	39
IT-Isp	0.663644	0.627511	0.240824	0.097478	31
IT-Sro	0.505766	0.46063	0.313084	0.049738	27
IT-Tra	**0.975979**	1.171652	0.048903	0.031703	38
RU-Bol	0.850432	0.709698	0.134604	0.116086	31
RU-Kul	0.733316	0.848257	0.06049	0.136232	27
SP-Ala	0.713496	0.717074	0.063549	0.024586	53
SP-Val	0.877502	1.179905	0.039867	0.028814	36
UK-NF2	0.65188	0.595508	0.298622	0.141059	24
UK-NFo	0.548066	0.447194	0.350382	0.104034	19
US-Ne1	**0.990885**	0.899885	0.079768	0.043275	23
US-Ne2	**0.985886**	0.87569	0.081371	0.051588	25
US-Ne3	**0.973074**	0.835216	0.099331	0.059037	25
All	0.903346	0.860216	0.105229	0.103321	501

5.3.4 Water leaving Reflectance

The results presented in this section present the level-2 FR quantitative validation performed over the full OLCI time series against situ fiducial reference measurements. OLCI data used in these sections correspond to the last processing baseline (IPF version 6.11, PB 2.23). In situ data collected originate from the following stations or buoys:

- AERONET-OC https://aeronet.gsfc.nasa.gov/new_web/ocean_color.html
- BOUSSOLE http://www.obs-vlfr.fr/Boussole/html/project/strategy.php
- MOBY https://www.star.nesdis.noaa.gov/sod/moby/gold/
- SLGO https://slgo.ca/en/

5.3.4.1 Level-2 products filtering procedure

The flags used in the computations of the statistics over OLCI macropixels correspond to S3VT recommended flags and are listed below:

- INVALID, CLOUD, CLOUD_AMBIGUOUS, CLOUD_MARGIN, SNOW_ICE, SUSPECT, HISOLZEN, SATURATED, RISKGLINT, WHITECAPS, AC_FAIL, OC4ME_FAIL, ANNOT_TAU06, ANNOT_ABSO_D, ANNOT_DROUT, RWNEG_O2 to RWNEG_O8, ANNOT_MIXR1.

Additional filtering includes time difference between in situ measurement and satellite over path below 6 hours, wind speed lower than 9 $m.s^{-1}$ and sun zenith angle lower than 60 degrees. Filtered mean and CV tests as described in Bailey and Werdell (2006) is also included in the filtering process.

Ref: W. Bailey *and P.J. Werdell, "A multi-sensor approach for the on-orbit validation of ocean color satellite data products", Rem. Sens. Environ. 102, 12-23 (2006).*

5.3.4.2 Results

5.3.4.2.1 OLCI-A

Figure 68 presented below represent the scatterplots and statistics of OLCI full resolution radiometric products against in situ data collected at AERONET-OC, BOUSSOLE, MOBY and SLGO since April 2016. The statistics are summarized in Table 14.

The total number of matchups varies from 22 to 848 depending on the wavelength. Most recent data of AERONET-OC have added new bands such as 400 nm, 620 nm, 665 nm.

Regression statistics are very good up to 560 nm with slopes between 0.891 and 0.998 (with an exception at 510 nm with 0.75, but the dynamics for that band are very small) and r^2 mostly around 0.8. The 665 nm band is clearly the most critical one with poor slopes and r^2 (0.611 and 0.597 respectively). At this stage of the mission, there are still no clues for the poor performance of this band. OLCI products are almost within the requirements (5% accuracy in the blue/green bands) as demonstrated by the RPD values.

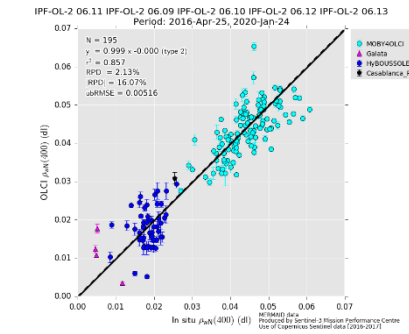
IPF-OL-2 06.11 IPF-OL-2 06.09 IPF-OL-2 06.10 IPF-OL-2 06.12 IPF-OL-2 06.13
Period: 2016-Apr-25, 2020-Jan-24
N = 195
y = 0.999 x -0.000 (type 2)
r² = 0.857
RPD = 2.13%
|RPD| = 16.07%
ubRMSE = 0.00516
OLCI ρw(400) (dl)
In situ ρw(400) (dl)
MERMAID data
Produced by Sentinel-3 Mission Performance Centre
Use of Copernicus Sentinel data [2016-2017]
N PERIOD
MOBY4OLCI 138 2016-Apr, 2020-Jan-24
Galata 4 2016-Jun, 2019-Oct-21
HyBOUSSOLE 52 2016-May, 2019-Sep-27
Casablanca_Platform 1 2019-Sep, 2019-Sep-08

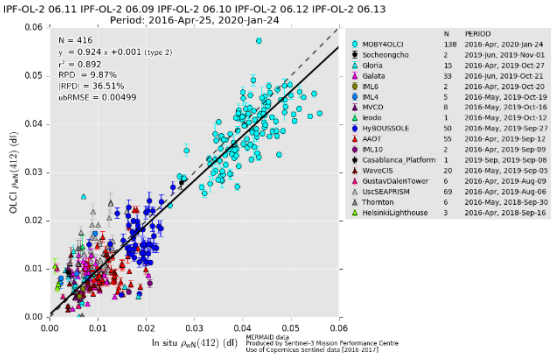
IPF-OL-2 06.11 IPF-OL-2 06.09 IPF-OL-2 06.10 IPF-OL-2 06.12 IPF-OL-2 06.13
Period: 2016-Apr-25, 2020-Jan-24
N = 416
y = 0.924 x +0.001 (type 2)
r² = 0.892
RPD = 9.87%
|RPD| = 36.51%
ubRMSE = 0.00499
OLCI ρw(412) (dl)
In situ ρw(412) (dl)
MERMAID data
Produced by Sentinel-3 Mission Performance Centre
Use of Copernicus Sentinel data [2016-2017]
N PERIOD
MOBY4OLCI 138 2016-Apr, 2020-Jan-24
Socheongcho 2 2019-Jun, 2019-Nov-01
Gloria 15 2016-Apr, 2019-Oct-27
Galata 33 2016-Jun, 2019-Oct-21
IML6 2 2016-Apr, 2019-Oct-20
IML4 5 2016-May, 2019-Oct-19
MVCO 8 2016-May, 2019-Oct-16
Ieodo 1 2016-May, 2019-Oct-12
HyBOUSSOLE 50 2016-May, 2019-Sep-27
AAOT 55 2016-Apr, 2019-Sep-12
IML10 2 2016-Apr, 2019-Sep-09
Casablanca_Platform 1 2019-Sep, 2019-Sep-08
WaveCIS 20 2016-May, 2019-Sep-05
GustavDalenTower 6 2016-Apr, 2019-Aug-09
UscSEAPRISM 69 2016-Apr, 2019-Aug-06
Thornton 6 2016-May, 2018-Sep-30
HelsinkiLighthouse 3 2016-Apr, 2018-Sep-16

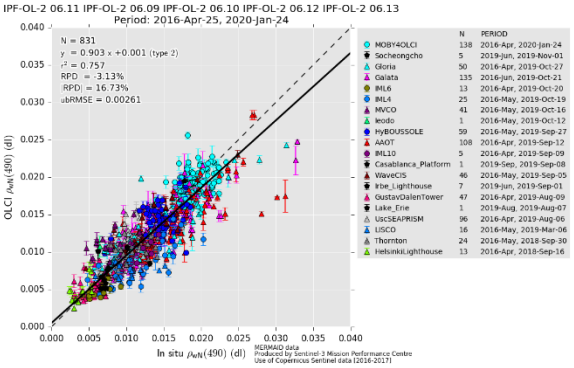
IPF-OL-2 06.11 IPF-OL-2 06.09 IPF-OL-2 06.10 IPF-OL-2 06.12 IPF-OL-2 06.13
Period: 2016-Apr-25, 2020-Jan-24
N = 831
y = 0.903 x +0.001 (type 2)
r² = 0.757
RPD = -3.13%
|RPD| = 16.73%
ubRMSE = 0.00261
OLCI ρw(490) (dl)
In situ ρw(490) (dl)
MERMAID data
Produced by Sentinel-3 Mission Performance Centre
Use of Copernicus Sentinel data [2016-2017]
N PERIOD
MOBY4OLCI 138 2016-Apr, 2020-Jan-24
Socheongcho 5 2019-Jun, 2019-Nov-01
Gloria 50 2016-Apr, 2019-Oct-27
Galata 135 2016-Jun, 2019-Oct-21
IML6 13 2016-Apr, 2019-Oct-20
IML4 25 2016-May, 2019-Oct-19
MVCO 41 2016-May, 2019-Oct-16
Ieodo 1 2016-May, 2019-Oct-12
HyBOUSSOLE 59 2016-May, 2019-Sep-27
AAOT 108 2016-Apr, 2019-Sep-12
IML10 5 2016-Apr, 2019-Sep-09
Casablanca_Platform 1 2019-Sep, 2019-Sep-08
WaveCIS 46 2016-May, 2019-Sep-05
Irbe_Lighthouse 7 2019-Jun, 2019-Sep-01
GustavDalenTower 47 2016-Apr, 2019-Aug-09
Lake_Erie 1 2019-Aug, 2019-Aug-07
UscSEAPRISM 96 2016-Apr, 2019-Aug-06
LISCO 16 2016-May, 2019-Mar-06
Thornton 24 2016-May, 2018-Sep-30
HelsinkiLighthouse 13 2016-Apr, 2018-Sep-16

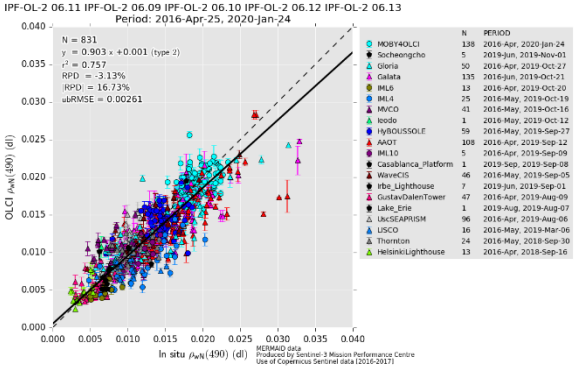
IPF-OL-2 06.11 IPF-OL-2 06.09 IPF-OL-2 06.10 IPF-OL-2 06.12 IPF-OL-2 06.13
Period: 2016-Apr-25, 2020-Jan-24
N = 831
y = 0.903 x +0.001 (type 2)
r² = 0.757
RPD = -3.13%
|RPD| = 16.73%
ubRMSE = 0.00261
OLCI ρw(490) (dl)
In situ ρw(490) (dl)
MERMAID data
Produced by Sentinel-3 Mission Performance Centre
Use of Copernicus Sentinel data [2016-2017]
N PERIOD
MOBY4OLCI 138 2016-Apr, 2020-Jan-24
Socheongcho 5 2019-Jun, 2019-Nov-01
Gloria 50 2016-Apr, 2019-Oct-27
Galata 135 2016-Jun, 2019-Oct-21
IML6 13 2016-Apr, 2019-Oct-20
IML4 25 2016-May, 2019-Oct-19
MVCO 41 2016-May, 2019-Oct-16
Ieodo 1 2016-May, 2019-Oct-12
HyBOUSSOLE 59 2016-May, 2019-Sep-27
AAOT 108 2016-Apr, 2019-Sep-12
IML10 5 2016-Apr, 2019-Sep-09
Casablanca_Platform 1 2019-Sep, 2019-Sep-08
WaveCIS 46 2016-May, 2019-Sep-05
Irbe_Lighthouse 7 2019-Jun, 2019-Sep-01
GustavDalenTower 47 2016-Apr, 2019-Aug-09
Lake_Erie 1 2019-Aug, 2019-Aug-07
UscSEAPRISM 96 2016-Apr, 2019-Aug-06
LISCO 16 2016-May, 2019-Mar-06
Thornton 24 2016-May, 2018-Sep-30
HelsinkiLighthouse 13 2016-Apr, 2018-Sep-16

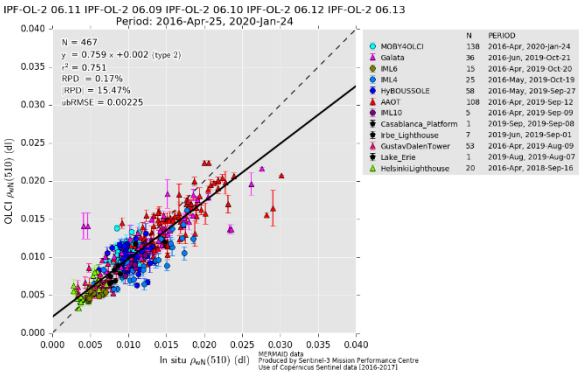
IPF-OL-2 06.11 IPF-OL-2 06.09 IPF-OL-2 06.10 IPF-OL-2 06.12 IPF-OL-2 06.13
Period: 2016-Apr-25, 2020-Jan-24
N = 467
y = 0.759 x +0.002 (type 2)
r² = 0.751
RPD = 0.17%
|RPD| = 15.47%
ubRMSE = 0.00225
OLCI ρw(510) (dl)
In situ ρw(510) (dl)
MERMAID data
Produced by Sentinel-3 Mission Performance Centre
Use of Copernicus Sentinel data [2016-2017]
N PERIOD
MOBY4OLCI 138 2016-Apr, 2020-Jan-24
Galata 36 2016-Jun, 2019-Oct-21
IML6 15 2016-Apr, 2019-Oct-20
IML4 25 2016-May, 2019-Oct-19
HyBOUSSOLE 58 2016-May, 2019-Sep-27
AAOT 108 2016-Apr, 2019-Sep-12
IML10 5 2016-Apr, 2019-Sep-09
Casablanca_Platform 1 2019-Sep, 2019-Sep-08
Irbe_Lighthouse 7 2019-Jun, 2019-Sep-01
GustavDalenTower 53 2016-Apr, 2019-Aug-09
Lake_Erie 1 2019-Aug, 2019-Aug-07
HelsinkiLighthouse 20 2016-Apr, 2018-Sep-16

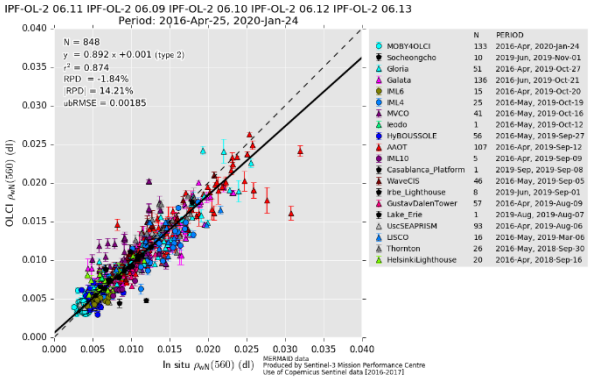
IPF-OL-2 06.11 IPF-OL-2 06.09 IPF-OL-2 06.10 IPF-OL-2 06.12 IPF-OL-2 06.13
Period: 2016-Apr-25, 2020-Jan-24
N = 848
y = 0.892 x +0.001 (type 2)
r² = 0.874
RPD = -1.84%
|RPD| = 14.21%
ubRMSE = 0.00185
OLCI ρw(560) (dl)
In situ ρw(560) (dl)
MERMAID data
Produced by Sentinel-3 Mission Performance Centre
Use of Copernicus Sentinel data [2016-2017]
N PERIOD
MOBY4OLCI 133 2016-Apr, 2020-Jan-24
Socheongcho 10 2019-Jun, 2019-Nov-01
Gloria 51 2016-Apr, 2019-Oct-27
Galata 136 2016-Jun, 2019-Oct-21
IML6 15 2016-Apr, 2019-Oct-20
IML4 25 2016-May, 2019-Oct-19
MVCO 41 2016-May, 2019-Oct-16
Ieodo 1 2016-May, 2019-Oct-12
HyBOUSSOLE 56 2016-May, 2019-Sep-27
AAOT 107 2016-Apr, 2019-Sep-12
IML10 5 2016-Apr, 2019-Sep-09
Casablanca_Platform 1 2019-Sep, 2019-Sep-08
WaveCIS 46 2016-May, 2019-Sep-05
Irbe_Lighthouse 8 2019-Jun, 2019-Sep-01
GustavDalenTower 57 2016-Apr, 2019-Aug-09
Lake_Erie 1 2019-Aug, 2019-Aug-07
UscSEAPRISM 93 2016-Apr, 2019-Aug-06
LISCO 16 2016-May, 2019-Mar-06
Thornton 26 2016-May, 2018-Sep-30
HelsinkiLighthouse 20 2016-Apr, 2018-Sep-16

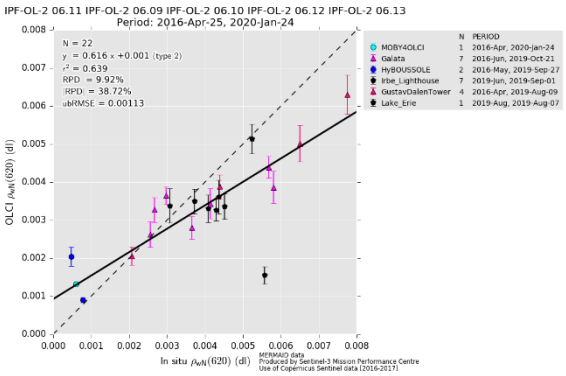
IPF-OL-2 06.11 IPF-OL-2 06.09 IPF-OL-2 06.10 IPF-OL-2 06.12 IPF-OL-2 06.13
Period: 2016-Apr-25, 2020-Jan-24
N = 22
y = 0.616 x +0.001 (type 2)
r² = 0.639
RPD = 9.92%
|RPD| = 38.72%
ubRMSE = 0.00113
OLCI ρw(620) (dl)
In situ ρw(620) (dl)
MERMAID data
Produced by Sentinel-3 Mission Performance Centre
Use of Copernicus Sentinel data [2016-2017]
N PERIOD
MOBY4OLCI 1 2016-Apr, 2020-Jan-24
Galata 7 2016-Jun, 2019-Oct-21
HyBOUSSOLE 2 2016-May, 2019-Sep-27
Irbe_Lighthouse 7 2019-Jun, 2019-Sep-01
GustavDalenTower 4 2016-Apr, 2019-Aug-09
Lake_Erie 1 2019-Aug, 2019-Aug-07

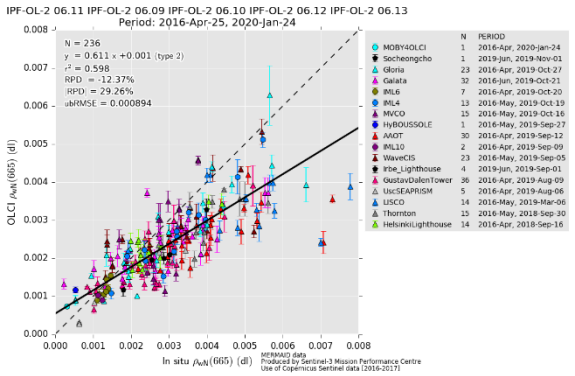
IPF-OL-2 06.11 IPF-OL-2 06.09 IPF-OL-2 06.10 IPF-OL-2 06.12 IPF-OL-2 06.13
Period: 2016-Apr-25, 2020-Jan-24
N = 236
y = 0.611 x +0.001 (type 2)
r² = 0.598
RPD = -12.37%
|RPD| = 29.26%
ubRMSE = 0.000894
OLCI ρw(665) (dl)
In situ ρw(665) (dl)
MERMAID data
Produced by Sentinel-3 Mission Performance Centre
Use of Copernicus Sentinel data [2016-2017]
N PERIOD
MOBY4OLCI 1 2016-Apr, 2020-Jan-24
Socheongcho 1 2019-Jun, 2019-Nov-01
Gloria 23 2016-Apr, 2019-Oct-27
Galata 32 2016-Jun, 2019-Oct-21
IML6 7 2016-Apr, 2019-Oct-20
IML4 13 2016-May, 2019-Oct-19
MVCO 15 2016-May, 2019-Oct-16
HyBOUSSOLE 1 2016-May, 2019-Sep-27
AAOT 30 2016-Apr, 2019-Sep-12
IML10 2 2016-Apr, 2019-Sep-09
WaveCIS 23 2016-May, 2019-Sep-05
Irbe_Lighthouse 4 2019-Jun, 2019-Sep-01
GustavDalenTower 36 2016-Apr, 2019-Aug-09
UscSEAPRISM 5 2016-Apr, 2019-Aug-06
LISCO 14 2016-May, 2019-Mar-06
Thornton 15 2016-May, 2018-Sep-30
HelsinkiLighthouse 14 2016-Apr, 2018-Sep-16

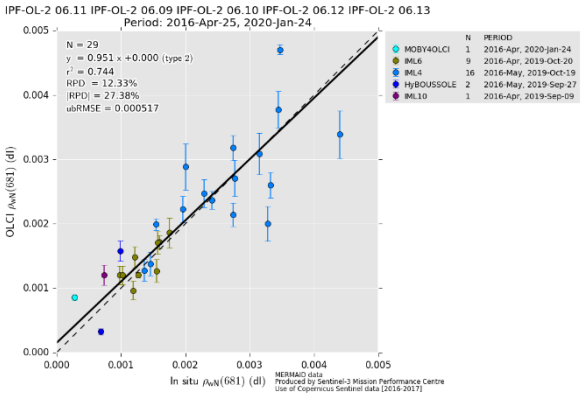

Figure 68: FR scatter plot of OLCI versus in situ measurements.

Table 14: Summary of OLCI-A FR statistics.

lambda	N	RPD	|RPD|	MAD	RMSE	slope	intercept	r2
400	195	2.13%	16.07%	-0.0003	0.0052	0.9987	-0.0003	0.8571
412	416	9.87%	36.51%	-0.0010	0.0051	0.9245	0.0006	0.8920
443	563	-1.76%	26.69%	-0.0012	0.0038	0.9512	-0.0004	0.8572
490	831	-3.13%	16.73%	-0.0008	0.0027	0.9028	0.0005	0.7567
510	467	0.17%	15.47%	-0.0005	0.0023	0.7591	0.0021	0.7513
560	848	-1.84%	14.21%	-0.0005	0.0019	0.8916	0.0006	0.8742
620	22	9.92%	38.72%	-0.0006	0.0013	0.6160	0.0009	0.6388
665	236	-12.37%	29.26%	-0.0007	0.0011	0.6110	0.0005	0.5979
681	29	12.33%	27.38%	0.0001	0.0005	0.9508	0.0002	0.7444

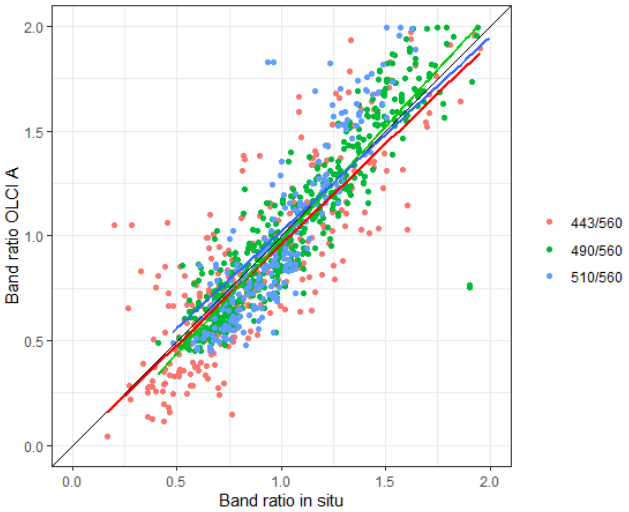

Figure 69: Band ratio validation between in situ and OLCI A.

Figure 69 shows the relationship between *in situ* blue-green and green band ratio and OLCI A band ratio. High correlation (r = 98%, $p > 0.05$) between *in situ* and OLCI A data has been found. Bias are lower than 5% with a slight underestimation of the 443/560 nm ratio. Relative percentage differences are also around 5% for each band ratio.

Summary:

Level 2 product validation against in situ measurements shows very good results up to 560nm. Longer wavelength shows poor statistics with less in situ data.

Due to lower signals and high variability for available data at 620 nm and to longer wavelengths, the performance of OLCI shows a percentage difference of 10% and -12% for 620 nm and 665 nm respectively, with an underestimation of higher values (see Table 14).

5.3.4.2.2 OLCI-B

Analyses were performed on the entire archives of OLCI B data until the 27th of January 2020. OLCI B vicarious calibration activities are still ongoing, then the discrepancies between *in situ* data and satellite data may be due to the missing calibration (Figure 70). Even with the systematic shift in the blue wavelength, *in situ* data and satellite data are well correlated with a coefficient higher than 60% for the wavelength between 400 nm and 620 nm (Table 15).

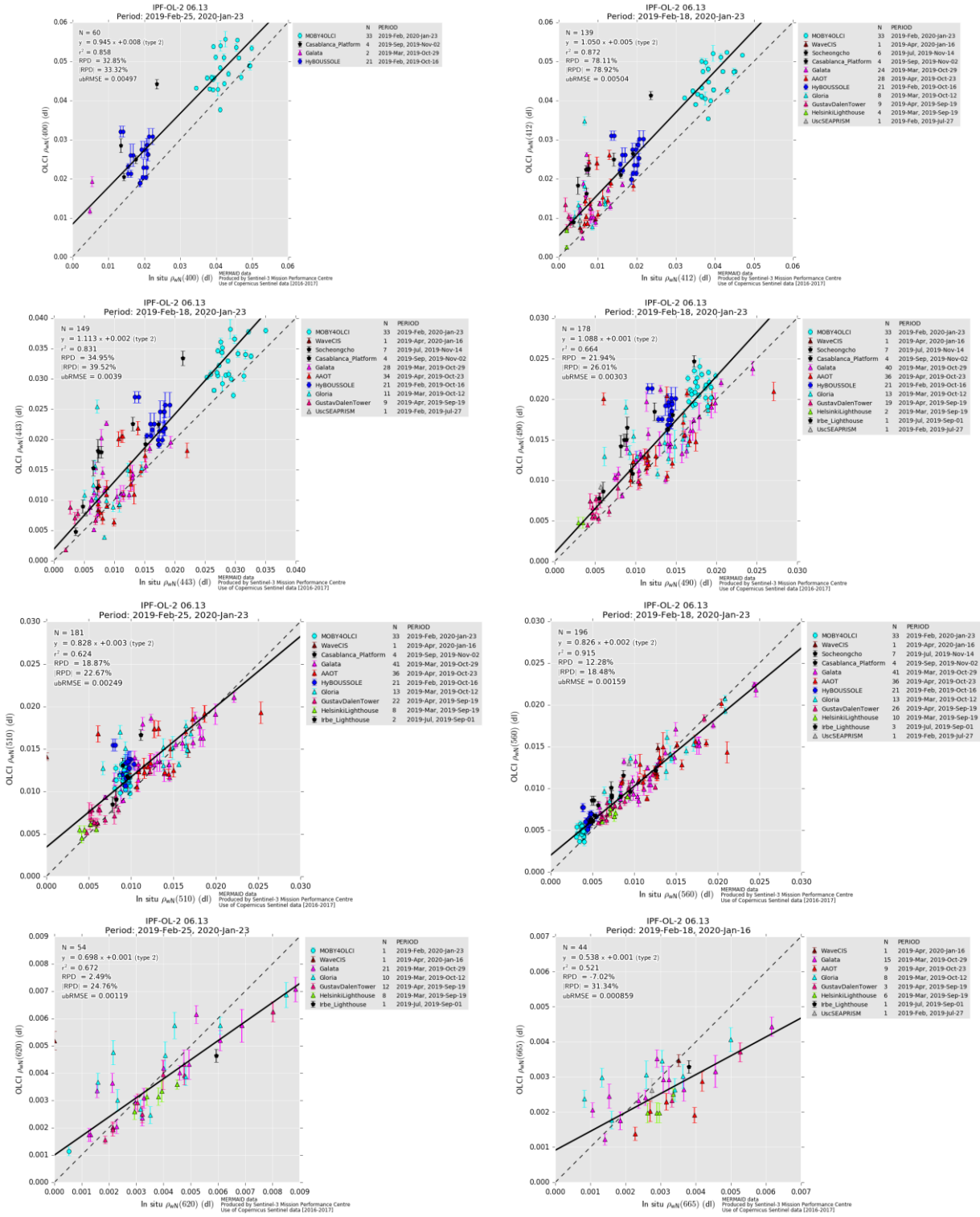

Figure 70: Validation scatter plot for OLCI B.

Table 15: OCLI B Validation Statistics

Lambda	N	RPD	|RPD|	MAD	RMSE	slope	intercept	r2
400	60	32.85%	33.32%	0.0066	0.0083	0.9448	0.0084	0.8582
412	139	78.11%	78.92%	0.0063	0.0081	1.0501	0.0054	0.8715
443	149	34.95%	39.52%	0.0036	0.0053	1.1130	0.0019	0.8307
490	178	21.94%	26.01%	0.0022	0.0038	1.0883	0.0011	0.6640
510	181	18.87%	22.67%	0.0016	0.0029	0.8277	0.0034	0.6242
560	196	12.28%	18.48%	0.0004	0.0016	0.8262	0.0020	0.9149
620	54	2.49%	24.76%	-0.0002	0.0012	0.6982	0.0010	0.6722
665	44	-7.02%	31.34%	-0.0005	0.0010	0.5379	0.0009	0.5208

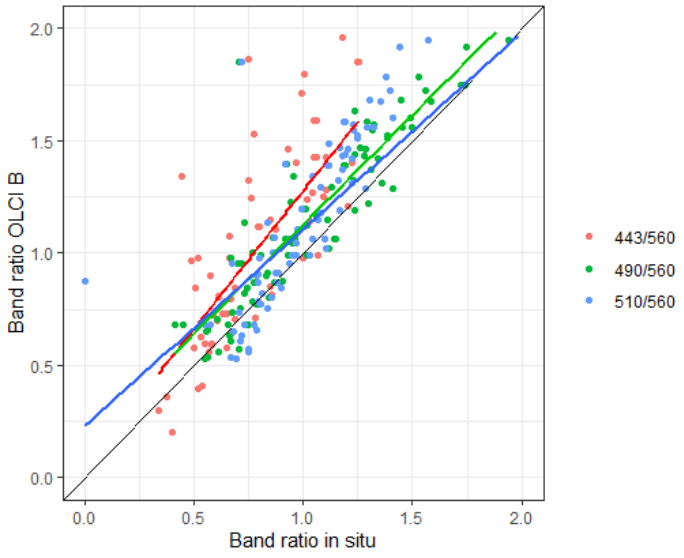

Figure 71: Band ratio validation between in situ and OLCI B.

Figure 71 shows the relationship between *in situ* blue-green and green band ratio and OLCI B band ratio. Bias are lower than 5% with a slight underestimation of the 443/560 nm ratio.

Summary:

S3B OLCI level 2 products have been released more recently and vicarious calibration activities are still on going. Therefore, only preliminary results are presented here. For the whole spectra, a high relative percentage difference (>15%) was found together with a systematic shift in the blue and blue-green (412, 443 and 490 nm) regions of the visible spectra.

5.3.5 Case 1 Chlorophyll product (OC4Me)

Figure 72 below present the statistics of OLCI OC4Me chlorophyll products against in situ measurements carried out at BOUSSOLE and on Bio-Argo floats. Please note that BOUSSOLE operations stopped in November 2017.

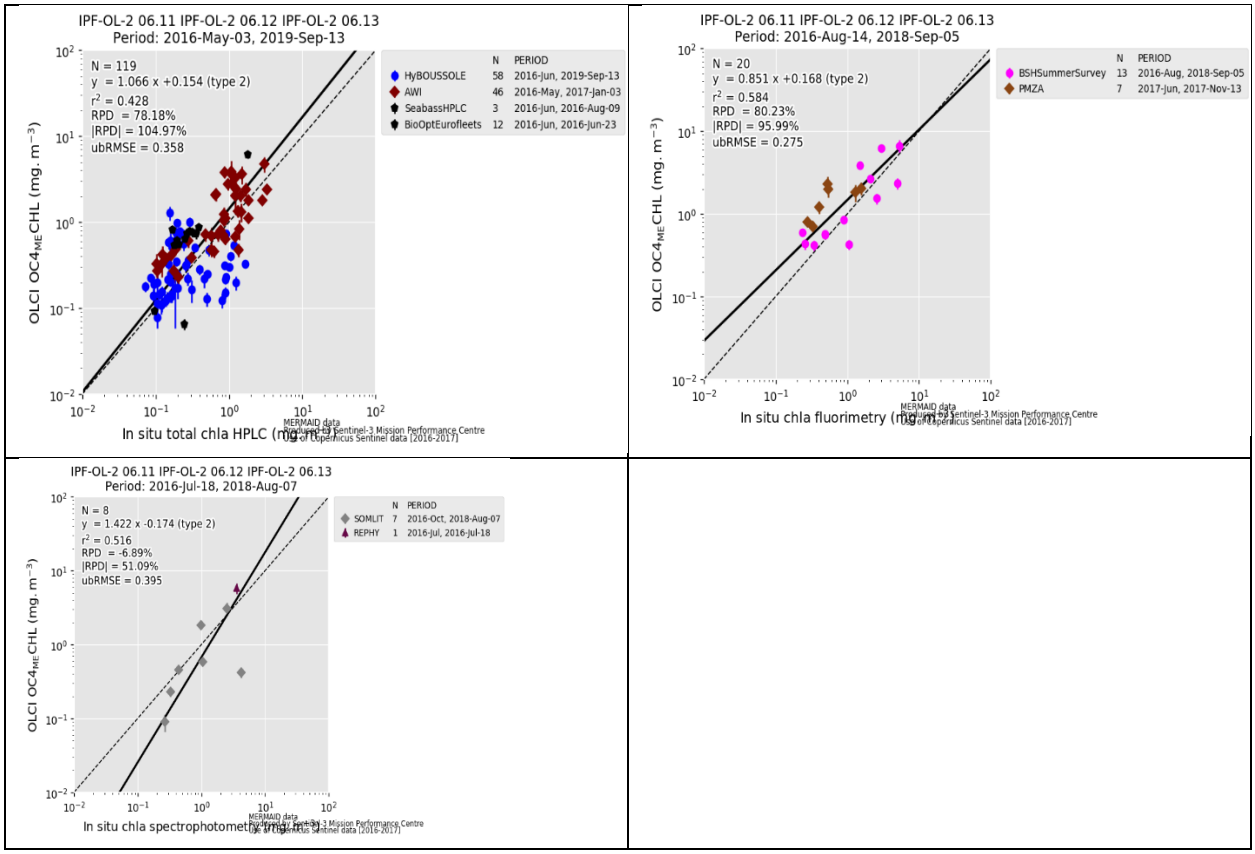

Figure 72: Chlorophyll statistics with HPLC (a), Fluorometric (b) data and Spectroscophotmetry (c).

The Chlorophyll-a algorithm validation was performed only on OLCI A data. Based only on HPLC Chlorophyll a value, OLCI OC4-Me products shows moderate positive correlation (r Pearson = 64%, p-value < 0.05 and RMSE = 0.38 $mg.m^{-3}$) with scattered data (Figure 72). With a bias of -30%, OLCI OC4-Me algorithm tends to underestimate in situ values of HPLC chlorophyll-a.

Fluorometric chlorophyll also shows a better correlation (r Pearson = 76%, p-value < 0.05 and RMSE = 0.32 $mg.m^{-3}$). These data are obviously of less quality but can nonetheless provide an indication of OLCI chlorophyll trends. In situ data shows low variability in the 0.1 to 1 mg/m^3 domain (mesotrophic water). No in situ measurement are in the oligotrophic domain.

Lambda	N	RPD	|RPD|	MAD	RMSE	slope	intercept	r2
CHL_OC4ME vs SPECT_chla_IS	8	-6.89%	51.09%	-0.1638	0.4275	1.4218	-0.1736	0.5163
CHL_OC4ME vs HPLC_chla_TOTAL_IS	119	78.18%	104.97%	0.1266	0.3795	1.0660	0.1544	0.4276
CHL_OC4ME vs Fluor_chla_IS	20	80.23%	95.99%	0.1767	0.3269	0.8515	0.1678	0.5843

Summary:

In situ chlorophyll concentration derived from HPLC analysis shows slight overestimation for higher values. Chlorophyll-a measurement shows some estimation errors, however this bias could be due to the low variability for in the HPLC in situ values (0.1-1 mg.m^{-3}).

More measurement needs to be gathered in order to have a better insight of OLCI estimation on oligotrophic waters.

5.3.6 Alternative Atmospheric Correction and products for complex waters

The products for (optically) complex waters comprise chlorophyll-a concentration (CHL_NN), total suspended matter (TSM_NN) and absorption from Gelbstoff and Detritus (ADG443_NN), each with an associated error product. These products are derived from top-of-atmosphere radiance using the so-called Alternative Atmospheric Correction (AAC) which is coupled with the retrieval of the water products. Both, the AAC and the retrieval of water IOPs are performed by neural networks, based on a consistent set of water leaving and top-of-atmosphere reflectances. The concentrations are derived by empirical relationships between the IOPs and the concentrations.

The simulations and training range of the neural nets implemented in the Ground Segment processing of OLCI-A and B, the so-called version 1 set of nets, focussed on optically complex waters. Thus, it is recommended that these products are used in mesotrophic and eutrophic waters exceeding 0.1 mg/m^3 in chlorophyll concentration. In 2018 a new set of neural nets has been developed, was tested by the S3VT community.

During 2020, the validation of the v2 nets was continued. Comparison with OC4ME product as well as with AERONET-OC stations was performed. As an example, the results of the analysis at the AERONET-OC station “Venice” is presented here. This is a site which is party in Case-1 and partly in Case-2 conditions. This should be favourable conditions for both products or ACs, respectively. Figure 73 shows the match-up comparison for the new V2 net (left) which achieves good agreement, in the ballpark number as the standard AC (right). Figure 74 shows a time series from July to November 2018 at, and the V2 net results compare much better with the OC4ME product compared to the V1 nets. Figure 75 shows a validation example along a transect in the North Sea (2.9.2018, in-situ data courtesy of BSH). In open North Sea waters, the V2 underestimates and the OC4ME overestimate the in-situ data. In the sediment loaded near shore coastal waters (right side of the plot) the V2 nets match fairly well the in-situ samples.

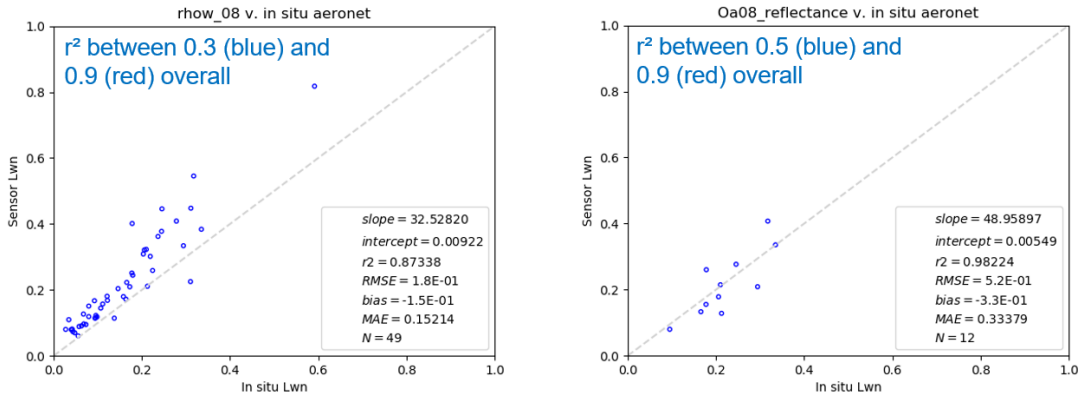

Figure 73: Match-up analysis at Aeronet-OC station "Venice" for band Oa08 (665nm) for the V2 nets (left) and the standard AC (right).

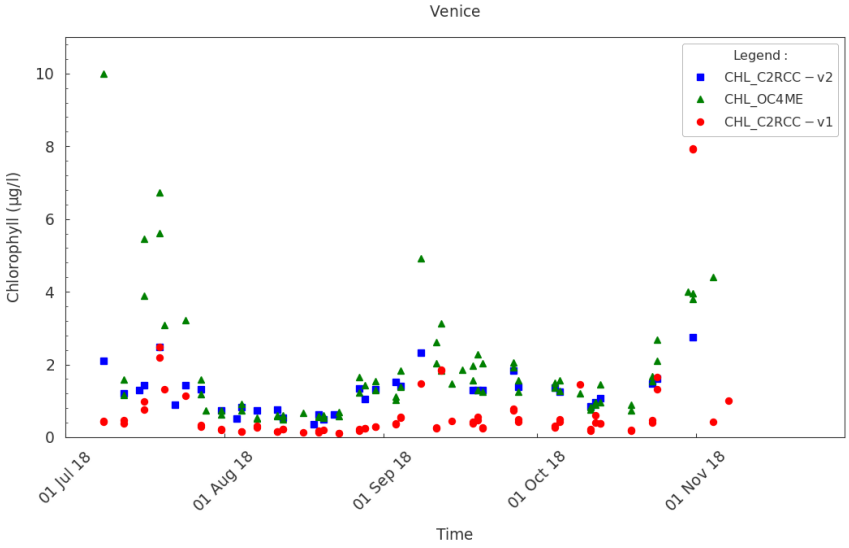

Figure 74: Comparison of V1 and V2 nets with the OC4ME product at Aeronet OC Venice station.

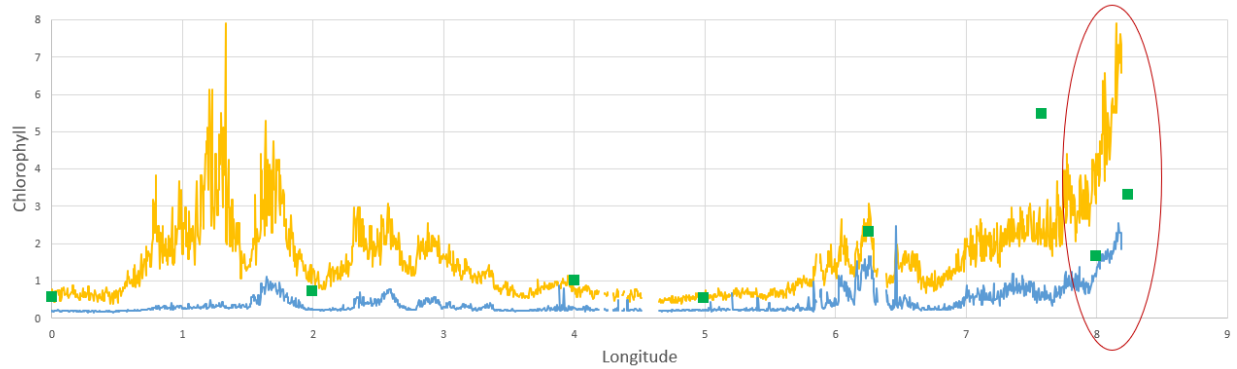

Figure 75: Comparison of the chlorophyll concentration between OC4ME (yellow), V2 nets (blue) and in-situ (green dots) along a transect in the German Bight (2.9.2018, in-situ data courtesy of BSH), from open North Sea waters (left) to near shore (right).

In 2019 it was decided by the QWG to recommend implementation of the so called Version 2 neural nets in the ground segment processing, for both, OLCI-A and B. This should take place as part of the IPF update connected with the reprocessing end of 2019/2020. During close interactions with the implementing team at ACRI, several inconsistencies between the SNAP C2RCC processor and the IPF were rectified.

The primary output of the neural nets are IOPs. These are converted into Chl and TSM concentrations using analytical formulas which are derived from in-situ measurements. During 2019 these relationships were revisited, taking recent measurements (courtesy of HZG) into account. A significantly changed conversion for TSM leads to a correction of an overestimation of TSM which was reported by S3VT members in the past.

In parallel with the validation of the V2 net, and the implementation in the ground segment processor, the scientific improvements of the neural nets has continued. We are currently working towards version 3 of the nets.

During 2019 the following actions were undertaken. The impact on the performance of the neural net AC and water products is continuously assessed:

- extension of the bio-optical model to clear waters
- update of the pure water absorption in the UV range; this is based on a publication by Mason et al 2015 and changes the pure water absorption at 400nm and 412nm significantly
- revisit of the covariance between the components of the bio-optical model
- re-formulation of the scattering components and their coexistence

The first points of the list above aim at improvements for clear water, so that the recommended cut at low Chl concentration can be removed or relaxed. First results show the improvements, and demonstrate also that this change impacts the performance of the AAC in sun glint conditions.

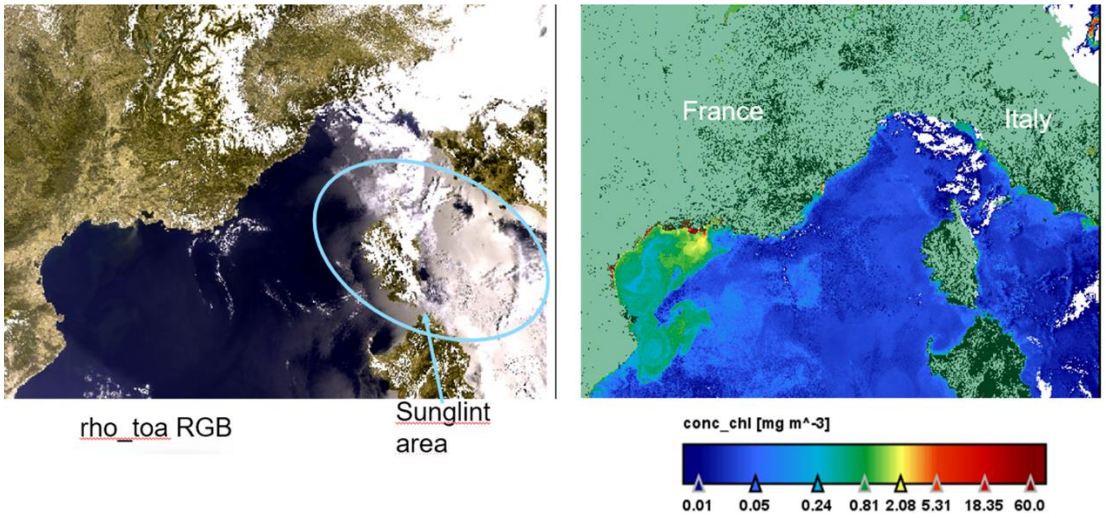

Figure 76: Demonstration of the improvements in resolving chlorophyll changes in clear water condition, due to the changes of the water model in the ongoing work of improving the neural nets. It also shows the improved performance in sun glint conditions.

5.3.7 Aerosol Optical Thickness and Angström Exponent

To validate OLCI's Aerosol product (aerosol optical thickness and Angstroem coefficient at 865 nm), we continuously compare it with data from AERONET (Holben et al 1998), AERONET-OC (Zibordi et al 2009) and MARITIME AERONET (Smirnow et al 2009). This is an ongoing process, where co-located data are collected and analysed. In contrast to last year, we switched to AERONET **V3** data. Only quality assured level data are used for OLCI A. For OLCI B we used AERONET level 1.5, since the amount is much larger. All OLCI-L2 ocean product types have been validated: full resolution and reduced resolution (*wrr, wfr*); near real time and non time critical (*NR*, *NT*). The ocean colour products from OLCI A and B have been taken from Eumetsats CODA (Copernicus Online Data Access, https://coda.eumetsat.int/#/home) or reprocessed OLCI A CODAREP (https://codarep.eumetsat.int/#/home) websites. Although the following quantitative comparisons are restricted to *full resolution non time critical,* the found results are valid for all product types.

5.3.7.1 AERONET comparisons with OLCI A

88000 OLCI-A scenes within the period of June 2016 to January 2020 have been analysed so far. For a matchup, the temporal distance between the satellite overpass and the AERONET acquisition was less than 60 minutes. Since, the AERONET L2 is extensively quality controlled, it is published with a delay of up to 1 year, thus the latest AERONET data is from early Summer 2019. Only OLCI measurements are used for the validation which are cloud-free (according to the standard cloud flags: *cloud, cloud margin and cloud ambiguous*) in an area of about 10x10 km^2 around the AERONET acquisition. Further, all recommended flags from *Sentinel-3 OLCI Marine User Handbook* (EUM/OPS-SEN3/MAN/17/907205) have been applied. Eventually, to reduce the influence of undetected (sub pixel or sub visual) clouds, only matchups have been used, where the standard deviation of the aerosol optical thickness within the 10x10

km^2 area was less than 0.2. Due to the fact, that most of the AERONET stations are on land, the number of matchups reduced to 690 only. The results are plotted in Figure 77.

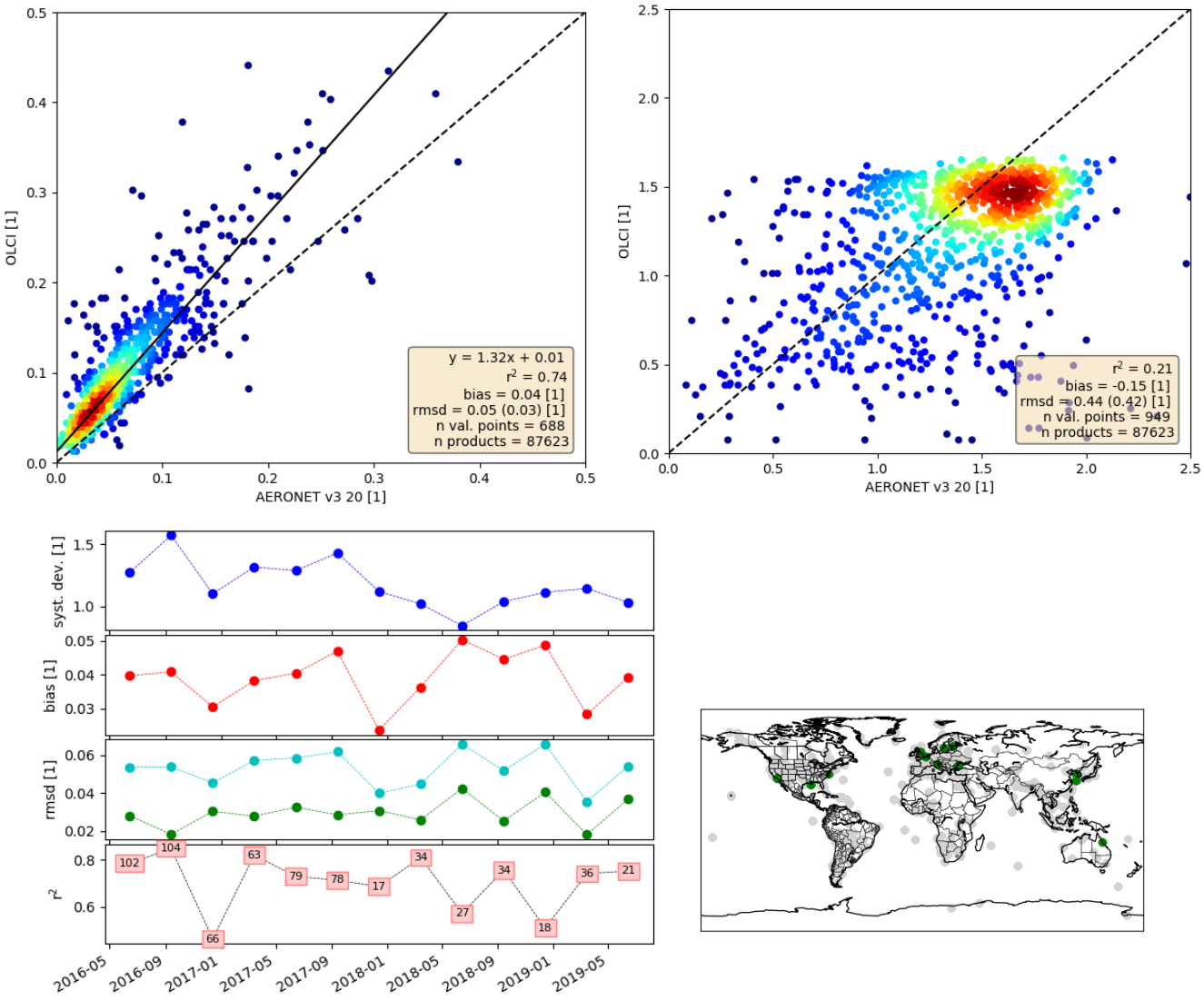

Figure 77: Upper left: OLCI aerosol optical thickness at 865nm against AERONET at 870nm, upper right: OLCIs Angström exponent at 865nm against the AERONET Angström exponent at 865 nm-440 nm. Lower left: Temporal evolution of different quality measures of the optical thickness comparison (from top to bottom: systematic deviation factor, bias, root mean squared difference (with and without bias correction), explained variance (number in boxes are the numbers of matchups). Lower right: positions of the used AERONET stations.

It becomes apparent, that:

- There is a highly linear relation between the AERONET and OLCI AOT, the explained variance is 0.8.
- The optical thickness of OLCI A is systematically overestimated by 20% - 50%, the majority of the cases is at around 35%.
- This leads to a systematic bias of 0.04.
- If the systematic overestimation is corrected, the root mean squared difference decreases from 0.05 to 0.03.
- There is only a weak (r2 = 0.2) linear relation for the Angstroem exponent.
- The majority of AERONET has an Angstroem of 1.6, whereas OLCI gives 1.4, thus OLCI underestimates the spectral extinction by 0.2.

All investigated quality measures show no significant temporal evolution. There is a slight improvement of the systematic deviation from 1.5 to 1.1, but the significance is low.

5.3.7.2 Marine AERONET comparisons with OLCI A

1400 OLCI-A scenes within the period of June 2016 to January 2020 have been analysed so far. For a matchup, the temporal distance between the satellite overpass and the AERONET acquisition was less than 60 minutes. Since, the maritime AERONET L2 is expensively quality controlled, it is published with a delay of up to 1 year, thus the latest data is from early Summer 2019. Only OLCI measurements are used for the validation which are cloud-free (according to the standard cloud flags: *cloud, cloud margin and cloud ambiguous*) in an area of about 10x10 km^2 around the AERONET acquisition. Further, all recommended flags from *Sentinel-3 OLCI Marine User Handbook* (EUM/OPS-SEN3/MAN/17/907205) have been applied. Eventually, to reduce the influence of undetected (sub pixel or sub visual) clouds, only matchups have been used, where the standard deviation of the aerosol optical thickness within the 10x10 km^2 area was less than 0.2. After this rigid filtering only 39 leftovers remain. The results are summarized in Figure 78 and Figure 77:

- There is a highly linear relation between the AERONET and OLCI AOT, the explained variance is 0.8.
- The data shows a systematic underestimation of 20%, contrary to the AERONET comparison. This is probably a sampling effect due to few points with high AOT.
- There is no linear relation for the Angström exponent.

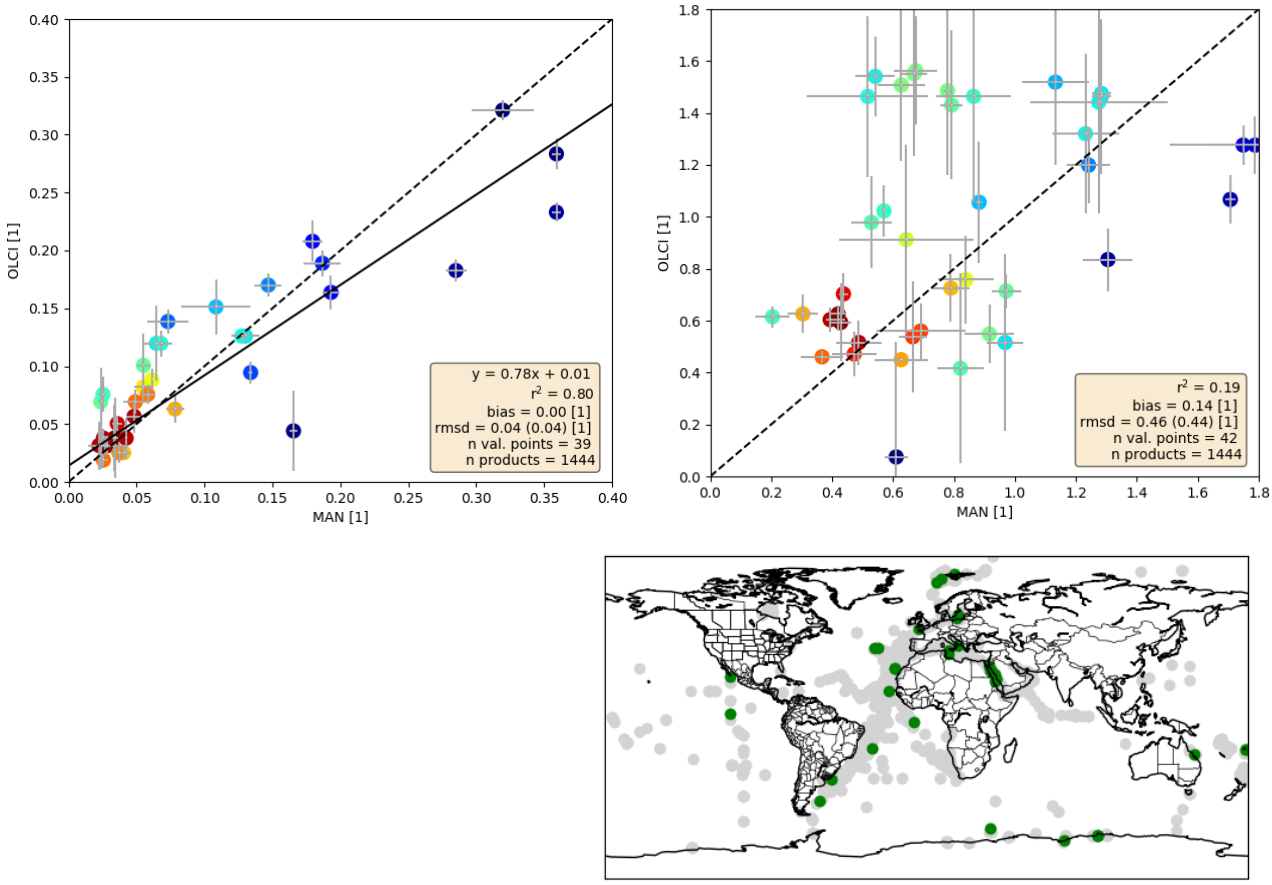

Figure 78: Upper left: OLCI aerosol optical thickness at 865 nm against maritime AERONET at 870 nm, upper right: OLCIs Angström exponent at 865 nm against the maritime AERONET Angström exponent at 865 nm-440 nm. Lower right: positions of the used cruises.

5.3.7.3 AERONET comparisons with OLCI B

36000 OLCI-B scenes within the period of June 2018 to January 2020 have been analysed so far. For a matchup, the temporal distance between the satellite overpass and the AERONET acquisition was less than 60 minutes. We used the AERONET L1.5, which is not is expensively quality controlled, but available in near time. As for OLCI A, only measurements are used for the validation which are cloud-free (according to the standard cloud flags: *cloud, cloud margin and cloud ambiguous*) in an area of about 10x10 km^2 around the AERONET acquisition. Further, all recommended flags from *Sentinel-3 OLCI Marine User Handbook* (EUM/OPS-SEN3/MAN/17/907205) have been applied. Eventually, to reduce the influence of undetected (sub pixel or sub visual) clouds, only matchups have been used, where the standard deviation of the aerosol optical thickness within the 10x10 km^2 area was less than 0.2. Eventually the number of matchups reduced to 60 only. The results are shown in Figure 79. It becomes apparent, that OLCI B behaves like OLCI A:

- There is a highly linear relation between the AERONET and OLCI AOT. The explained variance is 0.7.
- Similar to OLCI-A, OLCI-B systematically overestimates AOT by 40%.
- The pattern of the Angström comparison is as for OLCI A; a weak relation, the majority around 1.4 and a systematic underestimation of OLCI by 0.3.

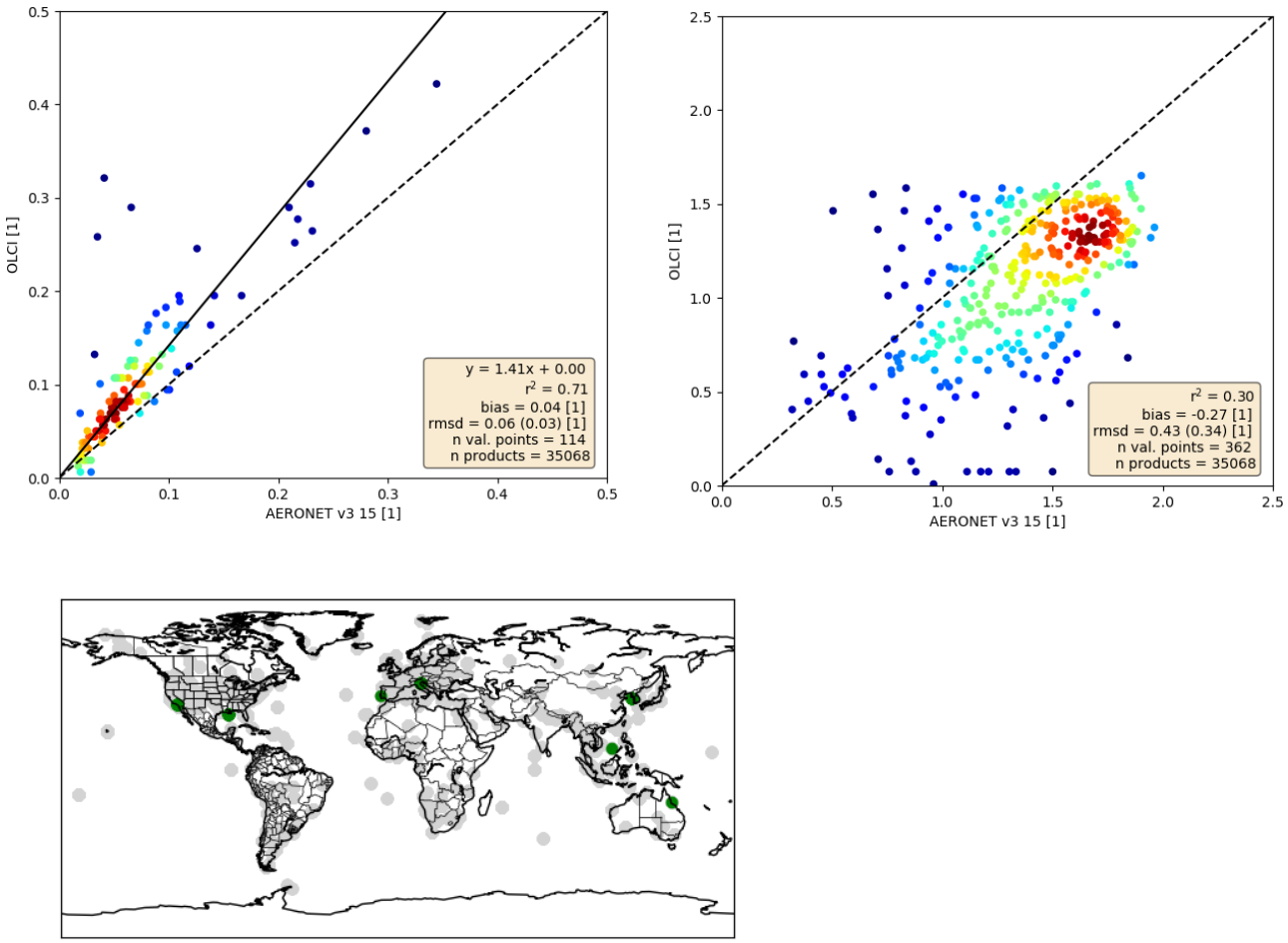

Figure 79: Upper left: OLCI aerosol optical thickness at 865nm against Aeronet v3 L1.5 AOT at 870nm, upper right: OLCIs Angström exponent at 865nm against the Aeronet v3 L1.5 Angström exponent at 865nm-440nm. The error bars correspond to the standard deviation within 10x10km (OLCI) or 60 minutes (AERONET). Lower: positions of the used AERONET stations.

5.3.7.4 Summary

The validation of OLCI aerosols products shows a high agreement for the aerosol optical thickness (*rmsd* ~ 0.02), if a systematic overestimation of around 40% is corrected. The Angström exponent agrees hardly (r^2 = 0.2), but the order of magnitude (1.6) is almost met (bias = -0.2). A validation of OLCI B using AERONET level 1.5 data, shows the same pattern as for OLCI A. The number of matchups with maritime AERONET is still too low to reach valid results.

5.3.7.5 References

- Holben, B. N., et al., AERONET—A federated instrument network and data archive for aerosol characterization, Remote Sens. Environ.,66, 1–16, 1998.)
- Smirnov, A., Holben, B.N., Slutsker, I., Giles, D.M., McClain, C.R.,Eck, T.F., Sakerin, S.M., Macke, A., Croot, P., Zibordi, G., Quinn, P.K., Sciare, J., Kinne, S., Harvey, M., Smyth, T.J., Piketh, S.,Zielinski, T., Proshutinsky, A., Goes, J.I., Nelson, N.B., Larouche,P., Radionov, V.F., Goloub, P., Krishna Moorthy, K., Matarrese, R.,Robertson, E.J., Jourdin, F., 2009. Maritime aerosol network as acomponent of aerosol robotic network. J. Geophys. Res. 114, 1—10, http://dx.doi.org/10.1029/2008JD011257.
- Zibordi G., B.Holben, I.Slutsker, D.Giles, D.D'Alimonte, F.Mélin, J.-F. Berthon, D. Vandemark, H.Feng,G.Schuster, B.Fabbri, S.Kaitala, J.Seppälä. AERONET-OC: a network for the validation of Ocean Color primary radiometric products. Journal of Atmospheric and Oceanic Technology , 26, 1634-1651, 2009.

6 Summary of performances – SLSTR

6.1 Instrument performances

6.1.1 Instrument temperatures

As a thermal infrared instrument, thermal stability and uniformity of the optical mechanical enclosure, OME is critical to the radiometric calibration. During normal operations, temperatures have remained generally stable and consistent during the reporting period, with gradual changes due to the seasonal cycle, which are consistent with the first two years of operations for SLSTR-A. The exceptions are when the normal mode was disrupted by instrument operations or anomalies – for example, the decontaminations performed in May for SLSTR-A and at in April and September for SLSTR-B.

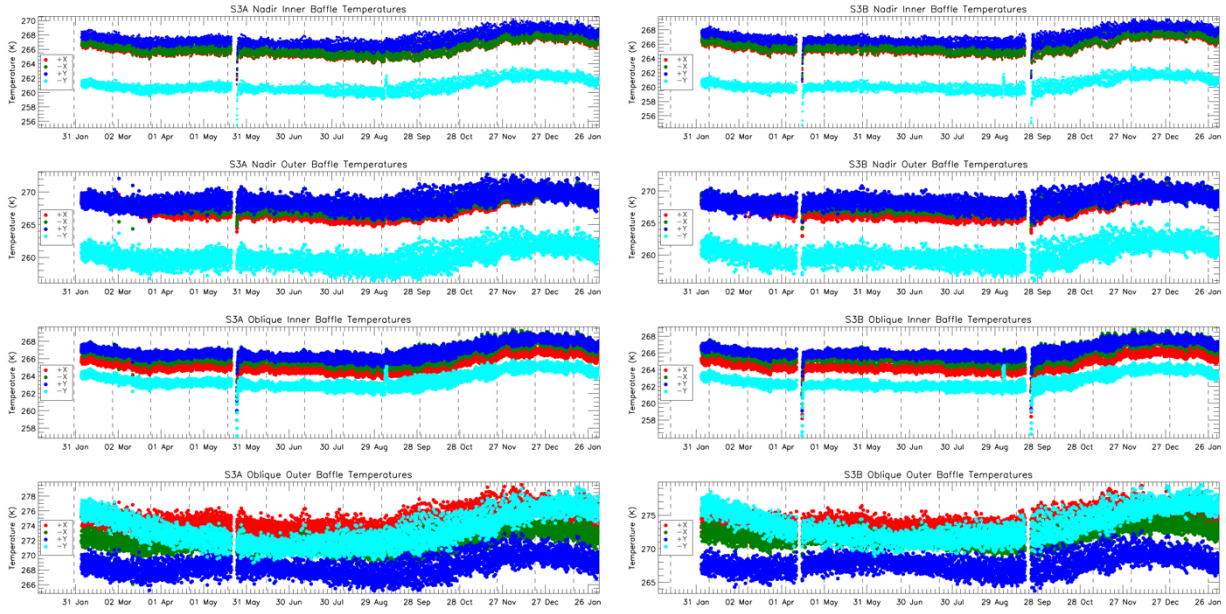

Figure 80: Baffle temperature trends for SLSTR-A (left) and SLSTR-B (right) from 1st Feb 2019 to end of Jan 2020. The vertical dashed lines indicate the start and end of each cycle.

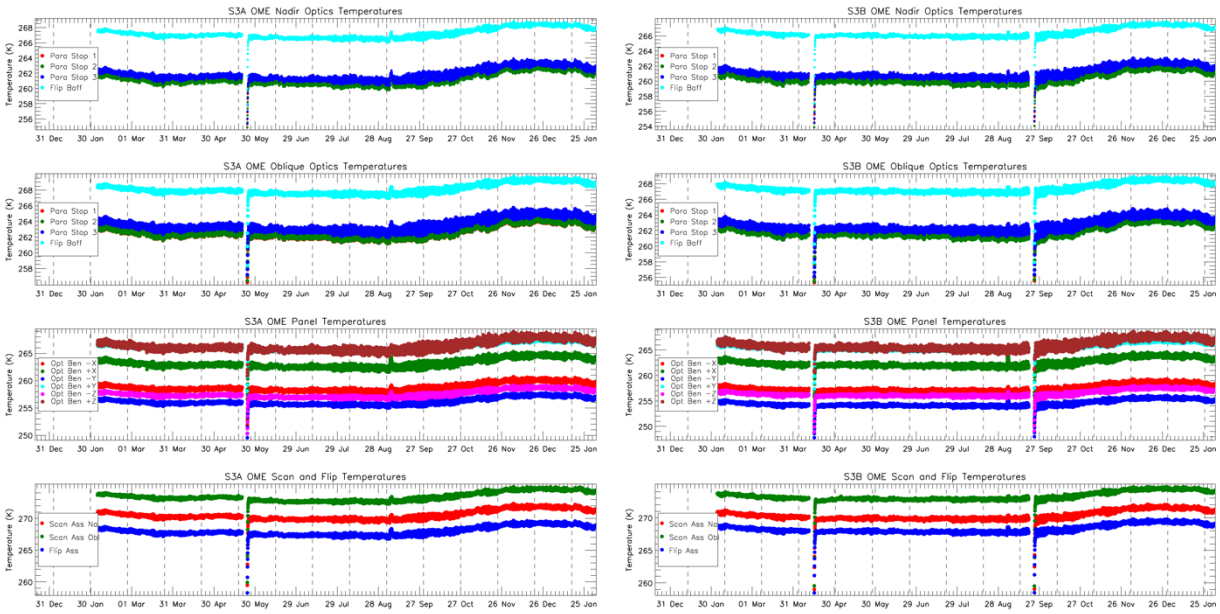

Figure 81: OME temperature trends for SLSTR-A (left) and SLSTR-B (right) from 1st Feb 2019 to end of Jan 2020, showing the paraboloid stops and flip baffle (top two plots) and optical bench and scanner and flip assembly (lower two plots). The vertical dashed lines indicate the start and end of each cycle.

6.1.2 Detector Temperatures

The cooler is performing well, maintaining the IR detectors between 84 and 88K – see Figure 82 and Figure 83. The IR FPA is affected by water ice contamination as is common for instruments with cryogenic optics, and was observed for all ATSR instruments. This affects the heat load on the IR FPA, which requires the cooler to run at increased drive levels and also affects the optical throughput of the channels. Therefore, periodic decontamination cycles are needed to remove the water ice from the cold surfaces. These were carried out in May for SLSTR-A and in April and September for SLSTR-B.

The IR detector temperatures gradually increase following each decontamination as the ice layer builds up and the cooler drive amplitude increases. The rate of increase in S8 temperature following each SLSTR-A decontamination since the beginning of the mission is plotted in Figure 84, and the rate of increase in cooler drive amplitude in Figure 85. The rate of increase in temperature is reducing over time, consistent with the reduced water ice contamination rates (see Section 6.1.7.7). However, the change in slope of the cooler drive amplitude appears to be lower than expected, indicating that further changes to the cooler cold tip set point may be needed in future.

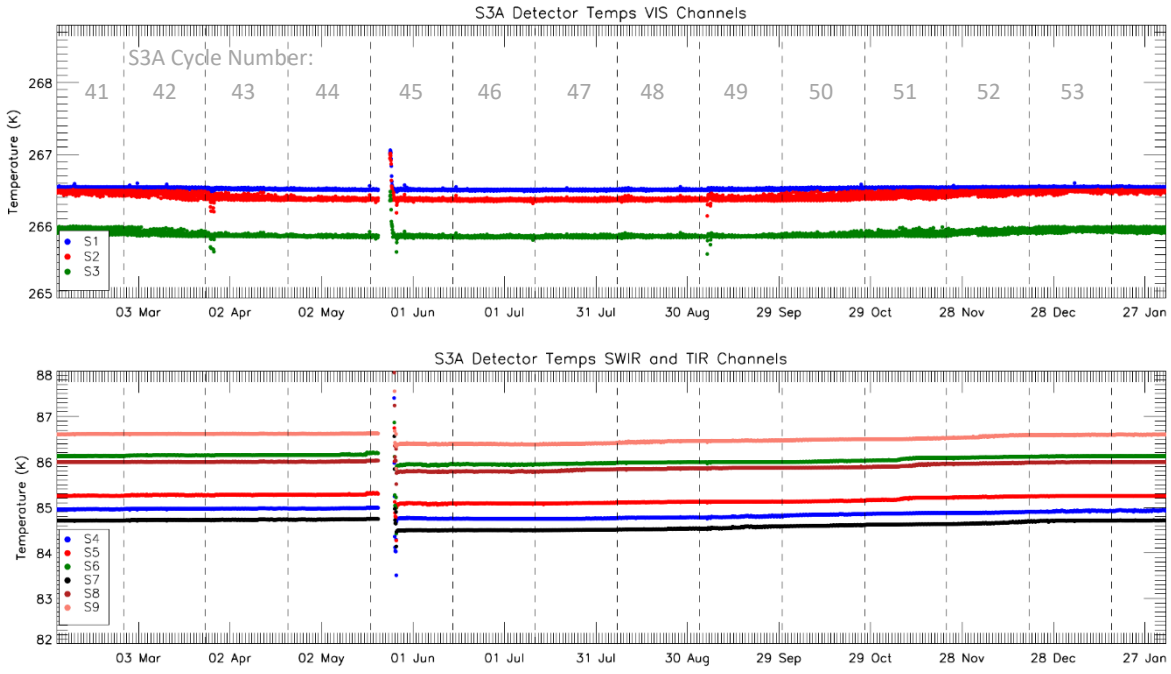

Figure 82: SLSTR-A detector temperatures for each channel from 1st Feb 2019 to end of January 2020. Discontinuities occur for the infrared channels where the FPA was heated for decontamination, or on 18th July when the cold tip temperature was increased. The vertical dashed lines indicate the start and end of each cycle.

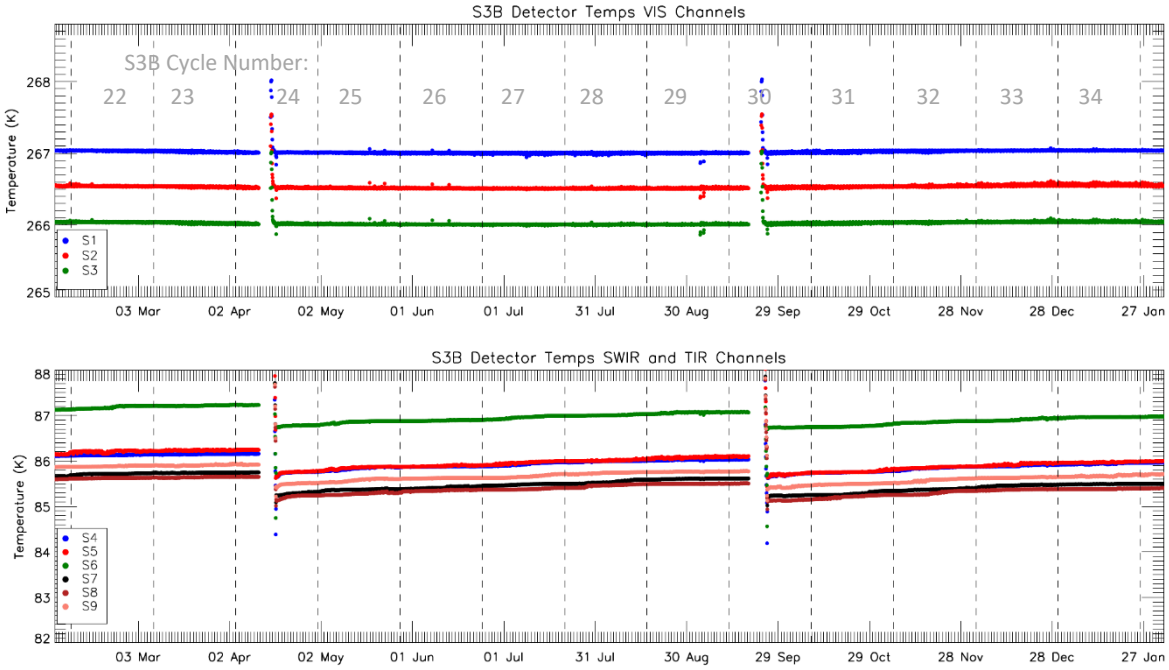

Figure 83: SLSTR-B detector temperatures for each channel from 1st Feb 2019 to end of January 2020. The discontinuity occurs for the infrared channels where the FPA was heated for decontamination. The vertical dashed lines indicate the start and end of each cycle.

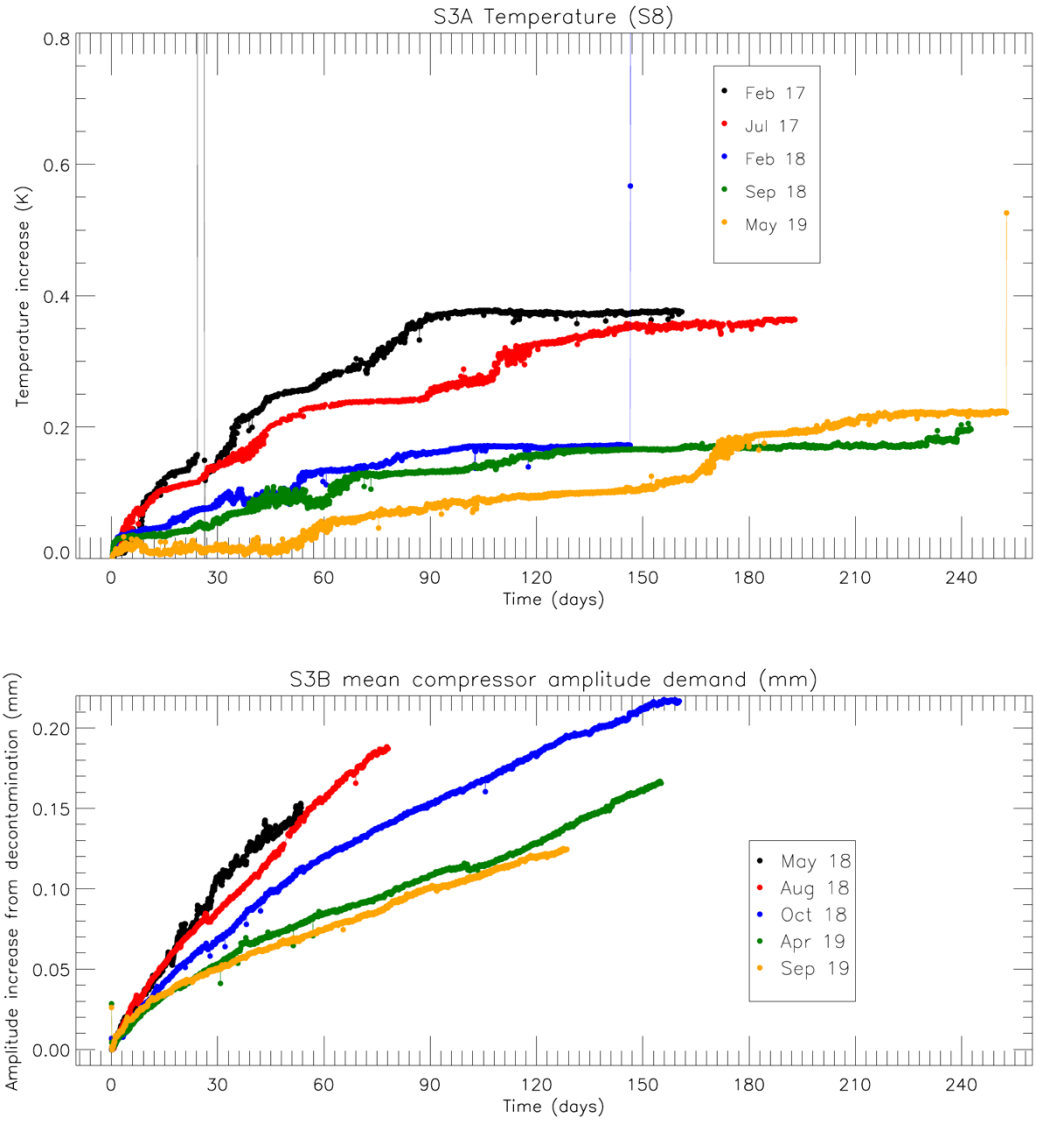

Figure 84: The increase in S8 temperature for SLSTR-A (top) and SLSTR-B (bottom) following recent decontaminations.

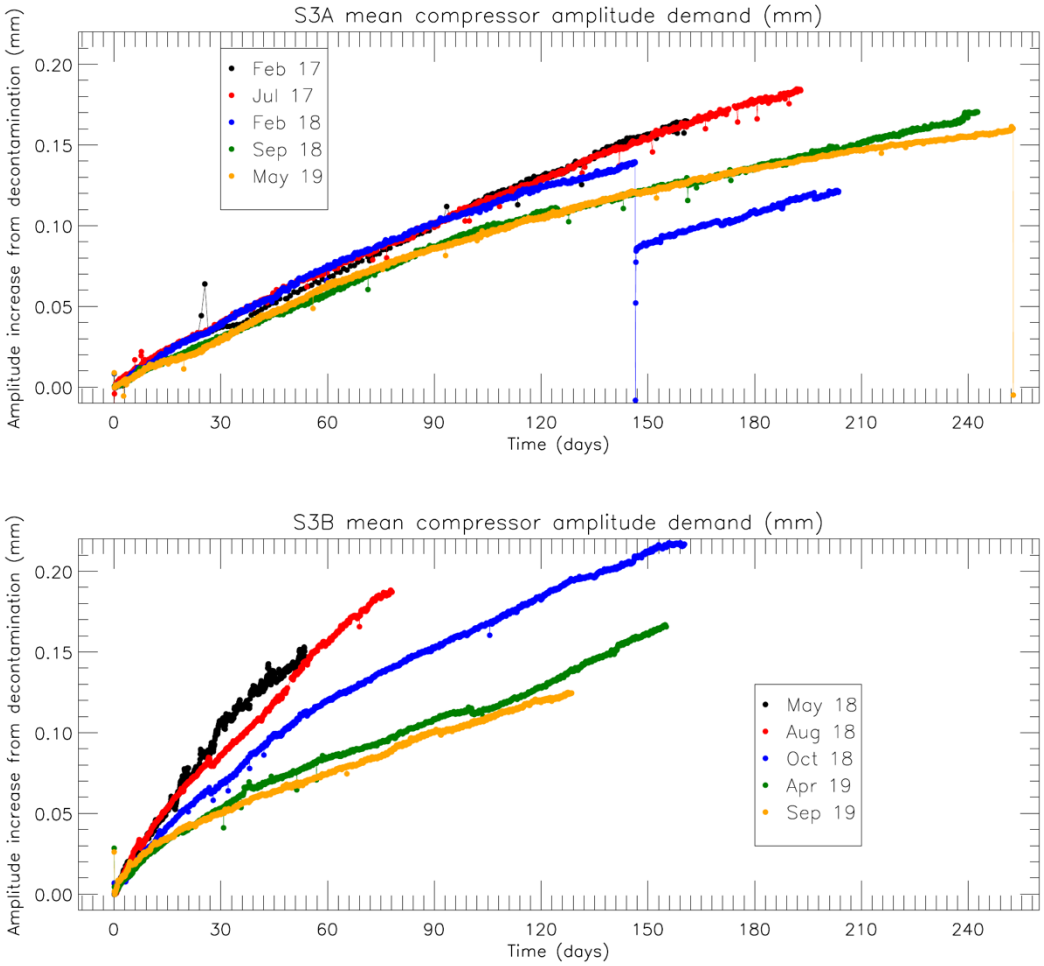

Figure 85: The increase in cooler drive amplitude following the last five decontaminations performed on SLSTR-A (top) and SLSTR-B (bottom). Note that the step in the blue line (February 2018 decontamination) after 145 days is due to the cooler cold tip temperature change in July 2018.

6.1.3 Scanner performance

The scanners have performed consistently since launch, operating within required limits. The scanners are controlled and monitored by absolute encoders mounted on the drive shafts. Scan jitter statistics for SLSTR-A are shown in Figure 87 and for SLSTR-B in Figure 89 with respect to the linear control law within each orbit.

6.1.3.1 SLSTR-A scanner performance

The scanner statistics for SLSTR-A in year 3 of the mission are given in Table 16. A comparison of the results with previous years shows general consistency.

The maximum and minimum deviation within each orbit gives a measure of the worst instantaneous jitter encountered, and this is shown by the green and black points in Figure 87. Histograms of maximum minus minimum deviation for year 3 are shown in Figure 86, with the peak of the (max-min) histogram at ~40”/20” for the scanners and ~70”/90” for the flip mirror (nadir/oblique). These values are as good or better than the previous years, showing that the scanners are performing well.

Table 16: SLSTR-A scanner and flip mirror jitter statistics the first three years of the mission.

View	Mirror	Largest mean deviation (”)			Largest standard deviation (”)			Maximum-minimum at peak of histogram (”)		
		2017	2018	2019	2017	2018	2019	2017	2018	2019
Nadir	scanner	0.8	1	1.4	3.6	3	4.8	36	39	38
	flip	0.4	0.4	0.4	7.4	8.6	7.4	92	69	68
Oblique	scanner	0.8	0.6	1	3.6	3.6	3.2	36	26	23
	flip	0.4	0.6	0.6	11.8	13.4	13.6	116	98	90

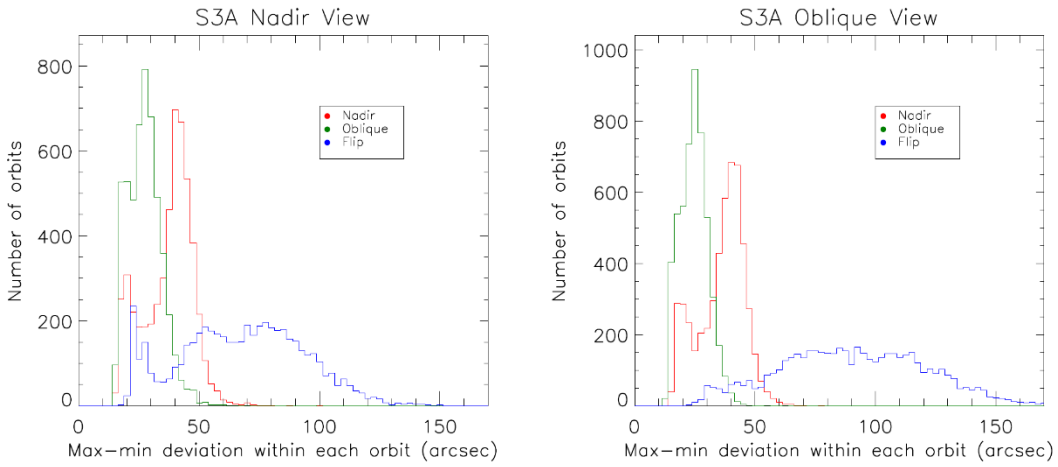

Figure 86: SLSTR-A histogram of max-min deviation of the scanners and flip mirror in each orbit for year 3 for nadir view (left) and oblique view (right).

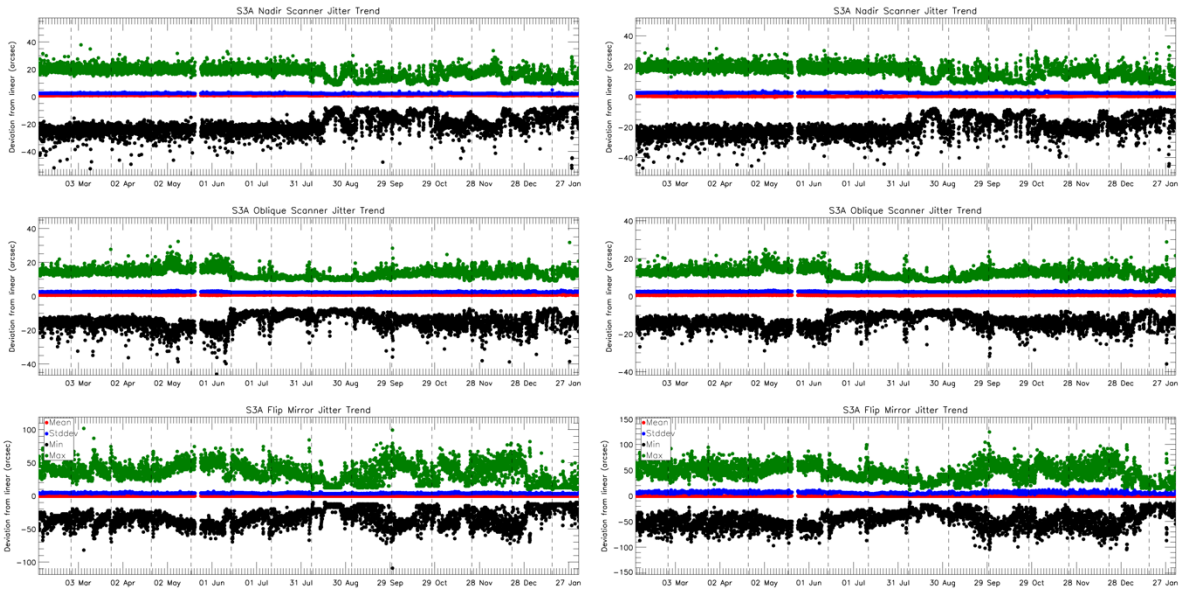

Figure 87: SLSTR-A scanner and flip jitter for year 3, showing mean (red), stddev (blue) and max/min (green/black) position compared to the expected one for the nadir view (left) and oblique view (right). The vertical dashed lines indicate the start and end of each cycle.

6.1.3.2 SLSTR-B scanner performance

The scanner statistics for SLSTR-B are shown in Table 17. They show that the mean deviation of the mirrors are consistent with the previous year. The flip mirror has a slightly higher worst standard deviation, although the shape of the standard deviation histogram is roughly consistent. The worst instantaneous jitter encountered for the flip mirror is higher than the previous year, with a change of 61” for nadir view and 33” for oblique view. Overall, the performance of SLSTR-B is worse than SLSTR-A, in particular for the flip mirror in nadir position.

The Level-1 pointing flags record when the scanner and flip jitter exceed thresholds set during commissioning phase. The threshold currently used for the flip mirror instantaneous position is 99”. Figure 88 shows that there are some orbits in nadir view when the maximum-minimum deviation exceeds 198” (twice the threshold), and this indicates that some L1 products will have the flip instantaneous pointing flag raised. The flip mirror jitter should be carefully monitored in future.

The jitter is calculated from the measured positions of the mirrors, which are also used to calculate the geolocation of each pixel. This means that the high values of flip jitter for SLSTR-B will not affect the absolute geolocation error for each pixel. However, it will affect the smooth sampling along the scan, and may lead an increased chance of empty image pixels which are cosmetically filled in the L1 products.

Table 17: SLSTR-B scanner and flip mirror jitter statistics (per orbit) for 1st February 2019 to 1st February 2020

View	Mirror	Largest mean deviation (")		Largest standard deviation (")		Maximum-minimum at peak of histogram (")	
		2018*	2019	2018*	2019	2018*	2019
Nadir	scanner	0.4	0.2	3.4	3.6	39	47
	flip	0.4	0.4	6.8	8.2	94	155
Oblique	scanner	3	3	5.6	5.8	56	56
	flip	0.6	0.6	9.4	12.6	87	120

** October 2018 to February 2019*

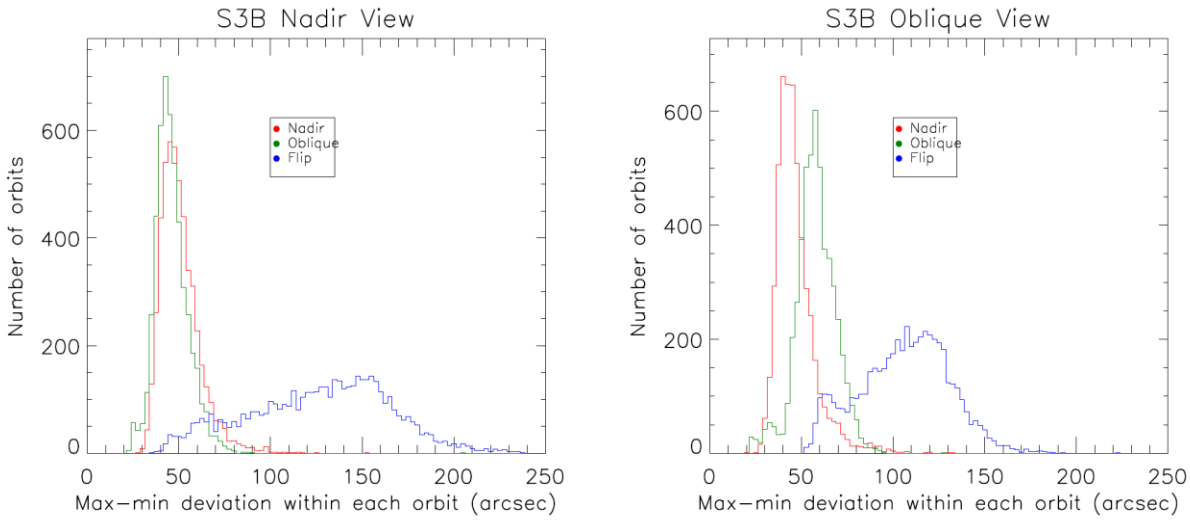

Figure 88: SLSTR-B histogram of max-min deviation of the scanners and flip mirror from February 2019 to February 2020.

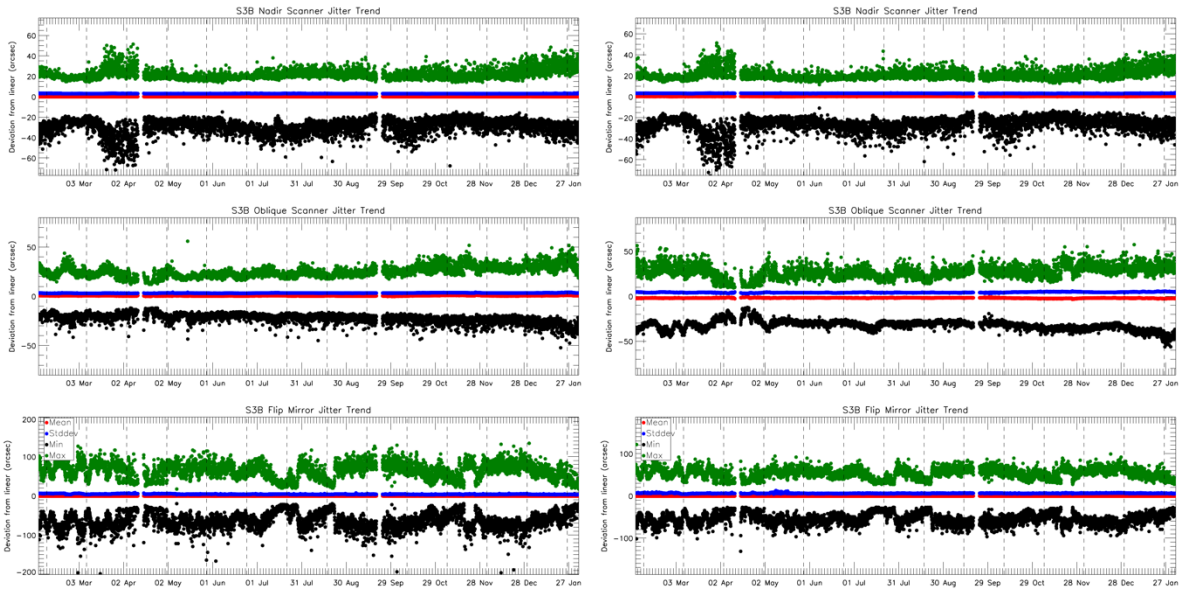

Figure 89: SLSTR-B scanner and flip jitter, showing mean (red), stddev (blue) and max/min (green/black) position compared to the expected one for the oblique view for February 2019 to February 2020. The vertical dashed lines indicate the start and end of each cycle.

6.1.4 Black-Bodies

The blackbodies have functioned well over the reporting period. The heated blackbody (+YBB) is being maintained by the heaters approximately 37-38 K above the cool blackbody (-YBB). The long-term trends show no discernible degradation in the performance of the heaters.

6.1.4.1 SLSTR-A Black-Bodies

Figure 90 shows the blackbody temperatures and baseplate gradients for SLSTR-A. During December 2019, the heated BB increased to above 304 K as the satellite approached perihelion. This is slightly higher than the temperature reached in previous years, although still within acceptable limits. The maximum BB temperature should be monitored carefully to ensure that the BBs remain below 305 K to avoid saturation of S7.

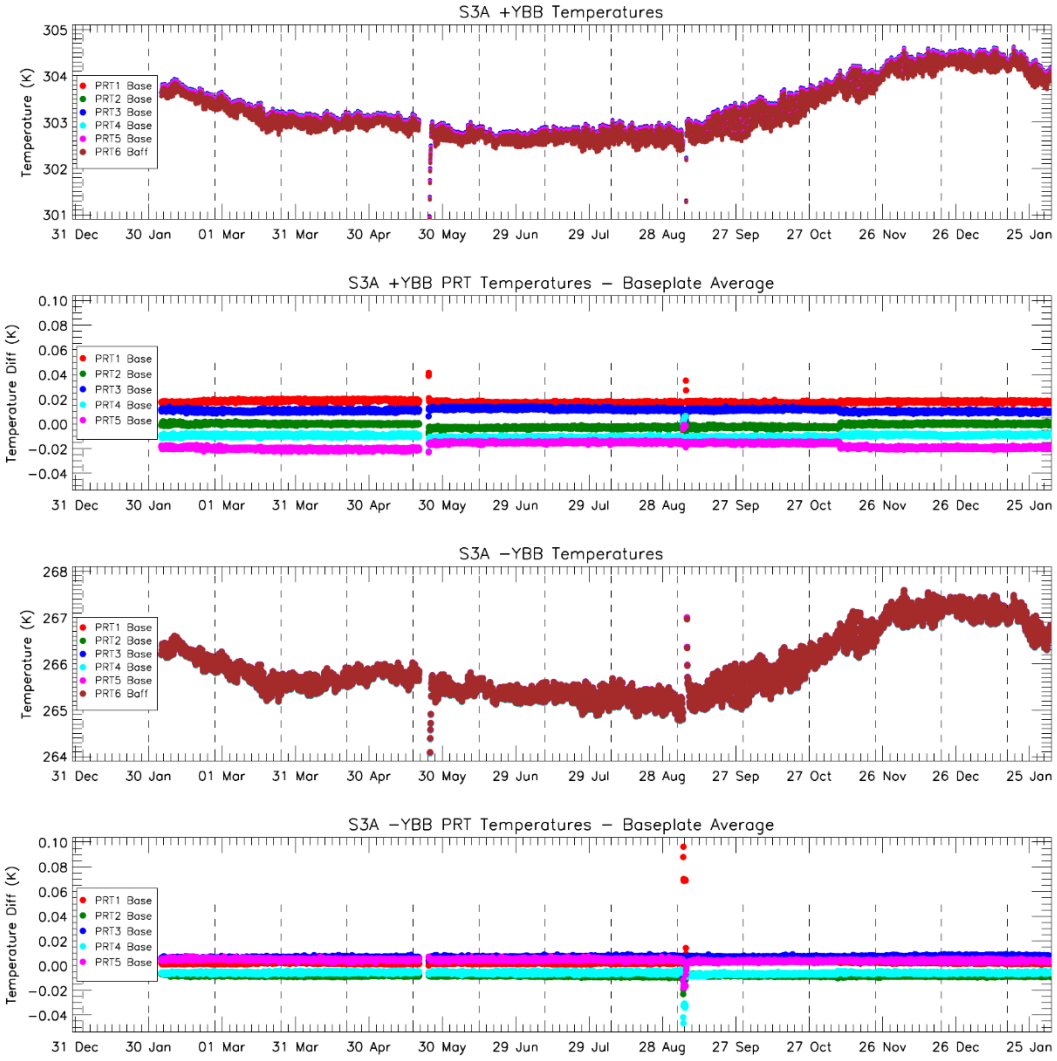

Figure 90: SLSTR-A blackbody temperature and baseplate gradient trends for Feb 2019 to Jan 2020. The vertical dashed lines indicate the start and end of each cycle. The discontinuity in May is due to the decontamination, and in September is due to a black-body crossover test.

6.1.4.2 SLSTR-B Black-Bodies

Figure 91 shows the blackbody temperatures and baseplate gradients for SLSTR-B. The difference of the 5 PRTs located on the blackbody baseplate with the average base temperature are also plotted in Figure 91. The spread in temperature of the baseplate PRTs is largest when the blackbody is heated. In particular when the +YBB is hot, PRT1 is warmer than the average by approximately 70 mK whereas the other PRTs all cluster closely together. This difference was expected before launch, and is consistent with measurements made during the ground testing.

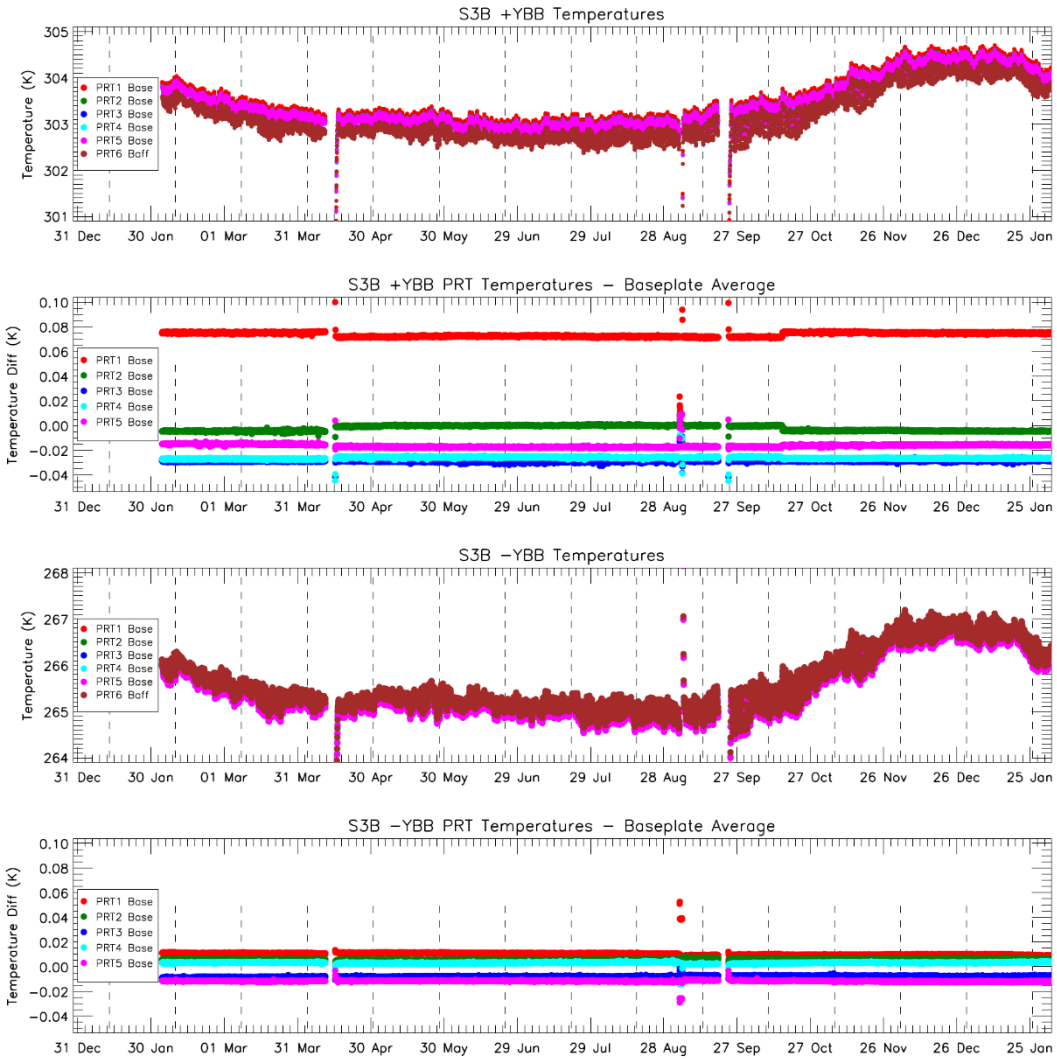

Figure 91: SLSTR-B blackbody temperature and baseplate gradient trends for Feb 2019 to Jan 2020. The vertical dashed lines indicate the start and end of each cycle. Discontinuities are caused by the decontaminations, and a black-body crossover test.

6.1.4.3 Blackbody Cross-Over Tests

Blackbody cross-over tests are carried out at yearly intervals to compare the radiometric signals in the thermal channels when the two blackbodies are at identical temperatures. The test is performed to

determine the effects of any drifts in the blackbody thermometer calibration or change in target emissivity caused by a deterioration of the black surface finish.

The method is based on that for AATSR on ENVISAT and has been performed for SLSTR during pre-launch calibration, then in-flight during commissioning and at yearly intervals to determine any changes in the blackbody performance.

It is important to note that this is not an absolute test of the blackbody performance since we do not have an independent method to evaluate the absolute radiances from the blackbodies on-orbit to sufficient accuracy (SLSTR is intended to have a radiometric error <0.1K which is at the limit for most space-borne instruments). However, we are able to deduce any relative calibration errors between channels or trends in the blackbody thermometer calibration or change in target emissivity caused by a deterioration of the black surface finish. The method does not distinguish which effect is dominant because the two are highly correlated. However, the results do provide a means to verify the uncertainty in the BB radiances.

The test was performed by switching the heated blackbody from the +YBB to the –YBB (and vice versa) and allowing the temperatures to cross over and stabilise. The most tests for this reporting period were performed between 3-6th September 2019, with crossover temperatures of 289.708/291.370 K for SLSTR-A and 289.245/290.643 K for SLSTR-B.

The analysis is performed by comparing the radiometric signals close to the cross-over times as a function of the baseplate temperatures as measured by the PRTs. Here, we can estimate the effective temperature difference between the two BBs from the slope dN/dT, which is obtained by a simple linear fit to the data. So,

$$\Delta T = \frac{dT}{dN}\Delta DN$$

The detector counts versus temperatures at the cross-over for the SLSTR-A test are shown in Figure 92 and for SLSTR-B in Figure 93. Figure 94 shows ΔT versus time for all of the BB cross-over tests performed to date, including the pre-launch measurements (5 tests for SLSTR-A and 3 tests for SLSTR-B).

For SLSTR-A, the results show that there has been some steady drift with time, and there is a possible correlation with the baseplate gradients for the second cross-over. For SLSTR-B, the results show a change from the pre-launch measurements to on-orbit, with the largest variations seen for S8 and S9 in the Nadir view. At the time of writing the cause of the differences is not fully understood. Further blackbody cross-over tests performed during the lifetime of the mission will show if this is an evolving trend or an artefact of the test conditions.

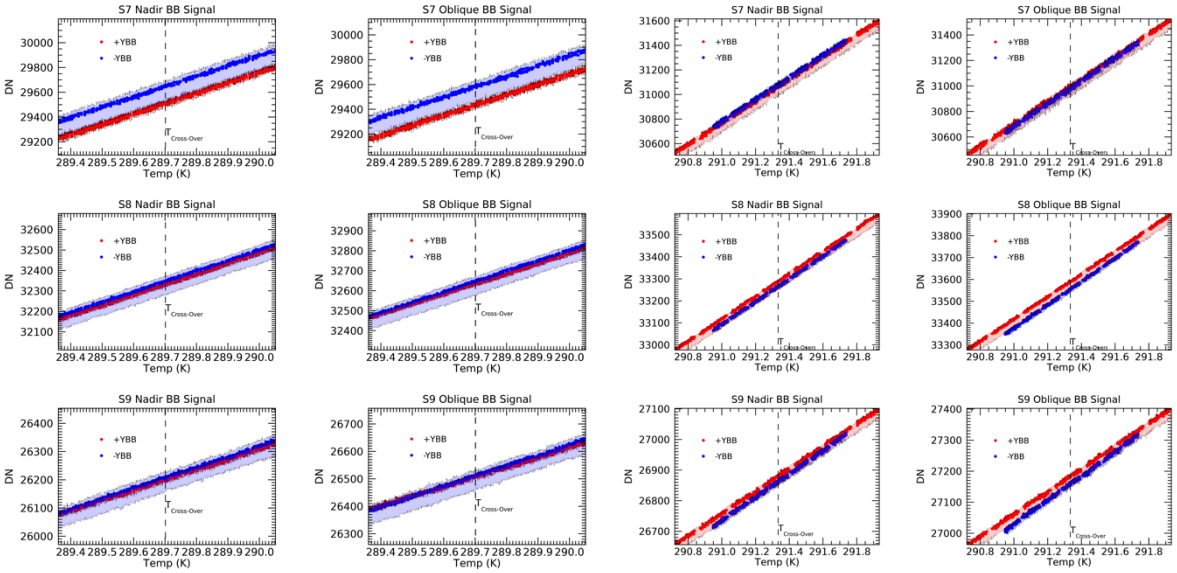

Part 1 Part 2

Figure 92: SLSTR-A detector counts vs. temperatures at the blackbody cross-over points for the BB cross-over test on 5th and 6th September 2019. The shaded area represents the range of values between the maximum and minimum baseplate temperatures. Part 1 of the test is shown on the left and part 2 on the right.

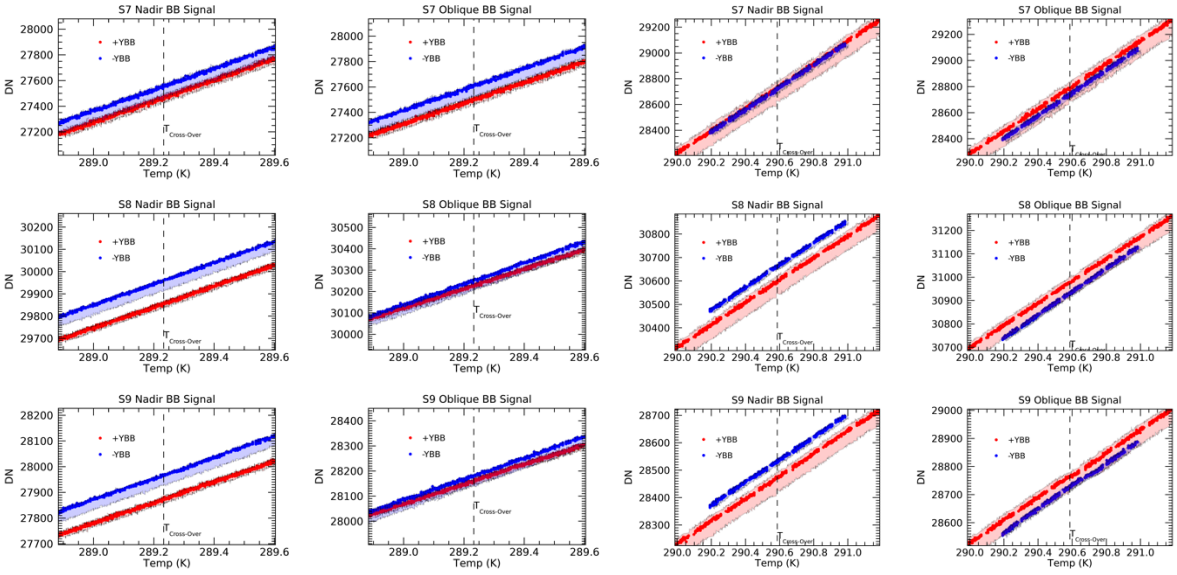

Part 1 Part 2

Figure 93: SLSTR-B detector counts vs. temperatures at the blackbody cross-over points for the BB cross-over test on 3rd and 4th September 2019. The shaded area represents the range of values between the maximum and minimum baseplate temperatures. Part 1 of the test is shown on the left and part 2 on the right.

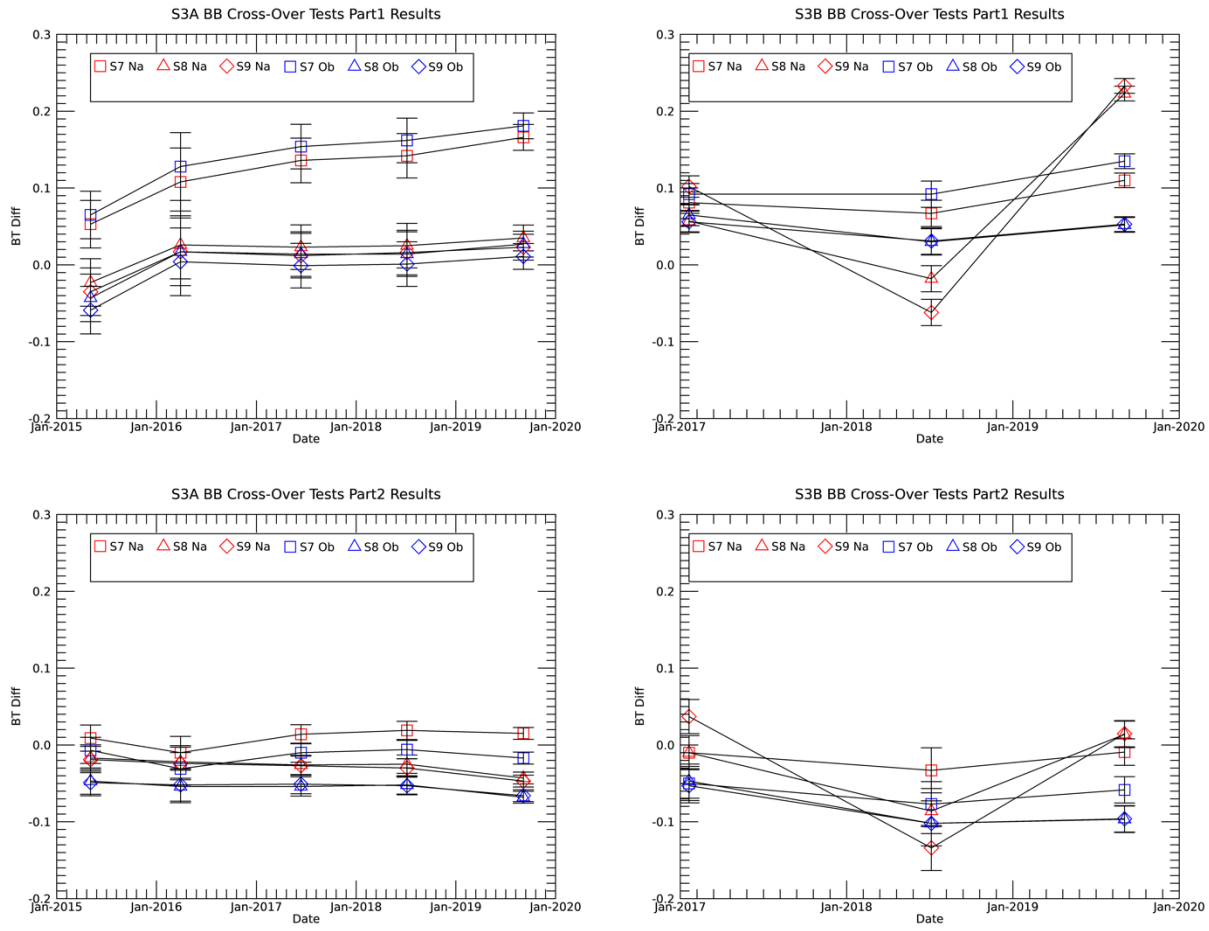

Figure 94: BT differences vs time for all of the blackbody cross-over tests performed to date (including pre-launch measurements) for SLSTR-A (left) and SLSTR-B (right). The part 1 crossover is shown in the top plots, and part 2 in the lower plots. Different colours indicate different channels (S7-S9) in nadir and oblique views. Error bars are derived from the blackbody temperature gradients and standard deviations of the BB signals during the cross-over.

6.1.5 VISCAL System

6.1.5.1 VISCAL illumination

The VISCAL system is illuminated by the Sun once per orbit. For the calibration signal to be used in L1 processing, it is important that the diffuser has a clear view of the full solar disk for at least 100 scans. If the illumination period is too short, then the IPF will not generate a VISCAL file. The number of scans where the VISCAL is fully illuminated is seasonally dependent and affected by the satellite attitude. So, it is important to keep track of the variation in the illumination period to make sure that it does not drop below the threshold needed for processing.

Figure 95 shows the variation of the number of clear scans covered by the VISCAL peak during the last year of operation for SLSTR-A and SLSTR-B in nadir and oblique views. The number of scans in the SLSTR-A VISCAL peak decreases from ~180 scans in January, to a minimum of ~125 scans in June. The number of

scans in the SLSTR-B VISCAL peak decreases from ~160 scans in January, to a minimum of ~125 scans in June. This variation is well correlated with the satellite beta angle, which is defined as the angle between the satellite orbital plane and the sun vector, and determines how much time the satellite is in direct illumination by the sun.

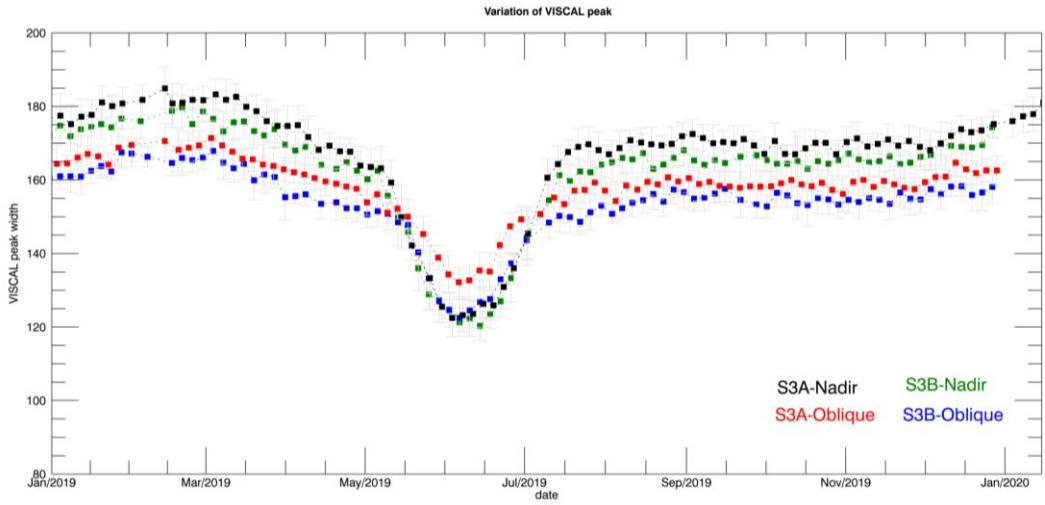

Figure 95: Variation of the SLSTR-A and SLSTR-B VISCAL peak width during the last year of operations for the nadir (black/green) and oblique (red/blue) views.

6.1.6 IR Channels

6.1.6.1 Dynamic Range and Digitisation

The TIR channels (S7-S9, F1 and F2) are all functioning with no reported loss of data or digital resolution. The IR gains show an increase as detector temperatures warm-up between decontamination cycles (Figure 96 and Figure 97). Comparisons between nadir and oblique views show that the radiometric gains are consistent (Figure 98), within 1-2%.

The IR offsets show small variations due to detector and optics temperature variations and these offset variations determine the minimum BTs detectable for channels S8 and S9, which also change with time. Note that each detector and odd/even pixels has different offset values.

The upper limit for brightness temperatures using the S7 channel was previously set to 305 K, and any pixel with a brightness temperature above this was filled with NaN in the Level-1 products. However, a change was made to the L1 processor on 15th January 2020 so that brightness temperatures of up to 311 K are available for the fire radiative power algorithm. Brightness temperatures between 305 and 311 K are not optimally calibrated and so are flagged as invalid_radiance, but since 15th January 2020, they have meaningful values present in the L1 images. The only exception is SLSTR-B in the oblique view, where the flag is only applied above 311 K – this will be fixed in the next processing baseline.

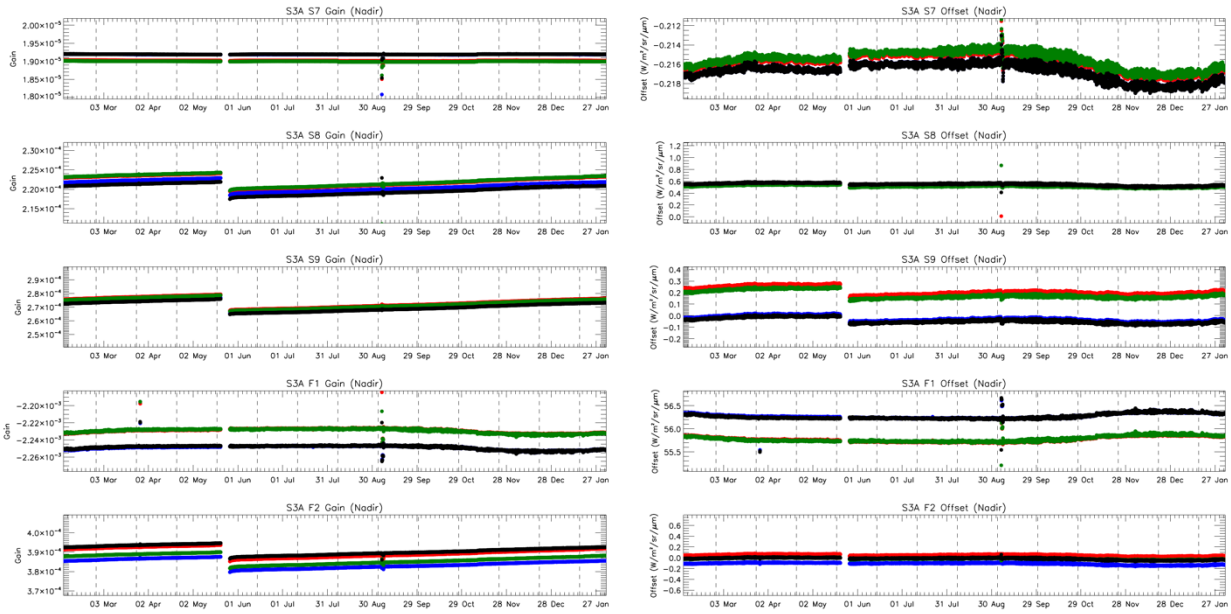

Figure 96: SLSTR-A gain (left) and offset (right) trends for the TIR channels in nadir view. The different colour symbols show the response for each of the detector elements and integrators in the channels. The discontinuities are due to the decontamination (May 2019) and instrument tests (March and September 2019).

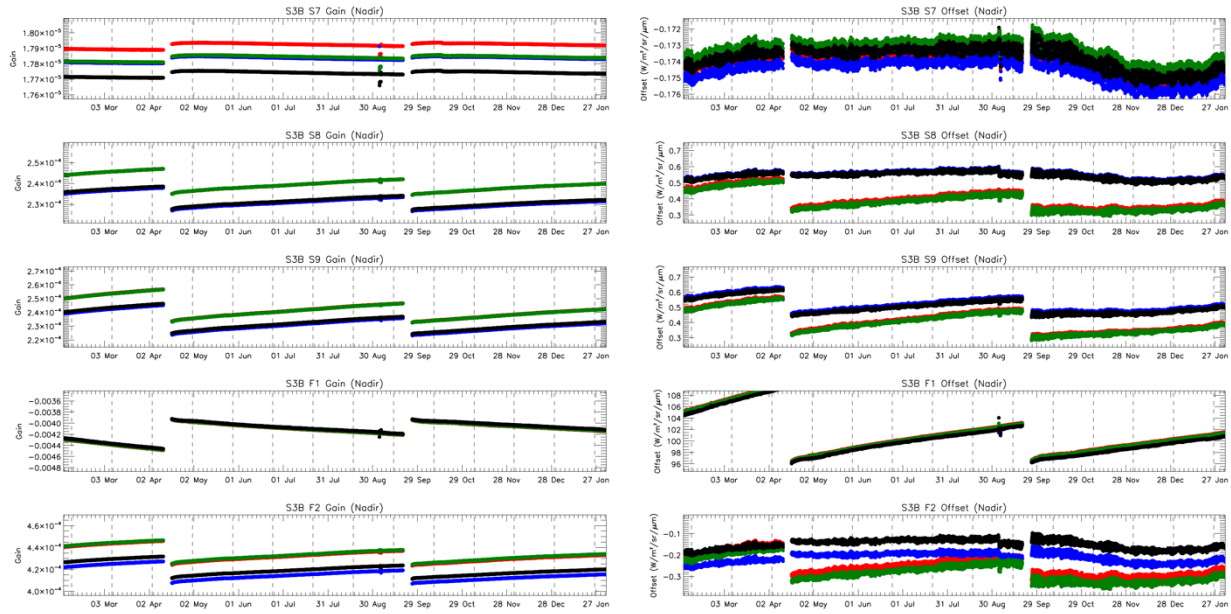

Figure 97: SLSTR-B gain (left) and offset (right) trends for the TIR channels in nadir view. The different colour symbols show the response for each of the detector elements and integrators in the channels. The discontinuities are due to the decontaminations (April and September 2019).

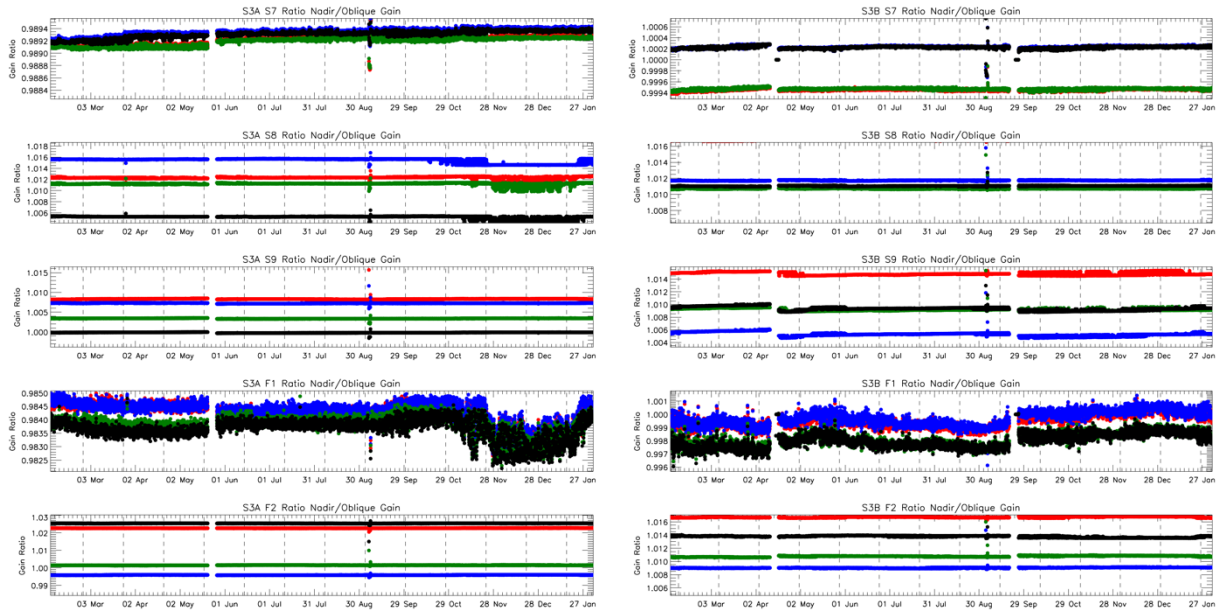

Figure 98: Ratio between nadir and oblique view gains for TIR channels for SLSTR-A (left) and SLSTR-B (right). The different colour symbols show each of the detector elements and integrators in the channels.

6.1.6.2 Radiometric Noise

The thermal channel NEDT values derived from the on-board blackbody sources are consistent with previous operations and within the requirements – see Figure 99 and Table 18 and Table 19. Noise levels haven't changed significantly following the decontaminations. The NEDT levels are roughly consistent between SLSTR-A and SLSTR-B, except for F1, which shows more orbit-to-orbit variation and higher noise values. This may be caused by motional chopping of the F1 detectors, which are known to be close to the edge of the aperture for SLSTR-B.

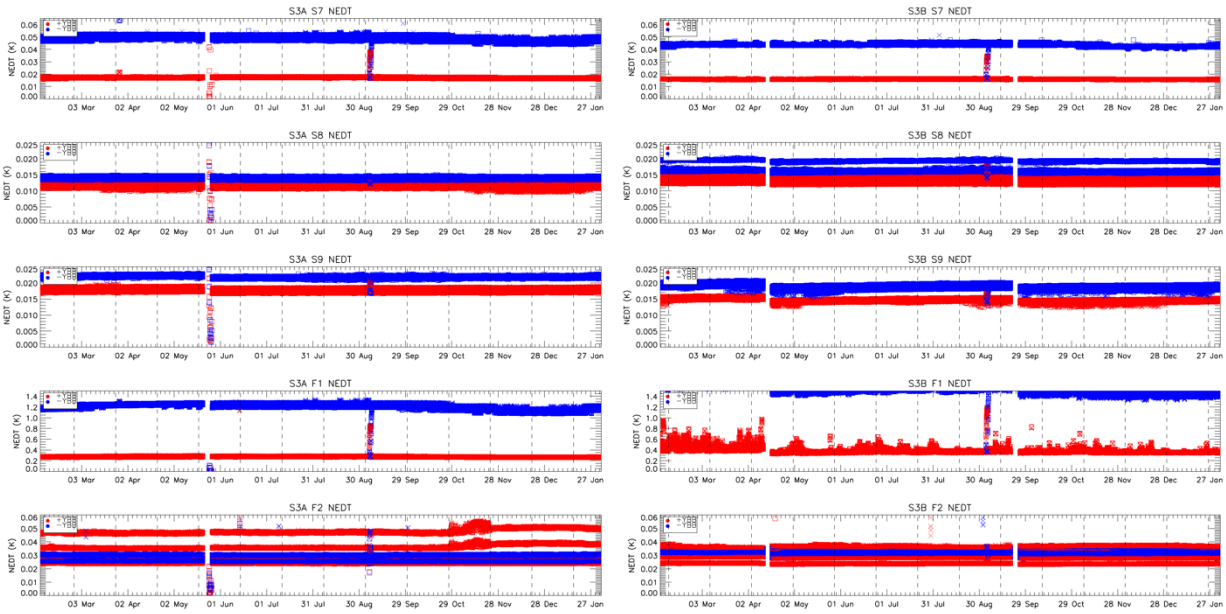

Figure 99: NEDT trend for the thermal channels for SLSTR-A (left) and SLSTR-B (right). Blue points were calculated from the cold blackbody signal and red points from the hot blackbody.

Table 18: NEDT for SLSTR-A in cycles 041-053 averaged over all detectors for both Earth views towards the hot +YBB (top) and the cold -YBB (bottom).

SLSTR-A		Cycle 041	Cycle 042	Cycle 043	Cycle 044	Cycle 045	Cycle 046	Cycle 047	Cycle 048	Cycle 049	Cycle 050	Cycle 051	Cycle 052	Cycle 053
+YBB temp (K)		303.67	303.26	303.04	303.04	302.77	302.67	302.69	302.73	302.93	303.28	303.78	304.06	304.21
NEDT (mK)	S7	17.3	17.3	17.4	17.3	17.6	17.6	17.6	17.6	18.0	17.2	17.1	16.8	16.8
	S8	11.5	11.5	11.5	11.5	11.5	11.4	11.4	11.5	11.5	11.4	11.4	11.2	11.2
	S9	18.0	18.1	18.2	18.2	17.7	17.7	17.7	17.8	17.9	17.8	17.9	17.8	17.9
	F1	272	275	279	281	280	281	282	281	296	273	271	266	265
	F2	34.0	33.8	33.7	33.7	33.7	33.9	33.9	33.9	33.6	33.8	35.2	35.5	35.7

SLSTR-A		Cycle 041	Cycle 042	Cycle 043	Cycle 044	Cycle 045	Cycle 046	Cycle 047	Cycle 048	Cycle 049	Cycle 050	Cycle 051	Cycle 052	Cycle 053
-YBB temp (K)		266.27	265.77	265.60	265.77	265.50	265.35	265.29	265.23	265.43	265.81	266.48	266.86	266.94
NEDT (mK)	S7	48.8	50.1	50.4	50.4	50.5	49.9	49.9	49.8	48.5	49.3	48.2	47.0	46.6
	S8	14.2	14.3	14.3	14.3	14.1	14.2	14.1	14.1	14.0	14.1	14.1	14.0	14.0
	S9	22.0	22.2	22.3	22.4	21.6	21.7	21.7	21.8	21.7	21.9	21.9	21.9	21.9
	F1	1176	1223	1245	1253	1230	1233	1235	1234	1192	1212	1171	1134	1121
	F2	28.1	28.3	28.3	28.4	27.9	28.0	28.0	28.0	28.2	28.1	28.0	28.1	28.1

Table 19: NEDT for SLSTR-B in cycles 022-034 averaged over all detectors for both Earth views towards the hot +YBB (top) and the cold -YBB (bottom)

SLSTR-B		Cycle 022	Cycle 023	Cycle 024	Cycle 025	Cycle 026	Cycle 027	Cycle 028	Cycle 029	Cycle 030	Cycle 031	Cycle 032	Cycle 033	Cycle 034
+YBB temp (K)		303.55	303.22	303.08	303.09	302.97	302.91	302.91	302.97	303.17	303.41	303.96	304.33	304.33
NEDT (mK)	S7	16.1	16.0	16.0	16.0	16.2	16.3	16.2	16.8	16.0	16.0	15.9	15.7	15.7
	S8	13.4	13.4	13.1	12.9	13.0	13.1	13.2	13.3	12.9	12.8	12.9	12.9	12.9
	S9	15.2	15.3	14.5	14.3	14.4	14.6	14.7	14.9	14.3	14.1	14.2	14.3	14.5
	F1	474	436	400	366	378	390	379	403	376	372	370	364	357
	F2	30.1	29.8	30.0	30.0	30.0	30.0	29.9	29.8	29.9	30.0	30.2	30.2	30.1

SLSTR-B		Cycle 022	Cycle 023	Cycle 024	Cycle 025	Cycle 026	Cycle 027	Cycle 028	Cycle 029	Cycle 030	Cycle 031	Cycle 032	Cycle 033	Cycle 034
-YBB temp (K)		265.65	265.26	265.10	265.21	265.11	265.00	264.93	264.92	265.11	265.51	266.25	266.68	266.61
NEDT (mK)	S7	43.9	44.0	43.8	43.9	43.9	44.5	44.8	43.5	44.4	44.0	42.8	42.4	42.4
	S8	17.2	17.2	16.9	16.8	16.8	16.9	17.0	16.9	16.8	16.7	16.7	16.7	16.8
	S9	19.4	19.6	18.6	18.2	18.4	18.6	18.8	18.8	18.3	18.1	18.2	18.3	18.4
	F1	2048	1870	1754	1574	1615	1675	1633	1584	1618	1573	1538	1513	1481
	F2	31.5	31.6	31.0	30.7	30.7	30.9	31.1	31.1	30.7	30.5	30.5	30.6	30.7

6.1.7 VIS/SWIR Channels

6.1.7.1 Radiometric gain variation SLSTR-A

Overall the S1-S6 channels are functioning well with no reported loss of data or digital resolution.

The main issue affecting the S1-S3 channels are oscillations in the radiometric response due to the build-up of ice on the optical path within the FPA. This is illustrated in Figure 100, which shows the variation of the radiometric gain derived from the VISCAL signals. These oscillations were observed for the corresponding channels on ATSR-2 and AATSR. Periodic decontamination of the IR FPA is necessary to remove the water ice contamination.

The trends of the radiometric gain variation clearly show where the decontamination took place, and that the signal was reset afterwards. During the decontamination, only the VIS channels are operating and the SWIR channels are switched off, causing a gap in the trends due to the loss of data.

The radiometric responses of S4-S6 appear to be more stable and not affected by the build-up of water ice contamination, Figure 101. There is a seasonal cycle of the response of ±1% that could be caused by variations in the solar zenith angle on the diffuser or partial vignetting of the Sun's disc by the VISCAL baffle.

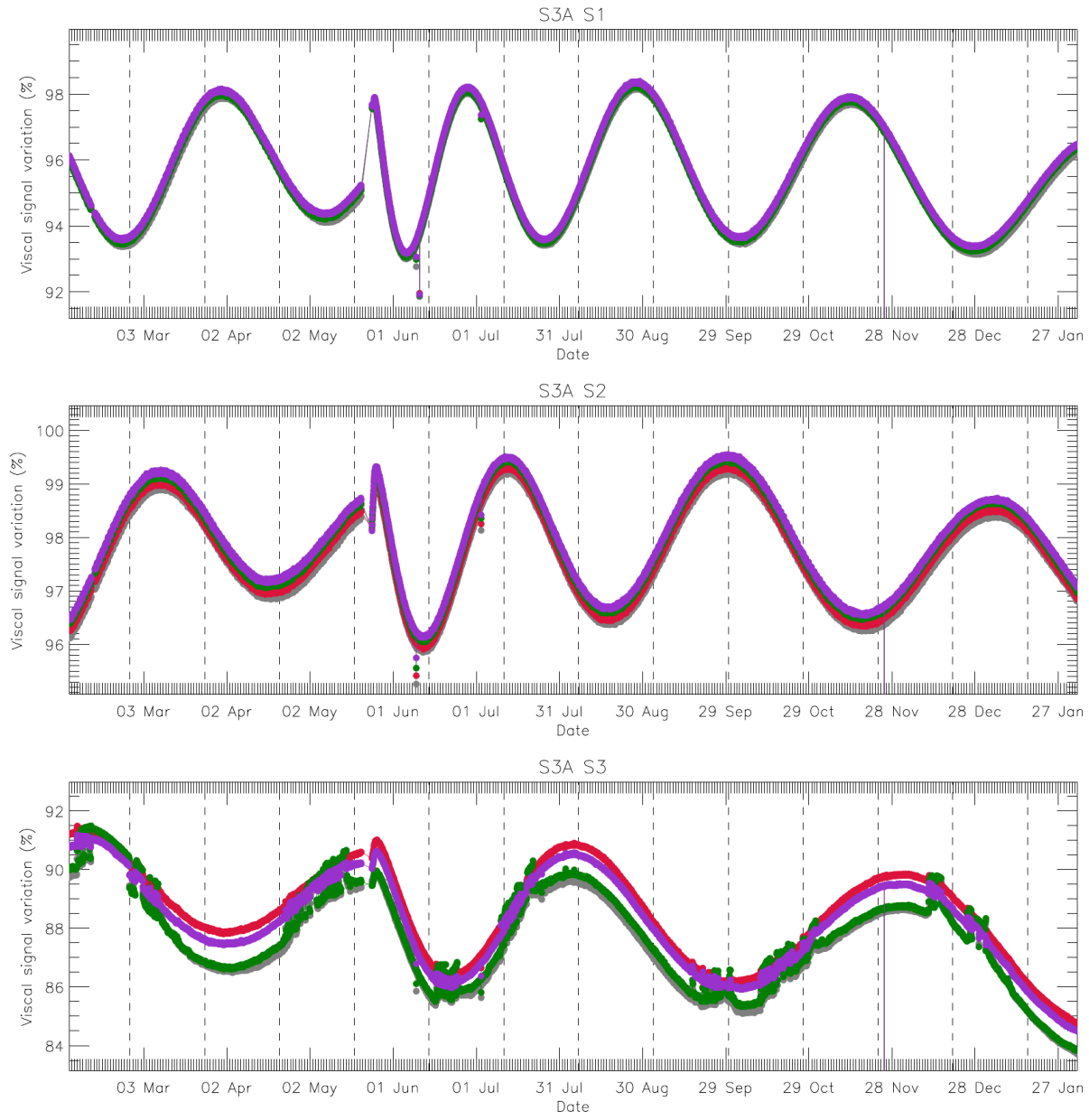

Figure 100: Gain trend for VIS channels (nadir view) for SLSTR-A. The data have been adjusted to allow for the variation of the solar intensity. The oscillations in the signal are due to the build-up of a thin condensation layer causing a thin film interference effect. The different colour symbols show the response for each of the 4 detector elements in the VIS channels.

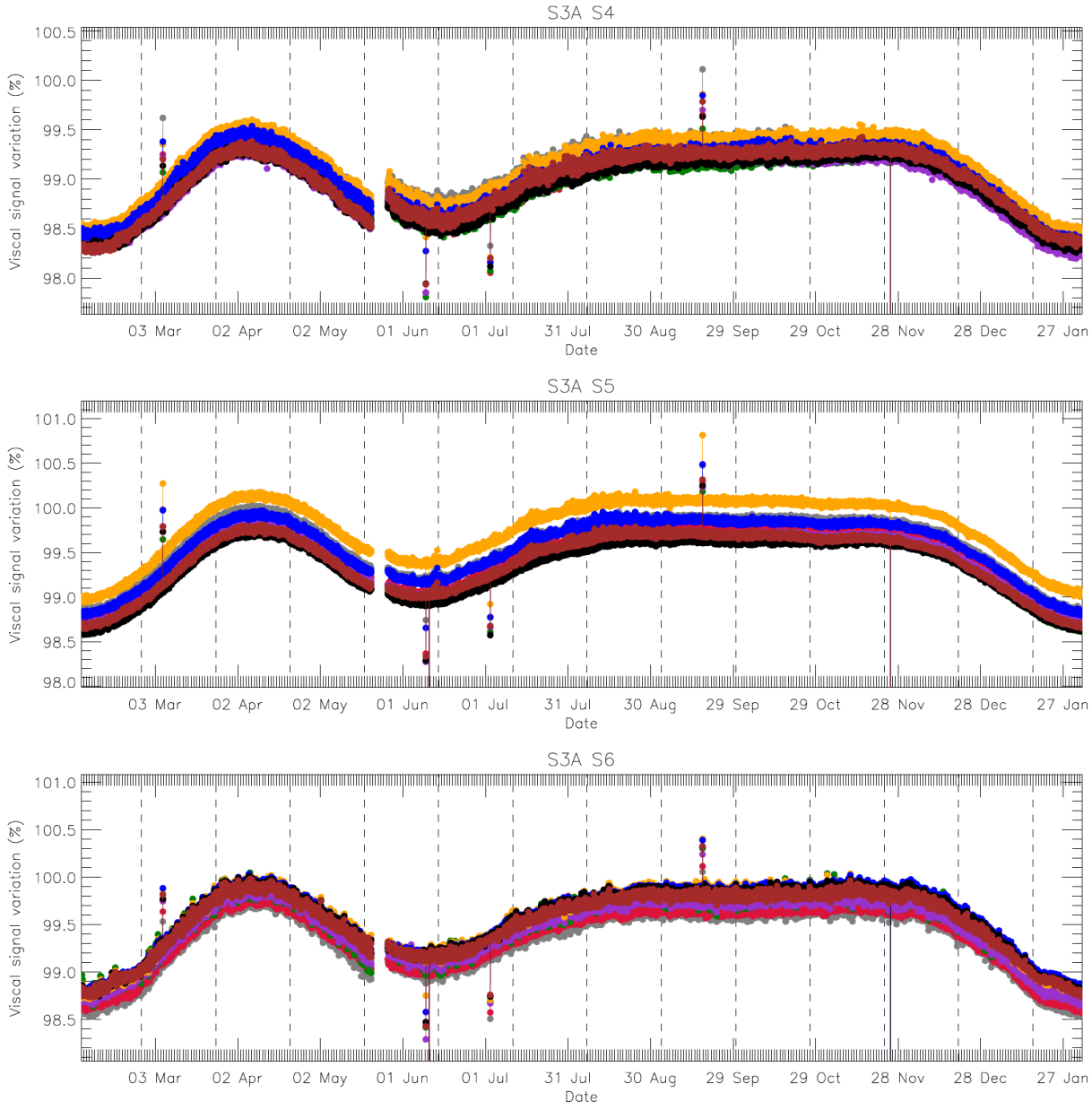

Figure 101: Gain trend for SWIR channels (nadir view) for SLSTR-A. Outliers in the plots are due to gaps in L0 data or decontamination cycles. The different colour symbols show the response for each of the 8 detector elements of the A and B stripes of the SWIR channels.

.

6.1.7.2 Radiometric gain variation SLSTR-B

As in SLSTR-A, one of the main issues affecting the S1-S3 channels are oscillations in the radiometric response due to the build-up of ice on the optical path within the FPA. However, there is also a problem with S1 and S2 in particular, which show noisy behaviour and numerous drops in signal as shown in Figure 102. This gives 2-3% errors in the radiometric calibration of these channels. The effect has been the subject of a major NCR led by ESA-ESTEC. A number of candidate root causes have been identified, with the most likely due to motional chopping of the VIS detectors by an internal aperture in the VIS optical bench. Because the effect appears to be random it is most likely affecting all the data for S1 and S2.

The radiometric responses of S4-S6 appear to be more stable and not affected by the build-up of water ice contamination, Figure 103.

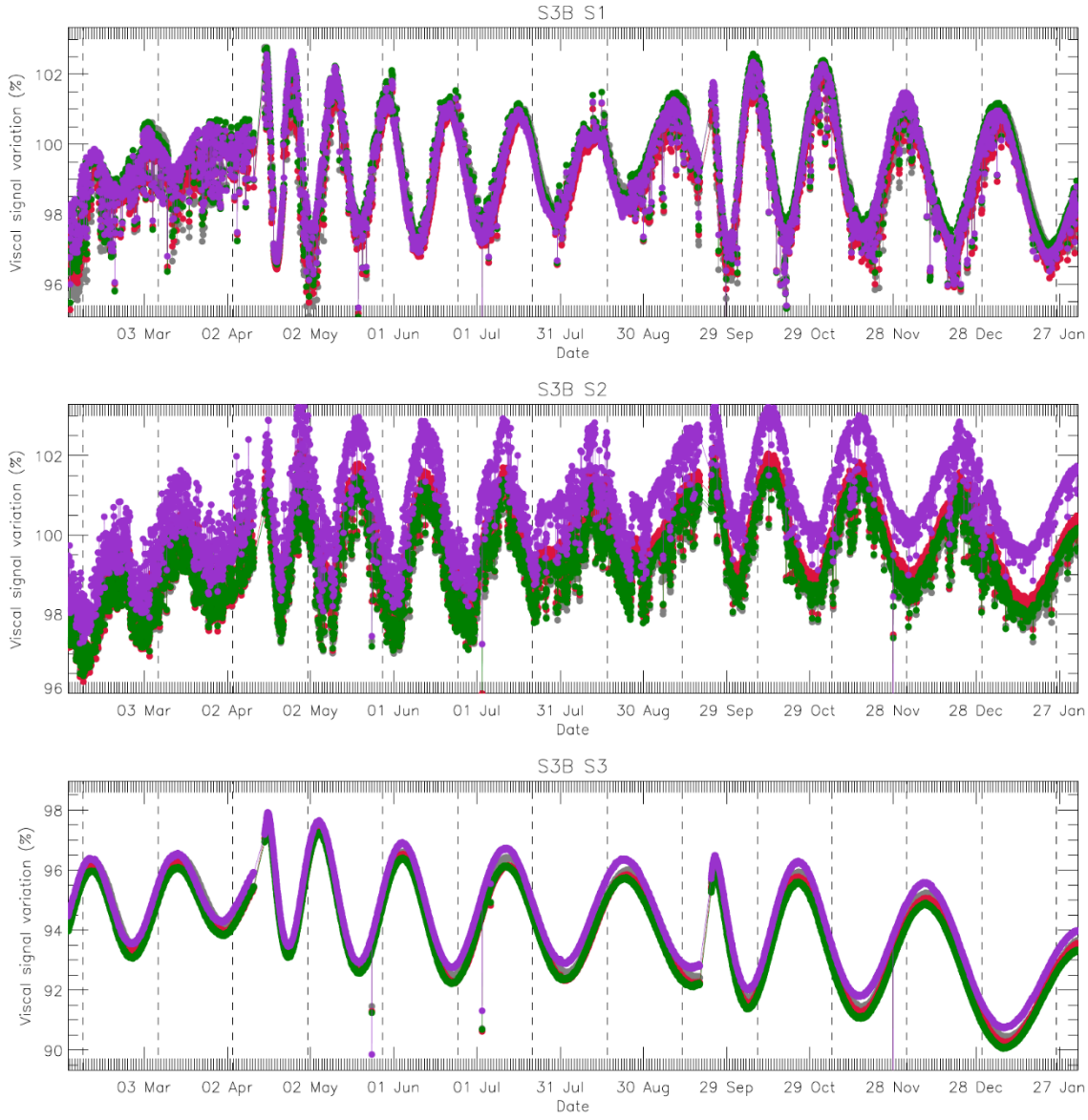

Figure 102: Gain trend for VIS channels (nadir view) for SLSTR-B. The data have been adjusted to allow for the variation of the solar intensity. The oscillations in the signal are due to the build-up of a thin condensation layer

causing a thin film interference effect. The different colour symbols show the response for each of the 4 detector elements in the VIS channels.

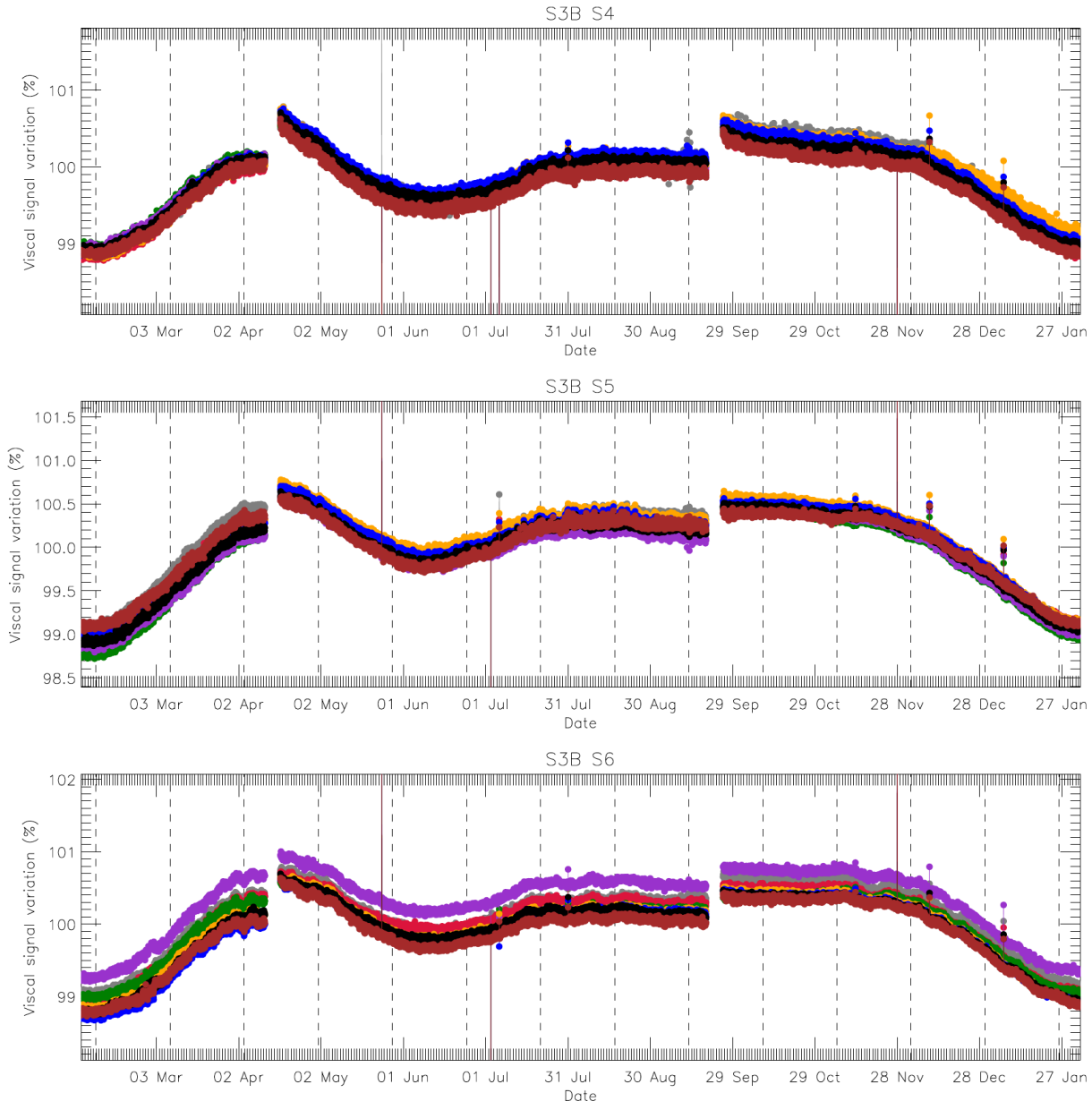

Figure 103: Gain trend for SWIR channels (nadir view) for SLSTR-B. Outliers in the plots are due to gaps in L0 data or decontamination cycles. The different colour symbols show the response for each of the 8 detector elements of the A and B stripes of the SWIR channels.

6.1.7.3 Dark signal variation SLSTR-A

The dark signal variation derived from the nadir blackbody signals for the VIS and SWIR channels is stable – see Figure 104 and Figure 105.

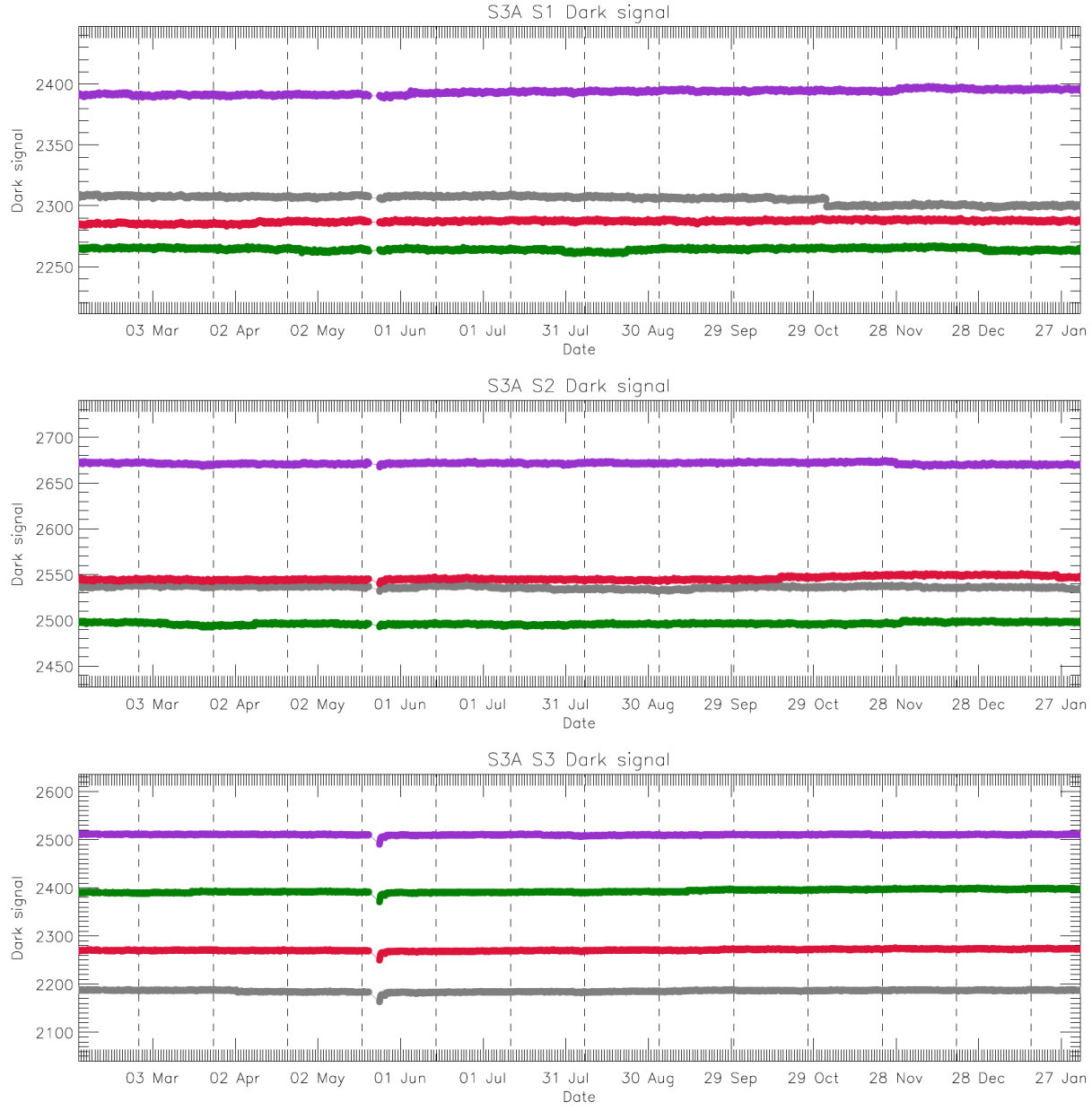

Figure 104: Dark signal trend for VIS channels (nadir view) for SLSTR-A. The different colour symbols show the signal for each of the 4 detector elements in the VIS channels. The gap in May is due to the decontamination.

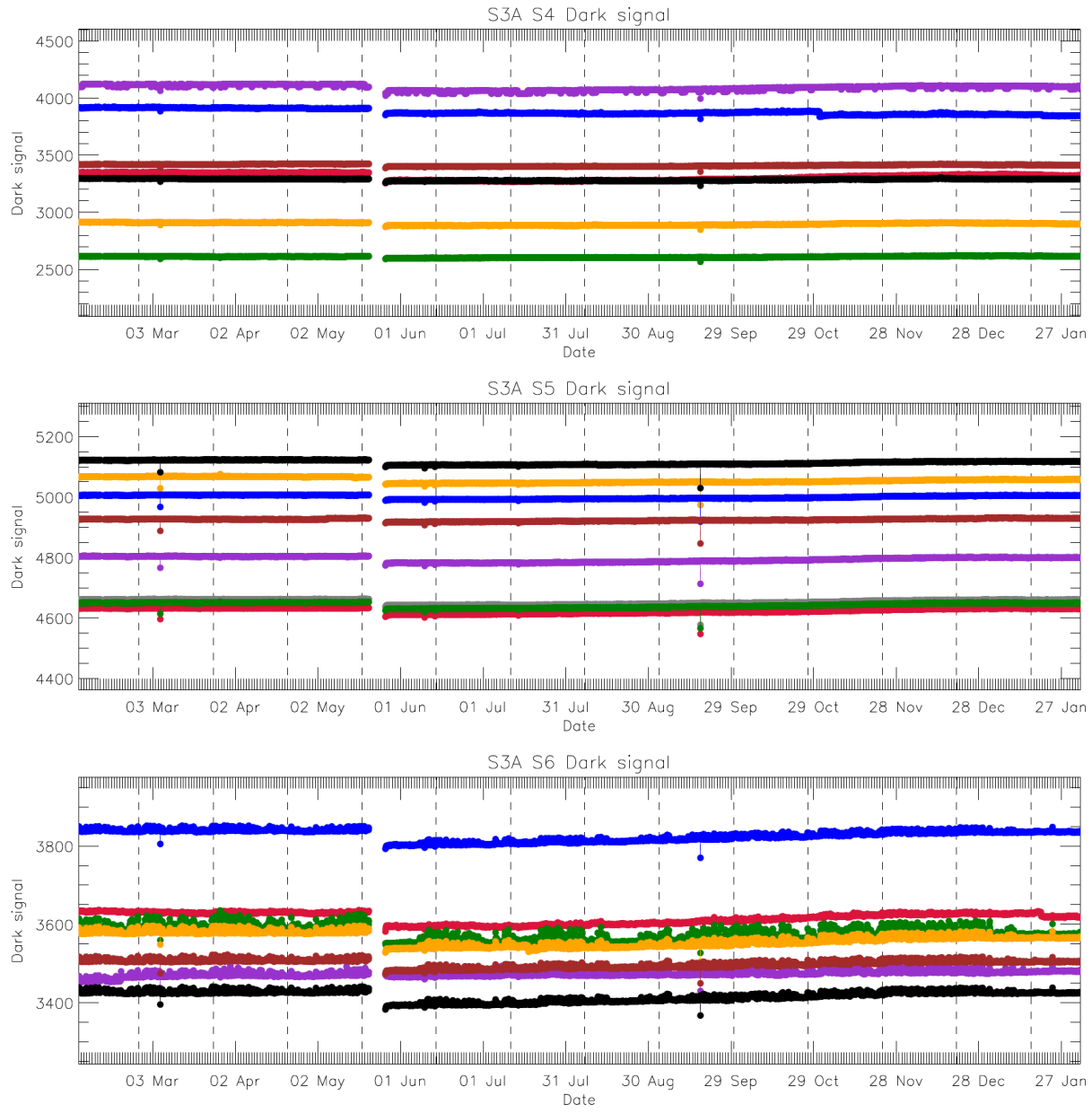

Figure 105: Dark signal trend for SWIR channels (nadir view) for SLSTR-A. The different colour symbols show the signal for each of the 8 detector elements of the A and B stripes of the SWIR channels. The gap in May is due to the decontamination.

6.1.7.4 Dark signal variation SLSTR-B

The dark signal variation derived from the nadir blackbody signals for the VIS and SWIR channels is stable for SLSTR-B (Figure 106).

The dark signal measured by the SWIR channels is stable and presents a gap at the end of September due to the loss of data during the decontamination (Figure 107).

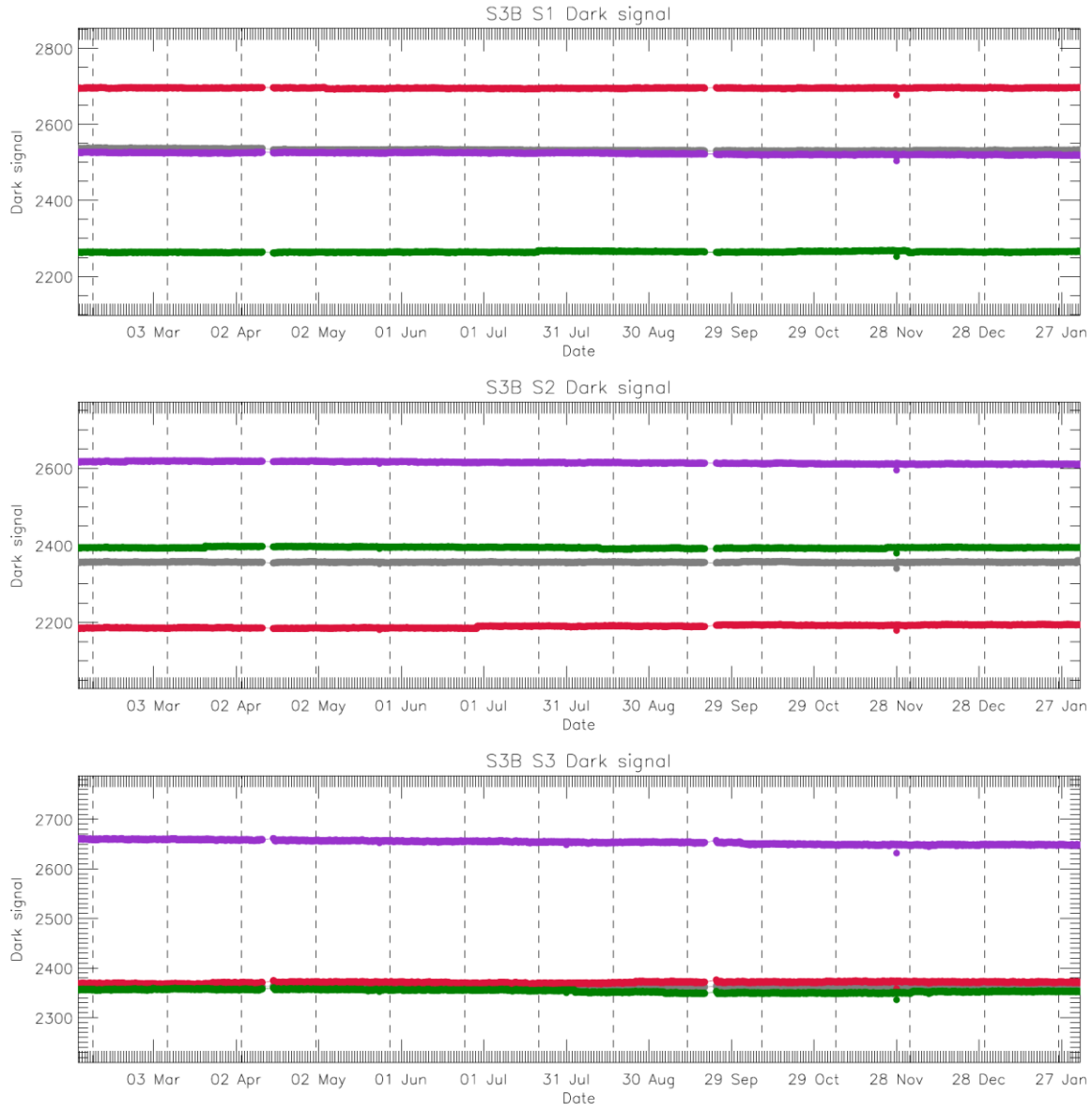

Figure 106: Dark signal trend for VIS channels (nadir view) for SLSTR-B. The different colour symbols show the signal for each of the 4 detector elements in the VIS channels.

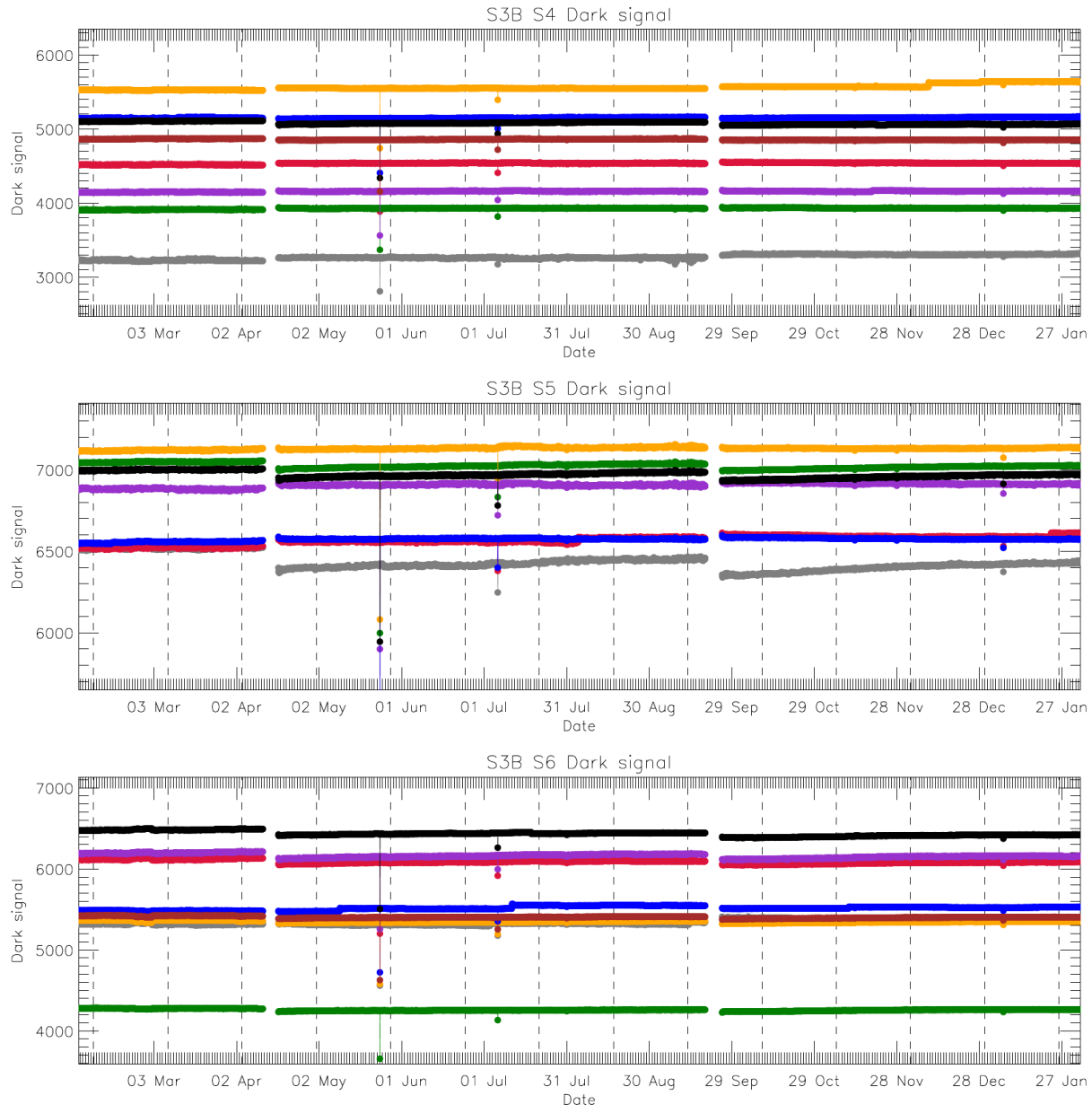

Figure 107: Dark signal trend for SWIR channels (nadir view) for SLSTR-B. The different colour symbols show the signal for each of the 8 detector elements in the SWIR channels.

6.1.7.5 Radiometric noise for SLSTR-A

The VIS/SWIR channel signal-to-noise ratio is derived from the VISCAL signal at full solar illumination. The measurements show that the SNR is stable and consistent over the year and largely unaffected by anomalies and decontamination.

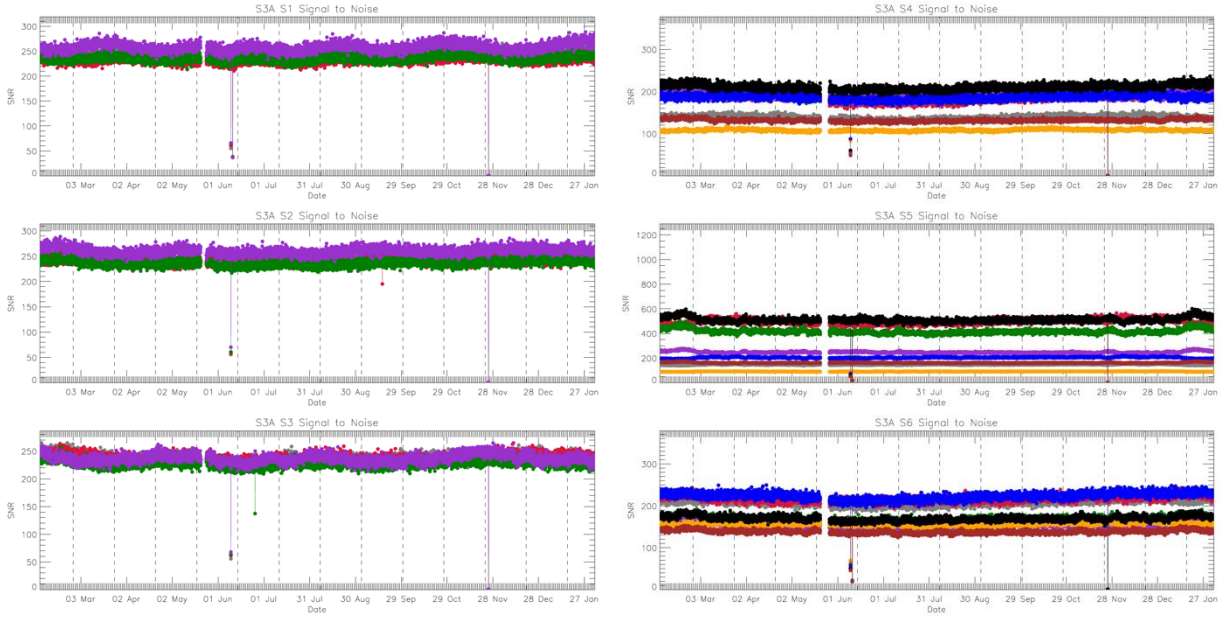

Figure 108: SLSTR-A VIS and SWIR channel signal-to-noise. Different colours indicate different detectors.

6.1.7.6 Radiometric noise for SLSTR-B

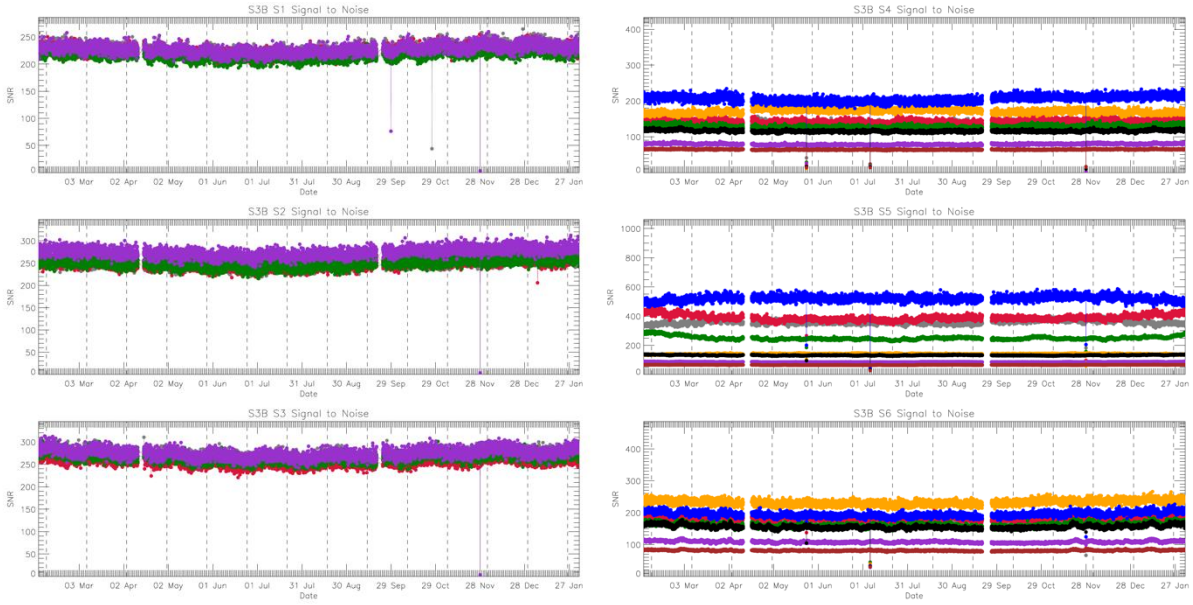

Figure 109: SLSTR-B VIS and SWIR channel signal-to-noise. Different colours indicate different detectors.

6.1.7.7 Contamination

The monitoring of the VISCAL signal shows that the performance of the VIS and the SWIR channels has been affected by the build-up of a condensation layer on the FPA. The build-up of condensation on the optics was expected since similar patterns were observed previously in AATSR and ATSR-2.

The periodic pattern observed in the VISCAL signals depends on the rate of build-up of the condensation layer and the wavelength of the channel. So, an estimation of the layer thickness can be obtained from the oscillations in the visible channels signal that occurred at x= $\lambda/2$, λ, $3\lambda/2$, etc.

The growth of the ice layer is slow and decontamination activities are performed only once or twice per year. The rate of growth of the ice layer has reduced significantly with respect to that observed after the first cool down. It is expected that the rate of build-up will decrease with time resulting in longer periods between decontamination cycles.

Figure 110 shows the growth of the condensation layer on the SLSTR-A and SLSTR-B FPA.

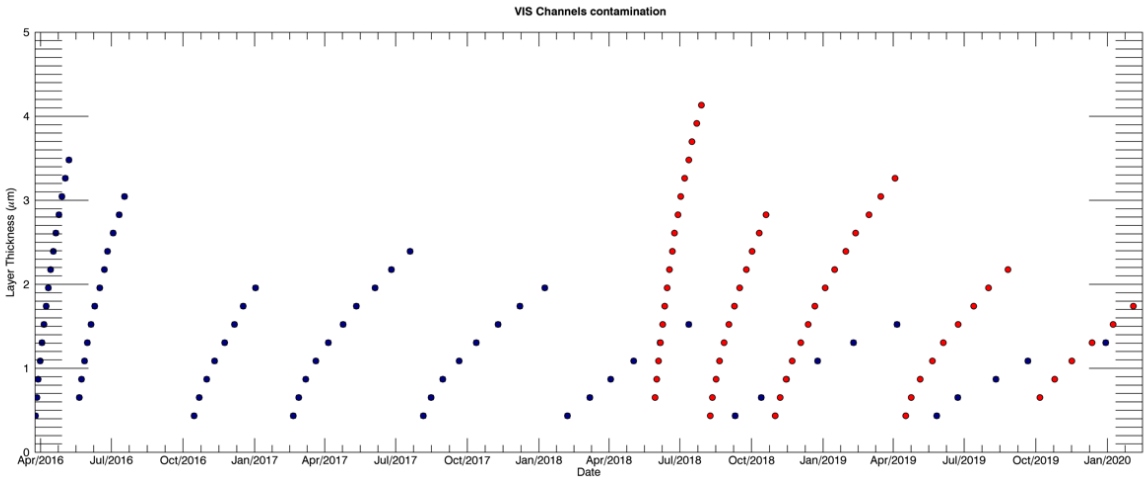

Figure 110 Condensation layer thickness throughout the mission for SLSTR-A (blue) and SLSTR-B (red)

6.2 L1 products performances

6.2.1 TIR Channel Calibration

6.2.1.1 SLSTR comparisons with IASI

The absolute radiometric calibration of the IR channels is being validated by EUMETSAT using comparisons against IASI-A and B (Tomazic et al 2018). Comparisons were performed during the commissioning phases for SLSTR-A and SLSTR-B. Currently there are no updates since 2018. The mission requirement is that the absolute radiometric calibration should be accurate to 0.2 K traceable to ITS-90, and that at a minimum this should be met in the temperature range between the two blackbodies.

The latest results have not changed since the previous annual report – i.e. from Tomazic et al (2018). These results confirmed very good performance with almost no bias (<0.1 K) for channels S8 and S9 in the nadir view over the temperature range 220 – 280 K.

6.2.2 VIS/SWIR Channel Calibration

Vicarious calibration methods are used to verify the radiometric calibration of the SLSTR visible (VIS) and shortwave infrared (SWIR) channels, and currently two methods are used.

1. Inter-comparisons of SLSTR with similar sensors such as OLCI, AATSR and MODIS using stable desert targets.

2. Compare SLSTR observed radiances over scenes containing sun-glint against the predicted top-of-atmosphere radiances computed radiative transfer models.

Both approaches provide consistent results. Table 20 and Table 21 show the relative differences obtained with the different calibration methods.

For analysis over desert sites we have used the extractions provided by the S3ETRAC tool, which contain the sensor reflectance values, cloud fraction, geometric and meteorological information needed for the analysis. For analysis over sun-glint regions we have used L1 products directly rather than the S3ETRAC analysis as the latter only contains a single value, and the analysis requires the full image context to model the sunglint.

6.2.2.1 Inter-comparisons of SLSTR over desert sites

The analysis performed follows the methodology used for the comparisons of AATSR with MERIS and MODIS-A (see Smith and Cox 2013). The analysis needs to take into consideration a number of effects:

- Temporal differences: in particular, direct comparisons of SLSTR with AATSR or MERIS are not possible because the latter are no longer operating. Also, sensors such as MODIS-A do not observe the site at the same time. So, to perform the comparisons we compare for the same view/solar geometry assuming that the site is stable over long timescales.

- Spectral differences: although SLSTR and OLCI have common spectral bands, the spectral responses are not exactly the same, which can give rise to differences in spectral reflectance of a few percent if not accounted for. Hence, we need to account for differences in atmospheric transmission and surface spectral reflectance.
- Geometric differences: although the method attempts to perform the comparisons with the same view/solar geometry, an exact match is not always possible. To account for this, we construct a basic geometric model from the reference sensor to interpolate to the correct geometry.

The data are extracted by S3ETRAC tool over a series of pre-defined sites. These sites have been selected for their appropriate optical properties to validate the radiometry of optical sensors. Table 20 shows the desert sites and their geographical limits used for the assessment and monitoring of the VIS and SWIR radiometric calibration.

Table 20: The list of these sites and their geographical limits

Site	North Latitude	South Latitude	East Longitude	West Longitude
CEOS_ALGERIA-3	30.82	29.82	8.16	7.16
CEOS_ALGERIA-5	31.52	30.52	2.73	1.73
CEOS_LIBYA-1	24.92	23.92	13.85	12.85
CEOS_LIBYA-4	29.05	28.05	23.89	22.89
CEOS_MAURITANIA-1	19.9	18.9	-8.8	-9.8
CEOS_MAURITANIA-2	21.35	20.35	-8.28	-9.28
RAL_Algeria-1	24.3	23.3	0.1	-0.9
RAL_Algeria-2	26.59	25.59	-0.88	-1.88
RAL_Algeria-4	30.54	29.54	6.09	5.09
RAL_Arabia-1	19.38	18.38	47.26	46.26
RAL_Arabia-2	20.63	19.63	51.46	50.46
RAL_Arabia-3	29.42	28.42	44.23	43.23
RAL_Sundan-1	22.24	21.24	28.72	27.72
RAL_Niger-1	20.17	19.17	10.31	9.31
RAL_Niger-2	21.87	20.87	11.09	10.09
RAL_Niger-3	22.07	21.07	8.46	7.46
RAL_Egypt-1	27.62	26.62	26.6	25.6
RAL_Libya-2	25.55	24.55	20.98	19.98
RAL_Libya-3	23.65	22.65	23.6	22.6
RAL_Mali-1	19.62	18.62	-4.35	-5.35

6.2.2.1.1 Results of inter-comparisons of SLSTR-A over desert sites

Figure 111 shows the combined results for all the desert sites when SLSTR-A is compared with AATSR in nadir view, for the VIS and S5 channels.

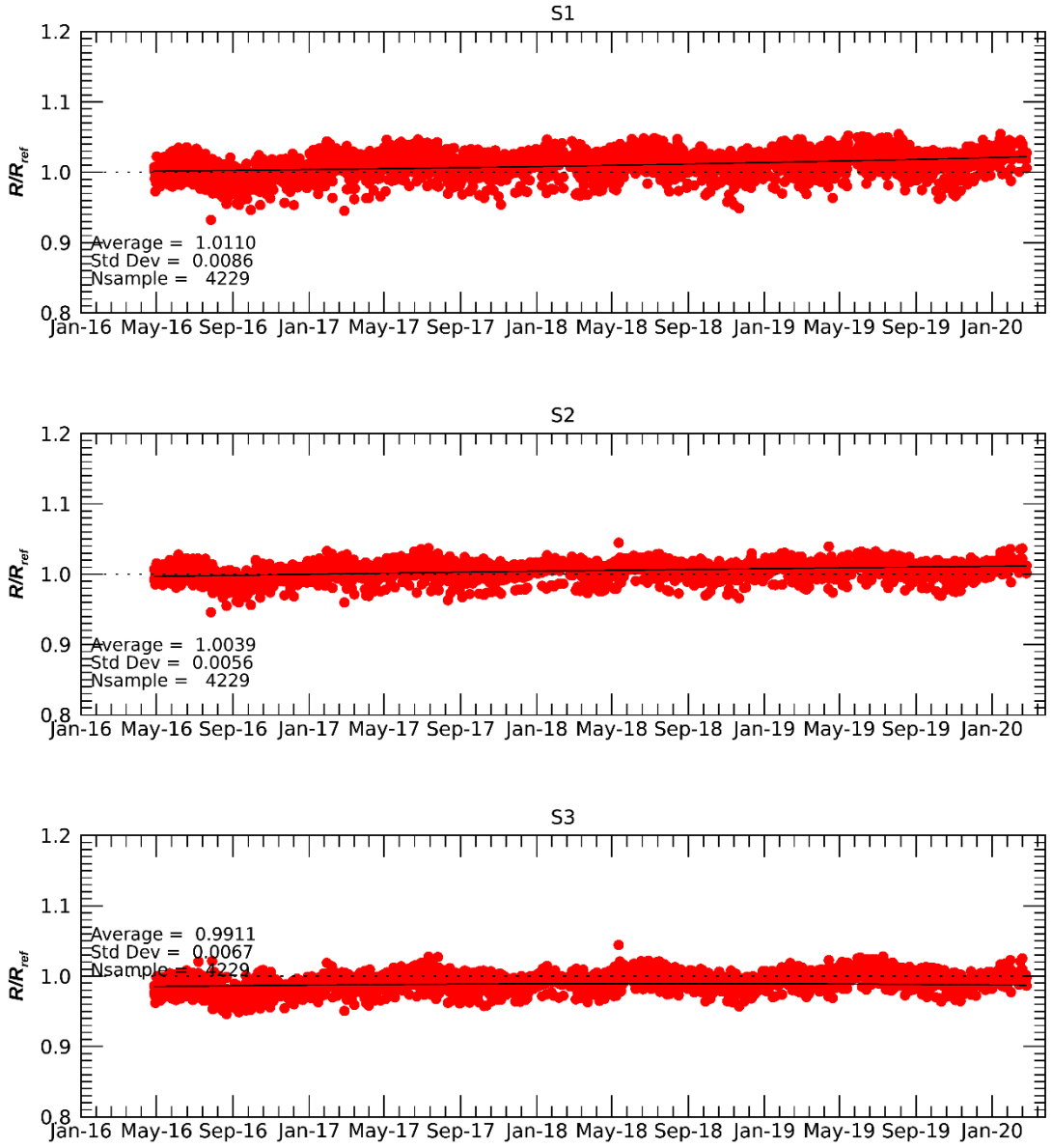

Figure 112

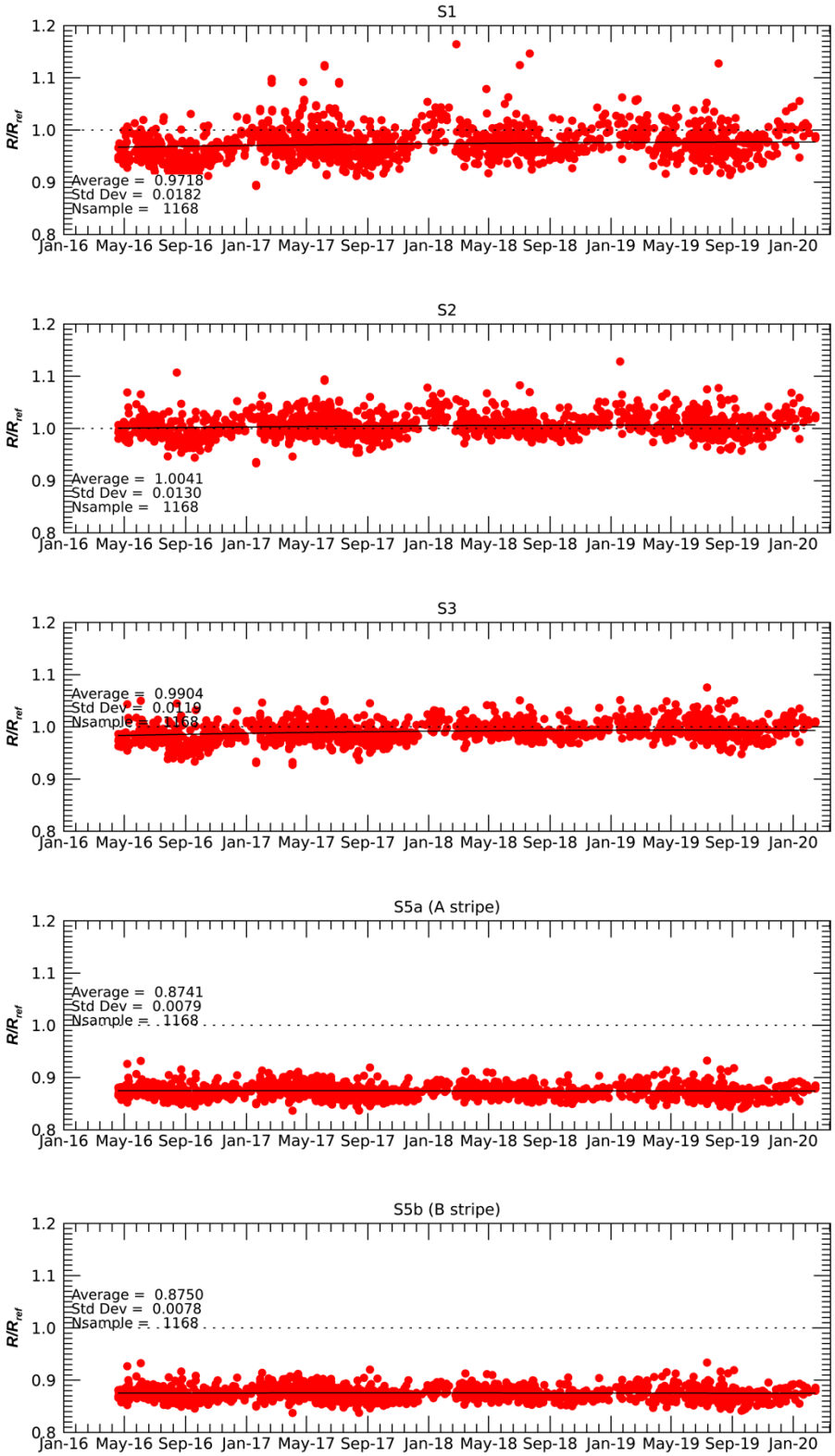

Figure 111: Comparisons of SLSTR-A S1-S3 and S5a and S5b channels vs. the corresponding channels for AATSR over desert sites.

Figure 112 shows comparisons between SLSTR-A and OLCI visible channels, and Figure 113 shows inter-comparisons between SLSTR-A and MODIS for the VIS and the SWIR channels.

Overall the calibration of SLSTR-A is very stable over the mission lifetime. However, there does appear to be a small drift of ~1% in channel S3.

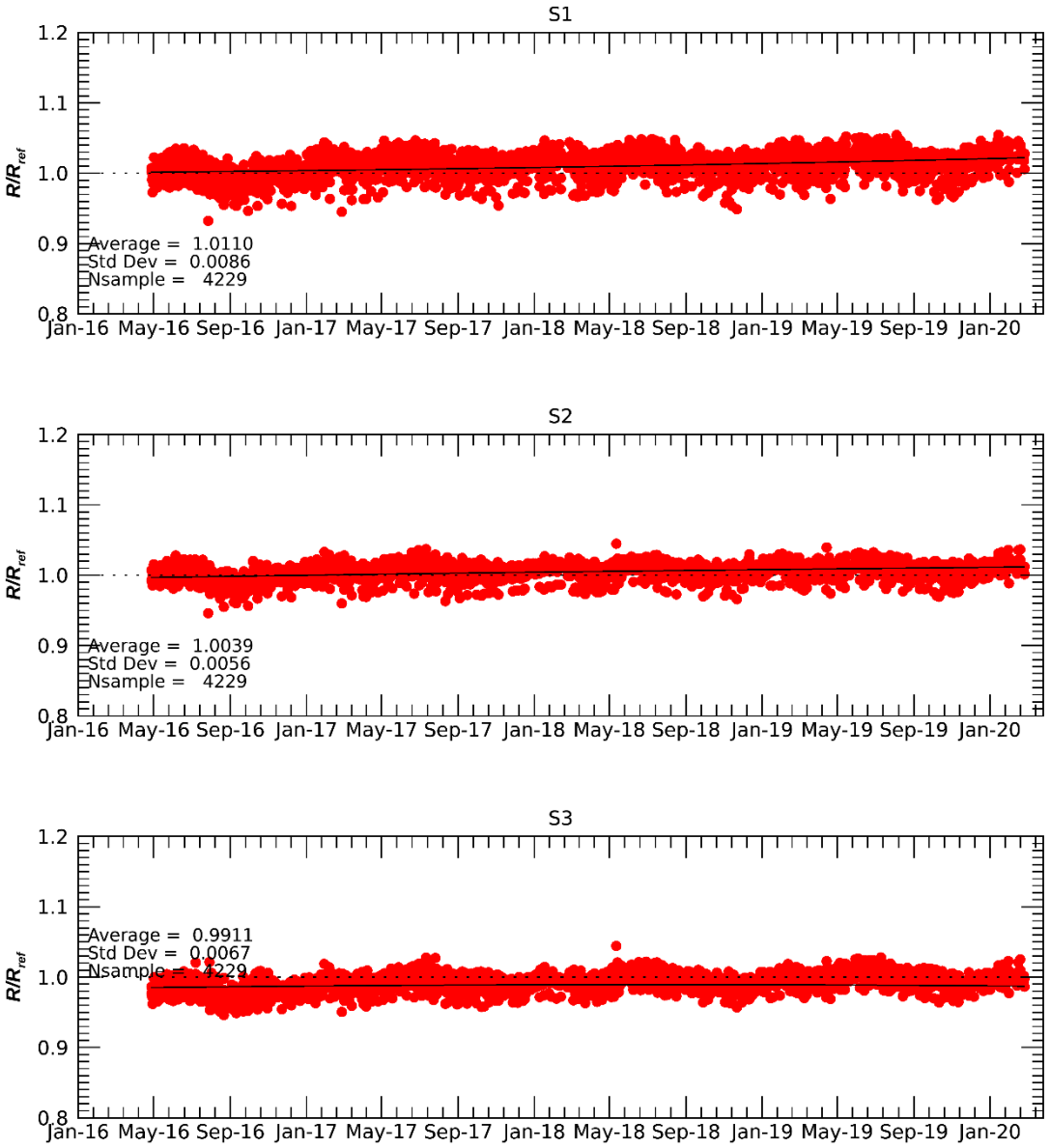

Figure 112: Inter-comparisons between SLSTR-A and OLCI VIS channels for all desert sites in nadir view.

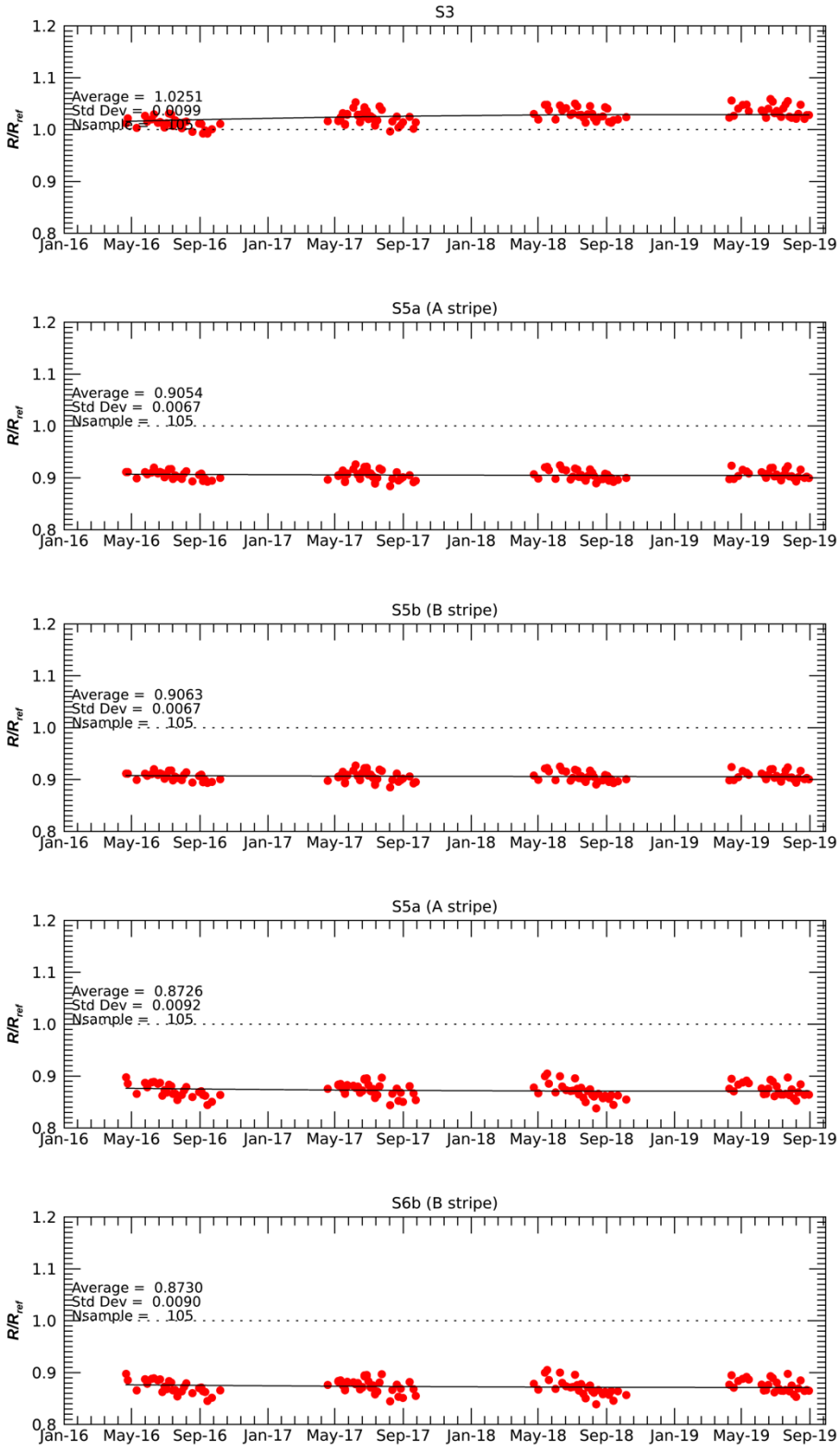

Figure 113: Inter-comparisons between SLSTR-A and MODIS NIR and SWIR channels for the Libia-4 site in nadir view.

While comparisons between SLSTR-A and OLCI show a good agreement for the visible channels with differences of less than 1%, the measured radiances by the SWIR channels are ~12% lower than those observed by MODIS and AATSR over deserts, respectively. A summary of the results is presented in Table 21.

Currently, the inter-comparisons between SLSTR-A and other sensors can only be performed in nadir view, since the SLSTR-A and the other sensors' oblique viewing geometry is not equivalent. Radiative transfer models over sun-glints can be used in order to analyse the SLSTR radiometric calibration in oblique view.

6.2.2.1.2 Results of Inter-comparisons of SLSTR-B over desert sites

Figure 114 shows the combined results for all the desert sites when SLSTR-B is compared with AATSR in nadir view, for the VIS and S5 channels. Figure 115 shows comparisons between SLSTR-B and OLCI visible channels, and Figure 116 shows inter-comparisons between SLSTR-B and MODIS for the VIS and the SWIR channels.

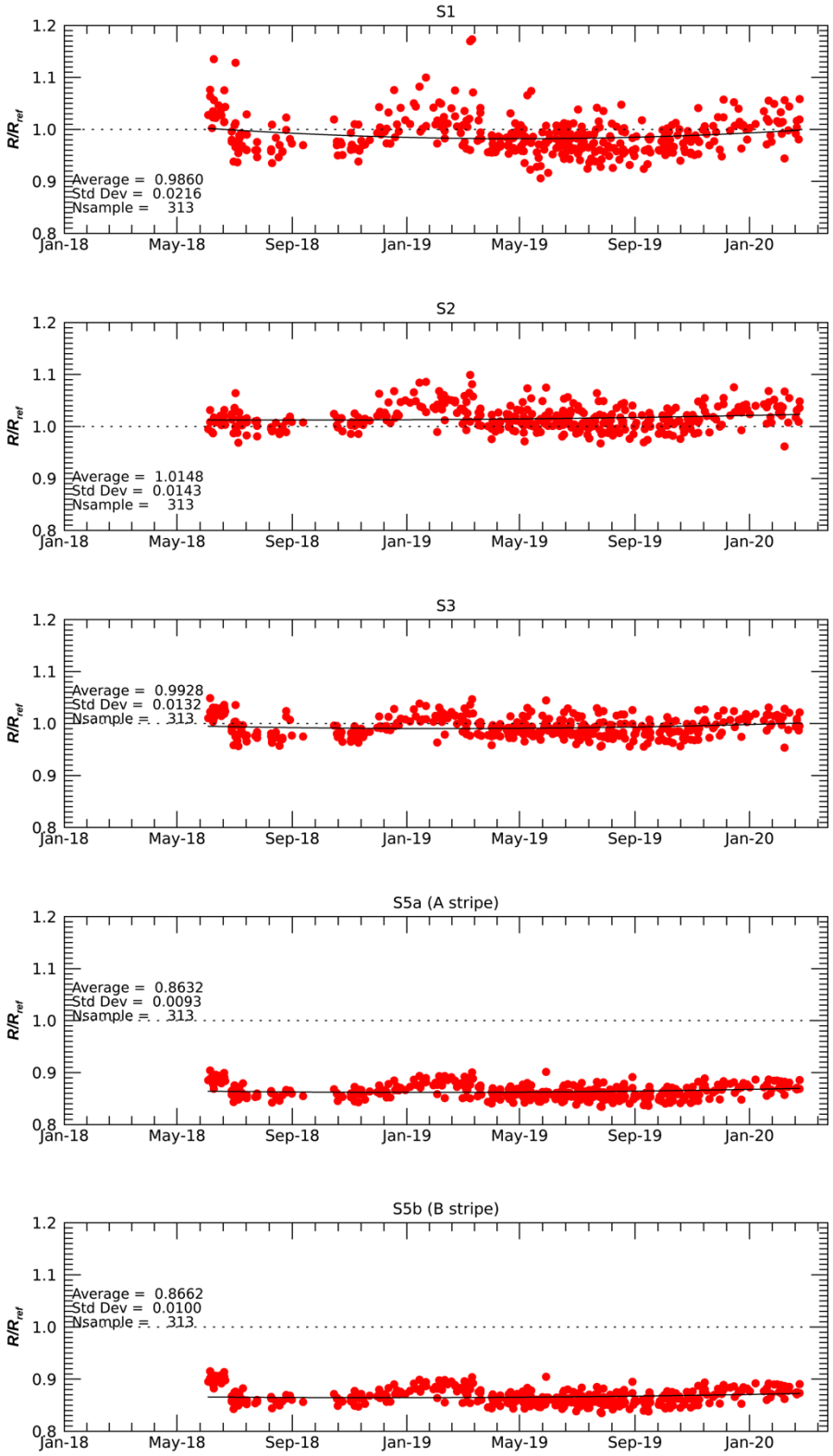

Figure 114: Comparisons of SLSTR-B S1-S3 and S5a and S5b channels vs. the corresponding channels for AATSR over desert sites.

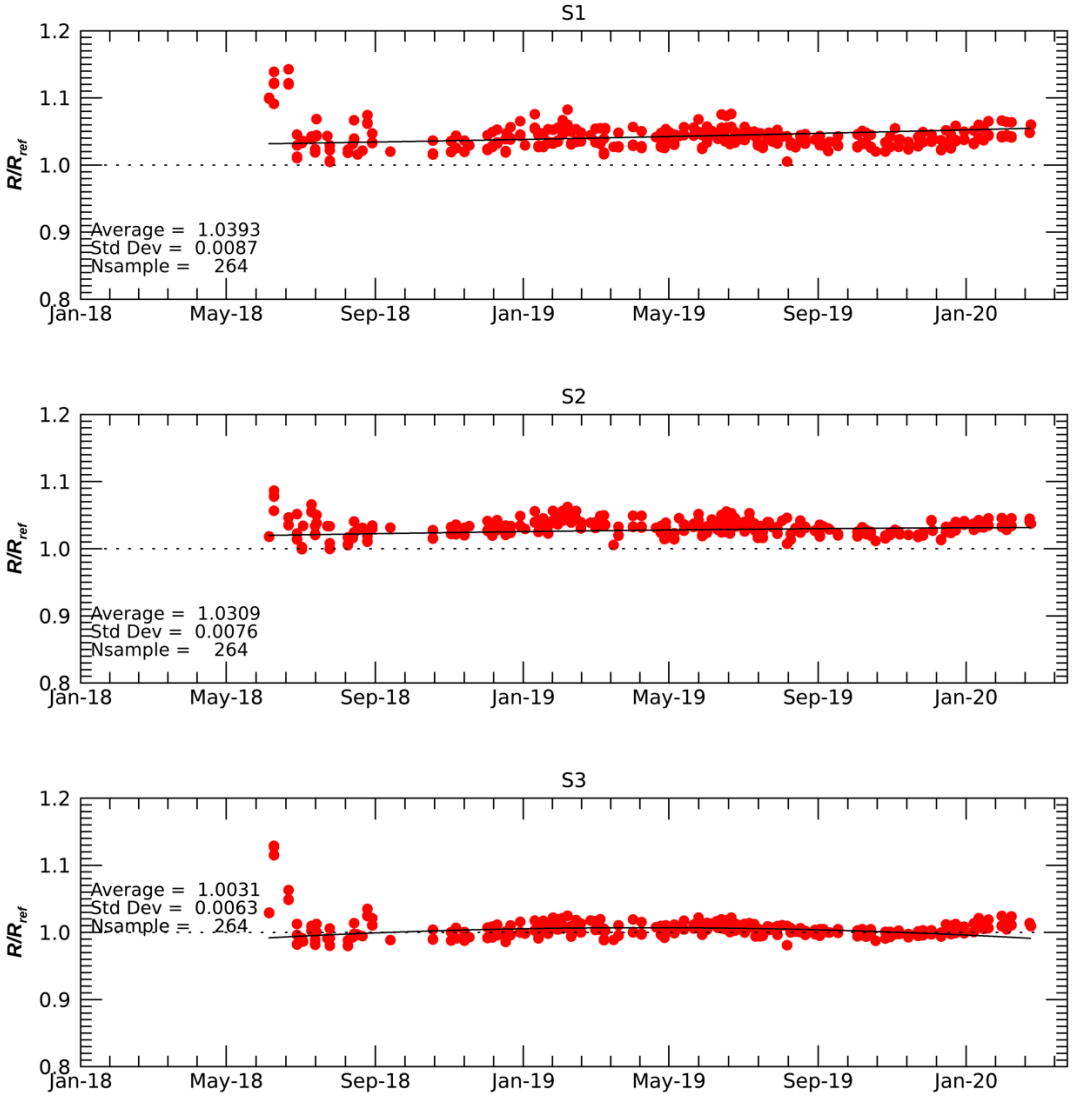

Figure 115: Inter-comparisons between SLSTR-B and OLCI VIS channels for all desert sites in nadir view.

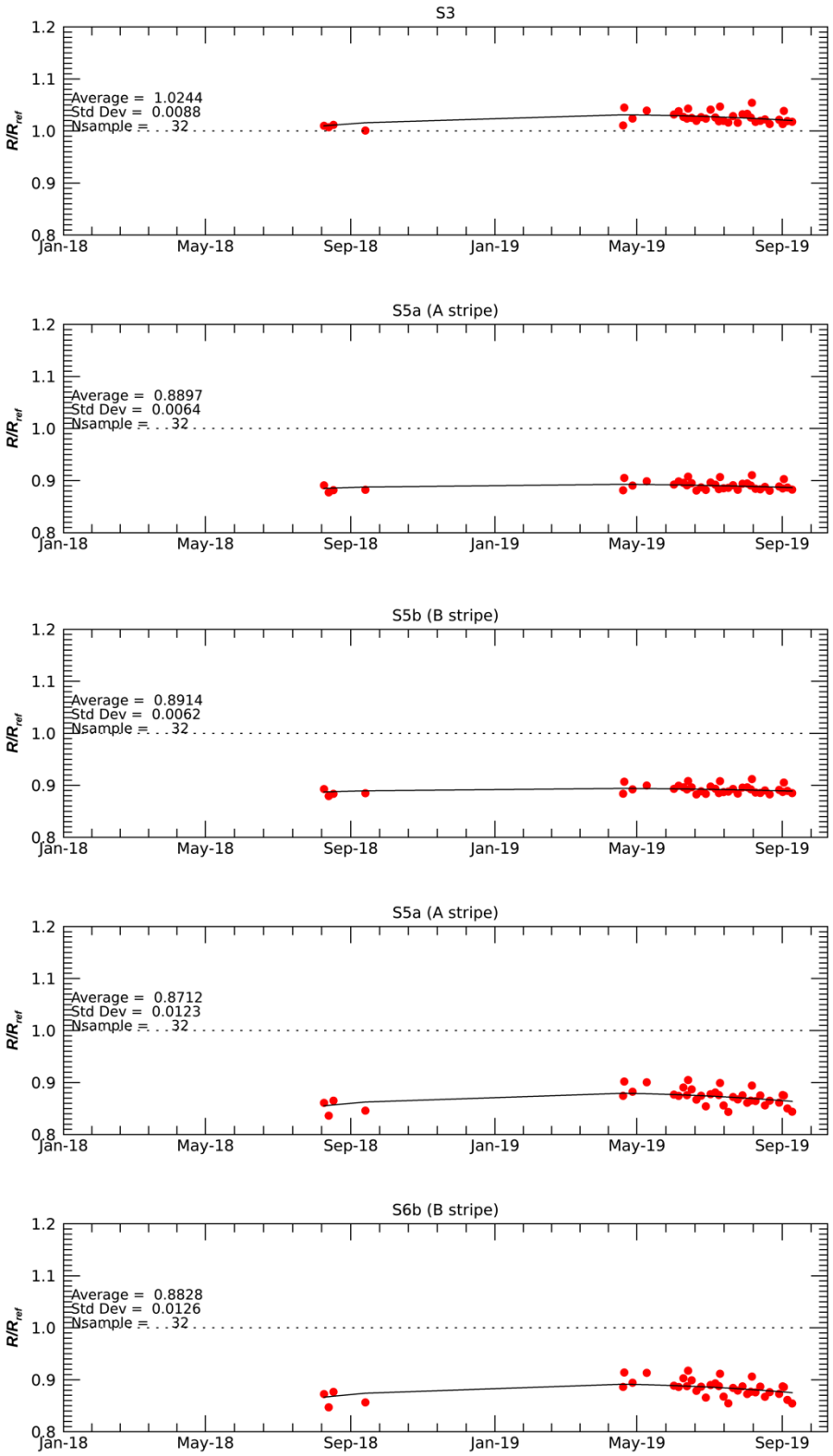

Figure 116: Inter-comparisons between SLSTR-B and MODIS VIS and SWIR channels for the Libia-4 site in nadir view.

Comparisons between SLSTR-B and AATSR show a good agreement for the visible channels with differences of less than 1%. However, comparisons between SLSTR-B and OLCI-B show that the measured radiances by the channels S1 and S2 are ~3.5% larger than those measured by OLCI-B.

For the SWIR channels, the measured radiances are ~12% and ~12% lower than those observed by MODIS and AATSR over deserts, respectively, showing good agreement between SLSTR-A and SLSTR-B at the SWIR channels. A summary of the results is presented in Table 22.

6.2.2.2 Inter-band calibration with radiative transfer models

The sun glint calibration method is an inter-band calibration procedure that uses the specular reflection of the sun on the ocean surface to transfer the absolute calibration of one reference spectral band to other spectral bands, from visible to shortwave infrared wavelengths.

The radiative transfer code was developed based on the Oxford-RAL Aerosols and Clouds (ORAC) retrieval algorithm and on the approach of Cox and Munk (1954). The model accounts for contributions to the observed reflectance from whitecaps, sun-glint and under-light over the Pacific Ocean. Level-1 products contain all the inputs needed for the modelling, except the aerosol optical depth, which are taken from AERONET observations.

This calibration method is a relative calibration of the SWIR channels with respect to the VIS channels. Therefore, only the SWIR channels models are shown in Figure 117 and Figure 118.

The relative difference of the measured radiances from the model for SLSTR-A is -9% and -15% for S5 and S6 in nadir view. The results are similar to the relative differences measured by MODIS and AATSR over deserts.

In the Pacific Ocean, sun-glints in the SLSTR oblique view occur only during three months between the middle of April and the end of August. Hence, only three months of oblique view data have been processed. At the beginning of 2019, the radiative transfer tool was updated to model actual values of methane abundance. The results indicate that the SLSTR-A measured radiances in oblique view for S6 are 1% lower than the predicted.

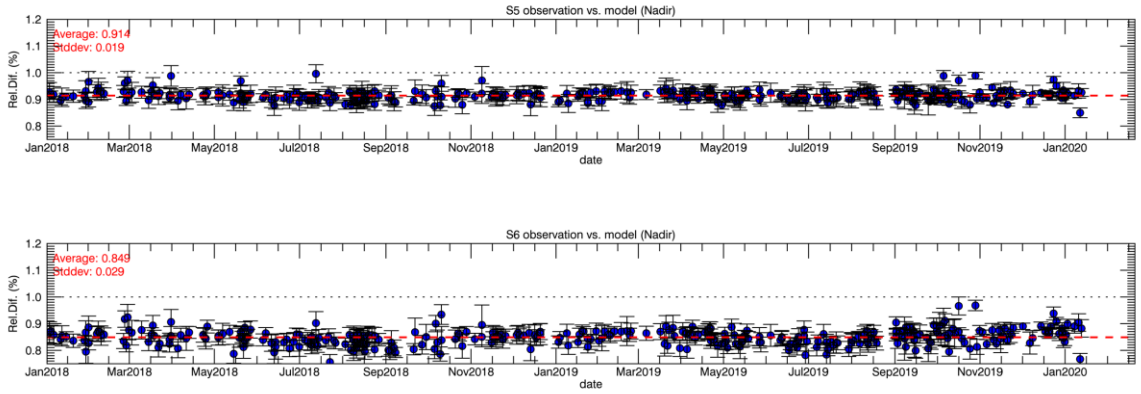

Figure 117: SLSTR-A measured radiance with respect to the computed radiance over sun-glints using radiative transfer models for the Nadir view.

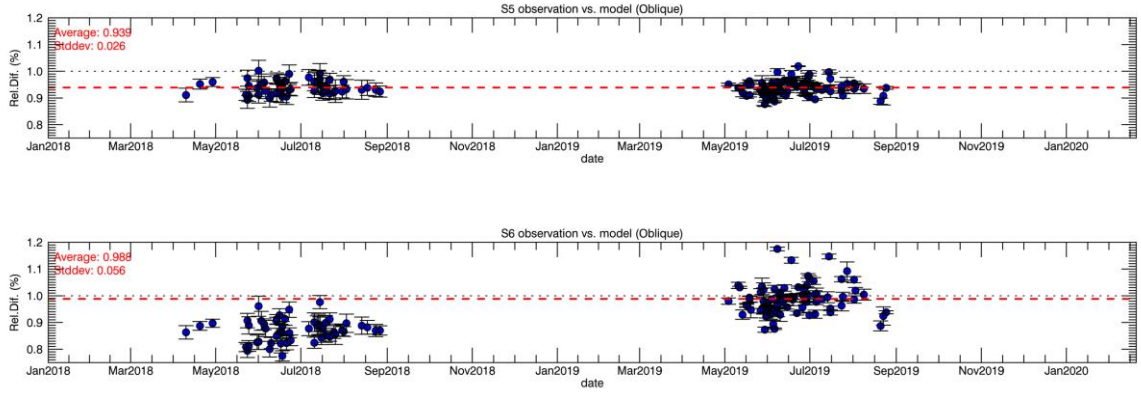

Figure 118: SLSTR-A measured radiance with respect to the computed radiance over sun-glints using radiative transfer models for the Oblique view.

6.2.2.3 Combined Results

The goal of the vicarious calibration analyses is to determine the offsets of SLSTR to a common reference that can be traced to a primary standard, and to implement these in the IPF.

In addition to the analysis performed by the MPC, independent studies by different groups have also been conducted to assess the post launch calibration of these channels. We have compared the results the analyses performed by RAL Space using comparisons with AATSR and MODIS-A over desert sites, CNES using the SADE/MUSCLE vicarious calibration system over desert sites, Rayference using a Radiative Transfer Model of the Libya-4 site, and the University of Arizona's comparisons against in-situ field measurements of the Railroad Valley Playa RadCalNet site.

The comparisons performed by RAL and CNES have been made against other satellite sensors where there are known differences that need to be accounted for. For example, previous analyses of AATSR found

systematic offsets compared to MERIS of approximately 1.03 for channels S1-S3. So, for instance, where AATSR is used as the reference for SLSTR channels S1-S3, the results are adjusted to MERIS by applying the corresponding difference reported in the literature. The analysis performed by Rayference and University of Arizona are independent of any satellite measurements and so no adjustment is needed.

For the reported uncertainties we attempt to combine the information provided using the Guide to expression of Uncertainties in Measurement (GUM). Uncertainties in the calibration factors are based on those reported by the different teams and are the best estimate at the time of writing.

Results presented in Table 21 and Figure 119 show good agreement within the reported uncertainties. We do not attempt to state which method is closest to the true value since all methods are relative to a different reference.

Table 21: Summary of Vicarious Radiometric Calibration Results performed by all groups. Comparisons are performed by comparing the measured reflectance vs. reference reflectance. Results presented here are the ratios R_{meas}/R_{ref}.

Nadir View

Method	S1		S2		S3		S5		S6	
	Rmeas/Rref	Uncert	Rmeas/Rref	Uncert	Rmeas/Rref	Uncert	Rmeas/Rref	Uncert	Rmeas/Rref	Uncert
MPC (RAL)	-	-	1.02	0.04	1.02	0.04	0.89	0.04	0.88	0.03
CNES	1.02	0.05	1.02	0.05	1.01	0.04	0.89	0.03	0.89	0.04
RTM (Rayference)	1.05	0.03	1.03	0.03	1.02	0.03	0.90	0.03	0.90	0.03
RailRoad Valley	1.02	0.04	1.02	0.04	1.02	0.04	0.92	0.04	0.88	0.04
Median	**1.02**		**1.02**		**1.02**		**0.90**		**0.89**	
Average	**1.03**	**0.03**	**1.02**	**0.02**	**1.02**	**0.02**	**0.90**	**0.02**	**0.89**	**0.02**
Weighted Average	**1.03**	**0.03**	**1.02**	**0.02**	**1.02**	**0.02**	**0.90**	**0.02**	**0.89**	**0.02**

Oblique View

Method	S1		S2		S3		S5		S6	
	Rmeas/Rref	Uncert	Rmeas/Rref	Uncert	Rmeas/Rref	Uncert	Rmeas/Rref	Uncert	Rmeas/Rref	Uncert
MPC (RAL)	-	-	1.04	0.04	1.06	0.04	0.95	0.04	-	-
CNES	1.03	0.06	1.04	0.07	1.04	0.05	0.95	0.06	0.89	0.08
RTM (Rayference)	1.09	0.03	1.07	0.03	1.07	0.03	0.99	0.03	0.96	0.03
RailRoad Valley	-	-	-	-	-	-	--	-	-	-
Median	**1.09**		**1.04**		**1.06**		**0.95**		**0.96**	
Average	**1.06**	**0.06**	**1.05**	**0.04**	**1.06**	**0.03**	**0.96**	**0.03**	**0.92**	**0.07**
Weighted Average	**1.07**	**0.05**	**1.05**	**0.03**	**1.06**	**0.03**	**0.97**	**0.03**	**0.94**	**0.05**

Note: Uncertainty estimates are based on the reported uncertainties at k=1 and do not necessarily account for all effects.

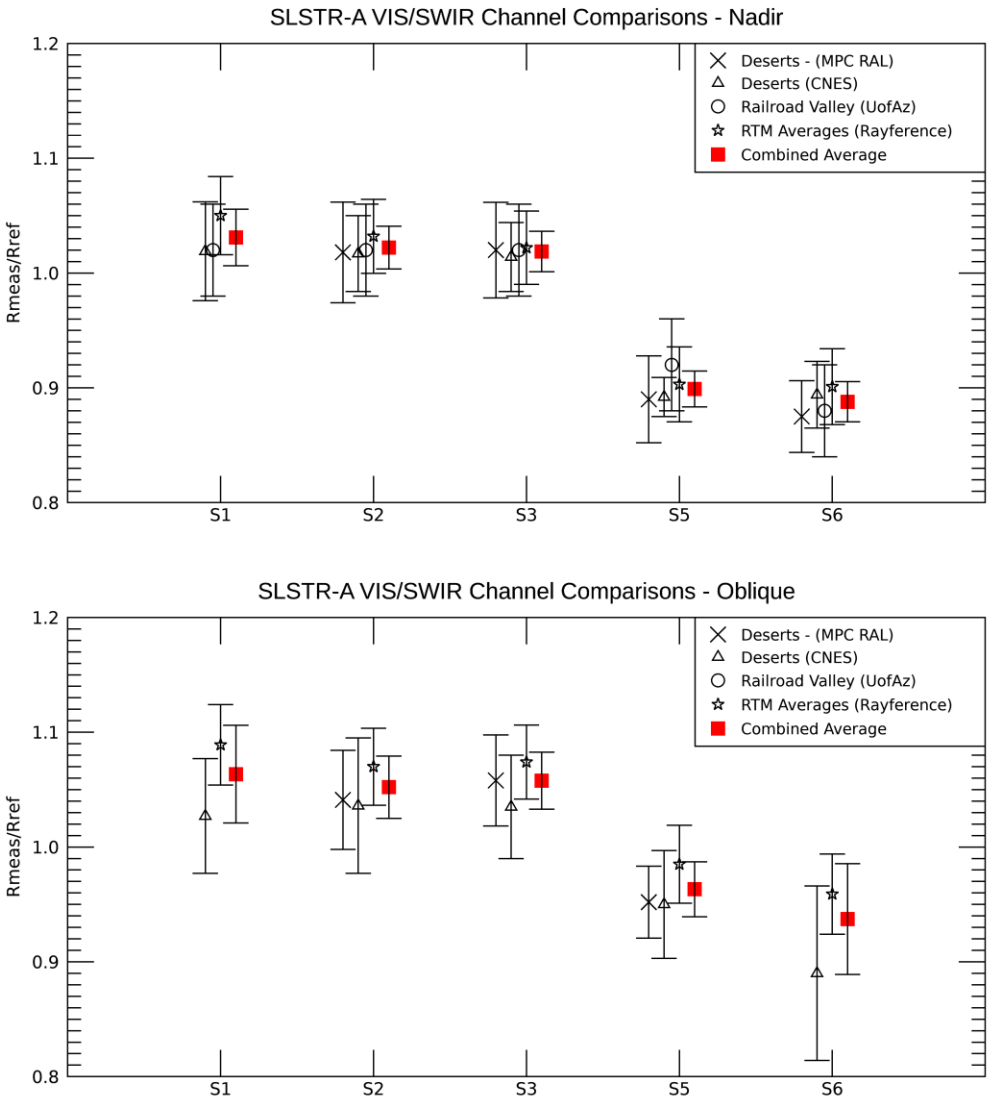

Figure 119: Summary of comparisons of SLSTR VIS/SWIR channel reflectances vs. Reference methods used to provide vicarious correction factors.

Using the combined weighted averages, we are able to provide vicarious adjustment factors to align SLSTR reflectances to MERIS and MODIS Aqua L1 calibrations, Table 22. This is on the basis that MERIS and MODIS calibrations have been assessed over many years and are considered as reference sensors in the VIS/SWIR and relative differences with other sensors are reported. Alignment to a different reference sensor, e.g. Sentinel-2 would be possible provided that relative differences and uncertainty estimates are provided. The correction factor is the inverse of the vicarious calibration results – i.e. $1/(R_{meas}/R_{ref})$.

Table 22: Proposed VIS-SWIR Calibration Adjustments Based on Vicarious Calibration analysis. Note S4 is not included because the vicarious calibration techniques do not extend to this band.

Nadir View

	S1	S2	S3	S5	S6
Correction	0.97	0.98	0.98	1.11	1.13
Uncertainty	0.03	0.02	0.02	0.02	0.02
Input Analysis	UoAz Rayference CNES	UoAz MPC (RAL) Rayference CNES	UoAz MPC (RAL) Rayference CNES	UoAz MPC (RAL) Rayference CNES	UoAz MPC (RAL) Rayference CNES

Oblique View

	S1	S2	S3	S5	S6
Correction	0.94	0.95	0.95	1.04	1.07
Uncertainty	0.05	0.03	0.03	0.03	0.05
Input Analysis	Rayference CNES	MPC (RAL) Rayference CNES	MPC (RAL) Rayference CNES	MPC (RAL) Rayference CNES	Rayference CNES

Note: Uncertainty estimates are at k=1.

6.2.3 Geometric Calibration

The verification of the geolocation accuracy of the SLSTR Level-1 products is performed using the GEOCAL tool developed by ACS under ESTEC contract and running within the MPC. GEOCAL monitors the geolocation performance in Level-1 images by correlation of images with ground control points (GCP). GEOCAL takes into account each GCP's pixel position, the predicted and the found direction cosines in the satellite control frame, and using the thermo-elastic quaternions, provides an estimation of the SLSTR orientation with respect to the satellite control frame in the form of boresight distortions angles, error estimates in the form of covariance matrices, and the optimal direction of each GCP.

Each Level-1 granule typically contains several hundred GCPs. Only GCPs with signal-to-noise ratio larger than 10 are taken into account to obtain a daily average of positional offsets in the across and along track directions.

Figure 120 presents the geolocation performance of SLSTR-A and SLSTR-B showing the average positional offsets in pixels (0.5 km) for Nadir and Oblique views during 2019.

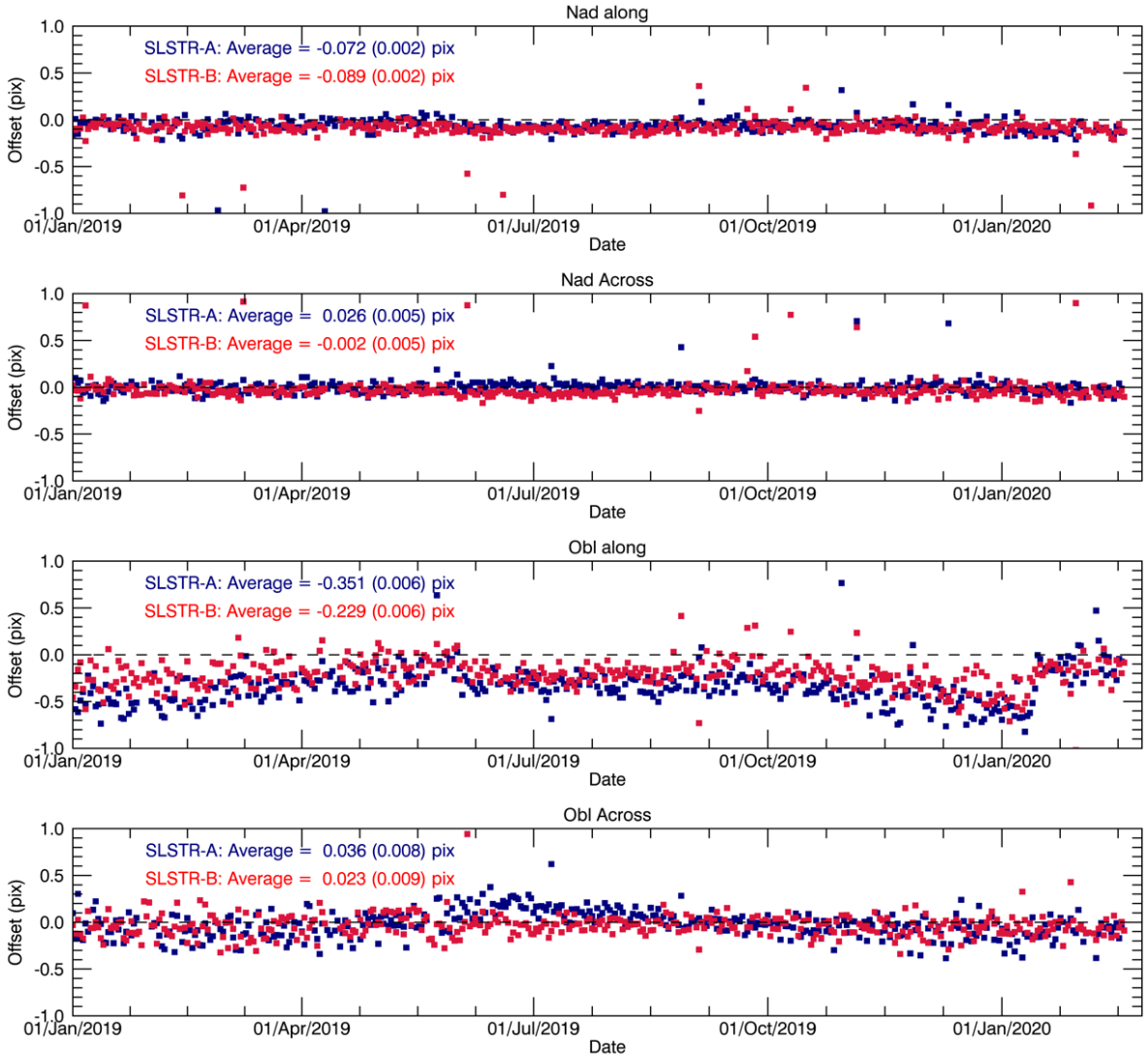

Figure 120: Daily offset results from the GEOCAL Tool analysis for Nadir view along and across track (top two plots) and Oblique view along and across track (bottom two plots), and for SLSTR-A (blue) and for SLSTR-B (red).

The positional offset in nadir view meets the mission requirements and remains constant throughout 2019 for both SLSTR-A and SLSTR-B. The average geometric offset for SLSTR-A and SLSTR-B is within 0.1 pixel in nadir view along- and across-track and in oblique view across-track. In oblique view, the offset varies seasonally. This offset variation is well correlated with a variation in the number of ground control points observed during the year, and is still within the requirements.

On the 15th January 2020, a new processing baseline was implemented which reduces the offset in the oblique view for both instruments.

Some satellite manoeuvres were performed throughout the year and although the manoeuvres only increase the positional offsets for two or three orbits, the offsets are big enough to affect the total daily average.

6.2.4 Cloud Screening

The Level 1 cloud screening monitoring continues in the third year of SLSTR-A operations, and second year of SLSTR-B. The cloud screening consists of the basic cloud mask that uses a set of 14 different tests that combine to form the 'summary_cloud' flag, the Bayesian, operating over ocean, and the Probabilistic, operating over land.

6.2.4.1 Summary of basic cloud tests

No specific algorithm development has taken place to the Basic Cloud Tests in the past year. Currently, all tests but one (infrared histogram test) are included in the summary cloud flag. A short test-by-test summary is provided below.

- Visible (NDVI) cloud test
  - The visible cloud test is a per-pixel test operating over land only. Two Normalised Differential Indices that are sensitive to vegetated and desert surfaces are calculated using the visible channels. An empirical-based look-up composed of a number of cloudy zones is used to determine if a pixel might contain cloud. There is, however, now an issue with this test missing patches of light cloud over vegetated areas. This could be fixed in the future by using land biome map in the algorithm.
- Fog/low stratus test
  - The fog/low stratus test is a per-pixel threshold test that only operates on both land and ocean at night. It uses brightness temperature differences between the 11 µm and 3.7 µm channels to determine if there is cloud present. However, cloud can still be missed at night time. This could be improved with further parametrisation of the look-up table.
- Gross cloud test
  - The gross cloud test identifies the coldest clouds, based on a threshold value on the 12 µm brightness temperatures. There is variation in the thresholds with latitude and season (month).
- Thin cirrus test
  - This test analyses the BT11-BT12 vs Threshold(BT11, across-track band). It operates on each view separately. This is a reliable test. There is some dependence on atmospheric path and therefore further tuning of the LUTs to reflect this may bring small improvements.
- Medium high cloud test
  - This test analyses BT3.7-BT12 vs Threshold(BT12). It operates on each view separately, only at night. The value of BT3.7 is always higher than BT12 due to partially cloud filled pixels and thin cirrus being present. There may be some discrepancies around twilight regions.

- 1.375 threshold test
  - This test analyses R1.375 vs Threshold(across-track band). It is based on the high absorption from water vapour in this band, meaning any signal in this channel is likely to be from cloud.
- 1.6/2.25 large and small scale histogram tests
  - The large-scale part of this test works on the basis that the signal received from clear-sky pixels will have a low value that has little variation, whereas any cloudy pixels will have a higher-varying bright signal. The pixels from a small area are formed into a histogram and the 'shape' of the low dark clear pixels is automatically identified from the brighter, wider peak of the cloudy pixels. The small-scale part of this test looks at the variability of the signal. It is intended to be used in sun-glinted regions when the large-scale test cannot be operated. These tests are not optimized for sun-glinted regions and significant cloud is still missed when the sun-glint flag is raised. It is recommended that an update to the algorithms be developed to counter this.
- Spatial coherence test
  - This test assesses the standard deviation of the measured BTs over a small area of ocean. It is assumed that over clear sky, the signal variation will be small against the background of a homogeneous ocean. This test has a tendency to over-mask cloud and is one of the priorities for algorithm development.
- Infrared histogram test
  - This test uses the 11 µm brightness temperature to identify cloud that all other tests may have missed. This is not a reliable test and when used in AATSR, was often seen to falsely classify clear-sky as cloud. It is rarely set. This test is not yet included in the summary cloud.

6.2.4.2 Summary of Bayesian test

The Bayesian cloud screening method makes use of measurements in the S2, S3, S5, S8 and S9 channels during the day and S7, S8 and S9 channels at night. These are compared to radiative transfer modelling and pre-calculated look-up tables to infer the probability of a pixel being cloudy given the observations and background meteorological state. The method has previously been applied successfully in the context of the ESA SST CCI to the AVHRR and other ATSR instruments.

6.2.4.3 Summary of Probabilistic tests

The Probabilistic Cloud Mask is implemented in the IPF at Level-1 and carried through to Level-2. Cloud contamination appears to be at a minimum, although there appears to be some excessive cloud clearing in some regions. This is supported by the sampling ratio, which is lower than would be expected over some parts of the globe. This follows a regular pattern, which is consistent from month to month. The cause is the lack of temporal interpolation of the ECMWF Skin Temperature in the meteorological input fields to the probabilistic clouds mask code in the IPF implementation. This issue has now been resolved in L1 release PB 2.59 (S3A) and PB 1.31 (S3B) on 15th January 2020.

6.2.4.4 Monitoring cloud masking performance

6.2.4.4.1 Confusion Matrices

Comparisons between the Basic and Bayesian cloud masks can be made using the SST matchup database. Over the year, the total number of matchups which have been masked as cloudy or clear by each of the Basic and Bayesian cloud tests have been counted, and compared to see how many points agree.

The confusion matrices below for daytime and night-time show the number of points (and the percentage of total points, rounded to the nearest integer) where the Basic and Bayesian have agreed that a point is cloudy or clear, and where the two algorithms disagree. We see that they agree that 73% of the total matchups are cloudy in day and night, which is in line with expected level given a mean global cloudiness. The Basic and Bayesian agree that 15% of the total matchups as clear for day and night. The matrix shows that the Bayesian considers 9% daytime (8% night) of the matchups to be clear when the Basic considers them to be cloudy, indicating an over-screening issue for the Basic test. The Bayesian considers only 2% of day and night points to be cloudy which the Basic considers to be clear.

A similar level of agreement is seen for SLSTR-B, although the statistics are different because each instrument is viewing a different location on the Earth with different amounts of cloudiness.

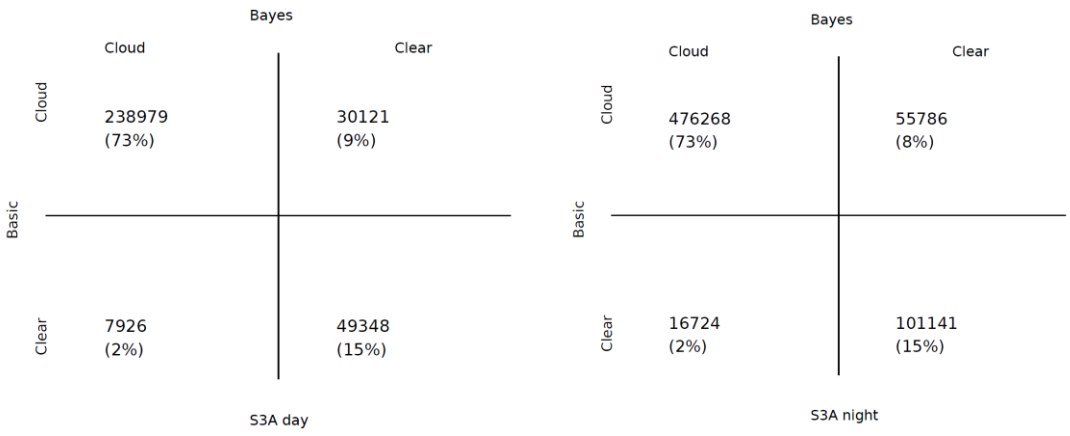

Figure 121: S3A cloud identification confusion matrices for matchups. Left shows daytime data and right shows night-time data.

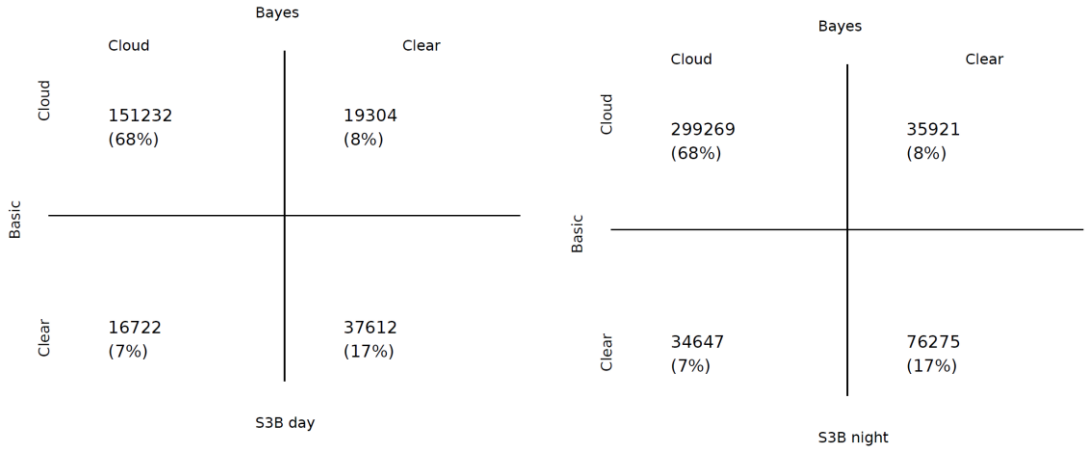

Figure 122: S3B cloud identification confusion matrices for matchups. Left shows daytime data and right shows night-time data.

6.2.4.4.2 Time series of cloud-free matchups

The performance of the cloud tests has been monitored using the SST matchup database. By looking for high SST biases, potential cloud missed can be identified and quantified. Figure 123 shows a time series for SLSTR-A of the total number of matchups found using each of the Basic and Bayesian cloud mask results for the N2, D2, N3 and D3 SST result. Also plotted are the number of matchups which give a high SST bias (>3K), a possible indicator of cloud contamination. For each SST algorithm, the Bayesian test results in more matchups, indicating that the Basic test may be over-masking cloud. However, the Basic also has more outliers than the Bayesian, indicating it is also missing some cloud. For the single-view SST algorithms, the Basic test has significantly more outliers than for the dual-view, indicating that when the Basic algorithms rely on the dual-view cloud tests to detect significant cloud that is being missed when only the single view is available outside the dual-view swath. For the N2 daytime matches, the number of outliers from the Basic cloud test that have the sun-glint flag set is significant. This is due to several of the daytime cloud tests being switched off in sun-glint, and the existing 'cloud in glint' test being inadequate.

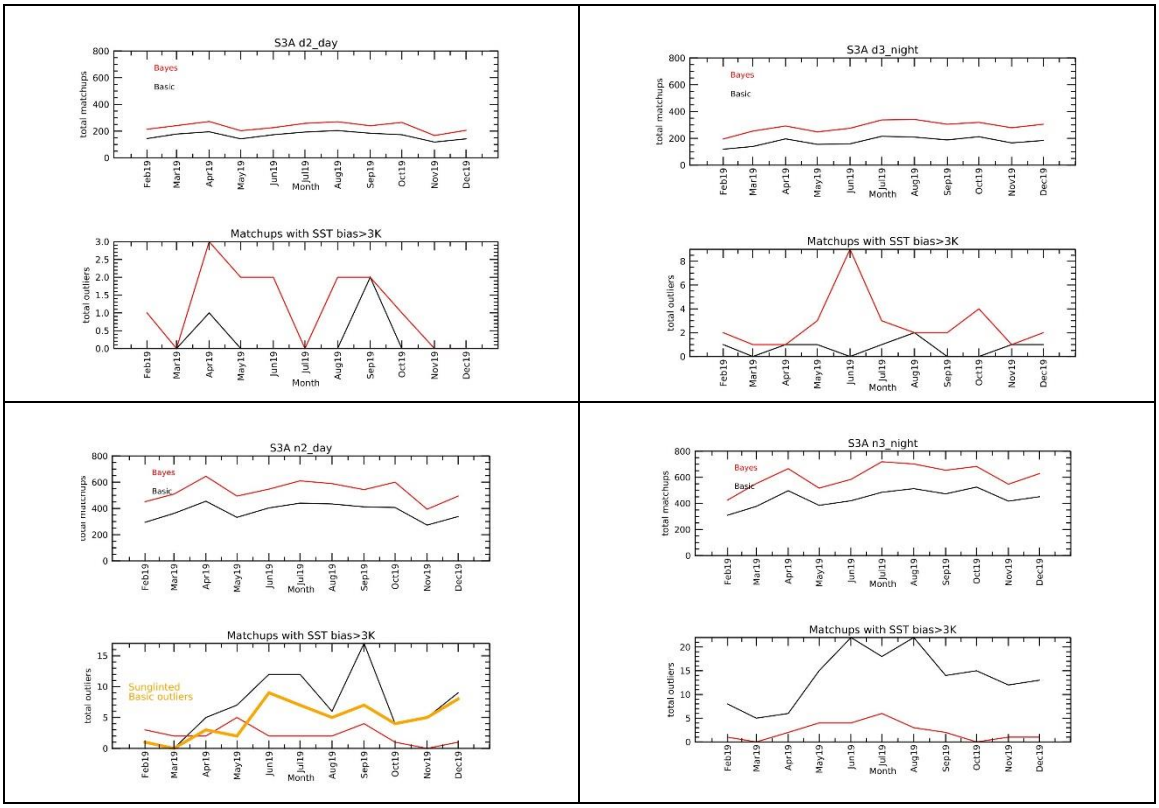

Figure 123: A time series of the total number of matchups indicated to be 'clear-sky' by the Basic and Bayesian masks for each of the 4 SST algorithms for SLSTR-A. The number of matchups with an SST bias > 3K is also plotted, as this can be indicative of unidentified cloud.

Similar plots have been produced for SLSTR-B over the same time period.

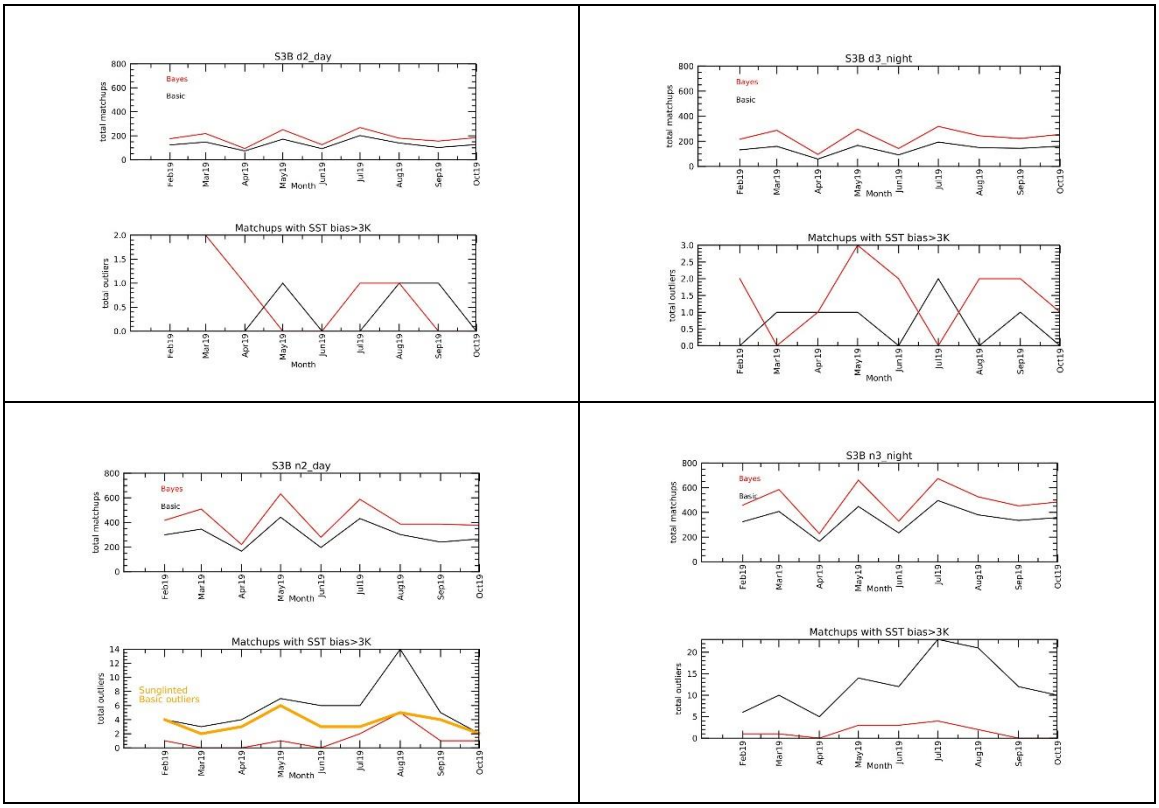

Figure 124: A time series of the total number of matchups indicated to be 'clear-sky' by the Basic and Bayesian masks for each of the 4 SST algorithms for SLSTR-B. The number of matchups with an SST bias > 3K is also plotted, as this can be indicative of unidentified cloud.

Using this analysis, it has also been possible to identify the causes of the most significant cloud misses:

- missed cloud when sun glint flag is raised in daytime
- reduction in cloud screening quality over nadir-only view due to lack of dual-view tests

6.2.4.4.3 Time series of cloudy matchups

Using the analysis of SST biases, it has also been possible to identify any issues with over-masking of cloud. By counting the number of matchups with a low SST bias (<1.5K), it is possible to infer whether a cloud test may be identifying clear-sky pixels as cloud. The Basic cloud test identifies a greater number of potential of false positives.

By breaking the false positives down into the individual cloud tests, it is possible to see which tests may be causing the over-screening. We see that by looking at the N3_night matchups, the Spatial Coherence test followed by the two view difference tests are responsible for most potential over-masking.

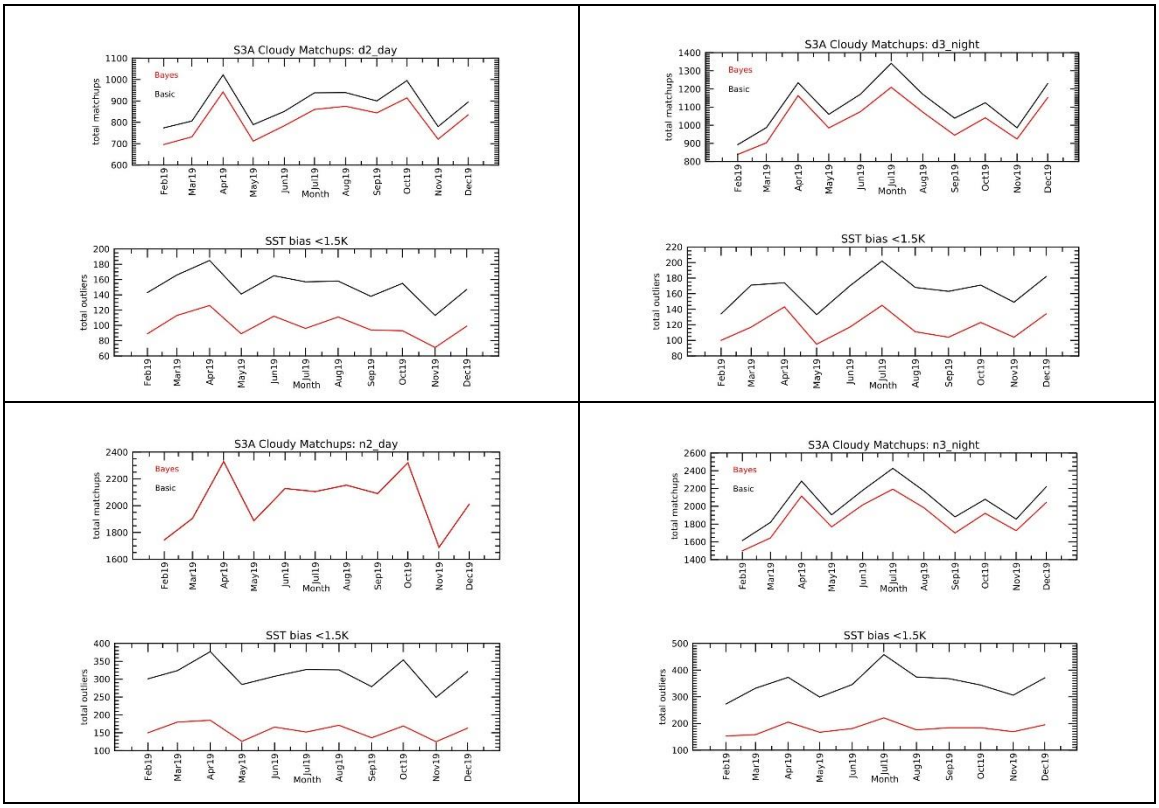

Figure 125: A time series of the total number of matchups indicated to be 'cloudy' by the Basic and Bayesian masks for each of the 4 SST algorithms for SLSTR-A. The number of matchups with an SST bias < 1.5K is also plotted, as this can be indicative of clear-sky being masked as cloud.

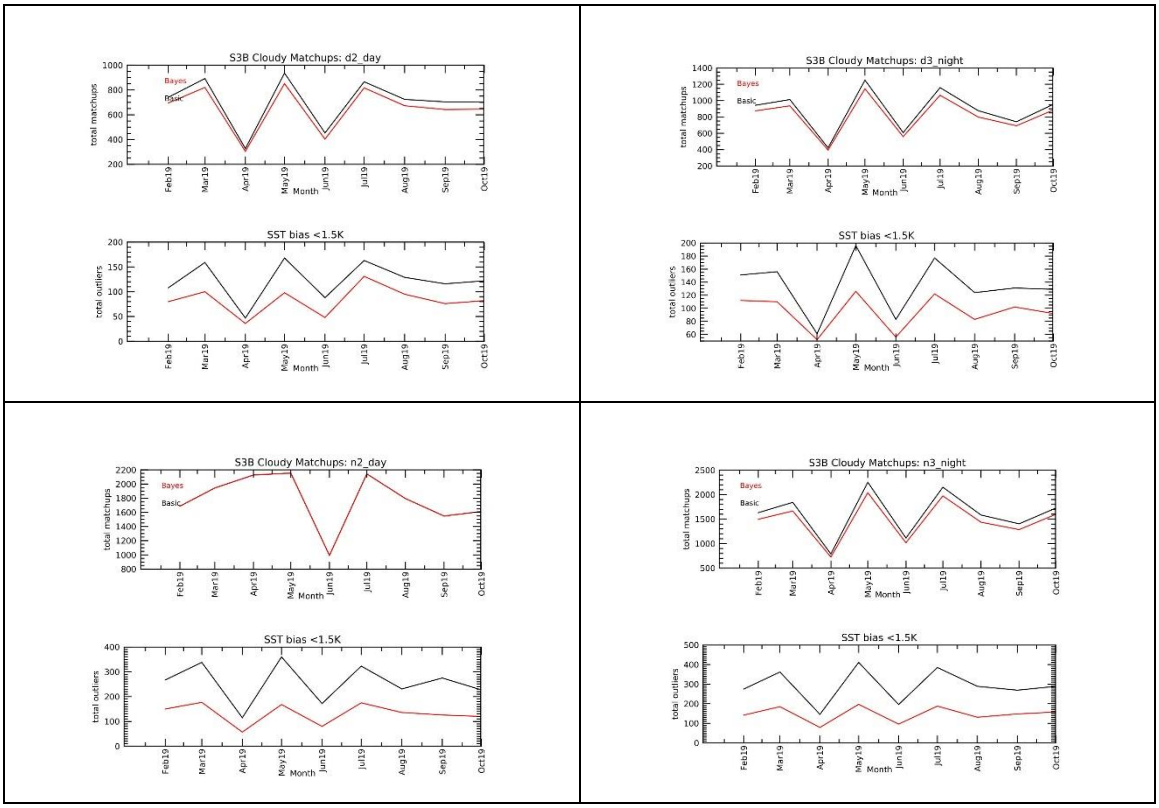

Figure 126: A time series of the total number of matchups indicated to be 'cloudy' by the Basic and Bayesian masks for each of the 4 SST algorithms for SLSTR-B. The number of matchups with an SST bias < 1.5K is also plotted, as this can be indicative of clear-sky being masked as cloud.

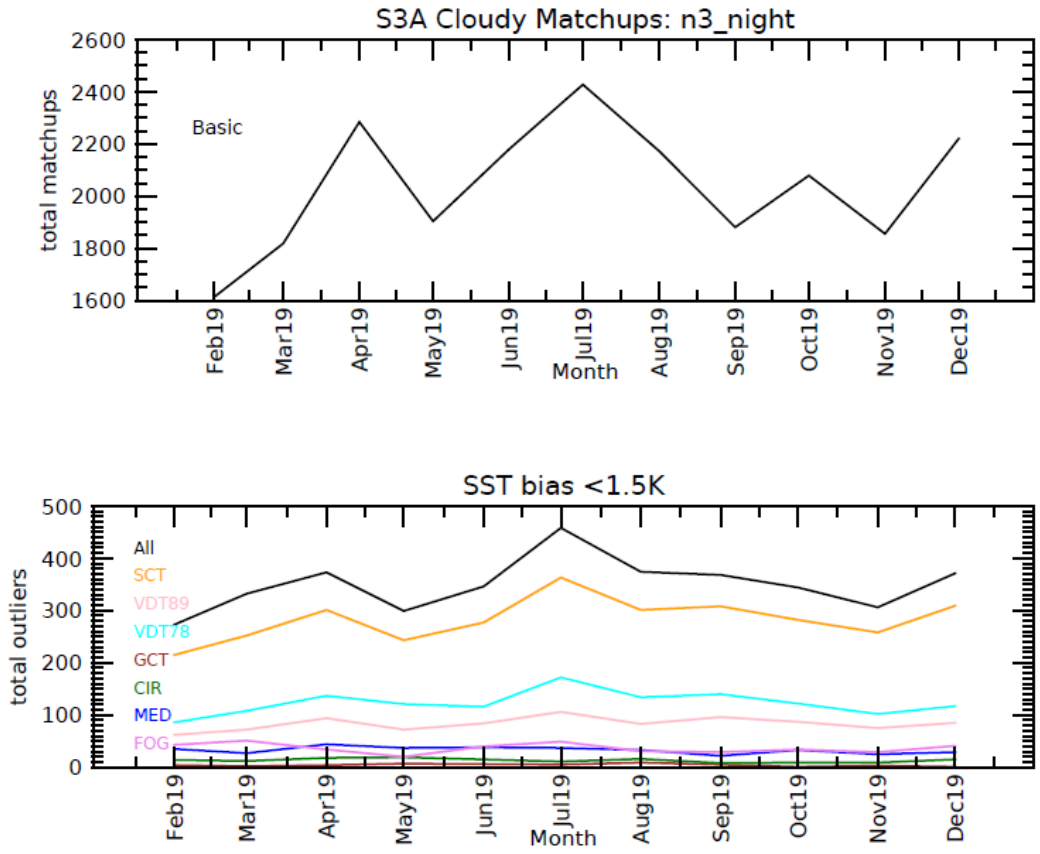

Figure 127: A time series of the total number of matchups indicated to be 'cloudy' by the Basic cloud masks for the N3_night SST algorithm for SLSTR-A. The number of matchups with an SST bias < 1.5K is also plotted determined by each separate cloud test.

The main issues with the basic cloud over-screening have been identified as,

- 11 µm SCT over-masking cloud
- View difference tests potentially over masking cloud

6.2.5 References

- Cox, C. and Munk, W., "Measurement of the Roughness of the Sea Surface from Photographs of the Sun's Glitter", Journal of the Optical Society of America, Vol. 44, Issue 11, p. 838 (1954)
- D. L. Smith and C. V. Cox, "(A)ATSR solar channel on-orbit radiometric calibration," IEEE Trans. Geosci. Remote Sens. 51(3), 1370–1382 (2013)
- Tomazic, I., O'Carroll, A., Corlett, G., Piolle, JF., Hewison, T., Burini, A., Montagner, F., Santacesaria, V., Dash, P., Donlon, C., Dransfeld, S., Smith, D. "Sentinel-3 SLSTR CAL/VAL activities for sea surface temperature measurements", Tallinn, Estonia, EUMETSAT Conference (2018)

6.3 L2 product performances

6.3.1 Sea Surface Temperature (SST)

The formal missions requirements specify that:

- S3-MR-400: Sentinel-3 shall provide SST measurement capability to at least the quality of AATSR on Envisat: SST shall be accurate to < 0.3 K @ 1 km spatial resolution and with improved swath coverage and
- S3-MR-980: Sentinel-3 SST measurements shall have a long-term radiometric stability goal of 0.1 K/decade (≤0.2K/decade threshold) for a 5 x 5 degree latitude longitude area.

The S3 OPT Cal/Val plan details several activities to verify the performance of the SST product. The most important of these activities is SLSTR-SST-CV-130, which involves validating SLSTR SST products with independent data from a number of sources (including FRM) from drifters, Argo, GTMBA and ship-borne radiometers. This activity will directly respond to both the formal mission requirements on SST. However, at this stage it is not possible to assess the stability (S3-MR-980) of the product owing to the very short timescale of data currently available. However, it is possible to make an initial assessment of SST product accuracy against drifting buoys over the short timescale of data available.

Match-ups to in situ data (drifters, Argo and moorings) were generated by the EUMETSAT OSI-SAF and EUMETSAT for reprocessed data. The dependence of the difference between SLSTR-A SST_{skin} and drifting buoy SST_{depth} for the year from 01/02/2019 to 31/01/2020 is shown in Figure 128. The results have been processed offline to ensure a consistent SST retrieval. No adjustments have been made for difference in depth or time between the satellite and in situ measurements. Daytime 2-channel (S8 and S9) results are shown in red, night time 2-channel results are shown in blue and night time 3-channel (with s7) results are shown in green. Solid lines indicate dual-view retrievals, dashed lines indicate nadir-only retrievals. Bold lines indicate statistically significant (95% confidence) results.

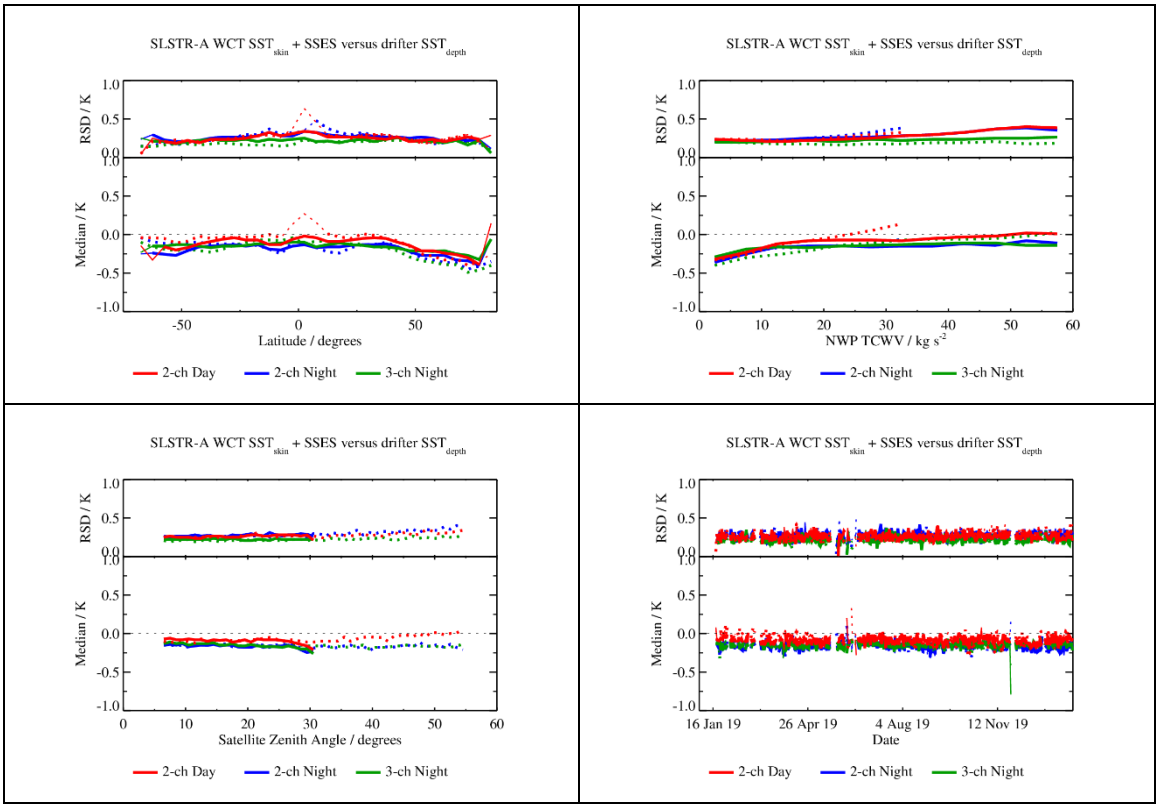

Figure 128: Dependence of median and robust standard deviation of match-ups between SLSTR-A SST_{skin} and drifting buoy SST_{depth} for 01/02/2019 to 31/01/2020 as a function of latitude, total column water vapour (TCWV), satellite zenith angle and date.

The spatial distribution of SLSTR-A/drifter match-ups for the period in Figure 129. Results are shown for the four main SST retrievals. No adjustments have been made for difference in depth or time between the satellite and in situ measurements.

Match-ups statistics (median and robust standard deviation, RSD) of SLSTR-A/drifter match-ups are shown in Figure 129. No adjustments have been made for difference in depth or time between the satellite and in situ measurements and so at night time (in the absence of diurnal warming) an offset of around -0.17K is expected.

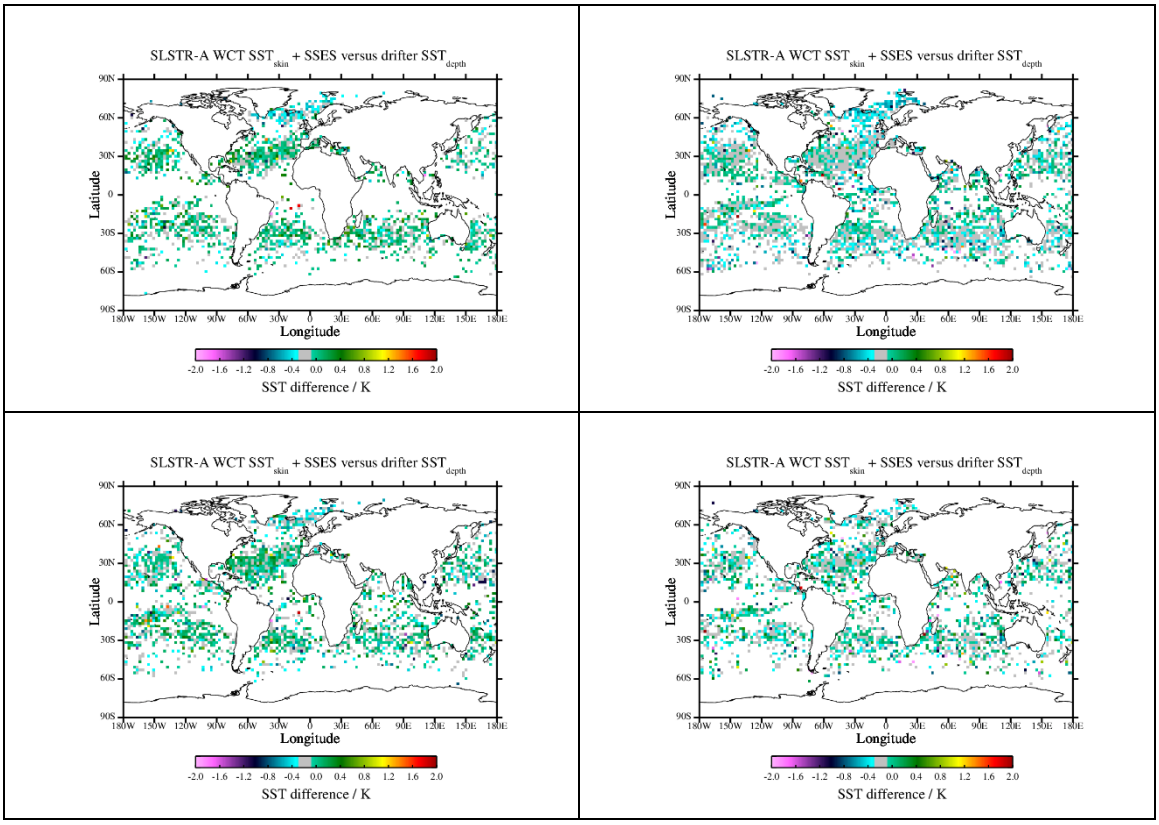

Figure 129: Spatial distribution of match-ups between SLSTR-A SST_{skin} and drifting buoy SST_{depth} for 01/02/2019 to 31/01/2020 for N2 (upper left), N3 (upper right), D2 (lower left) and D3 (lower right) retrievals.

Table 23: SLSTR-A drifter match-up statistics for 01/02/2019 to 31/01/2020.

Retrieval	Number	Median (K)	RSD (K)
N2 day	23015	-0.07	0.28
D2 day	26966	-0.09	0.27
N2 night	35200	-0.16	0.28
N3 night	46075	-0.15	0.22
D2 night	22961	-0.16	0.27
D3 night	22974	-0.15	0.22

The combination of the offset being close to -0.17 K with the calculated RSD values indicate SLSTR-A continues to provide SSTs mostly within its target accuracy (0.3 K) aside from the N2 retrieval. From the dependence on TCWV shown in Figure 128, we can see the N2 retrieval is not currently optimal for cases where the TCWV is > 35 kg/m^2, conditions which are especially challenging for the 2-channel nadir-only case. The dependence over time in Figure 128 indicates SLSTR-A has been stable over the year.

Results for SLSTR-B are shown in Figure 130 and Figure 131.

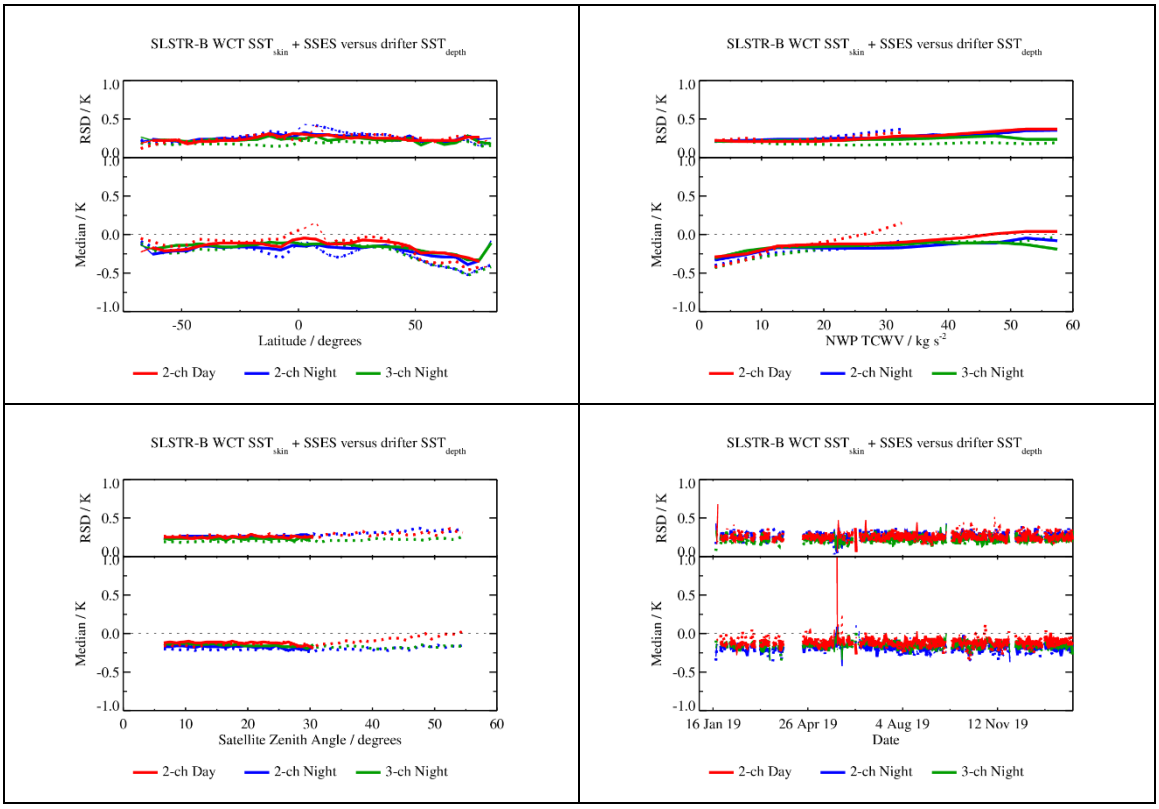

Figure 130: Dependence of median and robust standard deviation of match-ups between SLSTR-B SST_{skin} and drifting buoy SST_{depth} for 01/02/2019 to 31/01/2020 as a function of latitude, total column water vapour (TCWV), satellite zenith angle and date.

Match-ups statistics for SLSTR-B are shown in Table 24. Again, no adjustments have been made for difference in depth or time between the satellite and in situ measurements and so at night time (in the absence of diurnal warming) an offset of around -0.17 K is expected.

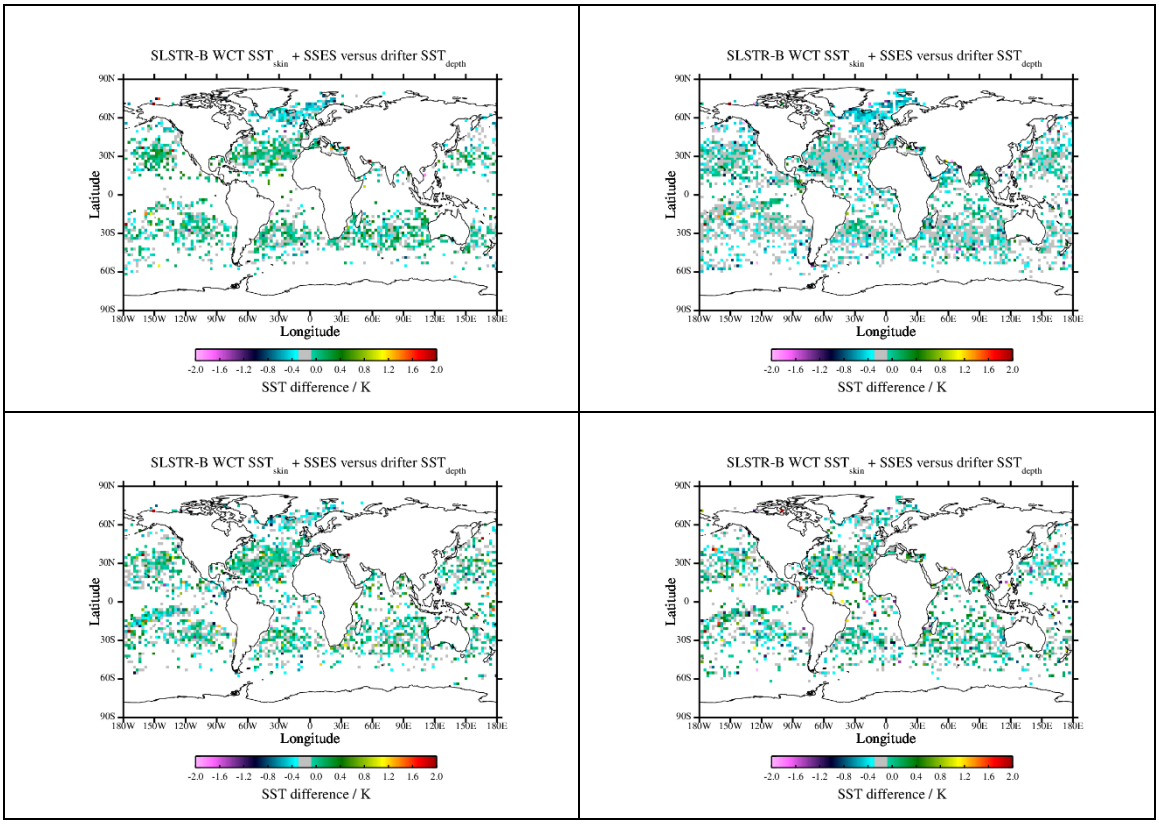

Figure 131: Spatial distribution of match-ups between SLSTR-B SST_{skin} and drifting buoy SST_{depth} for 01/02/2019 to 31/01/2020 for N2 (upper left), N3 (upper right), D2 (lower left) and D3 (lower right) retrievals.

Table 24: SLSTR-B drifter match-up statistics for 01/02/2019 to 31/01/2020.

Retrieval	Number	Median (K)	RSD (K)
N2 day	21540	-0.11	0.28
D2 day	23983	-0.12	0.25
N2 night	21304	-0.20	0.28
N3 night	41445	-0.17	0.21
D2 night	20698	-0.17	0.27
D3 night	20716	-0.15	0.24

6.3.2 Land Surface Temperature (LST)

The formal missions' requirement for LST specifies that:

- S3-MR-420: Sentinel-3 shall be able to measure Land Surface Temperature (LST) to an accuracy of < 1K with a resolution of 1 km at nadir. This capability shall not reduce the quality of the SST retrievals

A four-phase approach is detailed in the S3 OPT Cal/Val plan, which follows both the ESA LST validation protocol (Schneider et al., 2012) and the CEOS LPV Best Practices guide for LST (Guillevic et al., 2017):

- Comparison of satellite-retrieved LST with in situ measurements collected from radiometers sited at a number of stations spread across the Earth, for which the highest-quality validation can be achieved;
- Radiometric-based validation, which offers an alternative to validation with in situ LST measurements as it does not require measurements of LST on the ground, and can provide a viable alternative for long-term, semi-operational LST product evaluation at the global scale;
- Inter-comparisons with similar LST products from other sources such as AATSR, AVHRR, MODIS, SEVIRI, and VIIRS, which give important quality information with respect to spatial patterns in LST deviations;
- Time series analysis to quantify trends and to identify potential instrument drift or persistent cloud contamination.

We have focussed on the first and third approaches, with the second approach developed offline. The first responds directly to the formal mission requirements on accuracy for LST. The third provides the context to which the product exhibits consistency on a larger regional basis. The fourth approach is dependent on multi-year data and will be addressed once we have a minimum of 3-years routine operational Level-2 data.

The SLSTR-A SL_2_LST product from SLSTR went operational in the Sentinel 3 PDGS on 5th July 2017 with PB 2.16. No additional updates to the retrieval algorithm have been implemented in the IPF since. However, Processing Baseline 2.29 released on 4th April 2018 included the new Probabilistic Cloud Mask implemented in the IPF at Level-1 and carried through to Level-2. Furthermore, from 26th February 2019 an updated ADF of retrieval coefficients has been implemented in PB 2.47, IPF 06.14. We show results on a monthly basis from 1st March 2019 to 31st January 2020 to ensure consistency in the PB. In all cases the Probabilistic Cloud Mask is applied.

The SLSTR-B SL_2_LST product from SLSTR went operational in the Sentinel 3 PDGS on 26th February 2019 with PB 1.19 IPF 06.14. We show results on a monthly basis from 1st March 2019 to 31st January 2020. In all cases the Probabilistic Cloud Mask is applied.

For both SLSTR-A and SLSTR-B all matchups have been performed for non-time critical (NTC) only since this is deemed to be the data of highest quality.

For the in situ validation fifteen “Gold Standard” stations were used in the matchups process, seven from the SURFRAD network; two from the ARM network; three from the USCRN network; and three from the U. Leicester (UOL) deployments: i) Bondville, Illinois; ii) Desert Rock, Nevada; iii) Fort Peck, Montana; iv) Goodwin Creek, Mississippi; v) Penn State University, Pennsylvania; vi) Sioux Falls, South Dakota; vii) Table Mountain, Colorado; viii) Southern Great Plains, Oklahoma; ix) Barrow, North Slopes Alaska; x) Williams, Arizona; xi) Des Moines, Iowa; xii) Manhatten, Kansas; xiii) Chandigarh, India; xiv) Kanpur, India; and xv) Wicken Fen, UK. Overall the matchups show very good agreement between the satellite LST and the in situ LST across a broad range of LST values. This is the case for each of the “Gold Standard” stations (Figure 132 – SLSTR-A; Figure 133 – SLSTR-B).

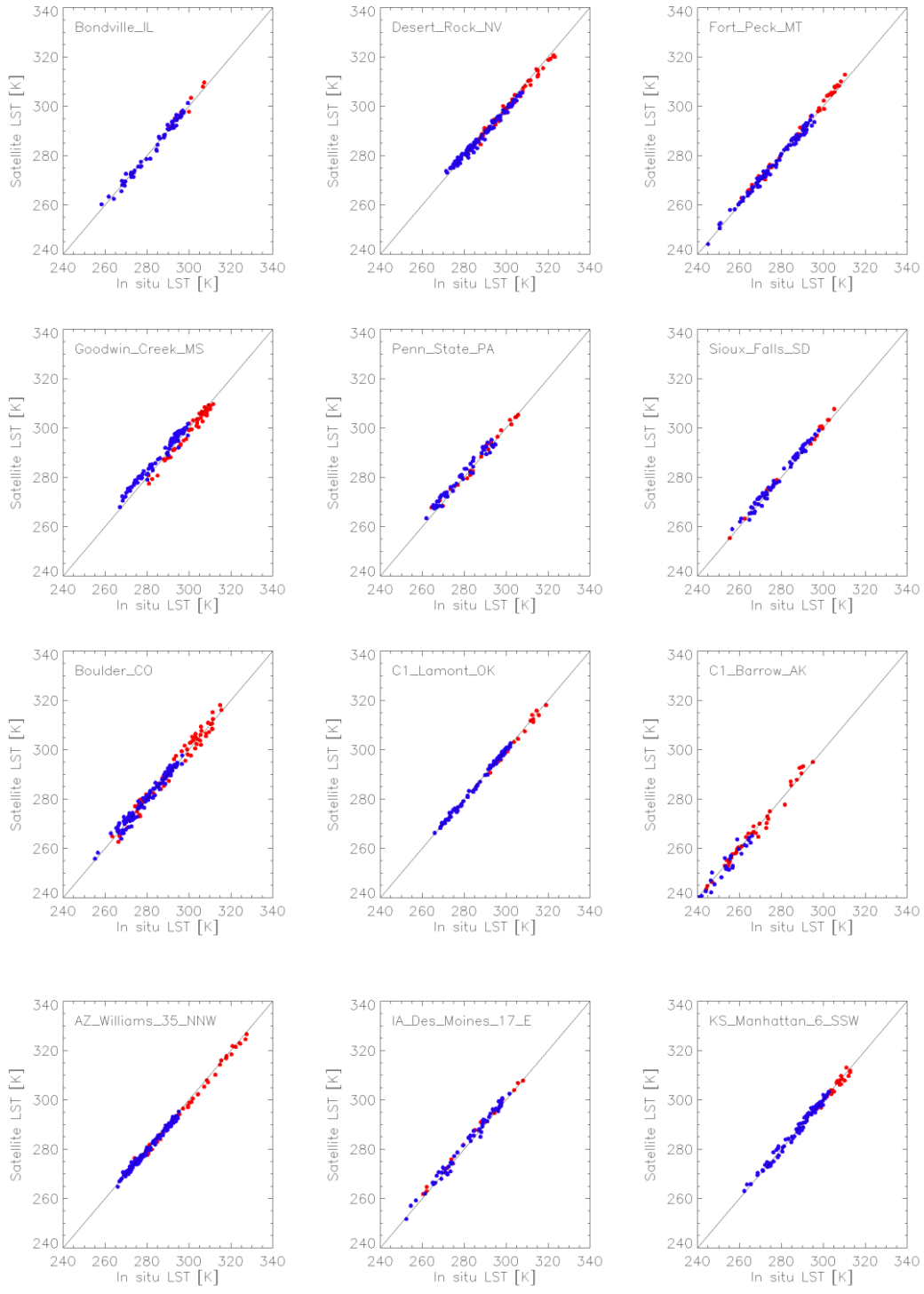
Bondville_IL
Desert_Rock_NV
Fort_Peck_MT
Goodwin_Creek_MS
Penn_State_PA
Sioux_Falls_SD
Boulder_CO
C1_Lamont_OK
C1_Barrow_AK
AZ_Williams_35_NNW
IA_Des_Moines_17_E
KS_Manhattan_6_SSW
Satellite LST [K]
In situ LST [K]
240
260
280
300
320
340

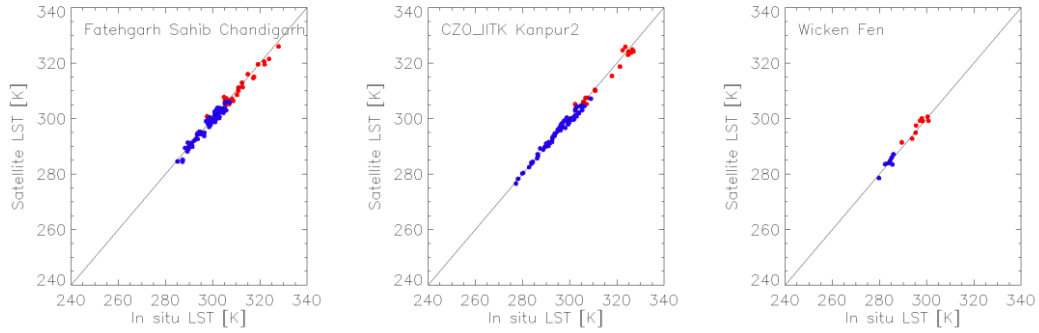

Figure 132: In situ validation of S3A SL_2_LST product at fifteen "Gold Standard" stations for the period 1st March 2019 to 31st January 2020

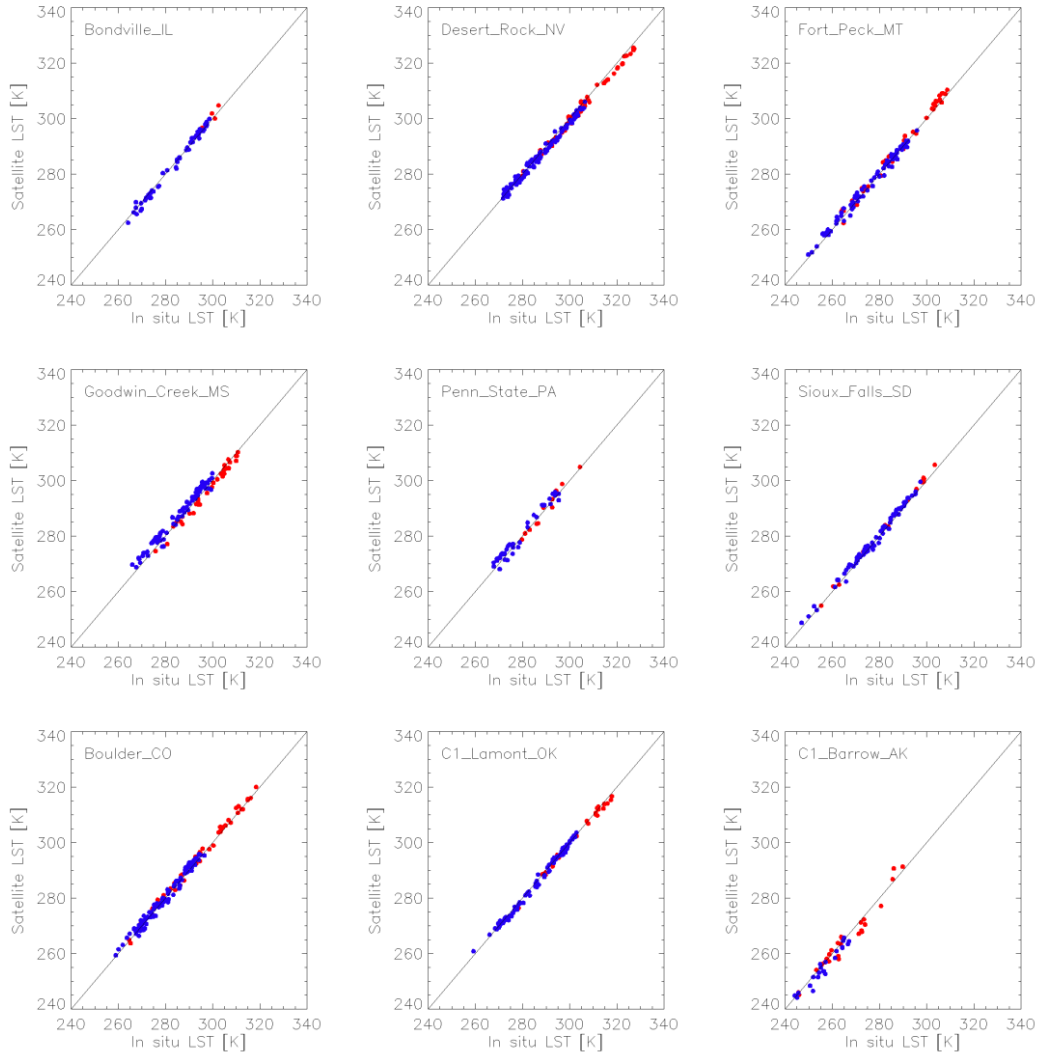

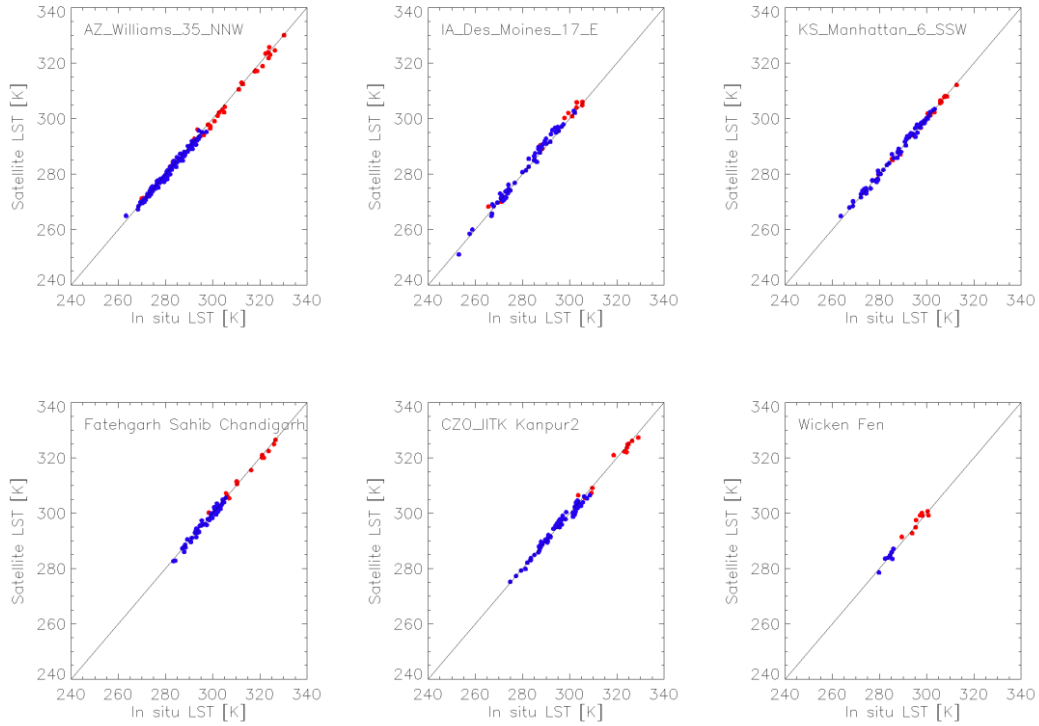

Figure 133: In situ validation of S3B SL_2_LST product at fifteen "Gold Standard" stations for the period 1st March 2019 to 31st January 2020.

The statistics are shown in Table 25 (SLSTR-A) and Table 26 (SLSTR-B). The number of matchups are provided together with the accuracy and precision. The accuracy can be directly compared with mission requirement S3-MR-420. For SLSTR-A, overall the absolute daytime accuracy is 0.81 K and the absolute night-time accuracy is 0.67 K. Both of which are within the mission requirements for LST. For SLSTR-B, overall the absolute daytime accuracy is 0.79 K and the absolute night-time accuracy is 0.64 K. Both of which are within the mission requirements for LST.

Table 25: Statistics of In situ validation for S3A SL_2_LST product at fifteen "Gold Standard" stations for the period 1st March 2019 to 31st January 2020

Network	Site	Day			Night		
		N	Acc.	Prec.	N	Acc.	Prec.
SURFRAD	Bondville	8	1.03	1.48	59	-0.04	1.35
SURFRAD	Table Mountain	65	0.21	2.28	108	0.30	1.59
SURFRAD	Desert Rock	63	-1.14	1.20	114	-0.60	1.37
SURFRAD	Fort Peck	34	1.18	1.06	90	0.08	1.20
SURFRAD	Goodwin Creek	50	-1.69	1.37	89	2.32	1.45
SURFRAD	Penn State University	25	0.36	1.44	51	1.46	1.70

SURFRAD	Sioux Falls	18	0.93	1.00	67	0.98	1.26
ARM	Southern Great Plains	21	-0.70	0.94	87	-0.28	0.72
ARM	North Slopes Alaska	41	-0.16	1.93	30	-1.07	2.41
USCRN	Williams, Arizona	42	-1.29	1.09	127	-0.64	0.87
USCRN	Des Moines, Iowa	15	1.31	0.97	60	0.90	1.39
USCRN	Manhatten, Kansas	24	-0.58	1.28	86	0.27	1.21
UOL	Chandigarh, India	27	-0.64	1.63	83	-0.37	1.25
UOL	Kanpur, India	17	-0.74	1.80	62	-0.19	1.08
UOL	Wicken Fen, UK	13	0.19	0.95	11	0.54	1.18

Table 26: Statistics of In situ validation for SL_2_LST product at fifteen "Gold Standard" stations for the period 4th April 2018 to 31st January 2019

Network	Site	Day			Night		
		N	Acc.	Prec.	N	Acc.	Prec.
SURFRAD	Bondville	4	1.07	1.46	52	-0.28	1.24
SURFRAD	Table Mountain	46	0.59	1.31	105	0.45	1.34
SURFRAD	Desert Rock	58	-1.17	1.13	105	-0.79	1.23
SURFRAD	Fort Peck	37	1.10	1.43	76	0.41	1.32
SURFRAD	Goodwin Creek	36	-1.63	1.15	78	1.88	1.49
SURFRAD	Penn State University	13	0.06	1.54	37	1.00	1.70
SURFRAD	Sioux Falls	14	1.07	0.88	77	0.78	1.06
ARM	Southern Great Plains	24	-0.81	0.94	83	-0.43	0.95
ARM	North Slopes Alaska	26	-0.74	2.44	26	-1.54	1.66
USCRN	Williams, Arizona	34	-0.61	1.30	116	-0.63	0.88
USCRN	Des Moines, Iowa	12	1.34	1.49	53	0.69	1.38
USCRN	Manhatten, Kansas	17	-0.31	0.74	67	0.12	0.94
UOL	Chandigarh, India	13	-0.30	1.15	65	-0.42	0.97

UOL	Kanpur, India	12	-0.40	1.55	65	-0.13	1.21
UOL	Wicken Fen, UK	9	0.61	1.44	8	0.05	1.18

For the satellite vs. satellite intercomparison both the SLSTR-A and SLSTR-B SL_2_LST products respectively were compared with the operational SEVIRI LST product available from the LSA SAF. Matchups were performed on a common 0.05° equal-angle grid following re-gridding of the Level-2 data. Individual matchups for a grid cell were only derived when the temporal difference between observation times was within 7.5 minutes, and both satellites were able to determine clear-sky LST for the grid-cell. These individual matchups were composited into monthly daytime and night-time differences. Monthly differences are shown in Figure 134 (SLSTR-A) and Figure 136 (SLSTR-B), with tabulated mean differences detailed in Table 27.

The differences are relatively consistent across different land cover types and regions of Europe and Africa. Higher differences occur at the edges of cloud masked features, suggesting some failures in one or other of the cloud algorithms for the respective products; or in areas of high topographical variance and towards the edge of the SEVIRI disk, a result of the differences in viewing geometry between the two instruments. For both SLSTR-A and SLSTR-B, overall all comparisons are generally within 1 K (Table 27) and all within the uncertainty range when considering the uncertainties from the reference products, and thus can be interpreted as consistent with each other.

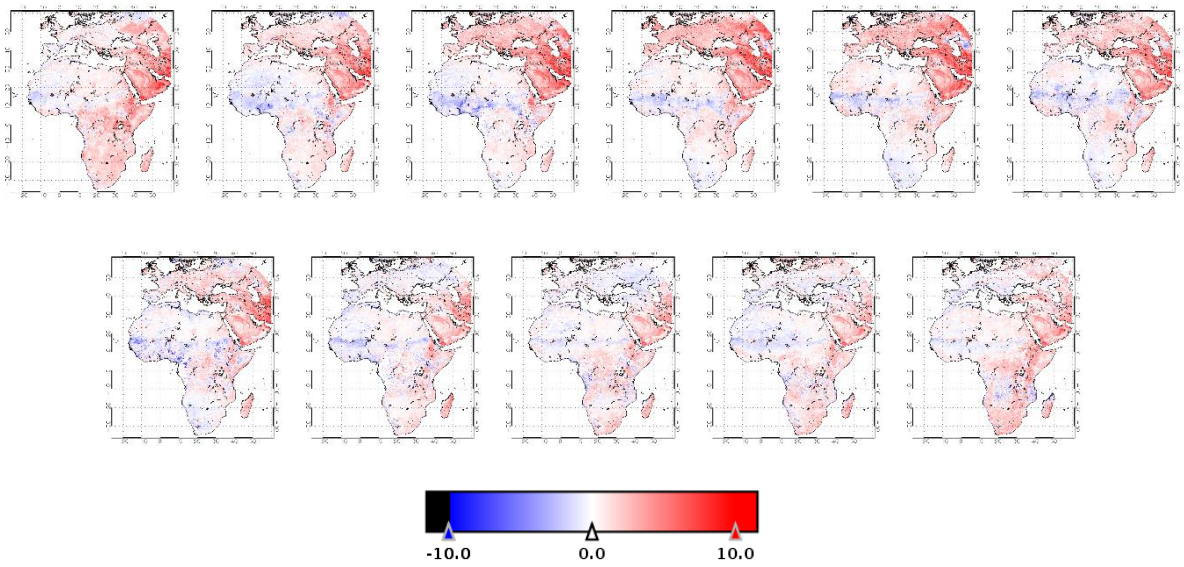

Figure 134: Monthly daytime LST difference between S3A SL_2_LST and operational SEVIRI from LSA SAF for each month from March 2019 to January 2020. Top row from left to right: Mar 2019, Apr 2019, May 2019, Jun 2019, Jul 2019, Aug 2019. Bottom row from left to right: Sep 2019, Oct 2019, Nov 2019, Dec 2019, Jan 2020.

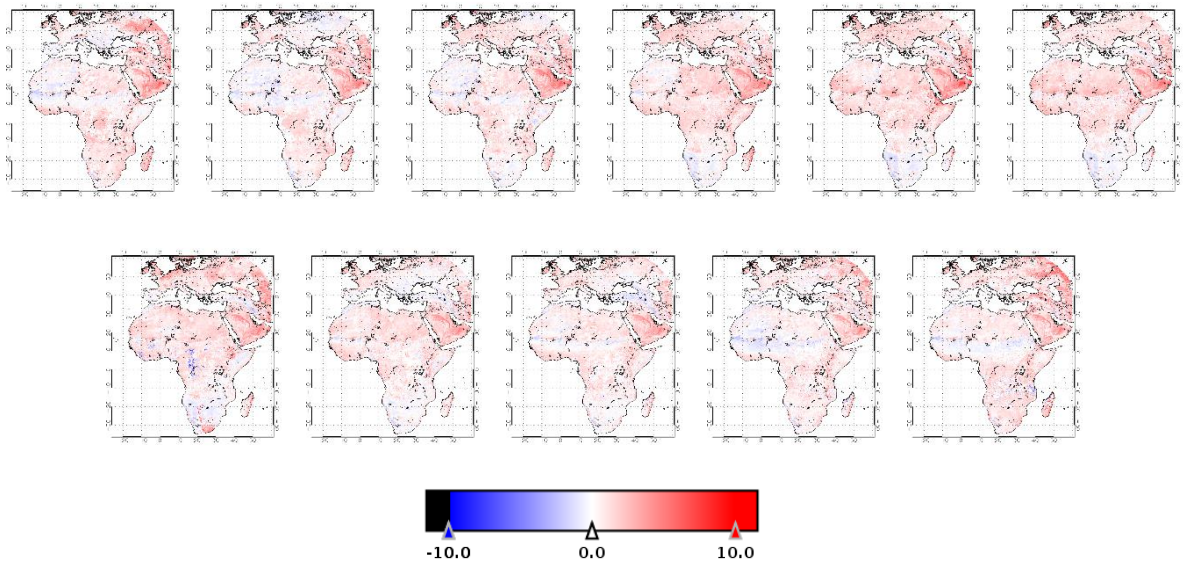

Figure 135: Monthly night-time LST difference between S3A SL_2_LST and operational SEVIRI from LSA SAF for each month from March 2019 to January 2020. Top row from left to left to right: Mar 2019, Apr 2019, May 2019, Jun 2019, Jul 2019, Aug 2019. Bottom row from left to right: Sep 2019, Oct 2019, Nov 2019, Dec 2019, Jan 2020.

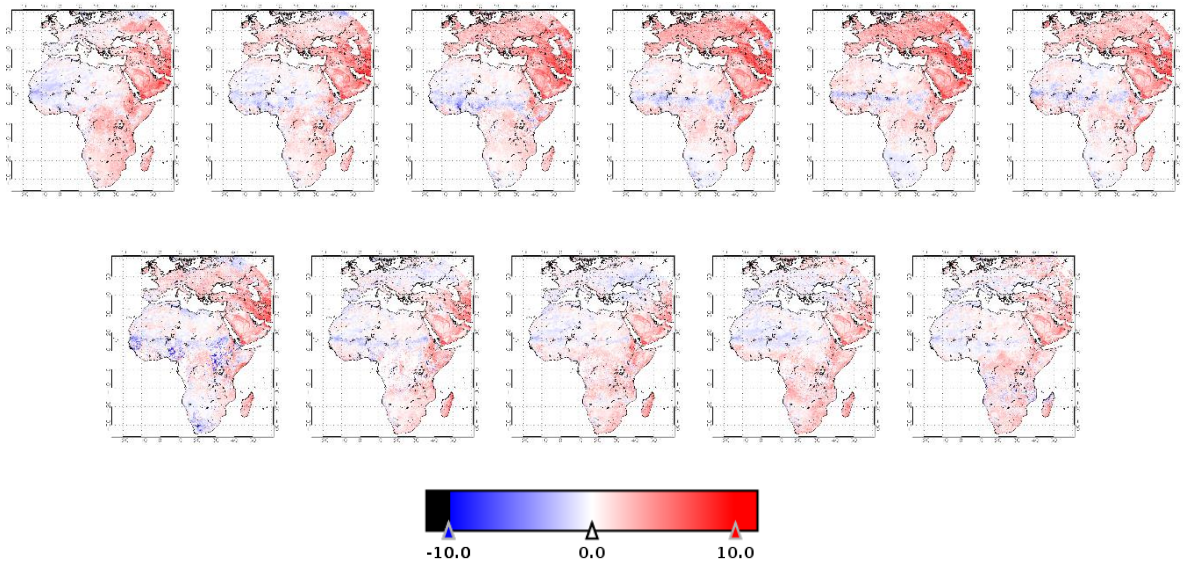

Figure 136: Monthly daytime LST difference between S3B SL_2_LST and operational SEVIRI from LSA SAF for each month from March 2019 to January 2020. Top row from left to right: Mar 2019, Apr 2019, May 2019, Jun 2019, Jul 2019, Aug 2019. Bottom row from left to right: Sep 2019, Oct 2019, Nov 2019, Dec 2019, Jan 2020.

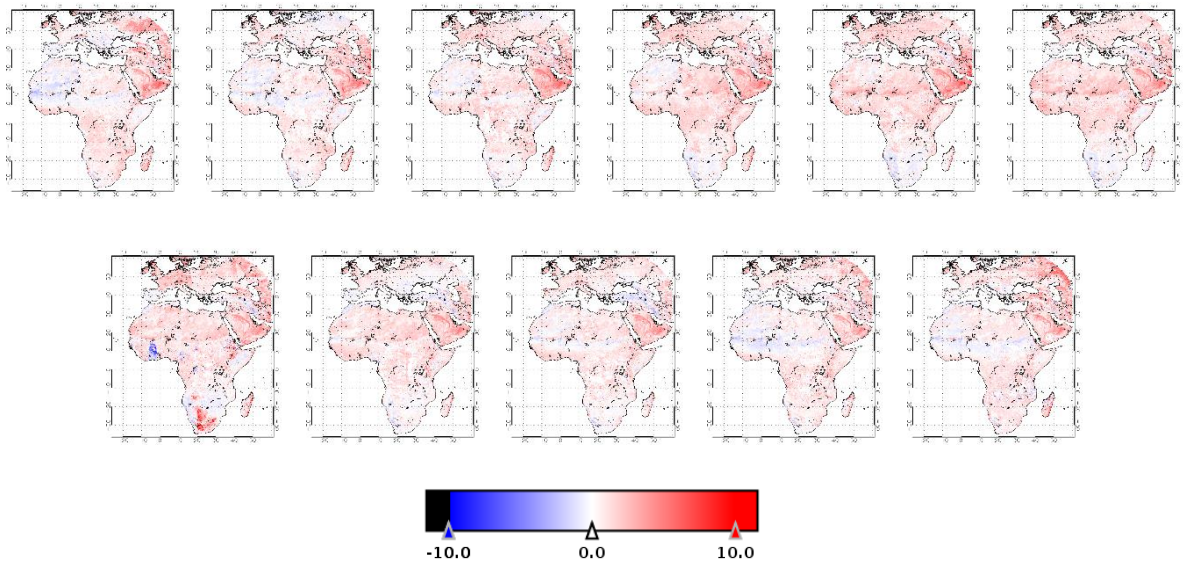

Figure 137: Monthly night-time LST difference between S3B SL_2_LST and operational SEVIRI from LSA SAF for each month from March 2019 to January 2020. Top row from left to right: Mar 2019, Apr 2019, May 2019, Jun 2019, Jul 2019, Aug 2019. Bottom row from left to right: Sep 2019, Oct 2019, Nov 2019, Dec 2019, Jan 2020.

Table 27: Statistics of monthly LST difference between SLSTR-A and SLSTR-B SL_2_LST and operational SEVIRI from LSA SAF over Africa for each month from February 2019 to January 2020

		02/19	03/19	04/19	05/19	06/19	07/19	08/19	09/19	10/19	11/19	12/19	01/20
S3A	Day	1.9	1.1	0.2	0.1	0.4	0.4	0.2	0.1	0.3	0.5	0.4	0.8
S3B	Day		0.9	0.6	0.5	0.6	0.7	0.5	0.1	0.6	0.8	0.8	0.6
S3A	Night	1.1	0.8	0.6	0.7	1.0	1.1	1.0	0.8	0.9	0.7	0.5	0.7
S3B	Night		0.6	0.6	0.8	1.0	1.1	1.1	1.0	1.0	0.7	0.6	0.6

Overall the validation and intercomparison indicate both the SLSTR-A and SLSTR-B SL_2_LST products are in line with expectations and meeting mission requirements. There are no distinct issues or non-physical values evident. Cloud contamination appears to be at a minimum, although there appears to be some excessive cloud clearing in some regions. This is supported by the sampling ratio which is lower than would be expected over some parts of the globe. This follows a regular pattern (see Figure 138 – S3A and Figure 139 - S3B for an example of March 2019). This pattern is consistent from month to month. The cause is the lack of temporal interpolation of the ECMWF Skin Temperature in the meteorological input fields to the probabilistic clouds mask code in the IPF implementation. This issue has now been resolved in L1 release PB 2.59 (S3A) and PB 1.31 (S3B) on 15th January 2020.

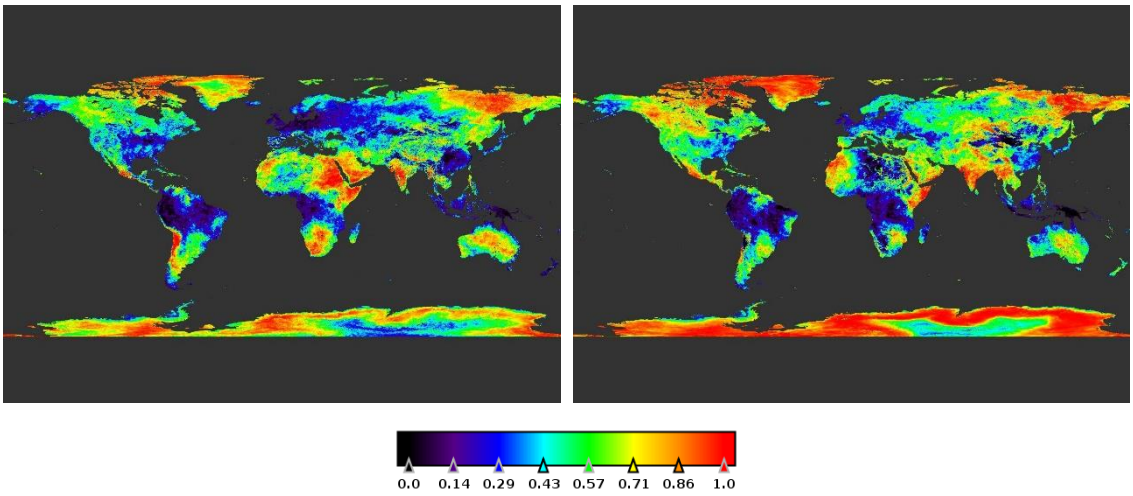

Figure 138: Monthly composites at 0.05° of S3A sampling ratio for March 2019: daytime composites (left); night-time composites (right)

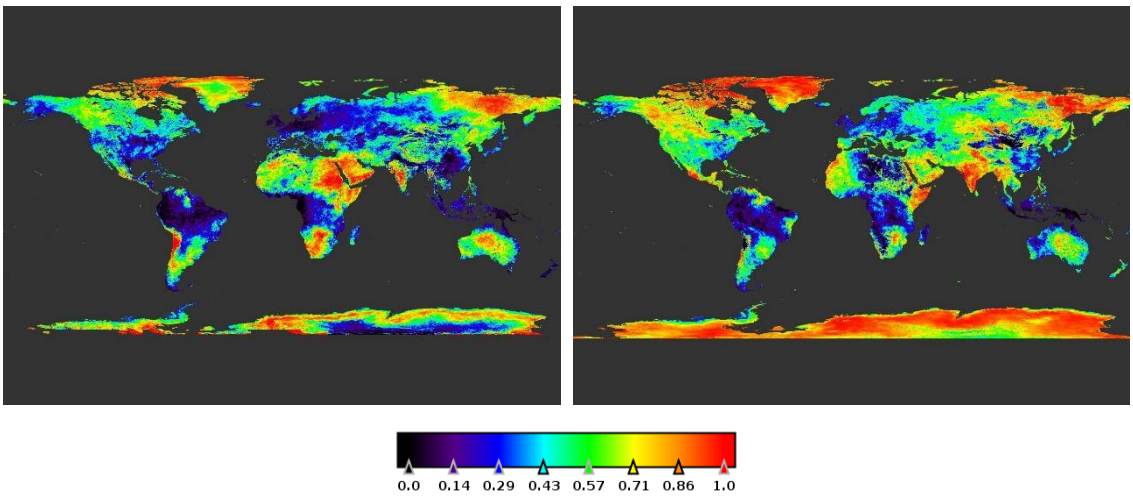

Figure 139: Monthly composites at 0.05° of S3B sampling ratio for March 2019: daytime composites (left); night-time composites (right)

6.3.2.1 Summary

The matchups with in situ observations show very good agreement across a broad range of LST values. This is the case for each of the "Gold Standard" stations. For SLSTR-A, overall the absolute daytime accuracy is 0.81 K and the absolute night-time accuracy is 0.67 K. Both of which are within the mission requirements for LST. For SLSTR-B, overall the absolute daytime accuracy is 0.79 K and the absolute night-time accuracy is 0.64 K, also both within the mission requirements for LST. This validation is complemented with satellite vs. satellite intercomparison between the SLSTR-A and SLSTR-B SL_2_LST

products and operational SEVIRI LST available from the LSA SAF. For Africa the mean monthly difference is generally < 1 K. This is the case both for SLSTR-A and SLSTR-B, and for both daytime and night-time comparisons. These are both within the SL_2_LST mission requirements and the uncertainty range when considering the uncertainties from the reference products. Thus, the two products can be interpreted as consistent with each other. There is some excessive cloud clearing in some regions for the probabilistic cloud mask, which follows a regular pattern across the globe. The cause is the lack of temporal interpolation of the ECMWF Skin Temperature in the meteorological input fields to the probabilistic clouds mask code in the IPF implementation. This issue has now been resolved in L1 release PB 2.59 (S3A) and PB 1.31 (S3B) on 15th January 2020.

7 Summary of performances – SYN

7.1 L1 products performances

7.1.1 Improved inter-instrument co-registration

The quality assessment of the misregistration data between OLCI and SLSTR has been done before February 2017, in particular with the inclusion of updated intra-instrument misregistration Auxiliary Data files. As a consequence, we focused on operational issues to ensure the production of SYNERGY products all over the globe and at any time.

The SYNERGY Level 1 processing is now performed without issue related to an incompatibility between SLSTR and OLCI products. The beginning of SLSTR L1B inputs products was effectively wrongly handled when midnight was crossed by these inputs. As a consequence, over Australia and the Eastern part of Asia, SYN L2 and VGT-like products included no radiometric data from SLSTR instrument. This issue is now corrected at Level 1 level and composite VGS products are no longer empty over these geographical areas (see Figure 140).

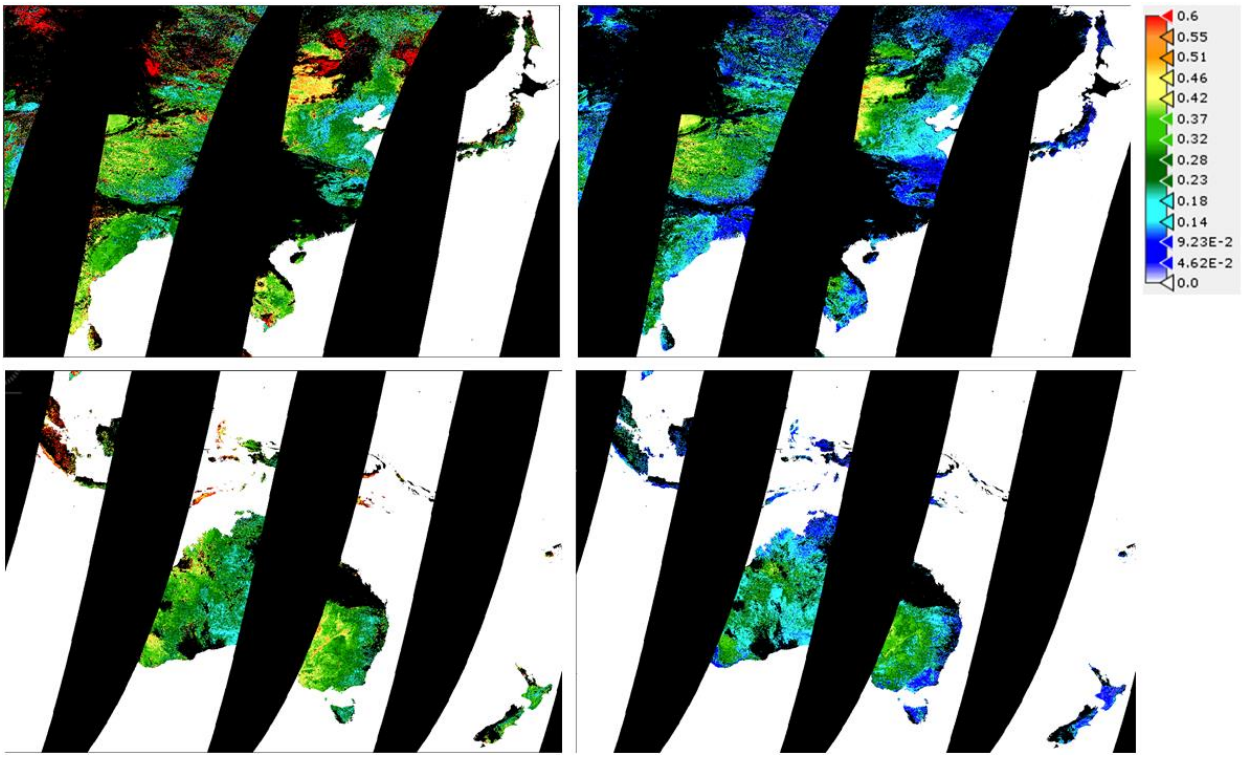

Figure 140 : Daily composite of surface reflectance associated with B3 (right column) and MIR (left column) channels over Australia and South-East Asia – 03/02/2018. White areas represent oceanic regions.

Some minor issues were also detected on SYN L1 outputs concerning S6 invalid measurements or 180° meridian interface.

7.2 L2 product performances

7.2.1 Recent algorithm evolutions

The quality assessment of SYNERGY L2 product has been performed this year following major evolutions included in the SYN L2 processor.

In July 2018, several evolutions have been included in the SYNERGY L2 processing module:

1. Improved interpolation to transfer aerosol information from super-pixel dataset resolution to 300m resolution
2. Reduction of cloud contamination applying a better filtering around cloud borders
3. Reduction of the Snow pixels contamination by discarding these pixels from aerosol retrieval
4. More consistent AOT climatology with the inclusion of the CAMS re-analysis.

In addition, several issues have been raised on SYN L2 product and corrected in 2018 (wrong interpolation of the SLSTR oblique view azimuth angle, rectangular patterns in case of large cloud cover, …).

In addition, in December 2018, several evolutions have been included in the SYNERGY VGT-like and SYNERGY VGT-S processing baseline. The purpose of these evolutions was to improve the consistency between SYN VGT-like products and PROB-V products:

1. Transferring the cloud/snow/quality information from SYN L2 processing module to VGT-like one
2. Modifying the projection on the 1 km plate carrée grid by introducing a stretched bi-cubic interpolation
3. Improving the status map computation
4. Modifying the VGT-S composite method by introducing several selection rules.

Thanks to all these evolutions, the global quality status of SYN L2, VGT-P like and VGT-S like products have been increased as shown by the following sections.

7.2.1.1 Reduction of the cloud and snow contamination

Three different cloud masks are defined during the SYN L2 cloud module. Pixels detected as cloudy pixels are labelled as SYN_cloud and discarded from the whole processing and from the final SYN L2 products. A margin, defined as a configurable parameter, is applied around all pixels detected as cloudy. Neighbours are then flagged as “cloud_margin”. Finally, a specific test is also performed to define the pixel “cloud_ambiguous” corresponding to the thin cirrus cloud.

To reduce cloud contamination in SYNERGY but avoid discarding too much pixels from the products, it has been decided to discard cloud_ambiguous and cloud_margin from the aerosol retrieval but not from the final SYN L2 product.

The impact of this evolution can be observed on Figure 141 and Figure 142 with a cloud contamination no longer present, except on some isolated and undetected pixels.

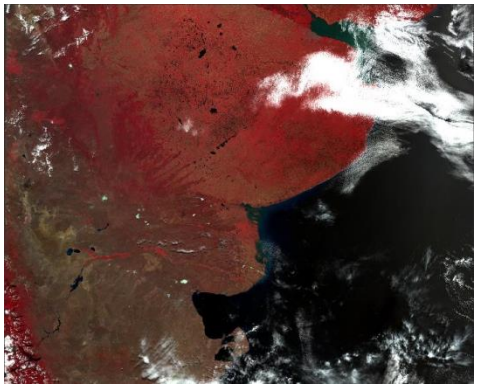

Figure 141 : RGB image from SLSTR L1b product over South America scene. A large cloud can be observed on the top-right side of this image.

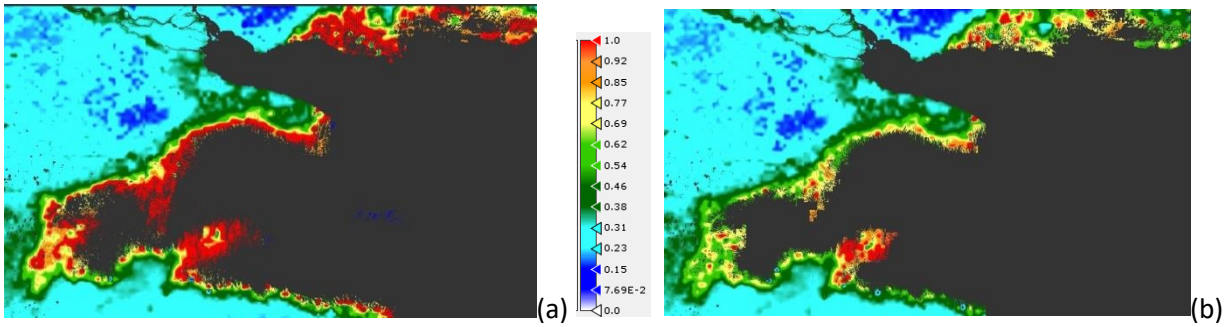

Figure 142 : SYN L2 Aerosol Optical Thickness derived from (a) 2017 - SYN L2 IPF and (b) updated SYN L2 IPF – zoom on the Top-right side of the image

Similarly, snow pixels are now discarded from the aerosol retrieval module, i.e. during the creation of the macro-pixels database and will no longer affect the aerosol retrieval.

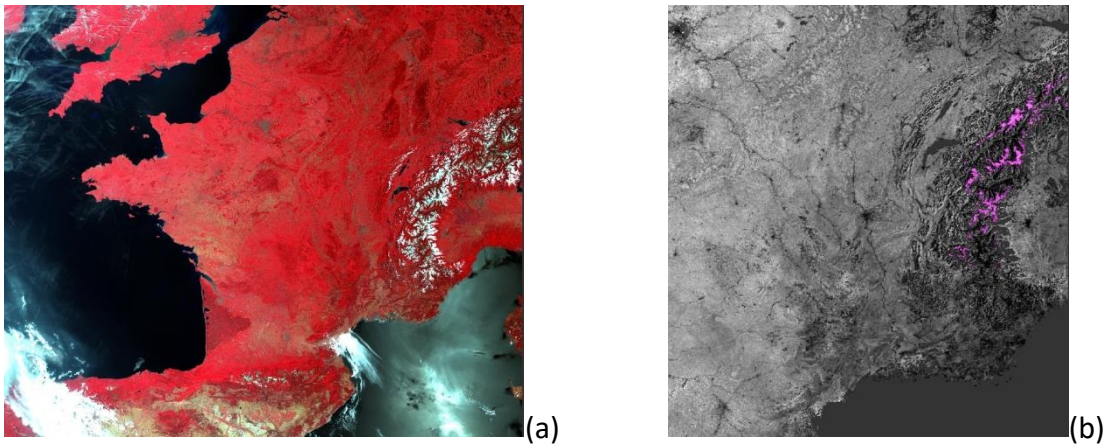
(a) (b)

Figure 143 : (a) RGB image from SLSTR L1b data over the clear-sky France scene. Snow cover is visible over the Alps on the right side of the image. The pixels detected as snow by the SYN L2 processing are represented in purple on the (b) SYN L2 SDR @865 nm – zoom on the right side.

The impact of this evolution can be seen on Figure 144 with a suppression of the high Aerosol values.

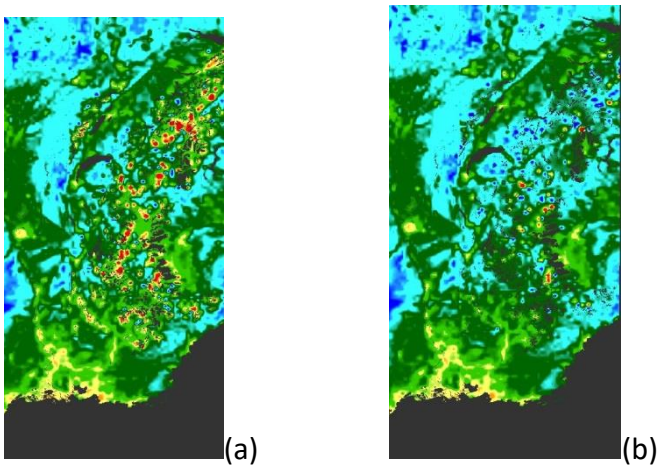
(a) (b)

Figure 144 : SYN L2 AOT@550nm provided by (a) 2017 - SYN L2 IPF and (b) updated SYN L2 IPF proving the impact of the rejection of the snow pixels from the aerosol retrieval.

7.2.1.2 Improvement of SYN VGT-P like products

These evolutions had two major impacts on VGT-P like gathered in Figure 146:

- A reduction of noise and an improvement of the geographical detail visible on VGT TOA reflectances
- An improvement of the status map with a better distinction between good and bad radiometry, cloud or clear-sky pixels.

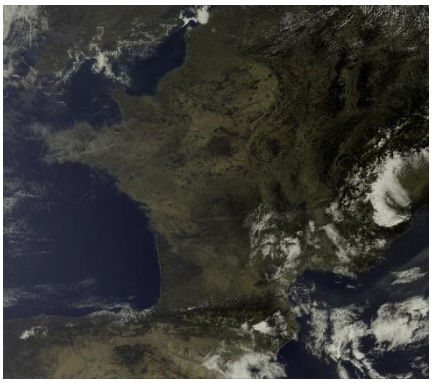

Figure 145 : OLCI L1 RGB on the scene used for verification in the following tables.

<table>
<tr><th>2017 SYN L2 status</th><th>Current SYN L2 VT-P like products</th></tr>
<tr><td colspan="2">Global improvement on B3 measurements - Visual aspect and differences between B3 TOA reflectances</td></tr>
<tr><td> 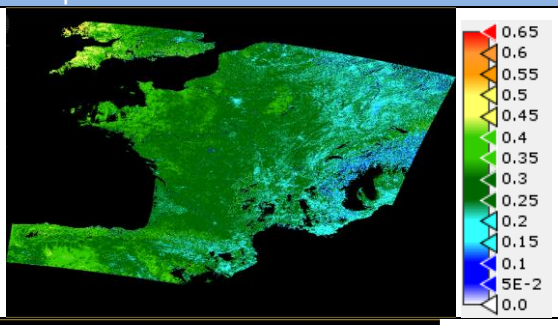
</td><td> 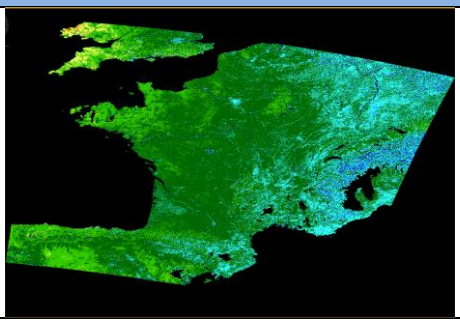 </td></tr>
<tr><td> 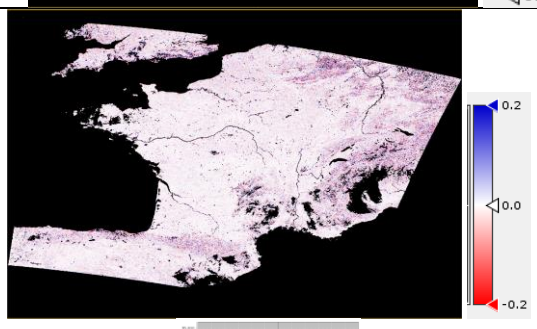

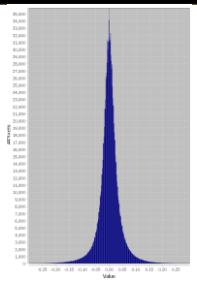
Difference [$B3_{before}$ – $B3_{after}$] : Visual aspect and histogram</td><td>Better handling of the border pixels (either close to coastline or close to cloud cover)
No drastic change in term of radiometry, except close to cloud coverage and snow pixels.</td></tr>
<tr><td colspan="2">Reduction of noise and smoother visual aspect – Zoom on MIR TOA reflectances over Devon and Cornwall regions</td></tr>
</table>

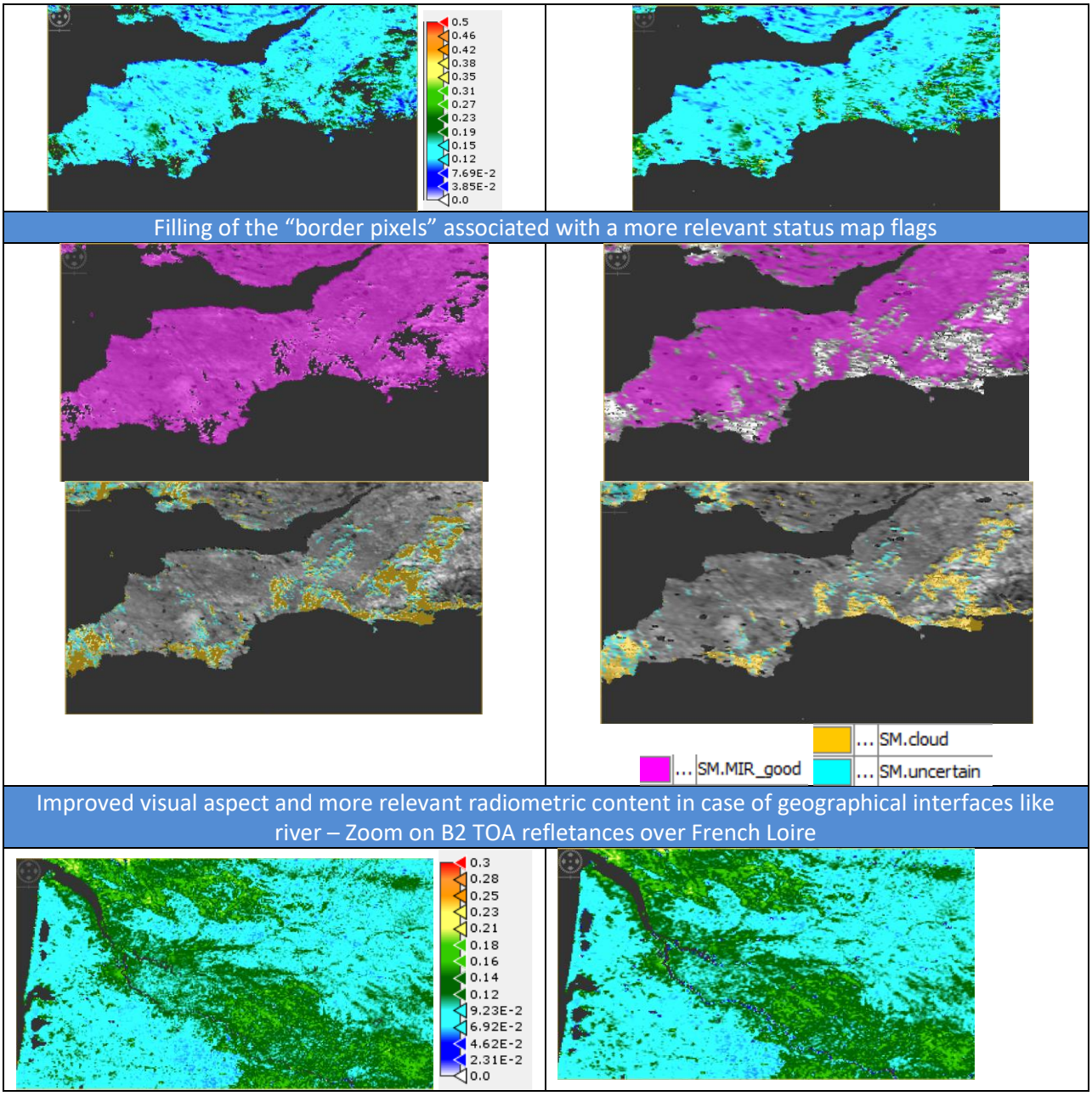

Figure 146 : Improvement of the overall quality of SYN L2 VGT-P products.

7.2.1.3 Improvement of SYN VGT-S like products

The improved selection rules for composite method can be observed on decadal composite with a reduction of noise and a more relevant and qualitative radiometric content.

In the following images, the daily composite has been performed only over the European zone from 23/09/2018 and 02/10/2018.

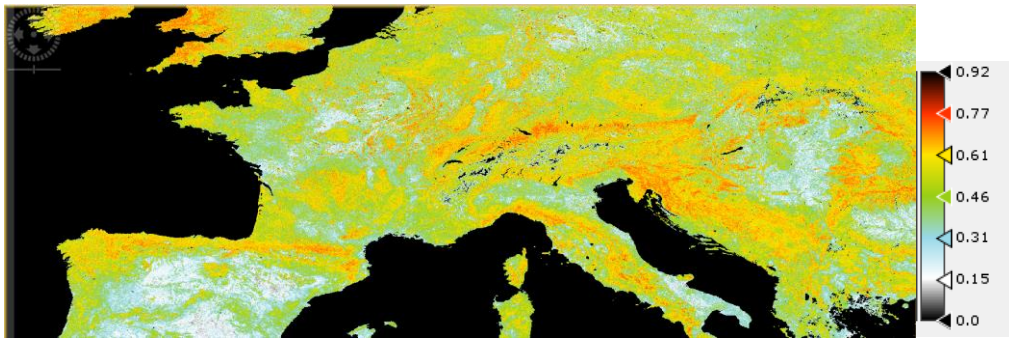

Figure 147 : Global aspect of NDVI provided by the decadal composite S3A_SY_2_V10____20180923T000000_20181002T235959_[..] using the 2017 version of IPF. Same colorbar is applied on Figure 147 and all following figures displaying NDVI.

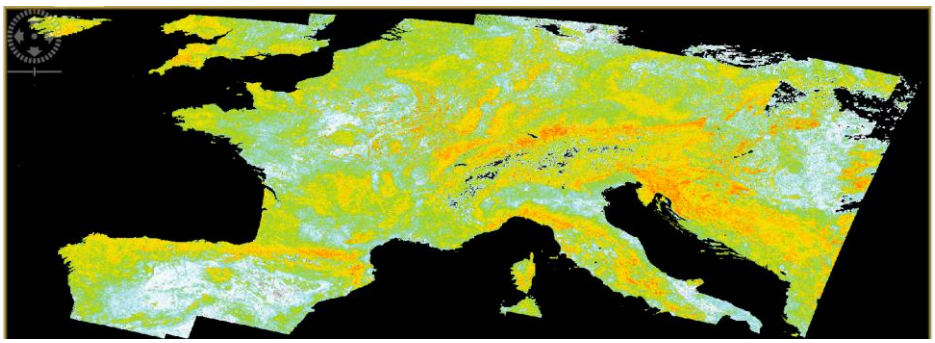

Figure 148 : Global aspect of NDVI provided by the decadal composite S3A_SY_2_V10____20180923T000000_20181002T235959_[..] using the current version of IPF.

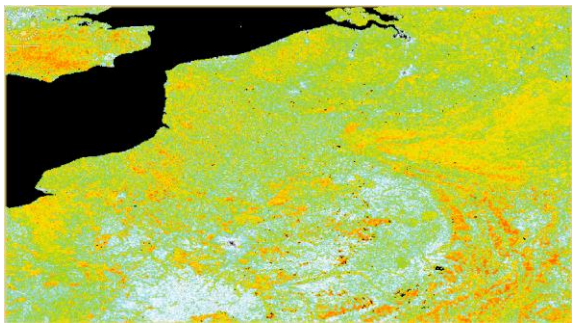
(a)
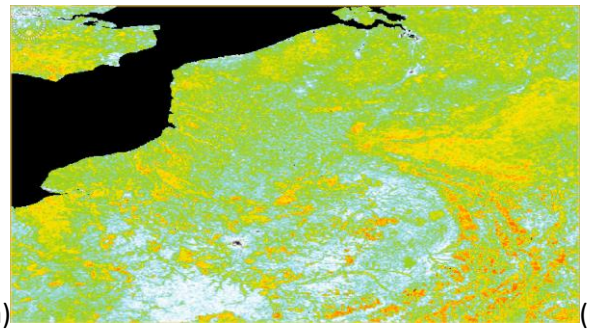
(b)

Figure 149 : Zoom on NDVI over North of France with (a) 2017 version of decadal composite and (b) the current version. The impact of selection rule is clear with lower but more relevant NDVI value in the second image.

7.2.2 SY_2_SYN Aerosol products and Surface Directional Reflectance

7.2.2.1 Methodology:

- The methodology consists in extracting the L2 SYN product in windows centred over AERONET test sites representing a large diversity of aerosol model, aerosol load and surface type, compare AOT retrieved from AERONET and SYN2 data, and finally compare atmospherically corrected reflectance using AERONET information and SYN 2 Surface Directional Reflectances.
- The tools needed are nominally, OLCI L1 and L2 SYN product extraction tool providing (~50x50 km) macro pixels around the AERONET sites preferably with the possibility to generate breakpoint outputs of the SYN algorithm, and raw analysis tools such as regression and statistics tool.

7.2.2.2 Results

Validation started when a first version of products with sufficient quality was produced within S3 MPC and delivered on 22th December 2017. It consisted of 1 week of global data. The data analysis is far from optimal because:

- Of the large data volume to handle
- Matchups with AERONET have to be done by ESL
- There is no link with corresponding L1 OLCI and L1 SLSTR, and thus difficulties to perform independent atmospheric correction, i.e. the key point to validate the surface reflectance SYN product
- The image reading within the SNAP environment is very long: a SYN2 orbit file took more than 10 minutes to open.

We first investigate AOT product, the most critical parameter.

- We looked at numerous flags and tried to find several combinations of them to select 'good' quality AOT products. We give an example of the product on Figure 150 with a first flag combination selection in order to filter out outliers. The overall feeling about the product is that the global coverage and the value range is correct but with obvious outliers, dubious spatial patterns and residual cloud contamination. We focus after on pixels for which the SYN 2 specific flags combination is valid: `!SYN.CLOUD & !SYN.PARTLY_CLOUDY & SYN.SUCCESS`.
- A regression analysis of SYN 2 AOT with AERONET coincident measurements was done for the whole test data set (1 week global). The location of the matchups is shown on Figure 151. After the selection of the good pixels, the cloud free matchups number is reduced from 155 to 53. The regression plots are shown in Figure 152. The correlation with AOT AERONET has improved and it gets closer to a quality standard for a best combination of flags, but it is at the cost of spatial cover and there is a very large bias (~0.2) and RMS (~0.3). It is clear that some cloud contamination remains.
- The AOT retrieval is done using a unique Aerosol model. That might be OK for use in atmospheric corrections, but it is less acceptable for an aerosol product.

- The uncertainty attached to the AOT exhibits unrealistic values.

Analysis of the Surface Directional Reflectances has just started, some spectra look realistic (see Figure 153), but:

- Unflagged outliers remain, as the behaviour of the flag SYN.SDR_OOR, which should detect out of range SDR, is dubious.
- The uncertainty attached to the SDR exhibits unrealistic values, and lots of NaN.
- For making progress in the SDR validation, it is mandatory to have child products, or directly NetCDF extraction of AOT, SDR's, L1B OLCI and SLSTR of 50x50 boxes around AERONET stations.

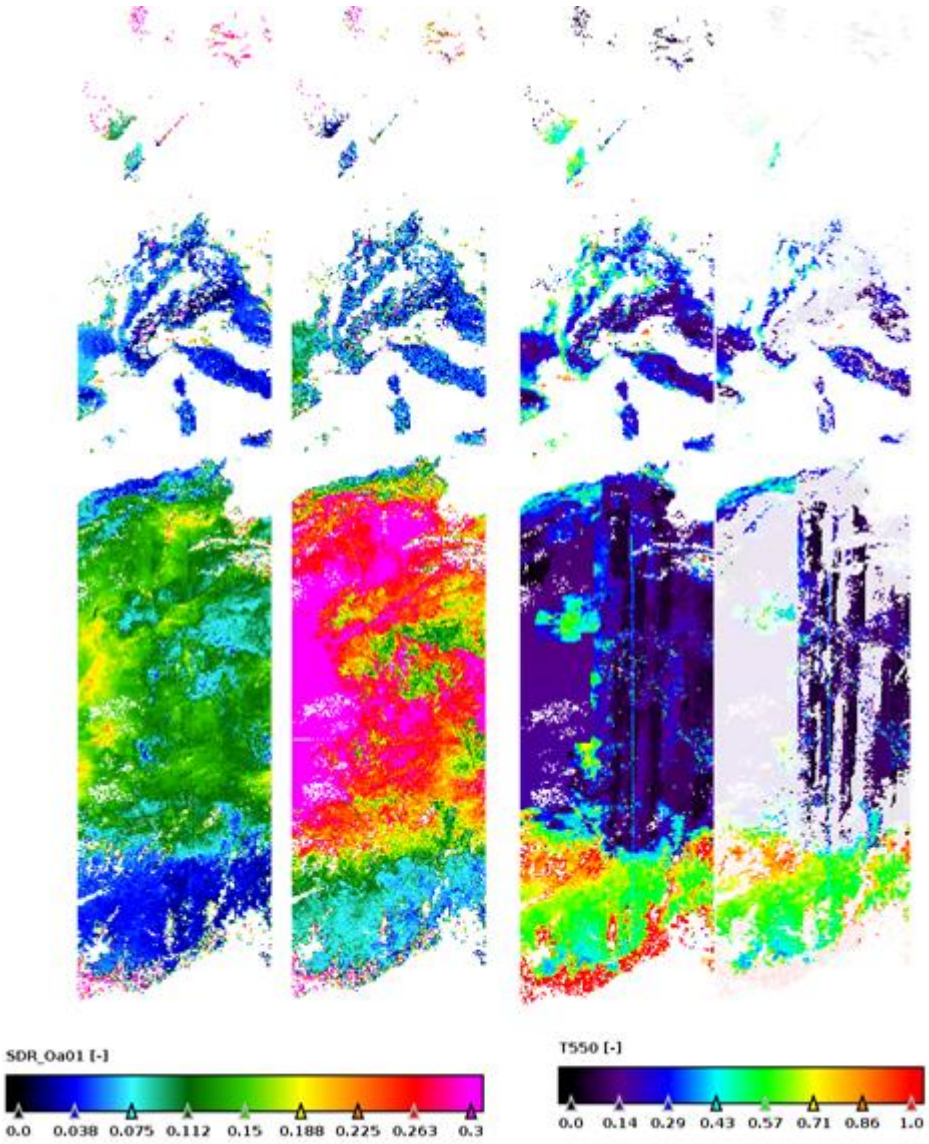

Figure 150: Example of SYN 2 orbit product over Sahara and Europe on 1st November 2016. (left) Surface Directional Reflectance (SDR) in OLCI band 1. (Middle) SDR in SLSTR band 1 Nadir. (Right) two AOT maps at 550 nm, one without and one with a white semi-transparent white mask added, selecting only pixels for which the SYN 2 specific flags combination is valid : !SYN.CLOUD & !SYN.PARTLY_CLOUDY & SYN.SUCCESS

!SYN.CLOUD

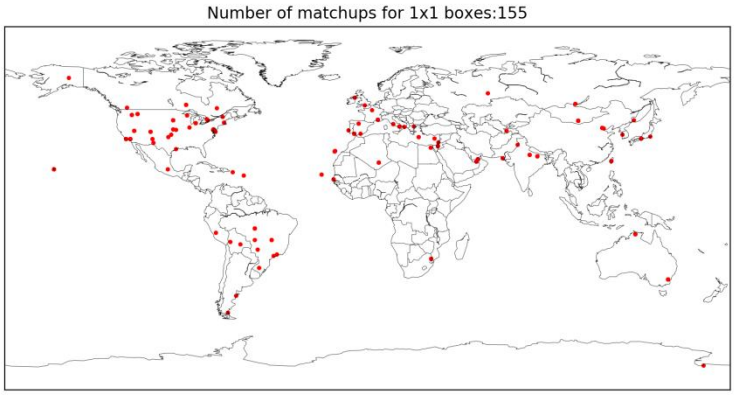

!SYN.CLOUD & !SYN.PARTLY_CLOUDY & SYN.SUCCESS

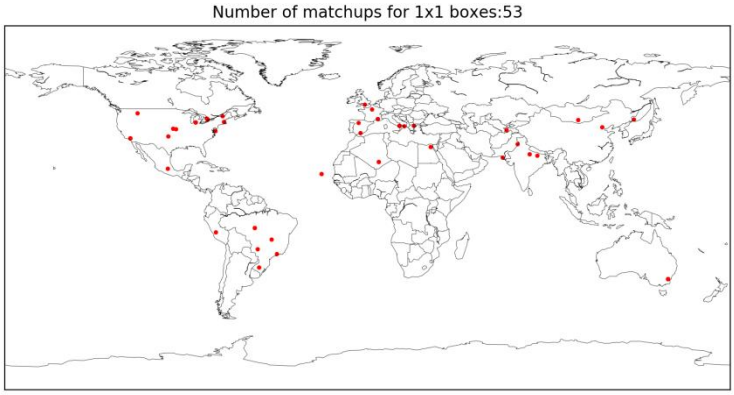

Figure 151: Locations of the SYN 2 AOT – AERONET matchups for one week of data starting on 1st November 2016. The matchups criteria are a coincident AERONET measurement in a +- ½ h window and a SYN 2 flag combination recalled above the plot.

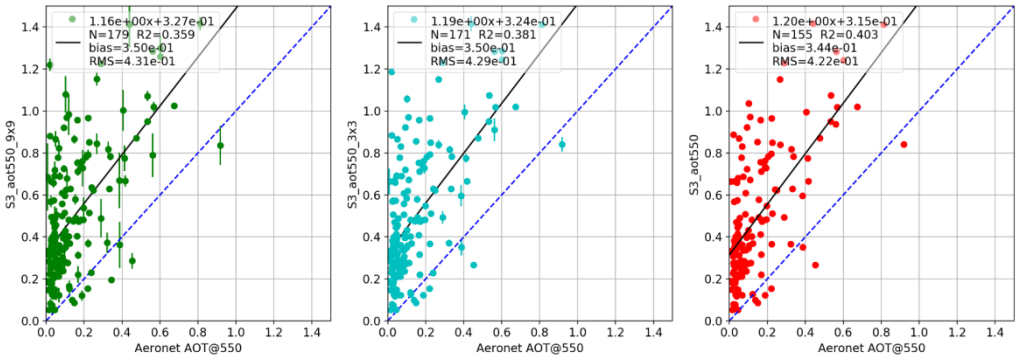

Selection : !SYN.CLOUD

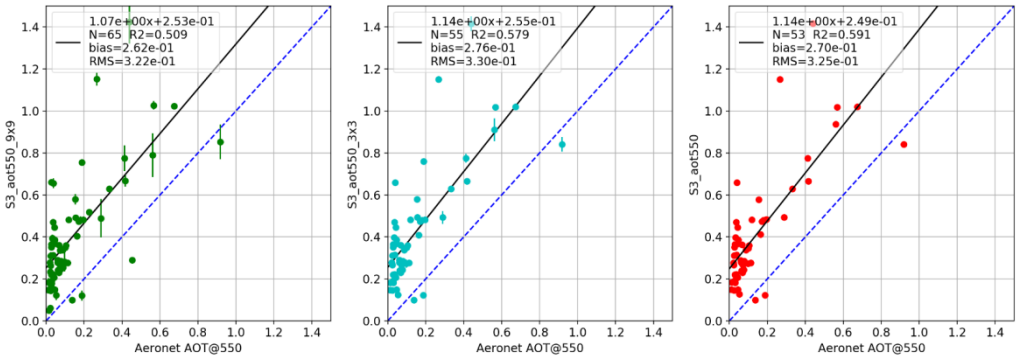

Selection : !SYN.CLOUD & !SYN.PARTLY_CLOUDY & SYN.SUCCESS

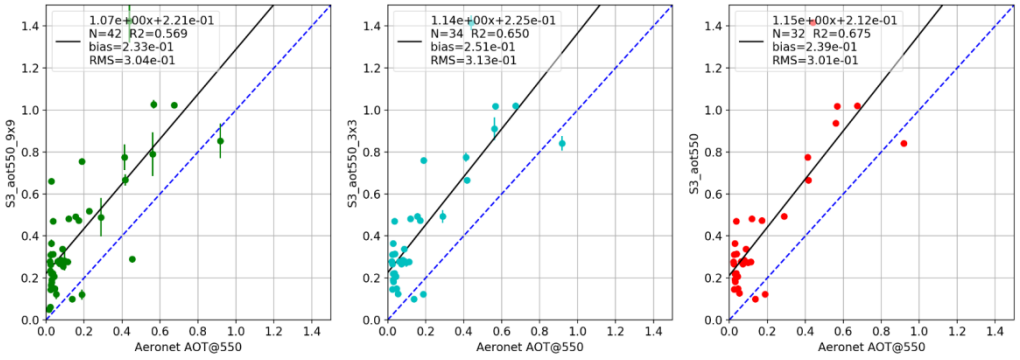

Selection : !SYN.CLOUD & !SYN.PARTLY_CLOUDY & SYN.SUCCESS & !SYN.TOO_LOW & !SYN.HIGH_ERROR & !SYN.NEGATIVE_CURVATURE & !SYN.AEROSOL_FILLED & !SYN.NO_SLO & !SYN.NO_SLN & !SYN.NO_OLC

Figure 152: AOT at 550 nm regressions between SYN 2 and AERONET data sets, for different selection rules of the SYN 2 pixels (top to bottom), and different sizes of the spatial averaging box for the SYN 2 data (from left to right : 9x9, 3x3 and 1x1 pixels boxes)

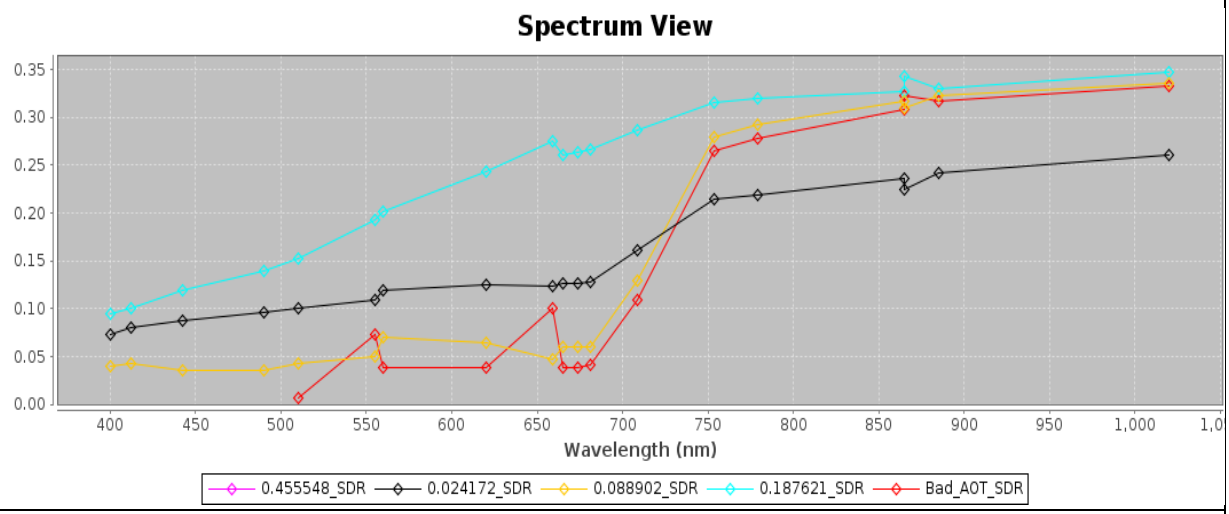

Figure 153: Spectra of the SDR for OLCI and SLSTR nadir bands for 4 pixels located in the AERONET matchups zones on 1st November 2016. (cyan) Tamanrasset, (black) Potenza, (orange) Rome, and (red) in Rome area where the SYN AOT retrieval looks dubious (labelled as 'Bad AOT'). The pink legend (Venice) has no corresponding spectrum as being above water it does not provide any SDR data. The AERONET mean AOT at 550 nm is indicated also in the legend of each curve (e.g. 0.024172_SDR means an average AOT of 0.024 at Potenza).

7.2.3 SY_2_VGP: consistency checks with PROBA-V Level2A

Preliminary consistency analysis was performed on a limited set of SY_2_VGP and PROBA-V Level2A segments.

7.2.3.1 Data and methods

Three S3A_SY_2_VGP segments were selected for the analysis (Table 28). For each of the segments, the corresponding PROBA-V Level2A segment was chosen. In all three cases, the S3A_SY_2_VGP segment overlaps with the 875 km wide swath of the right PROBA-V camera, which is tilted westwards, as is the case for OLCI. The viewing angles are therefore not expected to differ considerably, but this was not (yet) verified.

The S3A_SY_2_VGP status map shows very large areas with "SM.ice_or_snow = true". The status map was therefore not used to exclude pixels from the analysis. For PROBA-V L2A the status map was interpreted in order to exclude pixels labelled as cloud, snow/ice or water, or with bad radiometric quality or bad coverage in one of the spectral bands.

Table 28: Data used in the analysis

	Sentinel-3	**PROBA-V**
Segment	Reprocessed SYN data (IPF baseline 2.26, dd. 06/12/2017)	Collection 1, Level 2A
Oceania	S3A_SY_2_VGP____20161102T004347_20161102T012804_20171209T024702_2657_010_259_____LR1_R_NT_002.SEN3	PROBAV_L2A_20161102_012206_3_1KM_V102
Asia	S3A_SY_2_VGP____20161101T061252_20161101T065709_20171209T023146_2657_010_248_____LR1_R_NT_002.SEN3	PROBAV_L2A_20161101_062727_3_1KM_V102
North America	S3A_SY_2_VGP____20161107T170417_20161107T174834_20171211T235219_2657_010_340_____LR1_R_NT_002.SEN3	PROBAV_L2A_20161107_174339_3_1KM_V102

The geometric mean regression (GMR) model, i.e. an orthogonal regression model, is used to identify the relationship between the S3A_SY_2_VGP and the PROBA-V L2A TOA reflectances, because both data sets are subject to noise (Ji and Gallo, 2006). The GMR model minimizes the sum of the products of the vertical and horizontal distances (errors on Y and X) and is of the form

$$Y = a + b \cdot X \qquad (1)$$

with slope

$$b = sign(R)\frac{\sigma_Y}{\sigma_X} \qquad (2)$$

and intercept

$$a = Y - b \cdot X \qquad (3)$$

The σ_X and σ_Y are the standard deviations of X and Y, R is the correlation coefficient, and $sign()$ is the signum function that takes the sign of the variable between the brackets.

The coefficient of determination (R^2) indicates agreement or covariation between two data sets with respect to a linear regression model, summarizing the total data variation explained by this linear regression model.

$$R^2 = \left(\frac{\sigma_{X,Y}}{\sigma_X \cdot \sigma_Y}\right)^2 \qquad (4)$$

with $\sigma_{X,Y}$ the co-variation of X and Y. A disadvantage of R^2 is that it only measures the strength of the relationship between the data, but gives no indication if the data series have similar magnitude (Duveiller et al., 2016).

The Root Mean Squared Difference (RMSD) measures how far the difference between the two data sets deviates from 0 and is defined as:

$$RMSD = \sqrt{\frac{1}{n}\sum_{i=1}^{n}(X_i - Y_i)^2} \quad (5)$$

The RMSD expresses the overall difference, including random and systematic differences, in the same unit as the datasets themselves, i.e. % (TOA reflectance). The random and systematic differences are derived from the mean squared difference (MSD), defined as:

$$MSD = \frac{1}{n}\sum_{i=1}^{n}(X_i - Y_i)^2 \quad (6)$$

The MSD is further partitioned into the systematic mean product difference (MPD_s) and the unsystematic or random mean product difference (MPD_u), i.e. how much of the difference between X and Y is not 'explained' by the GMR model (Willmott, 1981). In order to be comparable to the RMSD in terms of magnitude, the root of the systematic and unsystematic mean product difference is used ($RMPD_s$ and $RMPD_u$):

$$RMPD_u = \sqrt{MPD_u} = \sqrt{\frac{1}{n}\sum_{i=1}^{n}\left(\left|X_i - \hat{X}_i\right|\right)\left(\left|Y_i - \hat{Y}_i\right|\right)} \quad (7)$$

with $\hat{X}_i$ and $\hat{Y}_i$ estimated using the GMR model fit and n the number of samples. Then,

$$RMPD_s = \sqrt{MSD - MPD_u} \quad (8)$$

The partitioning of the difference into systematic and unsystematic difference provides additional information to the RMSD on the nature of the difference between two data sets.

The Mean Bias Error (MBE) measures the average actual difference between two data sets and positive and negative differences between observations, and is defined as:

$$MBE = \frac{1}{n}\sum_{i=1}^{n}(X_i - Y_i) = \bar{X} - \bar{Y} \quad (9)$$

Although the MBE is not the best way to estimate the bias, it is used here because it retains the sign of the difference between the data sets, unlike the other metrics.

7.2.3.2 Results and discussion

Visual checks on the available S3A_SY_2_VGP products (20161101-20161107) showed that:

- Many segments show (very) little data content, with large areas labelled as 'NaN' in the spectral bands.
- Most pixels are labelled as 'ice_or_snow' in the SM (brown areas in Figure 154).
- The SM shows for most pixels a combination of 'ice_or_snow' and 'undefined', which is ambiguous.
- The 'NaN' pixel flagging in the spectral bands is unrelated to the information stored in the SM. It is not clear what is triggering the use of 'NaN' in the spectral bands, but it seems related to cloud or snow masking. TOA reflectance values should be available for pixels, regardless of clouds or snow cover (as is the case for SPOT-VEGETATION And PROBA-V). This allows the user to e.g. apply its own cloud/snow detection algorithms or perform analysis over snow pixels.

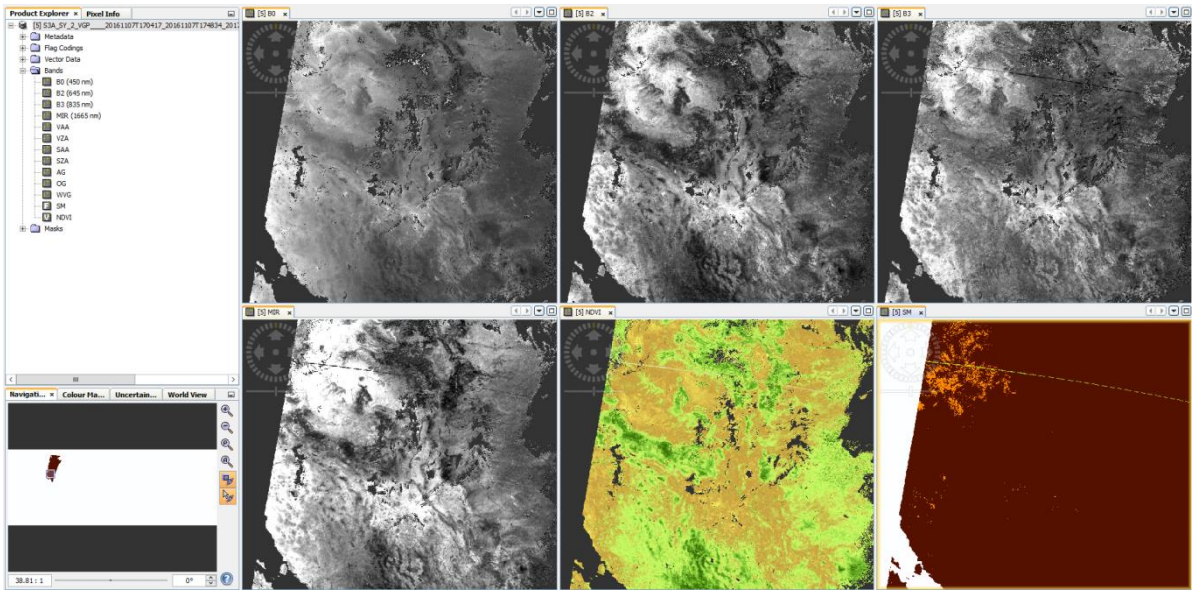

Figure 154 Visual checks on S3A_SY_2_VGP over the North America scene: 4 spectral bands, NDVI and SM (Brown = 254 = 1111 1110 = all 4 bands good quality, land, ice_or_snow, undefined; Orange = 250 = 1111 1010 = all 4 bands good quality, land, undefined; Green = 232 = 1110 1000 = bad SWIR, land, clear).

Figure 155 shows the results of geometric mean regression over the 3 segments and for the 4 spectral bands. Statistical analysis is summarized in Table 29.

For Blue, Red and NIR, correspondence is relatively high, with regression slopes close to 1, regression intercepts close to 0 and thus low systematic differences are found (below 3 %). The unsystematic differences (i.e. scatter around the regression line) are largest for the North America scene (around 5 %), possibly related to undetected clouds or snow, causing some scatter in the regression plots. The MBE fluctuates between positive and negative values, but remains in the range [-0.03; +0.02]. It is to be noted that differences might also be caused by different illumination conditions, related to different overpass

times between S3A and PROBA-V: in November 2016, the equator local overpass time of PROBA-V was around 10:41 a.m., while the overpass time of S3A is 10:00 a.m.

In contrast, the SWIR band shows very large systematic differences, with regression slopes in the range [1.4; 1.6] and systematic differences up to 17 % reflectance. The MBE is negative and in the range [-0.17; -0.13]: the PROBA-V L2A SWIR reflectance is systematically higher than S3 SYN VGP. It is not clear what is causing this discrepancy.

Table 29: Results of statistical analysis between S3A_SY_2_VGP and PROBA-V L2A TOA reflectances

	Segment	GMR intercept	GMR slope	R^2	MBE	RMSD	RMPDs	RMPDu	N
Blue	Oceania	0.069	0.640	0.49	-0.018	0.024	0.020	0.013	1178400
	Asia	0.038	0.962	0.70	-0.030	0.034	0.030	0.015	445455
	N. America	-0.019	0.983	0.54	0.023	0.054	0.023	0.049	188031
Red	Oceania	0.023	0.884	0.61	-0.003	0.030	0.006	0.029	1179641
	Asia	0.041	0.880	0.81	-0.012	0.023	0.014	0.019	447065
	N. America	-0.015	0.997	0.65	0.016	0.045	0.016	0.042	187386
NIR	Oceania	0.047	0.886	0.45	-0.021	0.043	0.022	0.037	1184469
	Asia	0.044	0.944	0.75	-0.030	0.037	0.030	0.022	447843
	N. America	-0.005	1.006	0.49	0.004	0.050	0.004	0.050	188636
SWIR	Oceania	0.067	1.599	0.48	-0.159	0.167	0.161	0.043	1176405
	Asia	0.082	1.476	0.70	-0.167	0.171	0.168	0.029	480847
	N. America	0.071	1.394	0.59	-0.129	0.138	0.131	0.044	191564

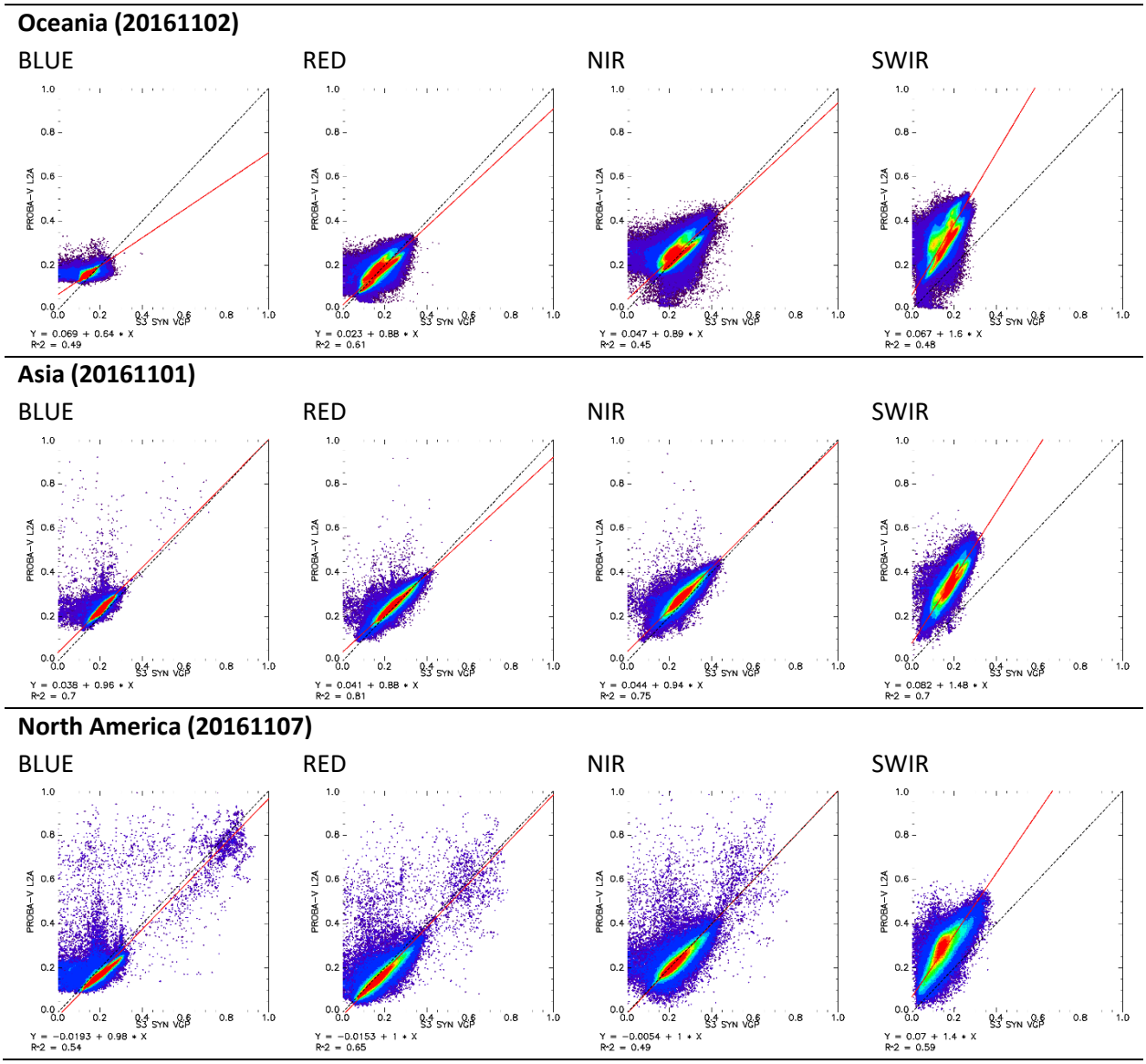

Figure 155 Geometric Mean Regression between S3_SYN_VGP and PROBA-V L2A TOA reflectances over the three segments

7.2.3.3 References

- Duveiller, G., Fasbender, D., Meroni, M., 2016. Revisiting the concept of a symmetric index of agreement for continuous datasets. Sci. Rep. 6, 1–14. doi:10.1038/srep19401
- Ji, L., Gallo, K., 2006. An agreement coefficient for image comparison. Photogramm. Eng. Remote Sens. 72, 823–833. doi:10.14358/PERS.72.7.823
- Sterckx, S., Benhadj, I., Duhoux, G., Livens, S., Dierckx, W., Goor, E., Adriaensen, S., Heyns, W., Van Hoof, K., Strackx, G., Nackaerts, K., Reusen, I., Van Achteren, T., Dries, J., Van Roey, T., Mellab, K., Duca, R., Zender, J., 2014. The PROBA-V mission: image processing and calibration. Int. J. Remote Sens. 35, 2565–2588. doi:10.1080/01431161.2014.883094
- Willmott, C.J., 1981. On the validation of models. Phys. Geogr. 2, 184–194.

8 Problems encountered in the reporting period

8.1 Product Notices Reports

Product notices are issued when a new processing baseline is deployed. Hereafter, for each instrument, the list of product notices issued are displayed.

8.1.1 OLCI

Table 30: List of OLCI Product Notices issued in 2019

Level	Thematic	Reference	Date of issue	Version	Last update	Comments
L2	Land	S3.PN.OLCI-L2L.02	25/01/2019	1.0		
L1	Global	S3.PN.OLCI-L1.05	21/05/2019	1.1	01/07/2019	PB 2.48 (S3A) and PB 1.20 (S3B)
L1	Global	S3.PN.OLCI-L1.06	30/07/2019	1.0		PB 2.55 (S3A) and PB 1.27 (S3B)
L1	Global	S3.PN.OLCI-L1.07	29/10/2019	1.0		PB 2.58 (S3A) and PB 1.30 (S3B)

8.1.2 SLSTR

Table 31: List of SLSTR Product Notices issued in 2019

Level	Thematic	Reference	Date of issue	Version	Last update	Comments
L2	Land	S3.PN.SLSTR-L2L.02	25/02/2019	1.0		
L1	Global	S3.PN.SLSTR-L1.04-R	01/10/2019	1.0		reprocessing PB 2.29 (S3A)
L1	Global	S3.PN.SLSTR-L1.07	25/11/2019	1.0		PB 2.59 (S3A) and PB 1.31 (S3B) - For TDS
L2	Land	S3.PN.SLSTR-L2L.03	25/11/2019	1.0		PB 2.56 (S3A) and PB 1.28 (S3B) - For TDS

8.1.3 SYN

Table 32: List of SYN Product Notices issued in 2019

Level	Thematic	Reference	Date of issue	Version	Last update	Comments
L2	Land	S3.PN.SYN-L2.03	27/02/2019	1.0		
L2	Land	S3.PN.SYN-L2.04	13/06/2019	1.0		PB 2.51 (S3A) and PB 1.23 (S3B)

8.2 Instrument anomalies

8.2.1 OLCI

The OLCI anomalies or events recorded by the S3MPC operators in 2019 are displayed in 2 forms:

- A calendar view, in Figure 156
- A table providing more details, in Table 33.

Sensor: OLCI
Year: 2019

Month	Day 1	2	3	4	5	6	7	8	9	10	11	12	13	14	15	16	17	18	19	20	21	22	23	24	25	26	27	28	29	30	31
January	A					B														B	A								A		
February						B									B		B														
March					A		B		B	A					B																
April					A			B									A		B										A	A	
May							A																	B				A	B	B	B
June	B								A	A				A														B			
July	B				B			A								A	B											B	B		
August							A																B								
September	B			A	A												A								B				B		
October							B					A					B	A		A										A	B
November				A								A			B			B		B							B				
December		A	B																					B							

This table indicates, for each calendar day, if an event occurred. Type of event is given below. Events affecting only S3A are tagged with 'A', events affecting only S3B are tagged with 'B' (nothing is displayed when it affects S3A and S3B). If both events occurred, the 2 colours are displayed in the cell. Readers are invited to consult the Product Notices related to each instrument.

Data Gap
Degradation or minor anomaly on product
Major anomaly

© S3MPC

Figure 156: OLCI anomalies/events in 2019

Table 33: List of OLCI anomalies in 2019

Date(s)	Event	Satellite		Description / Impact	Key words
		S3A	S3B		
01/01/2019	Missing frames	x		Missing frames due to RFI. Products including sensing period from 16:22:15 to 16:24:15 are affected	missing data frame isp RFI
04/01/2019	Data gap & Missing frames	x		Unstable signal caused uncorrectable frames. Products including sensing period from 04:57:18 to 05:15:18 are missing or degraded by missing frames	missing frame isp data gap svalbard
04/01/2019	Data gap & Missing frames		x	Sequencing errors and uncorrectable frames due to drop in signal. Products including sensing periods from 05:56:12 to 06:02:27 and from 06:22:14 to 07:32:15 are either missing or containing missing frames	missing frame isp data gap svalbard
05/01/2019	Missing frames	x		RFI from SuperView Products including sensing period from 20:04:01 to 20:07:01 are affected by missing frames	missing data frame isp RFI
05/01/2019	Data gap		x	Data gap from 21:17:52 to 23:55:53 No signal received due to antenna issue	missing frame isp data gap antenna
06/01/2019	Data gap		x	Data gap from 02:20:49 to 04:58:50 No signal received due to antenna issue	missing frame isp data gap antenna
20/01/2019	Missing frames		x	A few missing frames due to RFI FR products including sensing period from 07:21:50 to 07:24:50 are affected	missing data frame isp RFI
21/01/2019	Missing frames	x		A few missing frames due to RFI FR products including sensing period from 09:10:46 to 09:12:44 are affected	missing data frame isp RFI
29/01/2019	Missing frames	x		A band of about one hundred frames is missing due to RFI Products including sensing period from 07:25:39 to 07:27:39 are affected	missing data frame isp RFI
06/02/2019	Missing frames		x	A few frames missing due to RFI FR products including sensing period from 09:59:51 to 10:01:51 are affected	missing data frame isp RFI

Date(s)	Event	Satellite		Description / Impact	Key words
		S3A	S3B		
15/02/2019	Missing frames		x	A few frames missing due to RFI FR products including sensing period from 23:23:54 to 23:26:54 are affected	missing data frame isp RFI
17/02/2019	Missing frames		x	A few frames missing due to RFI FR products including sensing period from 20:33:27 to 20:35:27 are affected	missing data frame isp RFI
05/03/2019	Data gap (expected)	x		Due to instrument calibration, a gap is observed from 09:04:09 to 09:05:17	Instrument calibration data gap
05/03/2019	Missing frames	x		Missing frames due to RFI. FR L1-2 products including sensing period from 17:32:07 to 17:35:07 include one missing frame	missing data frame isp RFI
07/03/2019	Missing frames		x	Missing frames due to RFI Products including sensing period from 09:04:22 09:07:22 are affected	missing data frame isp RFI
09/03/2019	Data gap		x	Data gap from 05:29:21 to 08:07:27 No signal received due to antenna issue	missing frame isp data gap antenna
10/03/2019	Missing frames	x		Products including sensing period from 08:21:41 to 08:23:41 are affected by a large band of missing frames RFI with another spacecraft	missing data frame isp RFI
15/03/2019	Data gap (expected)		x	Due to instrument calibration, a gap is observed from about 09:05:31 to 09:08:00 depending on the product level	Instrument calibration data gap
05/04/2019	Data gap & Missing frames	x		Data gap from beginning of orbit, duration approx 537 seconds & missing frames. Partial data loss due to backend problems at the beginning of the pass.	missing data frame isp RFI
08/04/2019	Missing frames		x	Missing data detected for all product levels. Possible RFI from SKYMED4 at 16:47:33 and ALOS-2 16:52:54.	missing data frame isp RFI
17/04/2019	Missing frames	x		Missing frames due to RFI with SUPERVIEW-1. FR products including sensing period from 20:33:14 to 20:36:14 are affected.	missing data frame isp RFI

Date(s)	Event	Satellite		Description / Impact	Key words
		S3A	S3B		
19/04/2019	Missing frames		x	Missing frames due to RFI from Asnaro-2 Products including sensing period from 07:05:28 to 07:08:28 are affected	missing data frame isp RFI
29/04/2019	Data gap	x		Data gap from 14:05:51 to 16:43:30 No data received during downlink	no data downlink svl
30/04/2019	Missing frames	x		Missing frames due to predicted RFI from Alos 2. Products including sensing period from 16:57:52 to 17:00:52 are affected	missing data frame isp RFI
02/05/2019	Missing frames		x	Missing frames due to predicted RFI from Meteor M2 at 03:01:25utc.	missing data frame isp RFI
02/05/2019	Missing frames	x		Missing frames due to RFI, reported in CAMS, most likely RFI from Terra	missing data frame isp RFI
07/05/2019	Missing frames	x		Missing frames due to RFI, reported in CAMS Products including sensing period from 11:52:37 to 11:57:37 are affected	missing data frame isp RFI
24/05/2019	Missing frames		x	Sequence errors Products including sensing period from 00:13:58 to 00:19:58 are affected by missing frames	missing data frame sequencing error
28/05/2019	Missing frames	x		Missing frames due to RFI (Landsat 7), reported in CAMS. Products that include the sensing period 09:20:45 to 09:23:45 are affected by missing frames.	missing data frame isp RFI

Date(s)	Event	Satellite		Description / Impact	Key words
		S3A	S3B		
29/05/2019-31/05/2019	Data gap & Missing frames		x	Instrument error causing processing error due to data content (ground segment anomaly) Data gap covering sensing time L1/2: 20190529 13:46:40 to 20190531 12:21:52 (NRT) Data gap covering sensing time L1/2: 20190529 15:20:50 to 20190531 12:21:52 (NTC) Missing frames seen on NRT (NTC not yet recieved, to be checked)	instrument error data gap missing frames
01/06/2019	Missing frames		x	Missing frames due to RFI, reported in CAMS. Affecting sensing times 09:01:24 09:04:24.	missing data frame isp RFI
09/06/2019	Missing frames	x		Sequencing errors, impacting all VCIDs due to RFI from SkyMed 2 Products including sensing periods from 17:31:27 to 17:34:27	missing data frame isp RFI
10/06/2019	Missing frames	x		Sequencing errors and uncorrectable frames RFI from GCOM-C1 Products including sensing periods from 12:05:18 to 12:08:18	missing data frame isp RFI
13/06/2019	Missing frames		x	Sequencing errors and uncorrectable frames due to station controller (SCC) connection lost. Products including sensing periods from 03:17:11 to 03:20:11.	missing frames isp
13/06/2019	Missing frames	x		Missing frames due to RFI with known spacecraft (TDX-1). Products including sensing periods from 10:43:45 to 10:46:45.	missing data frame isp RFI
14/06/2019	Missing frames	x		Missing frames due to RFI with the sun. Products including these sensing periods impacted from 09:03:35 to 09:06:35.	missing data frame isp RFI
21/06/2019	Data gap (expected)	x		Due to instrument calibration, a gap is observed from 09:04:09 to 09:05:17	Instrument calibration data gap (S09)
21/06/2019	Missing frames		x	Missing frames have been observed in OLCI S3B products due to known RFIs with FORMOSAT 3E and SUPERVIEW-1. Products including these sensing periods impacted from 11:46:38 to 11:49:38.	missing data frame isp RFI
28/06/2019	Missing frames		x	Missing data detected for all product levels on 28/06/2019 due to RFI with sun. Products including these sensing periods impacted from 09:01:23 to 09:04:23 and 12:02:21 to 12:05:21.	missing data frame isp RFI

Date(s)	Event	Satellite		Description / Impact	Key words
		S3A	S3B		
01/07/2019	Data gap (expected)		x	Due to instrument calibration, a gap is observed from 09:05:47 to 09:06:56 in OLCI products.	Instrument calibration data gap (S09)
05/07/2019	Missing frames		x	Missing frames due to an RFI. Products with sensing times covering 20:40:00 to 20:43:00 are degraded.	missing data frame isp RFI
08/07/2019	Missing frames	x		Missing frames due to an RFI. Products with sensing times covering 20:07:03 to 20:10:03 aredegraded	missing data frame isp RFI
08/07/2019	Data Gap	x		A data gap from 13:48:23 to 19:47:59 has been detected for OLCI products. Missing frames have been detected for orbit 17651 products covering sensing period 14:45:01 to 14:46:59 are affected. Product with discarded NAVATT. Reported antenna issue at SVL.	data gap missing data frames
16/07/2019	Missing frames	x		Missing frames detected, cause unknown to date (22.07.2019) Products affected covering sensing time 08:18:40 to 08:21:40.	missing data frame unknown source
16/07/2019	Missing frames	x		Missing frames detected, cause unknown to date (22.07.2019) Products affected covering sensing time 09:59:39 to 10:02:39	missing data frame unknown source
17/07/2019	Data Gap		x	Data gap from 19:19:25 to 21:57:04. Antenna did not track the pass due to switch between backup to prime SCC.	data gap
29/07/2019	Missing frames		x	Sequencing errors caused from unpredicted RFI from CFOSAT. Products affected cover sensing times: 10:05:40 to 10:08:40.	missing data frame isp RFI
30/07/2019	Missing frames		x	Missing frames caused by SCC hardware disconnection at pass setup. Products affected coversensing times: 23:16:23 to 23:45:45.	missing data frame SCC hardware disconnect
07/08/2019	Missing frames	x		Missing frames due to an RFI with FORMOSAT-5. Products with sensing times covering 10:14:32 to 10:50:30 are degraded.	missing data frame isp RFI
23/08/2019	Missing frames		x	Missing frames due to an RFI with GCOM-C1. Products with sensing times covering 05:52:03 to 05:55:03 are degraded.	missing data frame isp RFI

Date(s)	Event	Satellite		Description / Impact	Key words
		S3A	S3B		
01/09/2019	Missing frames		x	Missing frames due to an RFI with RE1. Products with sensing times covering 09:01:21 to 09:04:21 are degraded.	missing data frame isp RFI
04/09/2019	Missing frames Data Gap	x		Missing frames due to drop in signal strength caused by snow on radome. Products with sensing times covering 10:12:19 to 10:18:19 are degraded. A data gap is also present from 10:14:56 to 10:17:37.	missing data frame data gap
05/09/2019	Discarded Navatt Data Gap	x		Discarded NAVATT for products covering sensing times 07:36:01 to 08:20:09. Missing data for RO/034 & AO/18487 (in products) from 04:58:09 to 07:36:01 due to an antenna not running	discarded navatt data gap antenna
17/09/2019	Missing frames	x		Missing frames due to an RFI with SuperView-1. Products with sensing times covering 21:09:51 to 21:12:51 are degraded.	missing data frame isp RFI
26/09/2019	Data gap Missing frames		x	PDHU Memory Scrubbing activity impact Data gaps have been are observed on 26/09/2019 for NTC products covering periods: 08:13:20 - 11:19:22 3h 11:51:39 - 11:51:57 18" 13:28:28 - 13:32:55 4' Invalid products detected : 26/09/2019 from 20:23:38 to 20:26:19 27/09/2019 from 01:17:35 to 01:20:35	PDHU Memory Scrubbing activity
30/09/2019	Missing frames		x	Missing frames due to an RFI with SuperView-1. Products with sensing times covering 10:20:33 to 10:23:33 are degraded.	missing data frame isp RFI
07/10/2019	Missing frames		x	Cause as yet not identified - suspected to be antenna issue. Products with sensing times covering 10:08:39 to 10:11:39 are degraded.	missing data frame isp antenna
07/10/2019	Data gap (expected)	x		Due to instrument calibration a gap is detected from 09:04:14 to 09:05:23.	Instrument calibration data gap (S09)
12/10/2019	Missing frames	x		Sequence errors have caused missing frames, predicted RFI with GOSAT IBUKI. Products covering sensing times 03:18:43 to 03:22:23 are degraded.	missing data frame isp RFI

Date(s)	Event	Satellite		Description / Impact	Key words
		S3A	S3B		
17/10/2019	Data gap (expected)		x	Due to instrument calibration a gap is detected from 09:05:41 to 09:07:41	Instrument calibration data gap (S09)
18/10/2019	Missing frames	x		Missing frames have been caused by an RFI with TERRA . Product sensing times affected are from 02:23:19 to 02:26:17.	missing data frame isp RFI
20/10/2019	Missing frames	x		Missing frames - cause was predicted RFI with Flock 4A. Product sensing times affected are from 17:00:48 to 17:03:48.	missing data frame isp RFI
30/10/2019	Data gap	x		Data gap caused by issue at ground segment level. Gap is present from 04:38:41 to 07:16:23.	data gap
31/10/2019	Missing frames		x	Missing frames have been caused by an RFI with SUPERVIEW-1. Product sensing times affected are from 09:34:13 to 09:37:13.	missing data frame isp RFI
04/11/2019	Missing frames	x		Missing frames have been caused by an RFI with SUPERVIEW-1. Product sensing times affected are from 12:30:03 to 12:33:03.	missing data frame isp RFI
12/11/2019	Missing frames	x		Missing frames have been caused by an RFI with Landsat-7. Product sensing times affected are from 08:23:45 to 08:27:35.	missing data frame isp RFI
15/11/2019	Missing frames		x	Missing frames have been caused by an RFI with SKYMED 1. Product sensing times affected are from 14:48:26 to 14:51:26.	missing data frame isp RFI
18/11/2019	Missing frames		x	Missing frames have been caused by an RFI with TERRA. Product sensing times affected are from 01:45:59 to 01:48:59.	missing data frame isp RFI
20/11/2019	Missing frames		x	Missing frames detected, RFI with 0 CFOSAT. Products with sensing times affected are from 11:02:33 to 11:05:33.	missing data frame isp RFI
27/11/2019	Missing frames		x	Missing frames detected due to RFI collision with Terra Products with sensing times affected are from 23:17:10 to 23:23:10.	missing data frame isp RFI
02/12/2019	Missing frames	x		Missing frames diue to a reoccurrence of the PDHU Dump Error Anomaly. Products with sensing times affected are from 04:58:51 to 05:01:51.	PDHU Dump error anomaly
02/12/2019	Missing frames	x		Missing frames detected due to RFI with Skysat-A. Products with sensing times affected are from 23:20:42 to 23:26:42.	missing data frame isp RFI

Date(s)	Event	Satellite		Description / Impact	Key words
		S3A	S3B		
03/12/2019	Missing frames		x	Missing frames detected for OLCI, cause reported as probable snow on radome Products with sensing times affected are from 10:49:09 to 10:52:09.	missing data frame
24/12/2019	Missing frames		x	Missing frames due to RFI with SUPERVIEW-1 Products with sensing times affected from: 21:33:10 to 22:06:50	missing data frame isp RFI

8.2.2 SLSTR

The SLSTR anomalies or events recorded by the S3MPC operators in 2019 are displayed in 2 forms:

- A calendar view, in Figure 157
- A table providing more details, in Table 34

Sensor: SLSTR
Year: 2019

Month	Day 1	2	3	4	5	6	7	8	9	10	11	12	13	14	15	16	17	18	19	20	21	22	23	24	25	26	27	28	29	30	31
January	A				B															B	A								A		
February						B							B				B										A				
March					A		B		B	A			A																		
April		B			A			B			B	B	B	B	B	B	B|A		B										A		
May							A													A	A	A	A	A|B	A	A					
June				A	B									A						B		B						B			
July					B			A					A			A	B												B	B	B
August							A																B								
September	B		B	B	A	A											A		B	B	B	B	B	B	B	B	B			A	
October							B			B		A			A	B		A												A	B
November												A| B			B			B		B											
December		A							B		A							B					A	B							

This table indicates, for each calendar day, if an event occurred. Type of event is given below. Events affecting only S3A are tagged with 'A', events affecting only S3B are tagged with 'B' (nothing is displayed when it affects S3A and S3B). If both events occurred, the 2 colours are displayed in the cell. Readers are invited to consult the Product Notices related to each instrument. In case of ***Decontamination***, data are usually not available; if they are, they shall not be used.

- Data Gap
- Degradation or minor anomaly on product
- Major anomaly
- Decontamination

© S3MPC

Figure 157: SLSTR anomalies/events in 2019

Table 34: List of SLSTR anomalies in 2019

Date(s)	Event	Satellite		Description / Impact	Key words
		S3A	S3B		
JANUARY					
01/01/2019	Missing data	x		Productswith missing data 16:30:46 to 16:35:37	svalbard
04/01/2019	Missing data	x		Productswith missing data 05:12:18 to 05:38:38	svalbard
04/01/2019	Missing data		x	Productswith missing data 05:52:48 to 06:28:48	svalbard
05/01/2019	Data gap & Pointing errors		x	Production gaps and degraded products surrounding: 20190105: 21:53:04 to 23:43:35 (110') pointing errors: NRT: 28 SL_1 and 28 SL_2 (20190105 23:43:35 to 20190106 06:08:25) NTC: 64 SL_1 and 4 SL_2 (20190105 23:43:35 to 20190106 06:32:25)	svalbard
06/01/2019	Data gap & Pointing errors		x	Production gaps and degraded products surrounding: 20190106: 02:57:51 to 04:47:54 (110') pointing errors: NRT: 28 SL_1 and 28 SL_2 (20190105 23:43:35 to 20190106 06:08:25) NTC: 64 SL_1 and 4 SL_2 (20190105 23:43:35 to 20190106 06:32:25)	svalbard
20/01/2019	Missing data		x	Products with missing data 07:30:50 to 07:36:50	rfi, svalbard
21/01/2019	Missing data	x		Products with missing data 09:07:09 to 09:07:09	rfi, svalbard
29/01/2019	Missing data	x		Products with missing data 07:30:42 to 07:36:42	rfi, svalbard
FEBRUARY					
06/02/2019	Missing data		x	Products with missing data 10:05:40 to 10:11:40	rfi, svalbard
13/02/2019	Pointing errors		x	Products affected from 08:25:22 to 11:47:21	manoeuvre, pointing
17/02/2019	Missing data		x	Products with missing data between 21:14:34 to 21:23:34	rfi, svalbard
27/02/2019	Pointing errors	x		Products affected from 09:01:19 to T11:05:17	manoeuvre, pointing

Date(s)	Event	Satellite		Description / Impact	Key words
		S3A	S3B		
MARCH					
05/03/2019	Missing data	x		Products affected from18:05:07 to 18:11:07	rfi, svalbard
07/03/2019	Missing data		x	Products affected from 09:10:22 to 09:16:22	rfi, svalbard
09/03/2019	Missing data		x	Gap between 06:15:23 and 08:03:59, products at margins degraded pointing errors due to missing navatt from 08:06:00 to 09:26:00	svalbard, pointing
10/03/2019	Missing data	x		Affected between 08:13:15 and 08:25:15 with a small gap between 08:17:14 and 08:21:35	rfi, svalbard
13/03/2019	Pointing errors	x		Due to a planned out-of-plane manoeuvre products affected: NRT from 07:51:41 to 10:01:40; NTC from 06:58:56 to 10:22:40	manoeuvre, pointing
26/03/2019	Missing data	x		Due to commanding of S3A_RIO_OPER_0061 - SLSTR FEE S8 + S9 T_START (S3A_RIO_OPER_0061) products with missing data between - 10:54:19 to 11:02:18 and - 15:57:16 to 16:05:16	instrument, commanding, rio
27/03/2019	Missing data	x		Due to commanding of SLSTR FEE S7 configuration (S3A_RIO_OPER_0061) products with missing data between - 08:47:09 to 08:52:08 and - 13:50:06 to 13:58:06	instrument, commanding, rio
APRIL					
02/04/2019	Missing data		x	L1-2 NR and NT products including sensing period from 19:24:31 to 19:30:31 are affected by few missing frames either on S3 or on S4 band	missing scans data S3 S4
05/04/2019	Data gap	x		Partial data loss due to backend problems in beginning of pass reported at Svalbard. Products including sensing period from 12:01:29 to 12:37:56 are either missing or affected by missing data	Gap missing data scans svalbard

Date(s)	Event	Satellite		Description / Impact	Key words
		S3A	S3B		
08/04/2019	Missing data		x	Missing data due to RFI with SKYMED4 Products including sensing period from 15:21:26 to 15:27:26 are affected by missing data	rfi, svalbard
10/04/2019	Data gap & Pointing errors	x		Products gap from 20190410T09:48:34 to 20190410T09:54:30 Pointing errors flag raised on products sensed from 20190410T09:54:30 to 20190410T14:57:48. L1 products have DISCARDED_NAVATT raised in their manifests	Gap missing data, pointing , navatt,SLT PAC
10/04/2019	Data gap & Pointing errors		x	Products gap from 20190410T09:08:58 to 20190410T09:15:12 Missing data for products including sensing period from 20190410T080507 to 20190410T090858 Pointing errors flag raised on products sensed from 20190410T123305 to 20190410T155919. L1 products have DISCARDED_NAVATT raised in their manifest	Gap missing data, scans , pointing , SLT PAC
11/04/2019 to 17/04/2019	SLSTR-B Decontamination		x	Instrument decontamination. Products missing or degraded from 11/04/2019 12:00:54 to 17/04/2019 03:27:00	Decontamination
17/04/2019	Missing data	x		RFI from SUPERVIEW-1 reported on CAMS Products including sensing period from 21:18:14 to 21:27:14 are affected	rfi, svalbard
19/04/2019	Missing data		x	RFI from Asnaro-2 reported on CAMS Products including sensing period from 07:17:28 to 07:23:28 are affected	rfi, svalbard

Date(s)	Event	Satellite		Description / Impact	Key words
		S3A	S3B		
27/04/2019	Missing data	x		Missing data due to acquisition issue. Products including sensing period from 10:44:28 to 10:50:28 and from 12:29:07 to 12:31:27 are affected Note that this is an IPF issue which should be fixed when these products will be reprocessed in the future	acquisition, svalbard
29/04/2019	Data gap & degraded products	x		No SLSTR data available from 14:57:09 to 16:41:26 (data gap) Products including sensing period from 14:52:04 16:42:03 include missing data (5 NTC products) Products including sensing period from 16:41:26 to 18:23:02 affected by pointing errors (geolocation affected)	product gap missing data pointing navatt
MAY					
02/05/2019	Missing data		x	Sequence errors observed at SVL Products including sensing period from 02:42:04 to 02:51:04 are affected by missing data	sequence error, svalbard
02/05/2019	Missing data	x		Missing data due to RFI Products including sensing period from 23:36:27 to 23:45:27 are affected by missing data	rfi, svalbard
07/05/2019	Missing data	x		Missing data due to RFI Products including sensing period from 13:00:36 to 13:06:36 are affected by missing data	rfi, svalbard

Date(s)	Event	Satellite		Description / Impact	Key words
		S3A	S3B		
11/05/2019	Missing data		x	Degraded data due to processing issue Products including sensing periods from 10:42:20 to 10:48:20 or 12:27:00 to 12:29:19 are affected by missing data This issue should be fixed during the next reprocessing of the affected products	degraded data processing
20/05/2019 to 26/05/2019	SLSTR-A Decontamination	x		Instrument decontamination. Products missing or degraded from 20/05/2019 12:32:12 to 27/05/2019 11:48:06	Decontamination
24/05/2019	Missing data		x	Sequence errors Products including sensing period from 00:43:58 to 00:52:58 are affected by missing data	sequence error, svalbard
26/05/2019	Missing data	x		Missing data due to ground station issue Products including sensing period from 18:17:03 to 18:23:03 are affected by missing data	svalbard
28/05/2019	Missing data	x		Missing data due to RFI Products including sensing period from 09:56:45 to 10:05:45 are affected by missing data	rfi, svalbard
JUNE					
04/06/2019	Missing data	x		Missing data due to reoccurrence of AR/2202, PDHU PS dump corrupted (SLSTR packet affected) Products including sensing period from 08:28:27 to 08:34:27 are affected by missing data	dump packet corrupted
05/06/2019	Pointing errors		x	Products degraded by pointing errors due to planned satellite manoeuvre Products sensed from 06:40:39 to 08:24:38 are affected by the issue.	in-plane manœuvre, pointing, geolocation

Date(s)	Event	Satellite		Description / Impact	Key words
		S3A	S3B		
09/06/2019	Missing data	x		Missing data due to RFI from SkyMed 2 Products including sensing period from 18:07:27 to 18:13:27 are affected by missing data	rfi, svalbard
10/06/2019	Missing data	x		Missing data due to RFI from GCOM-C1 Products including sensing period from 12:35:18 to 12:41:18 are affected by missing data	rfi, svalbard
13/06/2019	Missing data		x	Sequencing errors and uncorrectable frames due to station controller (SCC) connection lost Products including sensing period from 03:38:11 to 03:44:11 are affected by missing data	sequence error, svalbard, station controller (SCC)
13/06/2019	Missing data	x		Missing data due to RFI with known spacecraft (TDX-1) Products including sensing period from 11:07:45 to 11:13:45 are affected by missing data	rfi, svalbard
14/06/2019	Pointing errors	x		Pointing errors (Nadir+Oblique) and "manœuvre" flag raised due to in-plane-manoeuvre Products including sensing period from 07:12:46 to 10:37:45 are degraded	manoeuvre, pointing
19/06/2019	Pointing errors		x	Products degraded due to planned satellite manoeuvre Level 1 products sensed from 05:37:02 to 09:02:01 are flagged with "manœuvre" tag and include pointing errors flag. Geolocation accuracy is affected	in-plane manœuvre, pointing, geolocation
21/06/2019	Missing data		x	Missing data due to RFIs Products including sensing period from 12:51:37 to 12:57:37 are affected by missing data	rfi, svalbard
28/06/2019	Missing data		x	Missing data due to RFIs with FormoSat 5 Products including sensing period from 12:44:21 to 12:50:21 are affected by missing data	CGS PACs connectivity
JULY					
05/07/2019	Missing data		x	Missing data due to RFI Products including sensing period from 21:13:00 to 21:22:00 are affected by missing data	rfi, svalbard

Date(s)	Event	Satellite		Description / Impact	Key words
		S3A	S3B		
08/07/2019	Missing data	x		Missing data due to RFIs Products including sensing period from 21:15:03 are 21:24:03 affected by missing data	rfi, svalbard
08/07/2019	Data gap & Degraded products	x		Due to an antenna failure, a large data gap is observed on 08/07/2019 from 14:46:58 to 19:46:50. Besides, products generated and including sensing periods from 14:40:06 to 21:30:03 are degraded either by missing data, pointing errors, or both issues.	gap, degraded, antenna
13/07/2019	Pointing errors	x		Geolocation accuracy degraded due to missing TM_0_NAT. Issue at satellite level Products with sensing period from 07:35:13 to 11:00:12 are affected by the issue	pointing, Navatt, TM_0_NAT
16/07/2019	Missing data	x		Missing data on products. Loss of frames during acquisition. Products with sensing period from 09:29:39 to 09:38:39 and from 11:16:38 to 11:22:38 are affected by the issue	sequencing error
17/07/2019	Data gap & Degraded products		x	Signal not properly received by antenna: a large data gap is observed from about 20:14 to 21:55. Besides products generated but within sensing period from 20:04:48 to 23:38:46 are degraded either by missing data, pointing errors, or both issues.	antenna data gap degradation
29/07/2019	Missing data		x	Missing data due to RFI Products including sensing period from 10:14:40 to 10:20:40 are affected by missing data	rfi, svalbard
30/07/2019	Missing data		x	Missing data due SCC hardware disconnection at pass setup Products including sensing period from 23:52:23 are affected by missing data	SCC hardware

Date(s)	Event	Satellite		Description / Impact	Key words
		S3A	S3B		
31/07/2019	Missing data		x	Missing data due SCC hardware disconnection at pass setup Products including sensing period until 00:01:23 are affected by missing data	SCC hardware
AUGUST					
07/08/2019	Missing data	x		Missing data due to RFI from FORMOSAT-5 Products including sensing period from 10:26:32 to 10:32:32 are affected by missing data	rfi, svalbard
23/08/2019	Missing data		x	Missing data due to RFI from GCOM-C1 Products including sensing period from 05:49:03 to 05:58:03 are affected by missing data	rfi, svalbard
28/08/2019	Degraded products & pointing errors		x	SLSTR products degraded by a planned in-plane-manœuvre. Reduced data quality for SLSTR from 09:50 to 12:06.	in-plane manœuvre
28/08/2019	Degraded products & pointing errors	x		SLSTR products degraded by a planned out-of-plane-manœuvre. Reduced data quality for SLSTR from 12:02 to 14:25.	out-of-plane manœuvre
SEPTEMBER					
01/09/2019	Missing data		x	Missing data due to RFI from RapidEye-1 . Products including sensing period from 10:12:21 to 10:18:21 are affected by missing data.	rfi, svalbard
03/09/2019	Degraded products		x	Data degraded due to blackbody crossover test covering sensing times from 03/09/2019 09:30	instrument-special-operation
04/09/2019	Degraded products		x	Data degraded due to blackbody crossover test covering sensing times until 04/09/2019 20:30.	instrument-special-operation
05/09/2019	Missing data & Data Gap	x		S3A SLSTR data gap found due to antena failure at Svalbard station between 05:54 and 07:36. PDU before and after degraded. Missing navatt files between 04:10:10 to 09:19:08.	antenna data gap degradation missing navatt

Date(s)	Event	Satellite		Description / Impact	Key words
		S3A	S3B		
05/09/2019	Degraded products	x		Data degraded due to blackbody crossover test covering sensing times from 05/09/2019 09:15	instrument-special-operation
06/09/2019	Degraded products	x		Data degraded due to blackbody crossover test covering sensing times until 06/09/2019 18:30.	instrument-special-operation
17/09/2019	Missing data	x		Missing data due to an RFI with SuperView-1. Products including sensing period from 21:45:51 to 21:54:51 are degraded by missing data	rfi, svalbard
19/09/2019 to 25/09/2019	SLSTR-B decontamination		x	Instrument decontamination Products are missing or degraded from sensing time 20190917T055317 to 20190925T114107	decontamination
26/09/2019	Data gap & Degraded products		x	PDHU Memory Scrubbing activity impact Products from sensing time 20190926T090643 can be missing (=data gap) or affected by pointing errors or missing data in products (=degraded products)	PDHU Memory Scrubbing activity
27/09/2019	Data gap & Degraded products		x	PDHU Memory Scrubbing activity impact Products until sensing time 20190926T021934 can be missing (=data gap) or affected by pointing errors or missing data in products (=degraded products)	PDHU Memory Scrubbing activity
30/09/2019	Missing data	x		Missing data due to an RFI with SuperView-1. Products including sensing period from 10:38:33 to 10:47:33 are affected by missing data	rfi, svalbard
October					
07/10/2019	Missing data		x	Missing data in products. Products including sensing period from 10:04:38 to 10:10:38 are affected by the issue.	

Date(s)	Event	Satellite		Description / Impact	Key words
		S3A	S3B		
10/10/2019	Pointing errors		x	Pointing errors due to satellite manœuvre. Products including sensing period from 10:04:38 to 10:10:38 are affected by the issue	manœuvre pointing
12/10/2019	Missing data	x		Missing data in products - sequencing error reported on CAMS. Products including sensing period from 03:10:23 to 03:16:23 are affected by the issue.	rfi, svalbard
15/10/2019	Degraded products	x		Degraded products due to planned satellite manœuvre. Products including sensing period from 06:25:49 to 06:39:48 are affected by missing data Products including sensing period from 06:57:48 to 08:41:47 are affected by pointing errors	manœuvre
16/10/2019	Pointing errors		x	Pointing errors due to planned satellite manœuvre. Products including sensing period from 05:51:58 to 09:16:57 are affected by the issue	manœuvre
18/10/2019	Missing data	x		Missing data due to an RFI with another spacefcraft. Products including sensing period from 02:14:17 to 02:23:17 are affected by missing data	rfi, svalbard
30/10/2019	Data gap & Degraded products	x		Ground segment anomaly Products including sensing period from 20191030T052502 to 20191030T071201 are either missing (=data gap) or degraded (pointing errors or missing data in products)	gap, degraded, pointing, missing

Date(s)	Event	Satellite		Description / Impact	Key words
		S3A	S3B		
31/10/2019	Missing data		x	RFI from SUPERVIEW-1 reported on CAMS Products including sensing period from 09:34:13 to 09:43:13 are affected by the issue	rfi, svalbard
November					
05/11/2019	Pointing errors	x	x	Pointing errors for SL_1_RBT NTC products due to missing Navatt. Navatt not available for processing due to a maintenance on PDGS side. S3A products from 20191105T093453 to 20191105T111852 affected (35 products) S3B Products from 20191105T085519 to 20191105T103918 affected (35 products)	pointing, Navatt, TM_0_NAT
12/11/2019	Missing data & Data Gap	x		S3A RFI causing data gap and missing frames Products from sensing time 20191112T080935 to 20191112T082735 are either missing or degraded	data gap, missing, RFI
12/11/2019	Missing data		x	RFI causing missing scans in products Products including sensing period from 16:57:58 to 17:03:58 are affected by the issue	rfi, svalbard
15/11/2019	Missing data		x	RFI causing missing scans in products Products including sensing period from 14:42:26 to 14:48:26 are affected by the issue	rfi, svalbard
18/11/2019	Missing data		x	RFI causing missing scans in products Products including sensing period from 01:39:59 to 01:48:59 are affected by the issue	rfi, svalbard
20/11/2019	Missing data		x	RFI causing missing scans in products Products including sensing period from 11:11:33 to 11:14:33 are affected by the issue	rfi, svalbard
27/11/2019	Pointing errors	x		Products degraded by pointing errors due to planned satellite manoeuvre Products sensed from 07:51:46 to 10:07:44 are affected by the issue	manœuvre, pointing, geolocation

Date(s)	Event	Satellite		Description / Impact	Key words
		S3A	S3B		
27/11/2019	Missing data		x	RFI causing missing scans in products Products including sensing period from 23:47:10 to 23:56:10 are affected by the issue	rfi, svalbard
December					
02/12/2019	Pointing errors	x		Pointing error flags raised on products as a consequence of PDHU dump anomaly. NAVATT are not missing then the issue could have no impact on products quality / geolocation accuracy. Products sensed from 04:28:51 to 09:36:04 are concerned	pointing, geolocation, PDHU
02/12/2019	Missing data	x		RFI causing missing scans in products Products including sensing period from 23:35:42 to 23:44:42 are affected by the issue	rfi, svalbard
09/12/2019	Missing data		x	Products including sensing period from 23:35:42 to 23:44:42 are affected by missing scans. Reason of the issue unknown	missing data scans
11/12/2019	Pointing errors	x		Pointing errors due to satellite manœuvre. Products including sensing period from 10:42:07 to 14:04:05 are affected by the issue	manœuvre pointing
18/12/2019	Pointing errors		x	Pointing errors due to satellite manœuvre. Products including sensing period from 06:59:23 to 10:24:22 are affected by the issue	manœuvre pointing
23/12/2019	Missing data	x		RFI causing missing scans in products Products including sensing period from 13:43:54 to 13:49:54 are affected by the issue	rfi, svalbard
24/12/2019	Missing data		x	RFI causing missing scans in products Products including sensing period from 21:51:10 to 22:00:10 are affected by the issue	rfi, svalbard

8.2.3 SYN

The SYN anomalies or events recorded by the S3MPC operators in 2019 are displayed in 2 forms:

- A calendar view, in Figure 158
- A table providing more details, in Table 35

Sensor: SYN
Year: 2019

Month	Day 1	2	3	4	5	6	7	8	9	10	11	12	13	14	15	16	17	18	19	20	21	22	23	24	25	26	27	28	29	30	31
January	A					B															A		A						A		
February						B							B		B		B										A				
March					A		B		B	A			B		B																
April					A			B		A	B	B	B	B	B	B	B|A		B										A		
May		B						A	A											A	A	A	A	A|B	A	A		A			
June					B				A										B												
July								A					A			A	B												B		
August																							B								
September	B		B	B	A	A													B	B	B	B	B	B	B	B				B	
October										B		A			A	B		A												A	B
November				A								A			B			B								A				
December		A									A							B												

This table indicates, for each calendar day, if an event occurred. Type of event is given below. Events affecting only S3A are tagged with 'A', events affecting only S3B are tagged with 'B' (nothing is displayed when it affects S3A and S3B). If both events occurred, the 2 colours are displayed in the cell. Readers are invited to consult the Product Notices related to each instrument.

Data Gap
SYN specific anomaly
OLCI or SLSTR anomaly which impacts SYN products

© S3MPC

Figure 158: SYN anomalies/events in 2019

Table 35: List of SYN anomalies in 2019

Date(s)	Satellite		Instrument			Impact/Description	Keywords
	S3A	S3B	OLCI	SLSTR	IPF SYN		
01/01/2019	x		o	o		Missing SDRs from OLCI and SLSTR inputs. 3 products, *1 over land, very small loss of data.	Missing data, Svalbard
04/01/2019	x		o	o		Missing SDRs from OLCI and SLSTR inputs. 10 products and gap. Located over ocean & land.	Missing data, Svalbard
04/01/2019		x	o	o		Missing SDRs from OLCI and SLSTR inputs. Products over land & ocean, total 3. gap.	Missing data, Svalbard
05 & 06/01/2019		x	o	o		Discarded navatt & gap reported, 34 products affected over land & ocean some missing SDRs noted.	Discarded navatt, missing data, Antenna, Svalbard
05/01/2019	x		o			Missing SDRs from OLCI input, 1 product over ocean	RFI, missing data, Svalbard
14/01/2019	x	x			o	Some products missing coverage / No coverage * 20 for S3A & S3B. To be updated for V10 and future product regeneration.	IPF update error
20/01/2019		x	o	o		Missing SDRs - 20/01/2019	RFI, Missing data, Svalbard
21/01/2019	x		o	o		Loss of SDR values in the SLSTR and OLCI input bands.	RFI, Missing data, Svalbard
23/01/2019	x				o	Loss of data for VG1 & V10 products (missing 1 orbit). gap for SYN/VGP & VGK products RO-289 AO-15277. Recovery not possible.	IPF update error
02/02/2020	x		o	o		Some missing data for SY_2_SYN products from OLCI (1) & SLSTR (2) inputs. 1 * VGP/VGK affected. 4 in total over land.	RFI, Missing data, Svalbard

Date(s)	Satellite		Instrument			Impact/Description	Keywords
	S3A	S3B	OLCI	SLSTR	IPF SYN		
06/02/2019	x	x	o	o		Missing SDRs over land * 3 products (1 OLCI input, 2 SLSTR input)	RFI, Missing data, Svalbard
13/02/2019		x		o		Products flagged with MANOEUVRE & DISCARDED NAVATT, missing data of vertical lines seen in all products. 2 orbits, impact over land & ocean.	Manœuvre, Missing data
15/02/2019		x	o			OLCI no_olc flag raised over 1 ocean product.	RFI, Missing data, Svalbard
17/02/2019		x	o			Loss of data from OLCI input	RFI, Missing data, Svalbard
27/02/2019	x			o		Possible geolocation impact since SLSTR input flagged pointing errors.	Manœuvre
28/02/2019		x			o	Gap from 12:48:01 to 15:26:10	gap, PDGS/Processing issue
05/03/2019	x		o	o		Missing data in SYN products, 1 product over the ocean so minimal impact	RFI, Missing data, Svalbard
05/03/2019	x		o			A gap for Synergy L2 products, and split products are noted due to an S09 OLC calibration. Impact can be observed in all products but is expected and cannot be recovered.	OLCI Calibration, split orbit, missing data, gap
05/03/2019	x		o	o		Missing data from SLSTR input in SY_2_SYN products and missing orbit 107 as input into VG1 & V10 products.	Missing data, Svalbard
06/03/2019		x			o	Gap from 03:26:18 to 06:04:25	gap, PDGS/Processing issue

Date(s)	Satellite		Instrument			Impact/Description	Keywords
	S3A	S3B	OLCI	SLSTR	IPF SYN		
07/03/2019		x	o	o		Missing data for two products over land one missing OLCI frames the other missing SLSTR scans.	RFI, Missing data, Svalbard
09/03/2019	x				o	Gap from 02:46:49 05:24:54	gap, PDGS/Processing issue
09/03/2019		x	o	o		Missing data in SYN products showing as vertical line. Discarded navatts may impact geolocation.	Antenna, Svalbard, missing data, gap
10/03/2019	x		o	o		Missing data from OLCI & SLSTR inputs.	RFI, Missing data, Svalbard
13/03/2019		x		o		Potentially missing data and degraded geolocation.	Manœuvre, missing data
15/03/2019		x	o			Missing data, split orbits and a gap due to short PDUs	OLCI Calibration, split orbit, missing data, gap
21/03/2019	x				o	Gap from 02:34:10 to 05:12:09	gap, PDGS/Processing issue
22/03/2019	x				o	Gap from 02:07:52 to 04:45:50	gap, PDGS/Processing issue
28/03/2019		x			o	Gap from 03:53:37 to 06:31:32	gap, PDGS/Processing issue
05/04/2019	x		o	o		- MISR, SYN gap: from 11:08:38 to 12:37:56 (89' - incl. night) - Shorter products for MISR, VGP and VGK: with start sensing 20190405T123756 - VG1 starting 20190405T111721 with missing data	RFI, missing data, Svalbard
07/04/2019	x				o	gap from 04:28:58 to 05:13:07	gap, PDGS/Processing issue
08/04/2019		x	o			Degraded gradule from 15:12:26 to 15:15:26	RFI, missing data, Svalbard
08/04/2019		x			o	Gap from 05:04:12 to 05:48:21	gap

Date(s)	Satellite		Instrument			Impact/Description	Keywords
	S3A	S3B	OLCI	SLSTR	IPF SYN		
10/04/2019	x				o	Gap from 03:00:16 to 03:54:16	gap
	x			o		Possible degraded geolocation/misregistration from 09:54:35 to 14:00:09	Geolocation, NAVATT
11-17/04/2019		x		o		Gap from 20190411 11:13:25 to 20190415 10:26:11 Degraded from 20190415 10:26:11 to 20190417 04:29:32	Decontamination, gap, Missing data
17/04/2019	x		o			20190417T203314_20190417T203614	RFI, missing data, Svalbard
19/04/2019		x	o	o		Degraded SYN from 07:05:28 to 07:08:28 and from 07:17:28 to 07:23:28 and VGT with start sensing 07:00:28	RFI, missing data, Svalbard
29/04/2019	x		o	o		Product gap products from 14:05:51 to 16:46:03 pointing errors due to navatt discarded 16:46:03 to 17:27:49	PDGS, missing data
02/05/2019		x		o		Affected garnule 01:37:05 01:40:05 by missing scans	RFI, missing data, Svalbard
08/05/2019	x				o	Gap from 04:22:12 to 05:06:34	gap
09/05/2019	x				o	Gap from 08:22:43 to 09:03:43	gap
2019/05/20 to 2019/05/26	x			o		Ongoing: - Gap from 20190520 11:38:27 to 20190526T113834	Decontamination, gap
24/05/2019		x	o	o		Degraded products from 00:13:58 to 00:19:58 and from 00:43:58 to 00:49:00	missing data, Svalbard
28/05/2019	x		o			Degraded PDU with start sensing 09:20:45	RFI, missing data, Svalbard
29/05/2019		x	o			SYNergy-B impact of OLCI Anomally 2019/05/29 Production (STC and NTC) has a gap from 20190529 13:46:40 to 20190531 12:21:52.	OLCI Anomally, gap

Date(s)	Satellite		Instrument			Impact/Description	Keywords
	S3A	S3B	OLCI	SLSTR	IPF SYN		
29/05/2019 to 02/06/2019	x	x			o	NTC production with gaps for: - S3A from 20190529T023737 to 20190602T102208 - S3B from 20190529T051959 to 20190602T094232 STC producttion complete.	PDGS, gap
05/06/2019		x	o	o		S3B Products affected by Manoeuvre from 06:42:59 to 09:02:06	Manœuvre, Missing data
09/06/2019	x		o			Degraded at PDU time 17:31:27 due to RFI	RFI, missing data, Svalbard
13/06/2019	x		o	o		SYNergy-A degraded by Manoeuvre - 07:15:06 to 11:14:59	Manœuvre
13/06/2019	x		o	o		Degraded PDU starting at 10:43:45 and between 11:07:45 to 11:13:45	RFI, missing data, Svalbard
13/06/2019		x	o	o		Degraded PDU starting at 03:17:11 and between 03:38:11 to 03:44:11	missing data, Svalbard
19/06/2019		x	o	o		Manoeuvre affecting products from 05:39:23 to 09:39:08	Manœuvre
08/07/2019	x		o	o		Production the 20190708 from 13:48:23 to 19:47:59	Svalbard, Antenna
13/07/2019	x		o	o		Degraded geolocation due missing NAVATT from 09:19:13 to 09:56:39	Geolocation, NAVATT
16/07/2019	x		o	o		RFI affecting PDUs 08:18:40 and 09:59:39	RFI, missing data, Svalbard
17/07/2017		x	o	o		Gap from 19:19:25 to 21:57:04 sensing and degraded with missing NAVATT from21:57:04 to 22:41:24	Gap, NAVATT, Geolocation
29/07/2019		x		o		Products with mssing data from 10:14:40 to 10:20:40	missing data, Svalbard
07/08/2019	x		o			RFI affecting PDUs 10:14:32 and from 10:26:32 to 10:32:32	RFI, missing data, Svalbard

Date(s)	Satellite		Instrument			Impact/Description	Keywords
	S3A	S3B	OLCI	SLSTR	IPF SYN		
23/08/2019		x	o	o		RFI affecting PDUs starting at 05:55:03	RFI, missing data, Svalbard
28/08/2019	x		o	o		Manoeuvre affecting products from 10:24:57 to 11:09:09	Manœuvre
28/08/2019		x	o	o		Manoeuvre affecting products from 08:46:26 to 12:50:09	Manœuvre
01/09/2019		x		o		RFI affecting PDU starting 090121	RFI, missing data, Svalbard
03/09/2019 and 04/09/2019		x		o		SLSTR-B Black body cross over test - from 09:30:00 the 03/09/2019 to 20:30:00 the 04/09/2019	SL Black body, degraded accuracy
05/09/2019 and 06/09/2019	x			o		SLSTR-A Black body cross over test - 09:15:00 the 05/09/2019 to 18:30:00 the 06/09/2019	SL Black body, degraded accuracy
05/09/2019	x			o		Gap from 04:58:09 to 07:36:01 sensing and degraded with missing NAVATT from 04:15:30 to 10:01:08	Gap, NAVATT, Geolocation
19/09/2019 to 25/09/2019		x		o		Gap from 20190919 06:37:02 to 20190923 09:19:35; degraded products from 20190923 10:54:17 to 20190925 07:24:24	Decontamination, Gap
26/09/2019		x	o	o		2 orbits missing: 08:13:20 to 11:20:20 and 18:44:12 to 21:23:05	Gap, NAVATT, Geolocation
30/09/2019		x	o			RFI affecting PDU starting at 10:20:33	RFI, missing data, Svalbard
10/10/2019		x		o		S3B Manoeuvre affecting products from 16:59:12 to 19:24:27	Manœuvre
12/10/2019	x		o			Sequence erros affecting PDU starting at 03:22:23	missing data
15/10/2019	x			o		S3A Manoeuvre affecting products from 07:03:48 to 07:47:47	Manœuvre

Date(s)	Satellite		Instrument			Impact/Description	Keywords
	S3A	S3B	OLCI	SLSTR	IPF SYN		
16/10/2019		x		o		S3B Manoeuvre affecting products from 07:38:47 to 08:23:03	Manœuvre
18/10/2019	x		o			RFI affecting PDU starting at 02:23:19	RFI, missing data
30/10/2019	x			o		1 orbit missing from 04:38:41 to 07:16:23 with degraded NTC products between 03:54:24 to 08:00:40	Gap, NAVATT, Geolocation
31/10/2019		x	o	o		RFI affecting PDUs from 09:34:13 to 09:43:13	RFI, missing data
04/11/2019	x			o		RFI affecting PDU starting at 12:30:03	RFI, missing data
11/11/2019	x	x			o	Missiing NAVATT in NTC (recoverable in future reprocessing): SYN-A from 09:42:52 to 10:27:09 SYN-B from 09:03:17 to 09:49:19	PDGS, NAVATT, Geolocation
12/11/2019	x		o			RFI affecting PDUs from 08:23:45 to 08:27:35	RFI, missing data
15/11/2019		x	o			RFI affecting PDU starting at 14:48:26	RFI, missing data
18/11/2019		x	o	o		RFI affecting PDUs from 01:43:04 to 01:48:59	RFI, missing data
27/11/2019	x			o		S3A Manoeuvre affecting products from 06:52:30 to 09:17:43	Manœuvre
02/12/2019	x			o		RFI affecting PDUs from 23:35:42 to 23:41:42	RFI, missing data
11/12/2019	x			o		S3A Manoeuvre affecting products from 10:52:30 to 13:17:39	Manœuvre
18/12/2019		x		o		S3A Manoeuvre affecting products from 07:09:57 to 09:35:02	Manœuvre

End of document